Applications of Laser Ablation Inductively Coupled Plasma Mass Spectrometry to Problems in Mineral Resource Geology

by

Daniel R. Blakemore

A dissertation submitted in partial fulfillment
of the requirements for the degree of
Doctor of Philosophy
(Earth and Environmental Sciences)
in the University of Michigan
2024

Doctoral Committee:

Professor Adam Simon, Chair
Professor Udo Becker
Professor Michael Craig
Professor Robert Holder
Professor Emeritus Stephen Kesler

Daniel R. Blakemore

blakemdr@umich.edu

ORCID iD: 0000-0002-6637-6081

Dedication

This dissertation is dedicated to my primary collaborator in life, Jennifer Reyné Davis. Without hyperbole or overstatement, I confidently say that I could not have done this without you, and I will be forever grateful. Thank you for believing in me.

Acknowledgements

Countless people have been of indefatigable support to me throughout my academic journey. I am truly lucky to have known so many amazingly brilliant and supportive humans.

Firstly, I owe unwavering gratitude to my advisor, Dr. Adam Simon. You are a role model in every sense of the word, possessing a rare combination of sheer brilliance, an extraordinary work ethic, deep compassion, and a firm commitment to making the world a better place. I admire so much about you, and I will be forever grateful for all you have done for my personal and professional life.

Secondly, to Drs. Stephen Kesler, Robert Holder, Udo Becker, and Michael Craig for your graciousness in serving on my committee. I feel so lucky to consider you my mentors, and have greatly enjoyed learning from you, being challenged by you, and for your helpful comments and suggestions to my projects.

To my project collaborators, Irene del Real, Martin Reich, Fernando Barra, John F.H. Thompson, Andrew Kylander-Clark, Willis E. Hames, Alicia M. Cruz-Uribe; and my friends and collaborators at the Gemological Institute of America: Aaron Palke, Ziyin (Nick) Sun, Alex Goodsuhm, Rachelle Turnier. Thank you for your support and encouragement.

Enormous gratitude is owed to my lab family: Chris Emproto, Andrés González, Maria Rodriguez-Mustafa, Jackie Kleinsasser, Allyson Murray, Evan Hirsh, Justin Casaus, José Tomás Ovalle, and Lydia Pinkham (and Natasha and Vladimir). I am honored and humbled to have shared my time at Michigan with the finest, most intelligent, and supportive lab group in the world. Thanks, in particular, to the newly minted doctor, Christopher Robert Emproto. We first met at a GSA sectional conference in 2017 while in undergrad, serendipitously ended up in the same MS program at Miami University and continued our paralleled lives at the University of Michigan in the Simon lab group. Cheers to finishing another degree together and to the inevitably intertwined future we are destined to have. It has been an honor to work (and quarantine) alongside you through the entirety of our graduate education.

To my Masters advisors and mentors at The Miami University (Ohio), Drs. Mark Krekeler, Claire McLeod and John Rakovan. Thank you all so much for providing me with the

most amazing education and experiences. I learned an incredible amount and I cherish my time at Miami because of you.

To Drs. Ralph Stearley, Gerry VanKooten, C. Renee Sparks and the entire faculty of Calvin University's Geology department. Never in my life have I felt more at home than my four years learning from you. Additional thanks to the Dice Family: Bruce, Carol, and Kevin, for your incredibly generous support of Calvin's geology department, and for your investment in my life. I will remember Bruce forever.

To John Christians of Grand Rapids Christian High School, my first mentor, who introduced me to the world of science and inspired my high-school self to set my goals high. Thank you for providing a space in AP chemistry and Science Olympiad for socially awkward kids like me to find community and their life-long professional interests.

To my mother Linda, my father John (Dr. B Sr.) and stepmom Diane. I am so lucky to have three endlessly supportive parents. To my favorite sibling Steph, thank you for always having my back. And to my dear friends Sam, Jack, Devin, Isaac—thank you for everything.

And lastly to Jenn Davis, to whom this dissertation is dedicated. You are the brightest, most driven, and overall, most amazing person I have ever known. Thank you for getting me to the finish line.

Table of Contents

List of Tables

List of Figures

List of Appendices

Abstract

Mining has been a defining driver of human progress since the beginning of organized civilization. Minerals extracted from the Earth not only gave humans the means to create tools and weapons, but ornamental gemstones and metals add to the rich culture we share as a species. Today, the need and desire for mining precious resources has never been higher. This demand results in an undeniable need to focus time, energy, and resources in the exploration of new deposits, and to better understand those deposits we currently rely on. This is the aim of mineral resource geochemistry: to better understand where, why, and how economically important mineral deposits form. This can be done via the analysis of the chemistry found within individual minerals from these deposits. Understanding the trace elements and specific isotopes that comprises a mineral—like a unique fingerprint—allow us to gain tremendous insights and draw broad conclusions on resource formation from microscopic amounts of sample material. It can be argued that no instrument more profoundly transformed the field of geochemical research than the laser ablation inductively coupled plasma mass spectrometer (LA-ICP-MS). Its ease of use, moderate cost, relatively rapid data collection compared to other geochemical techniques, ability to maintain spatial context within samples, and minimal sample preparation needed makes the LA-ICP-MS one of the most powerful tools in the geochemist's arsenal.

This dissertation investigates distinct applications of LA-ICP-MS to mineral resource and gemological research, the results of which add to our understanding of geologic resource formation and mineral provenance determination. Chapter 2 highlights the power of LA- ICP-MS *in situ* U–Pb dating for elucidating the geochronology of the Candelaria iron oxide-copper- gold deposit in Northern Chile. This is coupled with other geochronological techniques for a comprehensive study of the temporal evolution of one of the most important copper mines in the world. Chapters 3 and 4 utilize a comprehensive suite of LA-ICP-MS collected trace element data and a random forest machine learning algorithm to effectively determine the provenance of different gemstone material to a hyper-specific degree: Colombian emeralds and euclase in chapter 2, and Montana, USA,

sapphires in chapter 4. The results of this dissertation highlight the effectiveness, broad-reaching application, and versatility of LA-ICP-MS as a tool in mineral resource geology.

Chapter 1: Introduction

1.1 Introduction

Mining has been the defining driver of human progress since the beginning of organized civilization. So much so, that ages of antiquity are defined in terms of the dominant resource of the day: stone, copper, bronze, iron. Minerals extracted from the Earth not only gave humans the means to create tools and weapons, but ornamental stones and metals add to the rich culture we share as a species. Today, the need and desire for mining precious resources has never been higher. Precious metals such as lithium, cobalt, and rare earth elements are essential for modern day electronics we all enjoy on a daily basis. Iron is used to create steel for buildings and infrastructure and this demand is projected to substantially increase by as much as triple the demand between 2010 and 2050 as population increases force the demand for more infrastructure (Elshkaki et al., 2018). In 2023, 22,000 metric kilotons of copper were mined for important infrastructure, electrical and electronic equipment, and transportation (USGS, 2024). This resource is not only important for maintaining current infrastructure and equipment but copper is critical for generating renewable energy technology such as wind turbines, solar panels, and electric cars to move society towards renewable resource utilization. Copper is one of the resources with the fastest growing demand and this demand is projected to increase by 2-3% per year from now to 2050 (Kupiers et al., 2018). Additionally, the gemstone industry was valued at an estimated $33.38 billion (USD) in 2023 and is projected to increase to $55.96 billion by 2033 (Verghese, 2023). This demand results in an undeniable need to focus time, energy and resources in the exploration of new deposits, and to better understand those deposits we currently rely on.

This is the aim of economic geochemistry: to better understand where, why, and how economically important mineral deposits form. This can be done via the analysis of the chemistry found within individual minerals from these deposits. Understanding the trace elements and specific isotopes that comprises a mineral—like a unique fingerprint—allows us to gain tremendous insights and draw broad conclusions on resource formation from microscopic amounts of sample material.

It can be argued that no instrument more profoundly transformed the field of geochemical research than the laser ablation inductively coupled plasma mass spectrometer (LA-ICP-MS). The LA-ICP-MS allows for the relatively rapid collection of trace element and isotopic data, with a key advantage of preserving the geologic context of the sample via in-situ measurements. It is considered a semi destructive technique as it requires only a very small amount of material—leaving permanent ablation spots around 10-100 micrometers in diameter and typically about 10-50 micrometers in depth. Very simply, it works by a laser pulse ablating a sample and carrying the aerosolized particulate into an argon plasma, which then strips the electrons from the atoms in the particulate cloud, thereby ionizing them. The ionized material is then transported to a mass spectrometer which segregates the ionized material based on mass and charge. Since this information is unique to each element, elemental concentrations can be derived from this information. The combination of its ease of use, moderate cost, relatively rapid data collection compared to other geochemical techniques, ability to maintain spatial context within samples, and minimal sample preparation needed makes the LA-ICP-MS one of the most powerful tools in the geochemist's arsenal.

This dissertation investigates distinct applications of LA-ICP-MS to mineral resource and gemological research with resulting implications which add to our understanding of geologic resource formation and mineral provenance determination. Chapter 2 highlights the power of LA-ICP-MS *in situ* U–Pb dating for uncovering the geochronology of the Candelaria iron oxide-copper-gold deposit in Northern Chile. This is coupled with other geochronologic techniques for a comprehensive study of the temporal evolution of one of the most important copper mines in the world. Chapters 3 and 4 utilize a comprehensive suite of LA-ICP-MS collected trace element data and a random forest machine learning algorithm to effectively determine the provenance of different gemstone material to a hyper-specific degree: Colombian emeralds and euclase in chapter 2, and Montana, USA, sapphires in chapter 4. The results of this dissertation highlight the effectiveness, broad-reaching application, and versatility of LA-ICP-MS as a tool in mineral resource geology.

1.2 Laser Ablation Inductively Coupled Plasma Mass Spectrometry (LA-ICP-MS)

The idea for coupling a laser ablation system to a inductively coupled plasma mass spectrometer was first demonstrated by Allan Gray, in 1985 (Gray 1985), transforming the field of

in situ chemical analysis. A laser ablation system needs to have the ability to ablate target material by a photo-chemical process rather than physical disaggregation, and then be able to deliver target material to the inductively coupled plasma (ICP) in particles small enough that the plasma can be completely vaporized and ionized in order to avoid volatility related elemental and isotopic fractionation (Sylvester and Jackson 2016). Neodymium doped yttrium-aluminum garnets (Nd: YAG) are among the most common lasing mediums used in modern ablation systems, and typically operate in the deep ultraviolet range with wavelengths typically at 193 nm or 213 nm. Ruby (red corundum) interestingly, is also a lasing medium that was used in earlier LA-ICP-MS systems (e.g. Gray, 1985; Arrowsmith, 1987) and emitted photons in the visible light spectrum as a deep red color (693 nm). Shorter wavelength (and therefore higher energy) ultraviolet lasers are preferable to the longer because more materials can absorb higher energy photons, which results in a better ablation.

Once aerosolized by the laser ablation system, the particulate cloud is transported to the ICP by a carrier gas, most commonly helium, which is a non-reactive gas and is not an element of interest to measure using this system. The argon plasma torch of the inductively coupled plasma reaches extremely high temperatures at around ~6,000◦ K, approximately the surface temperature of the sun—hot enough to ionize most elements. Newly ionized material is then focused into a stream using a series of lenses and cones and are passed through into the mass spectrometer.

Most ICP-MS systems in use today are quadrupole mass spectrometers and single collector sector field mass spectrometers. The most common type of mass spectrometer (MS) used with LA-ICP-MS is a quadrupole MS, whose primary function is the collection of trace elements. The basis of a quadrupole MS is measuring the mass/charge (m/z) ratio of the ionized stream. The heart of the quadrupole consists of four parallel rods, two with negative potentials and two with positive potentials. These poles generate an oscillating quadrupolar electrical field from a combination of imputed direct current and radio frequency voltages. Ions pass through this field, and depending on their m/z, follow either a stable or unstable path. The precise control of the frequency voltages allow only ions with a specific m/z ratio to pass through the entire length of the quadrupole (stable path). Those ions that make it through the quadrupole are detected by an electron multiplier, which converts the ion signal to an electrical signal to be processed.

The multi-collector ICP-MS, while less common, is still deeply important for geological science. The multi collector allows for the highly precise collection of U and Pb isotopes, which is the basis for dating many different U-bearing minerals. After the ionized beam is transported out of

the ICP torch, the beam passes through a magnetic sector field which separates the ions based on their m/z ratio. This separation is needed to isolate the specific isotopes of interest. The separated ions are simultaneously detected by multiple collectors, each one dedicated to its own m/z ratio. The simultaneous isotope measurements reduce error associated with signal drift over time, which can be an issue with quadrupole MS, and is what allows this method to have enough precision for geochronology with U–Pb isotopes. Certain highly specialized laboratories are capable of splitting the ion stream from the ICP and sends half of the stream to a quadrupole MS, and half to a multi-collector, allowing for the collection of U–Pb isotopes for geochronology and trace elements simultaneously from the same sample spot, in a system aptly called split stream LA-ICP-MS (Kylander-Clark, 2013).

The ability to preserve geologic context within a sample is arguably the most important virtue of the LA-ICP-MS system for geologic research. Selecting spots to analyze within a polished thin section or epoxy mount allows the researcher to carefully pick and choose which minerals to hit without requiring individual mineral separation. This is particularly important in chapter 2 of this dissertation, where LA-ICP-MS spots were carefully chosen on datable accessory minerals, while maintaining the cross-sectional veinlet contexts, and other mineral-mineral relationships. The relatively small sample size required can also allow for future analysis to be completed on the very same samples.

The advantages of this technique for Earth science is obvious. In addition to trace elemental analysis with spot analysis quadrupole MS, or age dating with multi-collector MS, geochemists are finding ever increasingly creative ways of utilizing LA-ICP-MS, such as with fluid inclusion studies (e.g. Rusk et al., 2004; Catchpole et al., 2011; Chang et al., 2018; Zhao et al., 2020; Xie et al., 2023;), 2D chemical mineral mapping (e.g. Ubide et al., 2015; Dubosq et al., 2018; Chew et al., 2021; Chernonozhkin et al., 2021), and 3D chemical mapping (e.g. Słaby et al., 2011; Chirinos et al., 2014). Being able to obtain rapid, high-resolution elemental and isotopic data, while preserving geologic context is an invaluable tool for geologic research.The moderate financial cost of operation and general ubiquity across laboratories around the world also add to the plethora of advantages, and its importance is the common thread between each chapter in this dissertation.

1.3 Random Forest machine learning

No technology has quite captured the attention of society in recent years more so than the rapid advances in artificial intelligence (AI), specifically generative AI tools such as Open AI's (owned by Microsoft) ChatGPT or Google's Bard. Artificial intelligence is broadly defined as the capability of computer systems or algorithms to imitate intelligent human behavior, and machine learning (ML) can be thought of as a subset of AI which enables a computer to learn and perform tasks by analyzing a large dataset without being explicitly programmed (Merriam-Webster, 2024). Machine learning can be further subdivided into two subgroups: Supervised ML and unsupervised ML. Unsupervised ML algorithms use unlabeled data to find underlying structure (i.e. groupings, clusters, correlations) in data without pre-labeled input. Examples of popular unsupervised ML algorithms include: K-means clustering analysis, principal component analysis, hierarchical clustering, and Apriori algorithm. Supervised ML algorithms learn from a labeled dataset and are useful for solving classification problems. Some of the most widely used supervised ML algorithms include: Linear regression analysis, support vector machines, logistic analysis, naive Bayes, K-nearest neighbors, neural networks, adaptive boosting, decision tree classification, and random forest classification.

A major part of this dissertation involves the processing of LA-ICP-MS geochemical data in order to find patterns and derive meaning. As explained in detail in chapters 3 and 4, a random forest classification (RFC) machine learning model was determined to be the most appropriate, and most effective method for parsing large suites of LA-ICP-MS elemental data in regards to mineral provenance determination. The RFC model falls under the category of Classification and Regression Tree (CART) family of supervised machine learning algorithms, which is defined by the decision tree structure that aims to elucidate differences in a data set by variable to sort into categories via a branching list of boolean True/False questions. A decision tree starts with a root node, a variable which is then split into 2 paths (also called branches): a greater than or equal to, or a less than path in the case of quantitative data such as elemental concentrations. Each branch leads to another boolean True/False question called a "node" or "leaf", and the process of splitting continues recursively until there are no more features to split. One of the mathematical ways this algorithm decides where to split data is by using the Gini impurity—a measure of how often a randomly chosen element from the set would be incorrectly labeled if it was randomly labeled according to the distribution of the subset. The gini impurity can be calculated as follows:

$$1 - \sum_{i=1}^{C} (P_i)^2$$

Where P_i represents the proportion of the samples that belong to class *i* in a given set, and c equal to the number of classes. A gini impurity is calculated for each potential split, and chooses the one with the lowest value. The goal is to limit the Gini impurity. The relative simplicity and computational brevity of this equation makes it a popular option for CART algorithms, and also serves as the basis for calculating variable importance.

Another important principle of CART machine learning is the partitioning of data into testing and training data. Training data, as the name suggests, is used to train and develop the model. In supervised ML, the data is pre-labeled into classifications, and the training data is used to iteratively make predictions on which variables correspond to which category. Testing data is completely independent of this process, and is separated from the dataset before training. This data is later used to validate the effectiveness of the trained model by parsing unknown data through the trained model. Common data partitions are between 70-80% training, and 20-30% testing.

Stratified sampling is another important parameter of CART algorithms, especially when dealing with large datasets or with imbalanced classes (non-homoscedasticity). Stratified sampling ensures that each class is sampled representatively. This is critically important when building a model to ensure that both training data and testing data have elements from each class.

Evaluating the effectiveness of the ML model is of the utmost importance before practical implementation. One of the methods of doing so is cross validation. Cross validation first splits the data "k" number of times, into equal sized segments, or "folds". In the studies included in this dissertation, k = 10. For each unique group, the model is trained on k minus 1 folds, as the training set, then is validated on the remaining sets. This process is repeated k number of times, each using a different fold as the testing set. K-fold cross validation evaluates the effectiveness of the model with the metrics: Precision, recall, F1 score, and accuracy.

Precision, as a metric, is equal to the ratio of true positives over true positives plus *false positives*. Recall is similar to precision, but instead measures the ability of a model to capture actual

positives, with the ratio of true positives over true positives plus *false negatives.* The F1 score is the harmonic mean of the precision and recall, providing an overarching measure which balances both metrics, and is calculated as the precision multiplied by recall, then divided by the precision plus the recall, all multiplied by 2. Accuracy is arguably the most important metric for model evaluation, as it measures the overall correctness of the model, and is calculated by the true positives plus true negatives, divided by the total cases. Taken together these metrics help determine the overall effectiveness of a ML model.

The RFC is an ensemble learning model which builds off the decision tree structure (Breiman, 2001). This model constructs a multitude of individual decision trees, which all "vote" on a classification, and the classification with the most votes is the consensus pick. The RFC model has several key advantages over a single decision tree and other types of machine learning. First, and most importantly for handling high-dimensional data, is that it reduces overfitting. A single decision tree has a tendency to make arbitrary splits in the data to achieve a separation. Overfitting can be easily observed in a ML model by comparing the testing accuracy to the training accuracy. Ideally, these accuracies should be the same. However, almost always the training dataset will have a higher accuracy than the testing set. If the gap in accuracies between training and testing datasets are large, this is a clear indication of overfitting. The RFC can still have problems with overfitting if data is particularly noisy, but by relying on hundreds to thousands of decision trees, the risk of overfitting is minimized.

Other major advantages of using a RFC model is that the underlying assumptions required for many other statistical analyses are unneeded. For example, the need for homoscedasticity, and non-co-linearity which are required for parametric machine learning algorithms such as linear discriminant analysis, linear regression, support vector machines, among others. It can also incorporate non-quantifiable data, which presents opportunities for qualitative observations to be included in the model.

For a large geochemical dataset with potentially many elements and elemental ratios of interest, and a classification and prediction problem like mineral origin determination, the RFC model shows remarkable potential as will be discussed in chapters 3 and 4.

1.4 Applications of LA-ICP-MS to problems in mineral resource geology

The duality of the LA-ICP-MS to be used for geochronology and trace element studies makes it one of the most powerful tools available in geochemistry. It is especially powerful in economic geology where information regarding the formation of deposit timing and source can be derived from the chemical makeup of key minerals.

In chapter 2 of this dissertation, a multi-collector LA-ICP-MS is used to measure U and Pb isotopes of the minerals apatite, titanite, and magnetite from drill core samples from the Candelaria iron-oxide copper gold (IOCG) deposit located in northern Chile. Apatite ($Ca_5(PO_4)_3$ (F,Cl, OH)) and titanite ($CaTiSiO_5$) are common accessory minerals dated via U–Pb geochronology. Magnetite is not traditionally used as a geochronometer but was experimentally dated via U–Pb. These techniques are used in concert with Ar-Ar dating of the amphibole mineral actinolite ($Ca_2(Mg,Fe)_5Si_8O_{22}(OH)_2$) in an attempt to uncover new insights into the temporal evolution of the world class Candelaria IOCG deposit located in Northern Chile.

Understanding the formational history of IOCG deposits is a prominent topic of debate in the economic geology community, and is of broad societal importance as this type of deposit is a major source of copper globally. The geochronologic results provide insights into the temporal history of mineralization in the Candelaria IOCG deposit and improve the understanding of the evolution of this world-class mineral system.

In chapters 3 and 4 of this dissertation, I explore the other face of the LA-ICP-MS: its trace elemental capabilities using Quadraopole LA-ICP-MS. In the gemstone industry one of the most pressing issues is how to more accurately, and more specifically identify the provenance of a mineral (e.g. McClure et al, 2019, Vertriest et al. 2019). As is evident from the service offered at gem laboratories, there is a strong demand from consumers to know where their gemstones are from. Motivating factors which enhance the perceived value of a gem include the prestige of locality, ensuring the authenticity, personal or cultural significance, or wanting to have a documented anthropological history or story attached to an heirloom. In addition to the potential personal benefit to consumers, being able to reliably fingerprint a valuable mineral using its intrinsic and unchanging properties can also be an invaluable ethical tool used to prevent gems from mines using unethical practices from spreading on the market (i.e. conflict gems). Being able to better predict a mineral's provenance also has massive implications in exploration geology and mineral prospectivity (e.g. Rodriguez-Galiano et al. 2015, O'Brian et al, 2015; McKay and Harris,

2016; Hong et al., 2021, Bédard et al., 2022). For gemological laboratories, the motivation behind pursuing mineral origin research is to ensure the public's trust within the industry, and thus much effort is taken to develop reliable testing methodologies.

In order to make predictions on unknown minerals, a reliable methodology must be in place for pre-existing and meticulously documented samples. In the gemstone industry, obtaining samples with reliable provenance to use as reference poses a significant obstacle to developing such methods, as by their nature, gem material is rare, expensive, easy to transport leading to mistakes in tracing, and can come from areas of the world with varying degrees of political stability. The Gemological Institute of America (GIA) uses a grading system (A-F) to record the reliability of a gemstone's known provenance, with an A grade meaning a researcher from the GIA personally collected and documented the origin, an "F" rating given to a gem purchased from a vendor at an international market such as the annual Tucson gem and mineral show, and a "Z" grade meaning the location information is completely lost, unknown, or its information is put into doubt (Vertriest et al. 2019). While an A grade is obviously the gold standard of origin confidence, realistically for database compilation, B-C grade where gemstones are witnessed, purchased or collected from a trusted source near the mine are also generally acceptable confidence levels. Additionally, it may not even be possible to self-collect as many mines have shut down, or are otherwise inaccessible. Regardless of the degree of confidence in a gemstone's origin, the most important responsibility of a gem laboratory, museum or academic collection is to properly preserve these metadata.

Any instrument capable of obtaining chemical data can be used as a basis for a database. Common non-destructive methods include electron microprobe analysis, Raman spectroscopy, and x-ray fluorescence spectroscopy. The most limiting factor with these techniques is the relatively high elemental detection limit. More sensitive techniques such as thermal ionization mass spectrometry, solution ICP-MS are capable of much lower detection limits and the ability to measure specific isotopes, but are often highly destructive and very expensive. For the price of a small ablation hole barely visible to the eye, the LA-ICP-MS offers trace elemental resolution (down to parts per million and billion), quickly, at a moderate financial cost. Even on gem quality material, a carefully placed ablation spot is virtually undetectable to the human eye, which is why this is an ideal method to be used on precious samples such as gemstones.

Chapter 3 details the development of a hyper-specific provenance method applied to emeralds from Colombia. Colombian emeralds were chosen as the test samples for a number of reasons. Firstly, there is a strong desire in the gemstone industry to better understand where a

Colombian emerald comes from, as certain deposits carry more perceived value than others (i.e. Emeralds from the Muzo mining district in Colombia). Secondly, between the gem laboratories of Technological Development Center for the Colombian Emerald (CDTEC) and the Gemological Institute of America (GIA), a comprehensive suite of first-hand geolocated emeralds were available. Third, the differing mining area classifications allowed us to test origin determination capabilities at 3 increasing levels of specificity: (1) The mining belt (east and west) which have similar, yet unique geology, (2) the mining district, of which there are 9, and (3) the individual mine—in this study 40 mines were sampled and studied.

The successful provenance discrimination determined at each level as detailed in chapter 3, set the basis for the new complementary study outlined in chapter 4, where this method was applied to a different mineral system with alluvial and primary igneous sapphires (corundum) deposits in Montana, USA. By repeating this methodology on a different mineral system, new insights to this provenance determination methods were discovered, for example the consistent success of the RFC model as a way to determine mineral provenance on applied to quadrupole LA-ICP-MS data, and some of the limitations of using a mineral which has fewer sites for trace elemental substitution than does emerald. In both chapters 3 and 4, in addition to answering the question of "where does a mineral come from", geochemical data can also shed valuable insights into the underlying geologic processes of formation. With the case of Colombian emeralds, the heterogeneity of V and Cr between the two mining belts was a major result. And with the Montana sapphire study, the importance of Mg/Ti as an indicator of the primary formational oxygen fugacity was discovered. These chapters can act as a blueprint for future mineral origin determination studies.

Using both the geochronological and trace elemental capabilities of the LA-ICP-MS, this dissertation will demonstrate its incredible usefulness in application to problems in mineral resource geology.

1.5 References

Arrowsmith, Peter. (1987) Laser ablation of solids for elemental analysis by inductively coupled plasma mass spectrometry. Analytical Chemistry, 59, 1437–1444.

Bédard, É., De Bronac de Vazelhes, V., and Beaudoin, G. (2022) Performance of predictive supervised classification models of trace elements in magnetite for mineral exploration. Journal of Geochemical Exploration, 236, 106959.

Breiman, L. (2001) Random Forests. Machine Learning, 45, 5–32.

Catchpole, H., Kouzmanov, K., Fontboté, L., Guillong, M., and Heinrich, C.A. (2011) Fluid evolution in zoned Cordilleran polymetallic veins — Insights from microthermometry and LA-ICP-MS of fluid inclusions. Chemical Geology, 281, 293–304.

Chang, J., Li, J.-W., and Audétat, A. (2018) Formation and evolution of multistage magmatic-hydrothermal fluids at the Yulong porphyry Cu-Mo deposit, eastern Tibet: Insights from LA-ICP-MS analysis of fluid inclusions. Geochimica et Cosmochimica Acta, 232, 181–205.

Chernonozhkin, S.M., McKibbin, S.J., Goderis, S., Van Malderen, S.J.M., Claeys, P., and Vanhaecke, F. (2021) New constraints on the formation of main group pallasites derived from *in situ* trace element analysis and 2D mapping of olivine and phosphate. Chemical Geology, 562, 119996.

Chew, D., Drost, K., Marsh, J.H., and Petrus, J.A. (2021) LA-ICP-MS imaging in the geosciences and its applications to geochronology. Chemical Geology, 559, 119917.

Chirinos, J.R., Oropeza, D.D., Gonzalez, J.J., Hou, H., Morey, M., Zorba, V., and Russo, R.E. (2014) Simultaneous 3-dimensional elemental imaging with LIBS and LA-ICP-MS. Journal of Analytical Atomic Spectrometry, 29, 1292–1298.

Dubosq, R., Lawley, C.J.M., Rogowitz, A., Schneider, D.A., and Jackson, S. (2018) Pyrite deformation and connections to gold mobility: Insight from micro-structural analysis and trace element mapping. Lithos, 310–311, 86–104.

Hong, S., Zuo, R., Huang, X., and Xiong, Y. (2021) Distinguishing IOCG and IOA deposits via random forest algorithm based on magnetite composition. Journal of Geochemical Exploration, 230, 106859.

Kylander-Clark, A.R.C., Hacker, B.R., and Cottle, J.M. (2013) Laser-ablation split-stream ICP petrochronology. Chemical Geology, 345, 99–112.

L. Gray, A. (1985) Solid sample introduction by laser ablation for inductively coupled plasma source mass spectrometry. Analyst, 110, 551–556.

McClure, S.F., Moses, T.M., and Shigley, J.E. (2019) The Geographic Origin Dilemma | Gems & Gemology, 55, 457–462.

McKay, G., and Harris, J.R. (2016) Comparison of the Data-Driven Random Forests Model and a Knowledge-Driven Method for Mineral Prospectivity Mapping: A Case Study for Gold Deposits Around the Huritz Group and Nueltin Suite, Nunavut, Canada. Natural Resources Research, 25, 125–143.

Merriam-Webster (2024, January 11) Definition of artificial intelligence.

O'Brien, J.J., Spry, P.G., Nettleton, D., Xu, R., and Teale, G.S. (2015) Using Random Forests to distinguish gahnite compositions as an exploration guide to Broken Hill-type Pb–Zn–Ag deposits in the Broken Hill domain, Australia. Journal of Geochemical Exploration, 149, 74–86.

Rodriguez-Galiano, V., Sanchez-Castillo, M., Chica-Olmo, M., and Chica-Rivas, M. (2015) Machine learning predictive models for mineral prospectivity: An evaluation of neural networks, random forest, regression trees and support vector machines. Ore Geology Reviews, 71, 804–818.

Rusk, B.G., Reed, M.H., Dilles, J.H., Klemm, L.M., and Heinrich, C.A. (2004) Compositions of magmatic hydrothermal fluids determined by LA-ICP-MS of fluid inclusions from the porphyry copper–molybdenum deposit at Butte, MT. Chemical Geology, 210, 173–199.

Słaby, E., Śmigielski, M., Śmigielski, T., Domonik, A., Simon, K., and Kronz, A. (2011) Chaotic three-dimensional distribution of Ba, Rb, and Sr in feldspar megacrysts grown in an open magmatic system. Contributions to Mineralogy and Petrology, 162, 909–927.

Sneha Verghese (2023) Gemstone Market Outlook. Future Market Insights.

Sylvester, P.J., and Jackson, S.E. (2016) A Brief History of Laser Ablation Inductively Coupled Plasma Mass Spectrometry (LA–ICP–MS). Elements, 12, 307–310.

Ubide, T., McKenna, C.A., Chew, D.M., and Kamber, B.S. (2015) High-resolution LA-ICP-MS trace element mapping of igneous minerals: In search of magma histories. Chemical Geology, 409, 157–168.

Vertriest, W., Palke, A., and Renfro, N. (2019) Field Gemology: Building a Research Collection and Understanding the Development of Gem Deposits | Gems & Gemology. Gems & Gemology, 55, 490–511.

Xie, W., Zeng, Q.-D., Huang, L.-L., Zhou, L.-L., Fan, H.-R., Wu, J.-J., Wang, R.-L., and Zhu, H.-P. (2023) Composition and evolution of ore-forming fluids in the Sansheng porphyry W-Mo deposit, Inner Mongolia, NE China: Evidence from LA-ICP-MS analysis of fluid inclusions. Ore Geology Reviews, 158, 105481.

Zhao, Z.-H., Ni, P., Sheng, Z.-L., Dai, B.-Z., Wang, G.-G., Ding, J.-Y., Wang, B.-H., Zhang, H.-D., Pan, J.-Y., and Li, S.-N. (2020) Thermal regime reconstruction and fluid inclusion LA–ICP–MS analysis on intermediate-sulfidation epithermal Pb–Zn veins: Implications for porphyry Cu deposits exploration in the Xianhualing District, Anhui, China. Ore Geology Reviews, 124, 103658.

Chapter 2: The Temporal Evolution of the Candelaria Iron Oxide - Copper - Gold (IOCG) System, Chile: Insights from in situ U–Pb LA-ICP-MS of Apatite, Titanite, Magnetite and Ar/Ar of Actinolite

Co-authors: Maria A. Rodriguez-Mustafa, Irene del Real, Adam C. Simon, Robert M. Holder, Martin Reich, Fernando Barra, John F.H. Thompson, Andrew Kylander-Clark, Willis E. Hames, Alicia M. Cruz-Uribe

2.1 Abstract

Iron oxide-copper-gold (IOCG) and iron oxide-apatite (IOA) deposits are important sources of Cu and Fe, respectively, and in some deposits, by-product metals such as Ti, V, Co, U, Au, Ag, and rare earth elements (REE). Studies have interpreted the spatial and temporal relationship between IOCG and IOA deposits to indicate that both deposits are members of a single mineralizing system. The Candelaria IOCG deposit in Chile documents evidence of episodic pulses of magmatic-hydrothermal fluids that produced early magnetite- and actinolite-rich IOA-type mineralization that was overprinted by a later copper-rich fluid precipitating magnetite-, actinolite- and Cu-Fe- sulfide-rich IOCG mineralization. We tested this episodic formation hypothesis by dating actinolite–hornblende, apatite, magnetite, and titanite in samples from a 1,132 m drill core. Isotopic ratios of U and Pb in apatite, titanite, and magnetite were determined by laser ablation inductively coupled plasma mass spectrometry (LA-ICP-MS), and $^{40}Ar/^{39}Ar$ from an actinolite–hornblende sample. Apatite and titanite dates are generally consistent with published Re–Os dates for molybdenite of c. 115 Ma, which is the interpreted age of main-stage Cu-sulfide mineralization. The $^{40}Ar/^{39}Ar$ date for the actinolite-hornblende sample is 121.2 ± 0.6 Ma, and magnetite grains yielded U–Pb dates between 122.2 ± 7.9 and 147.5 ± 10.6 Ma. Together, the dates obtained for actinolite-hornblende, apatite, magnetite, and titanite provide evidence of episodic pulses of magmatic-hydrothermal mineralizing fluids forming the Candelaria deposit.

2.2 Introduction

Iron oxide-copper-gold (IOCG) and iron oxide-apatite (IOA) deposits host a diverse array of critical elements for modern technology and renewable energy, such as Cu, Fe, P, rare earth elements (REEs), Co, Au and U (e.g., Hitzman, 2000; Williams et al., 2005; Sillitoe, 2003; Groves et al., 2010; Barton, 2014; Reich et al., 2022). Copper is of particular global concern because it is the backbone for the global electricity infrastructure (Elshkaki et al., 2016). As global electricity demand increases and society transitions to renewable energy infrastructure such as utility scale solar and wind, the demand for copper is forecasted to increase between 275% and 350% by 2050 technologies (Kesler and Simon, 2015, Elshkaki et al., 2016). The increase also considers the global adoption of electric vehicles and grid-scale battery storage, among others. Thus, understanding the formation of copper-bearing mineral deposits is critical for improving the discovery of deposits necessary for sustainable production of copper from primary resources.

Although IOCG and IOA deposits are considered separate deposit types, several studies have suggested a genetic relationship in which IOA style mineralization represents the root of a larger, vertically connected, evolving IOA-IOCG deposit system (e.g., Espinoza et al., 1998; Sillitoe, 2003; Reich et al., 2016; Bilenker et al., 2016; Barra et al., 2017; Rodriguez-Mustafa et al., 2020; Reich et al., 2022). A key location to test this hypothesis is Chilean Iron Belt, and particularly, the Candelaria IOCG deposit in northern Chile (Fig. 2-1), where recent studies have proposed that IOA and IOCG mineralization styles may represent temporally distinct hydrothermal stages of the same system (del Real et al., 2021). The Candelaria mine in the Punta del Cobre district is one of the largest IOCG deposits in the world, containing > 743 Mt measured and infered reserves of Cu (Banerjee et al., 2023). Primary Cu mineralization in this district is hosted in the Punta del Cobre Formation, an Early Cretaceous, volcanic-clastic sequence (c. 135–132 Ma) overlain by marine sediments of the Chañarcillo Group that span between 132 and 130 Ma (del Real et al., 2018). The crustal-scale Atacama sinistral strike-slip fault system appears to have controlled fluid flow and mineralization in Candelaria as well as IOCG and IOA deposits in other parts of the Coastal Cordillera of northern Chile (del Real et al., 2018 and references therein). Previous work documented evidence that supports two discrete stages of mineralization at Candelaria: an earlier sulfide-poor, magnetite-, and actinolite-rich IOA style and a later magnetite-, actinolite-, biotite-, Cu-Fe-sulfide-rich IOCG stage (Rodriguez-Mustafa et al., 2020; del Real et al., 2021). Fe concentrations measured in Candelaria actinolite, which has been suggested to indicate changes in temperature (Lledó and Jenkins, 2008), suggest at least two distinct magmatic-

hydrothermal events in the Candelaria system, wherein actinolite grains record a first hotter growth event, overgrown by a subsequent hot, but lower temperature growth event, which could be explained by growth from two distinct pulses of magmatic-hydrothermal fluid flow within the Candelaria system (del Real et al., 2021).

This study tests the multi-episodic formation hypothesis by constraining the timing of hydrothermal events at Candelaria. We collected samples from a 1,132 m drill core that vertically traverses the Candelaria deposit extending from shallow Cu-Fe-sulfide IOCG mineralization and transitioning to magnetite–actinolite rich IOA-style mineralization with depth. U–Pb isotope ratios of apatite, magnetite, and titanite in thin sections from varying depths in the drill core (133 m to 1132 m) were measured via *in-situ* laser ablation inductively coupled plasma mass spectrometry (LA-ICP-MS). The geochronologic results provide insights into the temporal history of mineralization in the Candelaria IOCG deposit and improve the understanding of the evolution of this world-class mineral system.

2.3 Analytical Methods

Actinolite–hornblende in solid solution, apatite, magnetite, and titanite were documented using back scattered electron (BSE) imaging and energy dispersive X-ray spectrometry (EDS) on a JEOL JSM-7800F field emission scanning electron microscope (SEM) at the University of Michigan. A relatively coarse amphibole with actinolite–hornblende solid solution was also analyzed with a JEOL JXA-8600 electron microprobe at Auburn University. U–Pb isotopic ratios of apatite, magnetite, and titanite grains were measured analyzed *in-situ* by LA-ICP-MS. All apatite, all magnetite, and 3 of 7 titanite samples from four depths were analyzed via laser-ablation split-stream (LASS) ICP-MS using a Cetac/Teledyne Photon Machines 193 nm excimer Analyte laser with a HelExII cell connected to a Nu Instruments Plasma HR-ES MC-ICP-MS and an Agilent 7700X at the University of California, Santa Barbara following the procedures of Kylander-Clark et al. (2013) and Kylander-Clark (2020). Reference materials for analysis (run at standard intervals throughout each session) include MAD-UCSB (primary U-Pb ap; Apen et al., 2021), Durango (Paul et al., 2021), BRZ-1 (Apen et al., 2021), NIST612 (primary U-Pb mag; primary TE ap, ttn), BHVO (primary TE mag), MKED-1 (primary U-Pb ttn; Spandler et al., 2016), Y1710C5 (Spencer et al., 2013), BLR-1 (Aleinikoff et al., 2007) and Fish Canyon ttn (Schmitz and Bowring, 2001). Calculated ages for secondary reference materials for apatite and titanite were well

within 2% of their accepted values, and as such, final ages reported for unknowns should be accurate to the long-term reproducibility of 2%. Because no reference material yet exists for magnetite, NIST 612 glass was used as the reference material for U-Pb reduction (Kylander-Clark, 2020); because of this, accuracy can vary systematically from session to session so, relative ages may be comparable within each session, but are only qualitative from session to session. Titanite grains from four additional depths were analyzed using a NWR193UC Excimer laser coupled to an Agilent 8900 ICP-MS at the University of Maine, Orono. All data were processed using the commercially available software Iolite (Paton et al., 2011). Reported measurements are weighted mean ages and uncertainties are 2σ. Measurements were not corrected for common Pb to reduce uncertainty. Calculated U–Pb dates are the 95% confidence intervals of lower discordia intercepts.

No matrix-matched U–Pb reference material is available for magnetite U–Pb dating; therefore, magnetite dates were calculated using Mud Tank zircon standard (Black and Gulson, 1978) and NIST614 glass as the primary and secondary reference material, respectively. Actinolite–hornblende grains were separated drilling the vein directly and isotope ratios for $^{40}Ar/^{39}Ar$ geochronology were measured at the Auburn Noble Isotope Mass Analysis Lab (ANIMAL) at Auburn University. Additional method details are reported in Appendix A-1.

2.4 Results

Magnetite crystals commonly exhibit triple junctions and there are textural differences between the core and rim (Fig. 2-2a). Magnetite cores are porous and inclusion-rich; rims are non-porous and lack inclusions. Ablation spots were generally too large to discriminate between the core and rims and therefore represent whole grain dates. In BSE images, magnetite cores are darker than rims, consistent with greater abundances of minor and trace elements in the cores (Rodriguez-Mustafa et al., 2020). Two titanite grains also have a core–rim distinction in BSE images (Fig. 2-2b) and some titanite grains have irregular, sometimes globular grain boundaries and are often associated with or included within magnetite (Fig. 2-2c). Apatite grains are generally anhedral, clusters or vein or void fillings, and exhibit little to no zonation in BSE images (Fig. 2-2d). Apatite grains from deeper parts of the drill core often appear porous and inclusion rich.

New calculated dates are presented in Table 2-1, with uncertainties of 2 se. Most apatite dates were c. 115 Ma, regardless of textural setting or depth in the deposit (Fig. 2-3a). Titanite dates from two sample depths were also c. 115 Ma (sample depth 731 m: 115.4 ± 1.6 Ma; 817 m: 114.4 ± 2.3 Ma). Older titanite dated to c. 118 Ma (sample depth 1132 m: 118.7 ± 1.4 Ma), c. 126

Ma (sample depth 148 m: 126.1 ± 3.7 Ma; 1030 m: 126.9 ± 4.7 Ma), and c. 130 (sample depth 1101 m: 130.1 ± 2.7 Ma). A single titanite grain adjacent to a potassium feldspar vein dated to 90.8 ± 2.8 Ma. The actinolite-hornblende sample had sufficient weight percent K_2O (0.2 wt%) to be dated via the $^{40}Ar/^{39}Ar$ method and had the sufficient grain size (>100 μm in smallest dimension) to be separable (via drilling) and datable. Actinolite-hornblende from sample depth 731 m yielded a plateau age of 121.2 ± 0.6 Ma. Exploratory U–Pb magnetite dates from the 5 samples ranged from c. 122-147 Ma with 2se uncertainties around ± 10 Ma (Table 1, Fig 2-3b).

Samples from depths 731 m and 840 m are of particular interest because they preserve distinct cross-cutting relationships and therefore provide additional context for interpreting the dates. Sample depth 731 m has a vein of mushketovite (i.e., platy magnetite pseudomorph after hematite) cross-cutting the section laterally over a fine-grained altered groundmass, and a vein of actinolite-hornblende cross-cutting through the whole section (Fig. 2-4). When dates were calculated taking textural relationship into account, dates from apatite found in both the matrix and in the magnetite, vein are statistically indistinguishable (115.2 ± 2.5 Ma and 116.9 ± 0.9 Ma, respectively) and record the same date as the titanite found in the matrix (115.4 ± 1.5 Ma). The actinolite-hornblende yielded a plateau age of 121.2 ± 0.6 Ma (Fig. 2-4a & b).

Sample depth 840 m also featured a prominent mushketovite vein crosscutting a fine-grained matrix with patches of disseminated magnetite. Another vein of fine grained-magnetite can be seen cross-cutting the matrix in a different area of the section. Apatite from the large mushketovite vein gives a date of 115.4 ± 16.7 Ma, apatite from the matrix gives a date of 120.2 ± 6.6 Ma. Apatite associated with the fine-grained magnetite vein gives a date of 112.9 ± 2.6 Ma. Taken together, these three dates are not statistically distinguishable.

2.5 Discussion

New dates from this study and from previous works show strong evidence for a main hydrothermal mineralization at c.115 Ma. Published Re–Os dates for molybdenite, which is interpreted as coeval with Cu-Fe-sulfides in the shallow levels of the deposit, are 114.2 ± 0.6 Ma and 115.2 ± 0.6 Ma and constrain the age of Cu-Fe-sulfide IOCG mineralization (Mathur et al., 2002). These dates for sulfide mineralization are consistent with the $^{40}Ar/^{39}Ar$ dates of biotite and amphibole as determined in Marschke and Fontboté (2001) which ranged from 116.6 ± 1.2 Ma to 114.9 ± 0.5 Ma.

The nearby Copiapó batholith is a potential source of the magmatic-hydrothermal fluids for the Candelaria deposit (Marschik and Fontboté, 2001; Mathur et al., 2002; Arévalo et al., 2006), and ranges in age from 110–118 Ma (Marschik and Söllner, 2006). In our study, titanite and apatite dates that record c. 115 Ma hydrothermal event are contemporaneous with the San Gregorio unit of the batholith (115.5 ± 0.4 Ma, U–Pb in zircon), and dacitic dikes (112.8 ± 1.3 Ma and 115.2 ± 1.8 Ma, U–Pb in zircon) likely marking the same hydrothermal event (del Real et al., 2018). One titanite sample yielded a slightly older date of 118.7 ± 1.4 Ma, which is the same age as the La Brea unit of the Copiapó Batholith (118 ± 1 Ma, U–Pb in zircon, Marschik and Söllner, 2006) the largest and most prominent phase of the intrusion (del Real et al., 2018). Although hydrothermal mineralization and batholith emplacement are temporally correlated, there has not yet been a direct geochemical or field relationship connection determined to indicate the batholith is the direct source of the fluids (Marschik and Fontboté, 2001).

Most apatite and many titanite dates from this study are indistinguishable within uncertainty at c. 115 Ma. A single titanite grain in one sample (817m) associated with a potassium feldspar yielded younger dates of c. 90 Ma. This suggests possible additional, minor hydrothermal activity after the main c. 115 Ma mineralization event.

Sample 52 from 731 m depth features two cross-cutting veins over a fine-grained groundmass: A mushketovite vein cutting through the matrix, and an actinolite vein cross-cutting the magnetite (Fig. 2 - 4). Matrix apatite, vein apatite, and matrix titanite yielded statistically indistinguishable dates of c. 115 Ma, in agreement with the interpreted age of Cu-Fe mineralization (Marschik and Fontboté, 2001; Mathur et al., 2002). Titanite found in the matrix show irregular grain boundaries and strong lobate zoning around the margins, further

supporting the interpretation of these dates as an age of hydrothermal alteration via dissolution-reprecipitation (Fig. 2-2b, Putnis, 2009; Holder and Hacker, 2019). The presence of mushketovite in this sample also implies secondary interaction with a hydrothermal fluid, as mushketovite forms as a pseudomorphic reaction where hematite is replaced by magnetite, which is caused by a change in temperature or oxygen fugacity (Hu et al., 2020). The occurrence of mushketovite in many samples is evidence of more complex (re)crystallization processes, but this event(s) were not resolvable in this study via magnetite U–Pb dating.

Due to the distinct cross-cutting relationships of veins in this section, it is expected for the groundmass to be the oldest, followed by the mushketovite, with the actinolite–hornblende vein to be the youngest. However, the actinolite-hornblende yielded a plateau age of 121.2 ± 0.6 Ma—distinctly older than the c. 115 Ma apatite and titanite from this section. Unlike the titanite, BSE images and EMPA maps of actinolite-hornblende do not show any indication of hydrothermal alteration (Fig. 2-5). Candelaria actinolite-hornblende has been suggested to record different growth generations from distinct hydrothermal pulses (del Real et al., 2021), but this actinolite-hornblende appears to only record one single mineralizing event, as there are no apparent overgrowth zones, and the plateau age remains constant throughout step heating indicating no diffusive Ar loss following initial crystallization. It therefore appears that this actinolite date represents a distinct hydrothermal event at c. 121 Ma, which is consistent with a dacitic dike U-Pb zircon age of 121.9 ± 2.4 Ma (del Real et al., 2018), which was followed by a later hydrothermal event c. 115 Ma that reset the titanite and apatite in the groundmass of the andesitic host rock.

2.6 Magnetite dating: Promise and Limitations

Magnetite dates reported in this study range from 122.2 ± 7.9 Ma to 147.6 ± 10.1 Ma., with most falling c. 130 Ma (Table 2-1, Fig 2-3b). Because a primary, matrix-matched reference material for magnetite is yet to exist, these dates are only qualitative in nature. The analytical uncertainties are too large to precisely constrain distinct hydrothermal events, the dates are consistent with the maximum and minimum age constraints provided by the host rock andesites (~135 Ma, del Real 2018) and the c. 115 Ma hydrothermal mineralization, respectively (Fig. 2-3). The primary challenge with U–Pb dating of magnetite is the high concentration of common Pb often found in magnetite in combination with low concentrations

of U. This makes for low U/Pb and therefore makes it difficult to accurately measure this ratio: for example, sample 34 from 486 m depth (Fig. 2-6). An additional challenge to dating magnetite from Candelaria is that core and rim dates, which clearly record two generations of magnetite, were not statistically distinguishable (Fig 2-2a, d). With these caveats, the geologically reasonable results from this study show that U–Pb magnetite dating has promise as a geochronometer. Thus far, it has proven its ability to help broadly constrain the timing of magnetite mineralization, but not to discriminate between temporally close magnetite events due to relatively high uncertainties (~6-7%). Further work developing an analytical standard for this method is needed in order to reliably date magnetite going forward.

2.7 Summary

Most of the new apatite and titanite dates reported here are consistent with previously reported ages of sulfide mineralization (Re–Os, Molybdenite) at c. 115 Ma. Actinolite-hornblende and four titanite samples record other hydrothermal events at 118 Ma, 121 Ma, and 126 Ma. It was determined that these dates has no meaningful correlation with depth (Fig. 2-3). The new dates presented in this study present evidence supporting an episodic, multi-pulse model of formation for the Candelaria IOCG deposit. Magnetite U–Pb dates are less precise due to low U/Pb ratios, but still geologically useful and broadly consistent with the other dates reported here. Our results support a multi-phase hydrothermal model of formation of the Candelaria deposit, where an IOA style mineralization (magnetite-actinolite) is overprinted by the Cu-rich IOCG style mineralization.

2.8 Acknowledgments

A debt of gratitude is owed to Dr. Owen Neill at the University of Michigan for his assistance with scanning electron microscopy. This work was supported by the U.S. National Science Foundation under Grants EAR-2214119, EAR-2233425, EAR-1924192, EAR-1759200 and EAR-1759353, and Chilean Fondecyt grant #3200532. Any opinions, findings, and conclusions or recommendations expressed in this material are those of the author(s) and do not necessarily reflect the views of the National Science Foundation. Thanks to the AGeS program

for its support. All samples were obtained from the Candelaria deposit with permission from Lundin Mining. Lundin Mining is acknowledged for their field support.

2.9 Figures and Tables

Table 2-1. Summary of ages determined by U-Pb for titanite, apatite and magnetite, and Ar-Ar for actinolite.

Mineral	Comment	Age (Ma)	2SE	N	MSWD	p(X^2)	Depth
Titanite	C52	115.4	1.6	4	0.91	0.44	731
Titanite	C58	114.4	2.3	7	0.91	0.48	817
Titanite	C58 (Ttn adjacent K-spar vein)	90.8	2.8	3	3.4	0.064	817
Titanite	C11	126.11	3.66	24	4.2	1.7 x 10-10	148
Titanite	C65	126.92	4.7	26	1.2	0.27	1030.4
Titanite	C70	130.1	2.7	30	1.8	0.0049	1109.5
Titanite	C73	118.7	1.4	30	0.78	0.79	1132.1
Apatite	C43	106.6	8.8	8	0.82	0.57	618
Apatite	C52 (in mushketovite vein)	116.9	0.9	58	1	0.43	731
Apatite	C52 (in volcanic groundmass)	115.2	2.5	13	0.63	0.82	731
Apatite	C61 (ap in matrix)	120.2	6.6	5	1.9	0.1	840
Apatite	C61 (ap in mag vein 1)	115.4	16.7	7	1.4	0.21	840
Apatite	C61 (ap in mag vein 2)	112.9	2.6	19	2.3	0.0017	840
Apatite	C62	112.3	4.2	7	0.19	0.98	871
Apatite	C12	113	1.4	90	1.4	0.015	133
Magnetite	C12	122.2	7.9	26	0.25	1	133
Magnetite	C52	124.4	9	16	0.76	0.73	731
Magnetite	C58	128.3	8.5	8	0.75	0.63	817
Magnetite	C61	127.2	16.2	18	0.24	1	840
Magnetite	C61 (matrix mag)	130.7	11.5	19	0.85	0.64	840
Magnetite	C61 (mag vein 1)	137.5	11.9	11	0.59	0.64	840
Magnetite	C61(mag vein 2)	147.6	10.1	6	0.45	0.81	840
Magnetite	C62 (Magnetite in matrix)	130.9	7.3	29	0.53	0.91	871
Actinolite	C58	121.15	0.63	3	0.82	0.69	817

Notes: SE = standard error at 95% Confidence interval.

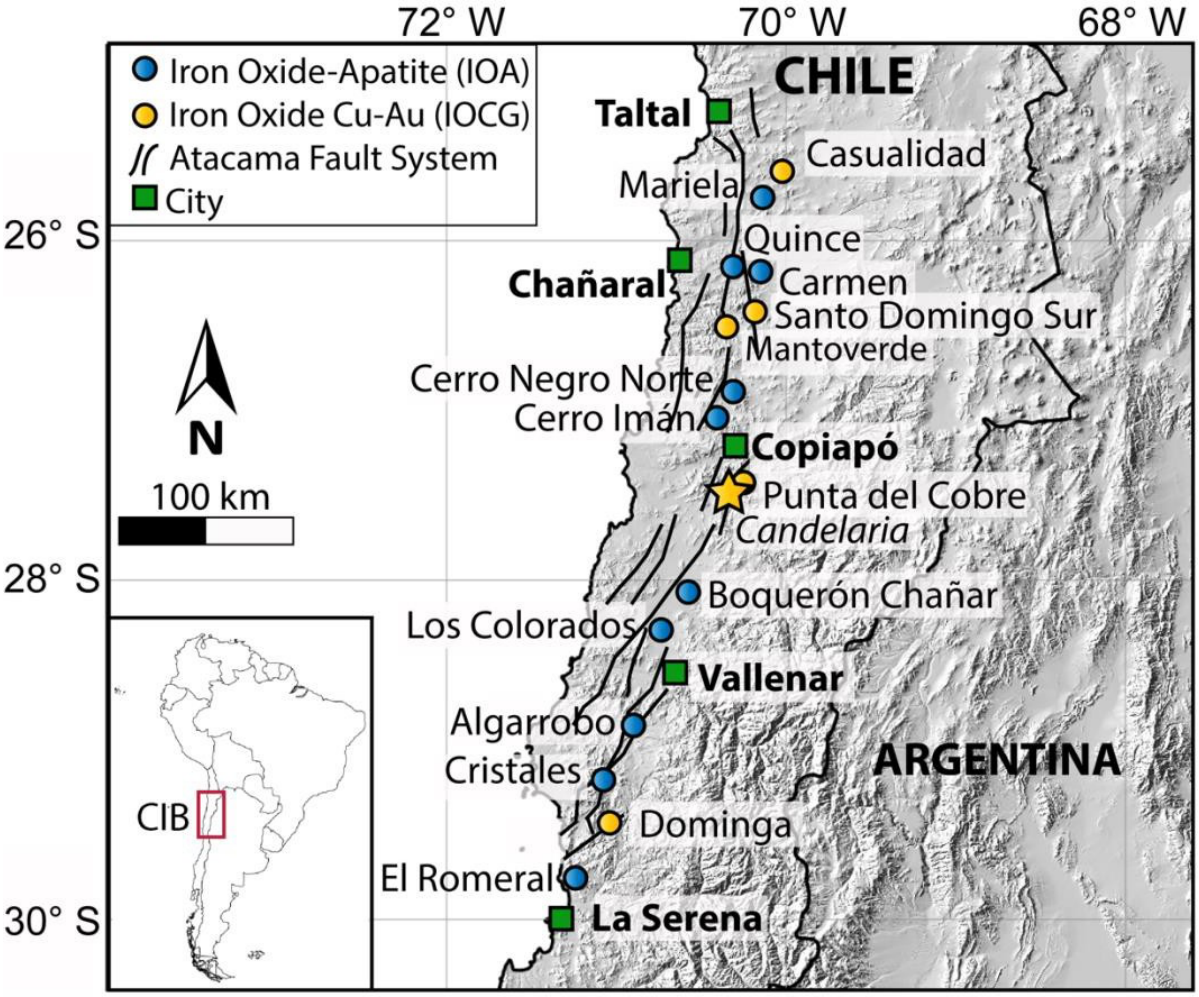

Figure 2-1: Map of the Chilean Iron Belt (CIB) highlighting the area's important IOA and IOCG deposits (modified from Rodriguez-Mustafa et al., 2020). The location of the Candelaria IOCG deposit is designated with a star. Note the proximal relationship between IOCG style deposits such as Candelaria and IOA deposits along the Atacama Fault System in northern Chile.

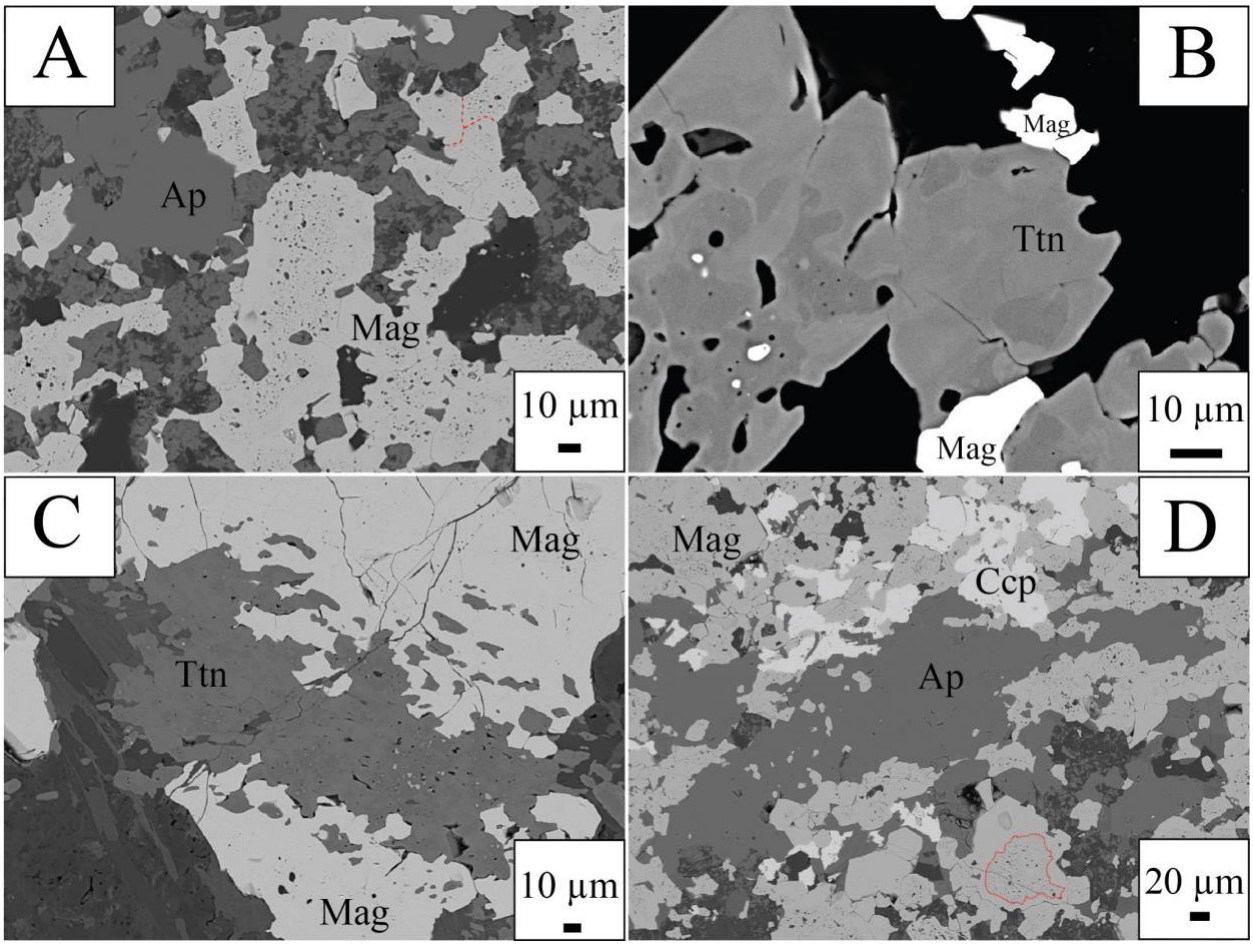

Figure 2-2: Representative BSE images. (Mag: magnetite, Ap: apatite, Ttn: titanite, Ccp: chalcopyrite) (A) Image of a hydrothermal apatite and magnetite. Note the difference in texture between the magnetite core (spongy, full of mineral inclusions and pits) and rims (non-spongy, inclusion free). The dashed red line denotes a triple junction between magnetite grains. (B) Titanite grain with increased contrast to highlight internal zonation. Internal zones appear blobby and porous with some associated magnetite. (C) Representative image of a commonly seen petrological relationship between titanite with magnetite in these samples. (D) Representative image of the Candelaria IOCG mineralization with chalcopyrite, apatite, magnetite. Outline of textural core-rim zoning in magnetite highlighted by the dashed red line.

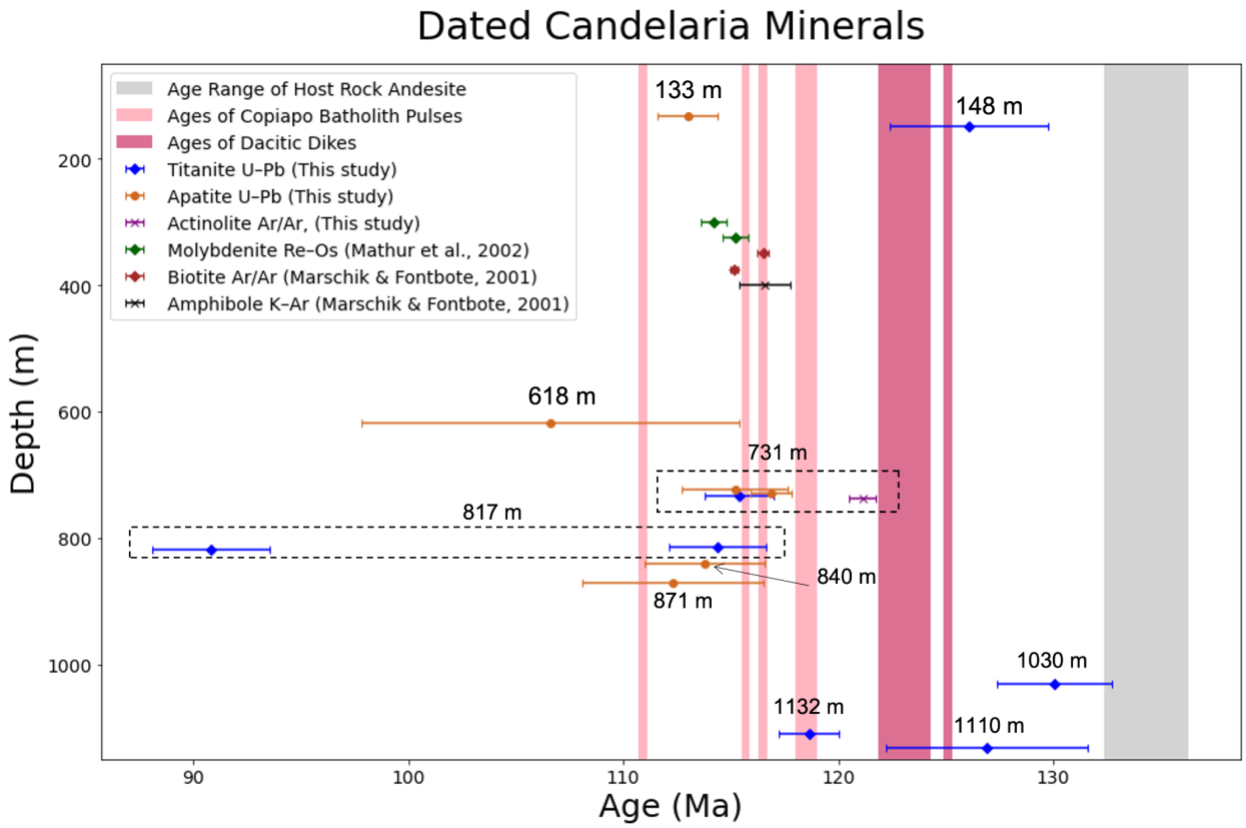

Figure 2-3a: Summary chart showing depths and dates with 2se uncertainties for minerals dated from the Candelaria IOCG, highlighting the temporal relationship with proximal igneous units. The colored vertical bars represent zircon U–Pb ages of magmatic activity reported by del Real et al (2018). From left to right, the light pink bars show ages of different pulses of the Copiapó batholith (Los Liros: 110.7 ± 0.4 Ma, San Gregorio: 115.5 ± 0.4 Ma, Adamelite (quartz monzonite porphyry): 116.3 ± 0.4 Ma, La Brea: 118.0 ± 1.0 Ma), the dark pink bars show the ages of pre-mineralization dacitic dikes (121.9 ± 2.4 Ma and 124.9 ± 0.4 Ma), and the gray bar shows the ages of the host rock andesite (upper andesite: 132.4 ± 2.9 Ma, lower andesite: 135.3 ± 1.0 Ma). Dates falling within the dashed boxes are from the same sample depth. Many dates calculated in this study cluster heavily around c. 115 Ma, which corresponds to the San Gregorio and Adamelite pulses of the Copiapó batholith, as well as previously published ages from Mathur et al. (2002) and Marschik and Fontboté (2001).

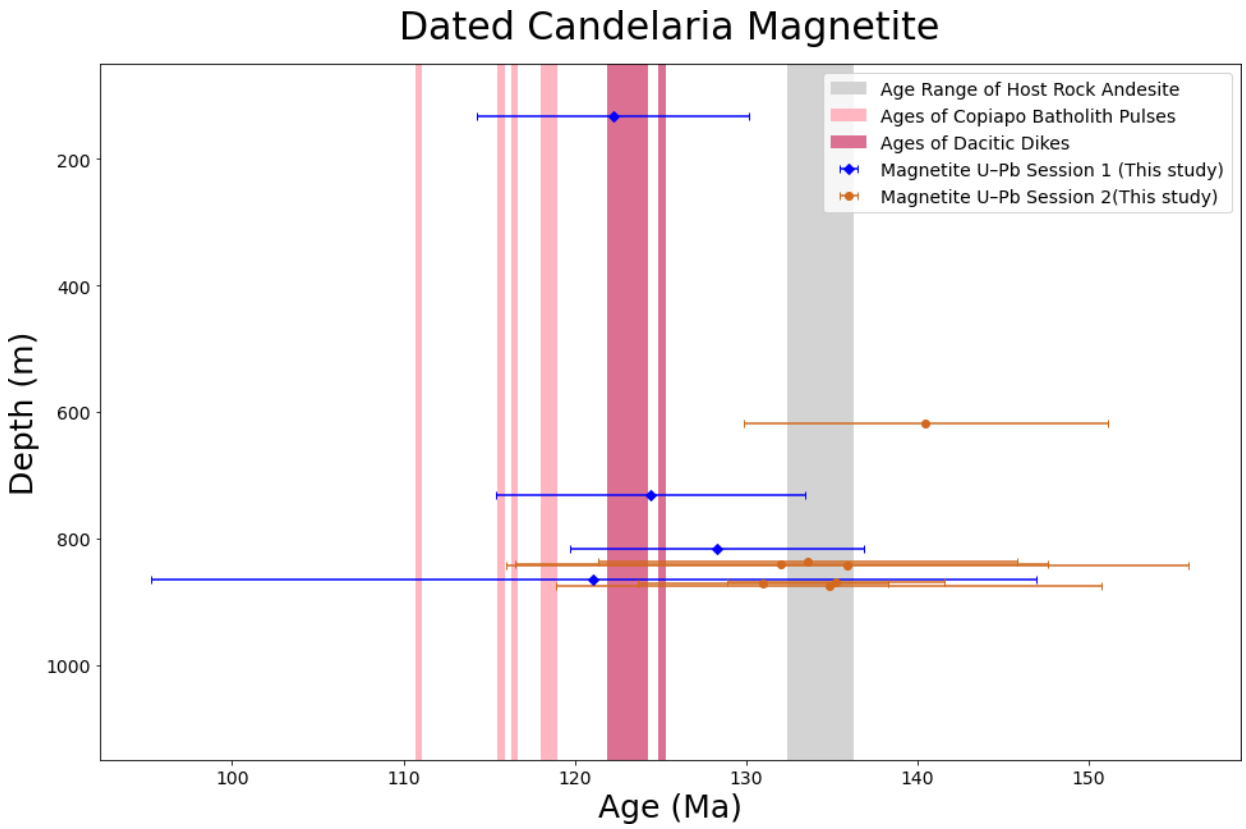

Figure 2-3b. Summary chart showing depths and dates with 2se uncertainties for exploratory magnetite/mushketovite dated. While the uncertainties are high, dates reported are interestingly geologically reasonable.

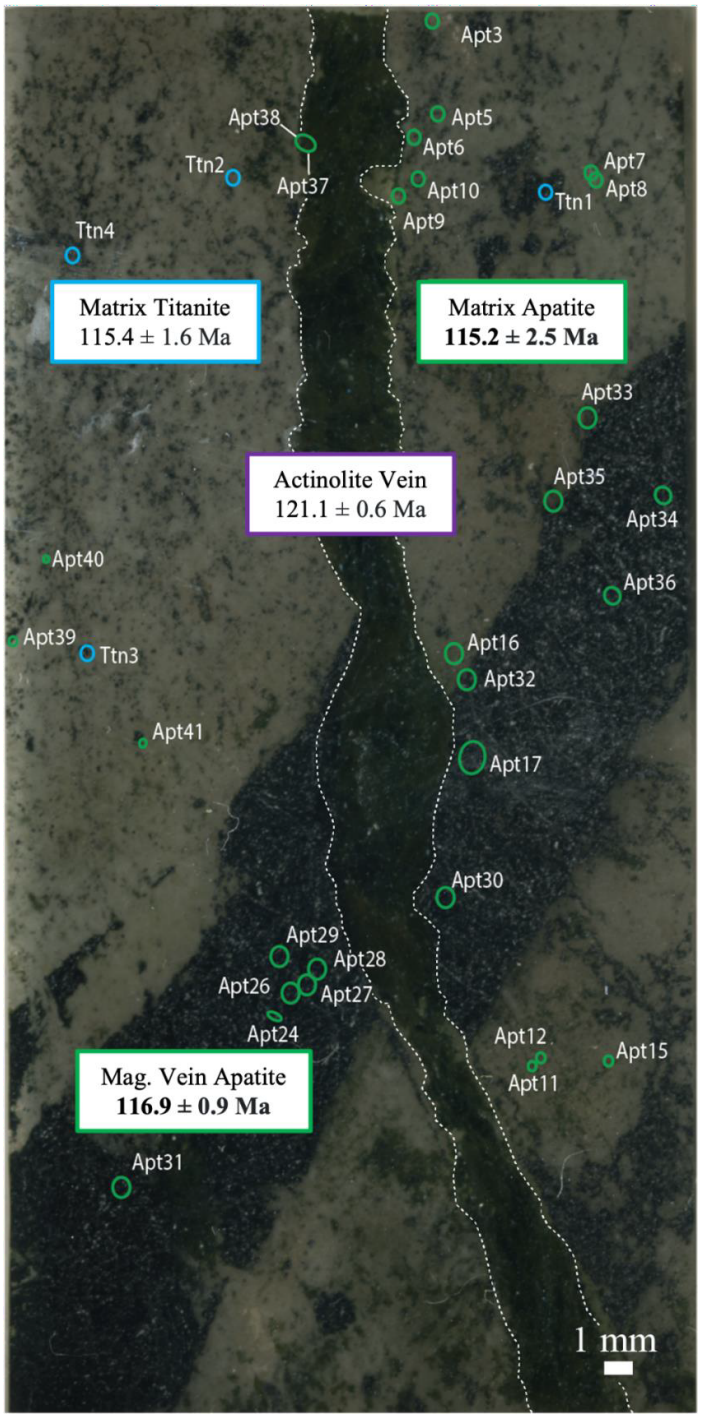

Figure 2-4a: Image of sample C52 from 731 m with locations of dated minerals, highlighting cross-cutting relationships, with the actinolite-hornblende vein outlined in a white dotted line. Apatite and titanite found in the matrix, and apatite in the magnetite (mushketovite) vein have the same calculated dates at c. 115 with overlapping 2se uncertainties. The actinolite-hornblende is distinctly older at 121.1 Ma. Green circles in the thin section image represent the locations of apatite dated, and blue represent the location of titanate dated. See text for discussion.

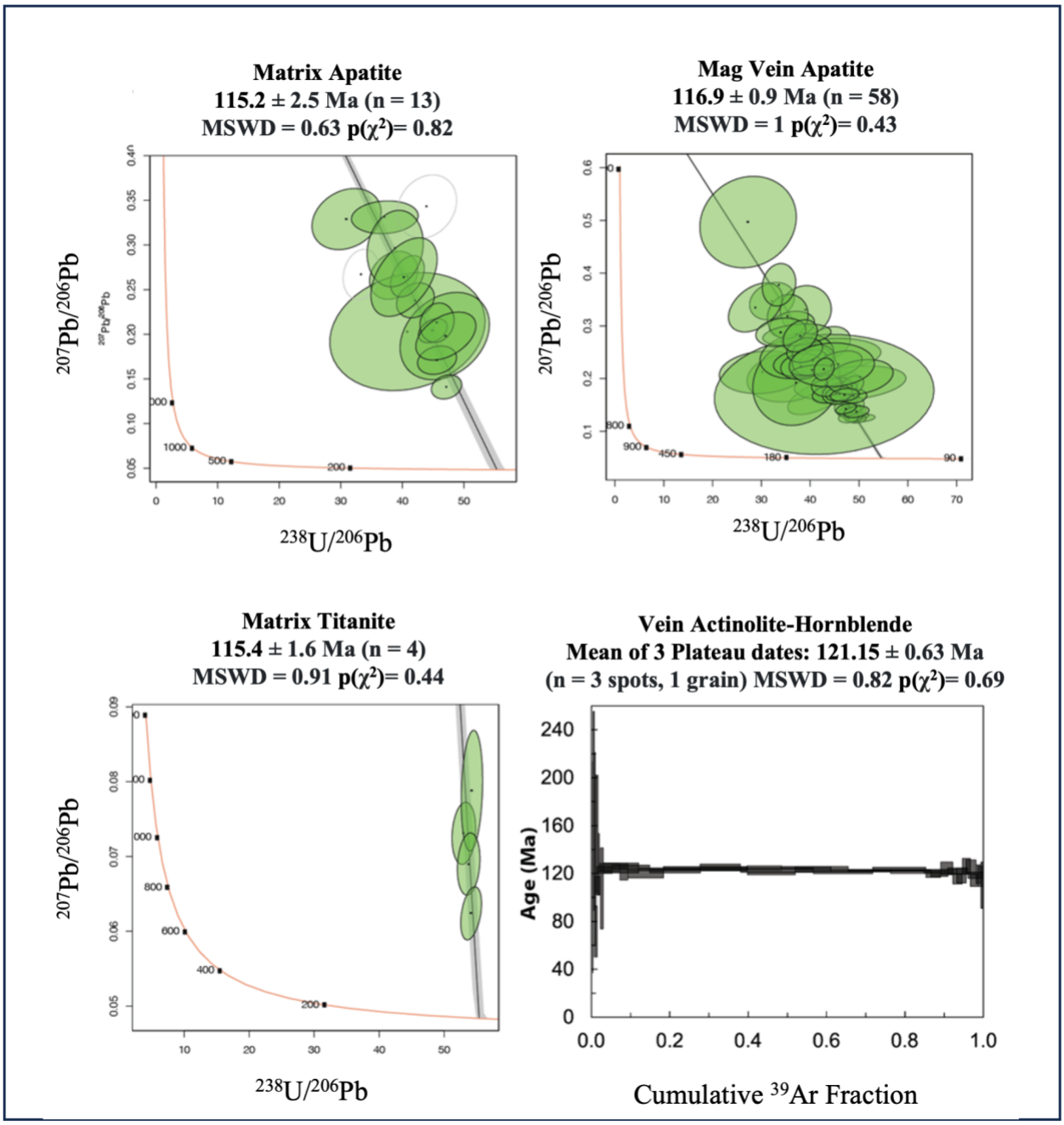

Figure 2-4b: Terra-Wasserburg diagrams for U–Pb dates of matrix apatite, titanite, and apatite found in the magnetite (mushketovite) vein, and $^{40}Ar/^{39}Ar$ age spectra of Actinolite-hornblende in sample C52 from 731 m depth.

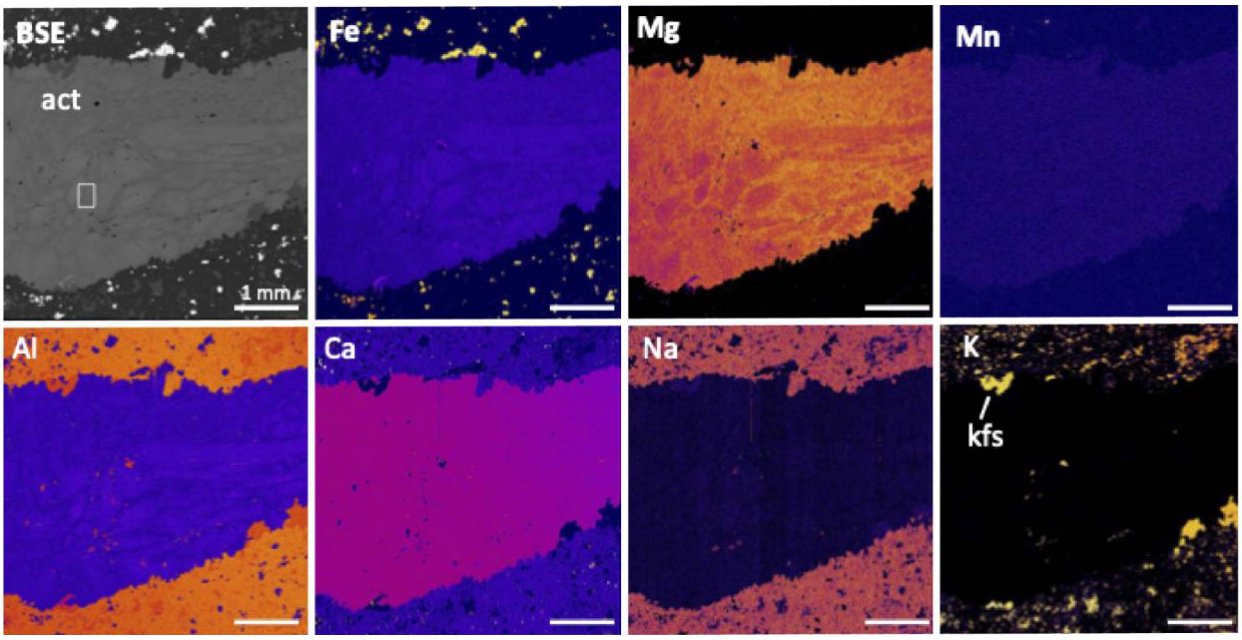

Figure 2-5: BSE image and WDS maps of the actinolite vein in sample C52 from the 731 m depth. Actinolite is generally homogeneous, with zoning in the BSE image due to Fe - Mg 1 exchange. K is present throughout the actinolite (averaging ~0.25 wt% K_2O), and accompanied by the coupled KAlSi-1 exchange, with cores slightly more enriched in K relative to the rim. Scale bar = 1 mm in each image.

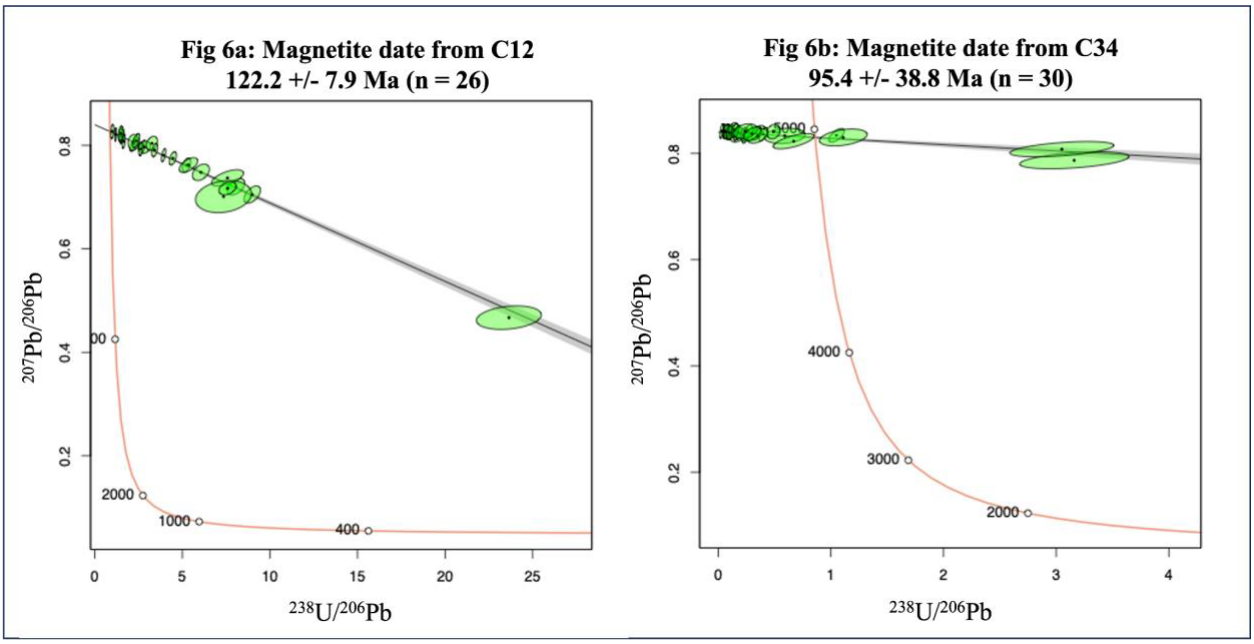

Figure 2-6: Terra-Wasserburg diagrams of magnetite U–Pb from samples C12 from (a) 133 m depth and (b) C34 from 486 m depth, highlighting the potential and limitations of magnetite U–Pb dating, respectively. Sample C12 has a date of 122.2 ± 7.9 Ma (MSWD = 0.25, $p(\chi^2) = 1$), whereas sample C34 has a date of 95.4 ± 38.8 Ma (MSWD = 0.19, $p(\chi^2) = 1$). The very high 2se uncertainty in sample C34 is due to high concentrations of common Pb, which is a key hindrance to the effectiveness of magnetite U–Pb dating.

2.10 References

Aleinikoff, J.N., Wintsch, R.P., Tollo, R.P., Unruh, D.M., Fanning, C.M., and Schmitz, M.D., 2007, Ages and origins of rocks of the Killingworth dome, south-central Connecticut: Implications for the tectonic evolution of southern New England: American Journal of Science, v. 307, no. 1, p. 63–118.

Apen, F.E., Wakabayashi, J., Day, H.W., Roeske, S.M., Souders, A.K., and Dumitru, T.A., 2021, Regional-scale correlations of accreted units in the Franciscan Complex, California, USA: A record of long-lived, episodic subduction accretion, in Wakabayashi, J., Dilek, Y., and Wakabayashi, J. eds., Plate Tectonics, Ophiolites, and Societal Significance of Geology: A Celebration of the Career of Eldridge Moores: Geological Society of America, p. 0.

Arévalo, C., Grocott, J., Martin, W., Pringle, M., and Taylor, G., 2006, Structural Setting of the Candelaria Fe Oxide Cu-Au Deposit, Chilean Andes (27°30′ S): Economic Geology, v. 101, no. 4, p. 819–841.

Banerjee, S., Zhang, B., Scott, C., MacDougall, C., and Dance, A., 2023, Technical Report for the Candelaria Copper Mining Complex, Atacama Region, Region III, Chile: CAPR002061.

Barra, F., Reich, M., Selby, D., Rojas, P., Simon, A., Salazar, E., and Palma, G., 2017, Unraveling the origin of the Andean IOCG clan: A Re-Os isotope approach: Ore Geology Reviews, v. 81, p. 62–78.

Barton, M.D., 2014, 13.20 - Iron Oxide(–Cu–Au–REE–P–Ag–U–Co) Systems, in Holland, H.D. and Turekian, K.K. eds., Treatise on Geochemistry (Second Edition): Oxford, Elsevier, p. 515–541.

Bilenker, L.D., Simon, A.C., Reich, M., Lundstrom, C.C., Gajos, N., Bindeman, I., Barra, F., and Munizaga, R., 2016, Fe–O stable isotope pairs elucidate a high-temperature origin of Chilean iron oxide-apatite deposits: Geochimica et Cosmochimica Acta, v. 177, p. 94–104.

Black, L., and Gulson, B., 1978, The Age of the Mud Tank Carbonatite, Strangways Range, Northern Territory: B.M.R.J. AUSTRAL. GEOL. GEOPHYS.; AUS; DA. 1978; VOL. 3; NO 3; PP. 227-232; BIBL. 1 P.; 6 ILL.

Elshkaki, A., Graedel, T.E., Ciacci, L., and Reck, B.K., 2016, Copper demand, supply, and associated energy use to 2050: Global Environmental Change, v. 39, p. 305–315.

Espinoza, S., Veliz, H., Esquivel, J., Arias, J., and Moraga, A., 1998, The Cupriferous Province of the Coastal Range, Northern Chile, in Camus, F., Sillitoe, R., and Petersen, R. eds., Andean Copper Deposits: New Discoveries, Mineralization, Styles and Metallogeny: Society of Economic Geologists, p. 0.

Groves, D.I., Bierlein, F.P., Meinert, L.D., and Hitzman, M.W., 2010, Iron Oxide Copper-Gold (IOCG) Deposits through Earth History: Implications for Origin, Lithospheric Setting, and Distinction from Other Epigenetic Iron Oxide Deposits: Economic Geology, v. 105, no. 3, p.641–654.

Harrison, M.T., 1982, Diffusion of 40Ar in hornblende: Contributions to Mineralogy and Petrology, v. 78, no. 3, p. 324–331.

Hitzman, M.W., 2000, Iron-oxide-Cu-Au deposits: what, where, when, and why. T.M. Porter (Ed.), Hydrothermal iron-oxide copper-gold & related deposits: a global perspective: Australian Mineral Foundation, p. 9–25.

Holder, R.M., and Hacker, B.R., 2019, Fluid-driven resetting of titanite following ultrahigh-temperature metamorphism in southern Madagascar: Chemical Geology, v. 504, p. 38–52.

Hu, X., Chen, H., Beaudoin, G., and Zhang, Y., 2020, Textural and compositional evolution of iron oxides at Mina Justa (Peru): Implications for mushketovite and formation of IOCG deposits: American Mineralogist, v. 105, no. 3, p. 397–408.

Kesler, S.E., and Simon, A.C., 2015, Mineral resources, economics and the environment: Cambridge University Press.

Kohn, M.J., 2017, Titanite Petrochronology: Reviews in Mineralogy and Geochemistry, v. 83, no. 1, p. 419–441.

Košler, J., Sláma, J., Belousova, E., Corfu, F., Gehrels, G.E., Gerdes, A., Horstwood, M.S.A., Sircombe, K.N., Sylvester, P.J., Tiepolo, M., Whitehouse, M.J., and Woodhead, J.D., 2013, U-Pb Detrital Zircon Analysis – Results of an Inter-laboratory Comparison: Geostandards and Geoanalytical Research, v. 37, no. 3, p. 243–259.

Kylander-Clark, A.R.C., 2020, Expanding the limits of laser-ablation U–Pb calcite geochronology: Geochronology, v. 2, no. 2, p. 343–354.

Kylander-Clark, A.R.C., Hacker, B.R., and Cottle, J.M., 2013, Laser-ablation split-stream ICP petrochronology: Chemical Geology, v. 345, p. 99–112.

Lledo, H.L., and Jenkins, D.M., 2008, Experimental Investigation of the Upper Thermal Stability of Mg-rich Actinolite; Implications for Kiruna-Type Iron Deposits: Journal of Petrology, v. 49, no. 2, p. 225–238.

Marschik, R., and Fontboté, L., 2001, The Candelaria-Punta del Cobre iron oxide Cu-Au (-Zn-Ag) deposits, Chile: Economic Geology, v. 96, no. 8, p. 1799–1826.

Marschik, R., and Söllner, F., 2006, Early cretaceous U-Pb zircon ages for the Copiapó plutonic complex and implications for the IOCG mineralization at Candelaria, Atacama Region, Chile.: Miner. Deposita, v. 41, p. 785–801.

Mathur, R., Marschik, R., Ruiz, J., Munizaga, F., Leveille, R.A., and Martin, W., 2002, Age of Mineralization of the Candelaria Fe Oxide Cu-Au Deposit and the Origin of the Chilean Iron Belt, Based on Re-Os Isotopes: Economic Geology, v. 97, no. 1, p. 59–71.

Paton, C., Hellstrom, J., Paul, B., Woodhead, J., and Hergt, J., 2011, Iolite: Freeware for the visualisation and processing of mass spectrometric data: Journal of Analytical Atomic Spectrometry, v. 26, no. 12, p. 2508–2518.

Paul, A.N., Spikings, R.A., and Gaynor, S.P., 2021, U-Pb ID-TIMS reference ages and initial Pb isotope compositions for Durango and Wilberforce apatites: Chemical Geology, v. 586, p. 120604.

Putnis, A., 2009, Mineral Replacement Reactions: Reviews in Mineralogy and Geochemistry, v. 70, no. 1, p. 87–124.

del Real, I., Thompson, J.F.H., and Carriedo, J., 2018, Lithological and structural controls on the genesis of the Candelaria-Punta del Cobre Iron Oxide Copper Gold district, Northern Chile: Ore Geology Reviews, v. 102, p. 106–153.

del Real, I., Reich, M., Simon, A.C., Deditius, A., Barra, F., Rodríguez-Mustafa, M.A., Thompson, J.F.H., and Roberts, M.P., 2021, Formation of giant iron oxide-copper-gold deposits by superimposed, episodic hydrothermal pulses: Communications Earth & Environment, v. 2, no. 1, p. 1–9.

Reich, M., Simon, A.C., Deditius, A., Barra, F., Chryssoulis, S., Lagas, G., Tardani, D., Knipping, J., Bilenker, L., Sánchez-Alfaro, P., Roberts, M.P., and Munizaga, R., 2016, Trace Element Signature of Pyrite From The Los Colorados Iron Oxide-Apatite (IOA) Deposit, Chile: A Missing Link Between Andean IOA and Iron Oxide Copper-Gold Systems? Economic Geology, v. 111, no. 3, p. 743–761.

Rodriguez-Mustafa, M.A., Simon, A.C., del Real, I., Thompson, J.F.H., Bilenker, L.D., Barra, F., Bindeman, I., and Cadwell, D., 2020, A Continuum from Iron Oxide Copper-Gold to Iron Oxide-Apatite Deposits: Evidence from Fe and O Stable Isotopes and Trace Element Chemistry of Magnetite: Economic Geology, v. 115, no. 7, p. 1443–1459.

Schmitz, M.D., and Bowring, S.A., 2001, U-Pb zircon and titanite systematics of the Fish Canyon Tuff: an assessment of high-precision U-Pb geochronology and its application to young volcanic rocks: Geochimica et Cosmochimica Acta, v. 65, no. 15, p. 2571–2587.

Sillitoe, R.H., 2003, Iron oxide-copper-gold deposits: An Andean view: Mineralium Deposita, v. 38, no. 7, p. 787–812.

Smye, A.J., Marsh, J.H., Vermeesch, P., Garber, J.M., and Stockli, D.F., 2018, Applications and limitations of U-Pb thermochronology to middle and lower crustal thermal histories: Chemical Geology, v. 494, p. 1–18.

Spencer, K.J., Hacker, B.R., Kylander-Clark, A.R.C., Andersen, T.B., Cottle, J.M., Stearns, M.A., Poletti, J.E., and Seward, G.G.E., 2013, Campaign-style titanite U–Pb dating by laser-ablation ICP: Implications for crustal flow, phase transformations and titanite closure: Chemical Geology, v. 341, p. 84–101.

Ullrich, T.D., Clark, A.H., and Stanley, C.J., 1999, The Candelaria copper-gold deposit, Region III, Chile: Paragenesis, geochronology and fluid composition: Mineral Deposits: Processes to Processing, v. Balkema, p. 201–204.

Williams, P.J., Barton, M.D., Johnson, D.A., Fontboté, L., De Haller, A., Mark, G., Oliver, N.H.S., and Marschik, R., 2005, Iron oxide copper-gold deposits: Geology, space-time distribution, and possible modes of origin: Economic Geology 100th Anniversary Volume, p. 371–405.

Chapter 3: Application of Random Forest Classification Machine Learning for Hyper-Specific Mineral Origin Determination Studies: Insights from Colombian Emerald and Euclase

Co-authors: Aaron Palke, Gabriel Angarita , Andres F. Gonzalez-Duran, Ziyin Sun, Javier Garcia Toloza, Camilo A. Betancur-Acevedo, Adam C. Simon

3.1 Abstract

One of the most pressing issues currently facing the gem industry is how to accurately determine the provenance of an unknown gemstone. This problem is particularly relevant with emeralds from Colombia, which are widely considered to be among the world's finest. Hence, there is a strong desire among traders and consumers to accurately determine the geographic origin of Colombian emeralds. Here, we used laser ablation inductively coupled plasma mass spectrometry (LA-ICP-MS) to measure elemental concentrations of emeralds from 40 mines from all 9 mining districts of the eastern and western Colombian emerald belts. These data were used to develop a random forest classification (RFC) machine learning algorithm to distinguish emeralds from among the Colombian belts, districts, and mines. The RFC method was proven highly effective at determining whether an unknown emerald was from the eastern or western mining belt (~98% accuracy) and determining the mining district of origin (~93% accuracy), and had moderately high effectiveness in determining the individual mine of origin (~85% accuracy). Using the variable importance list calculated from the RFC model, it was determined that the V/Cr ratio is the most

important variable in determining whether an emerald is from the Eastern or Western mining belt, with western emeralds having higher concentrations of V and lower concentrations of Cr than eastern belt emeralds. These elements are the primary chromophores that give emeralds their distinctive color, and the variability in V and Cr contents explains the wide range of hues of green observed among Colombian emeralds. The same method of coupling LA-ICP-MS data with a RFC model was also used on Colombian euclase from three of the same mines as the emeralds, and it was determined that the origin of an unknown Colombian euclase can be predicted with ~99% accuracy. An added benefit of the RFC model is that useful visualizations can be created utilizing the calculated variable importance list and calculated probabilities associated with its predictions. This allows for the creation of discriminant charts post-hoc, as well as probability heat maps that complement the RFC machine learning prediction. This method of (1) collecting a comprehensive database of LA-ICP-MS trace element data; (2) applying a random forest model to the data; (3) creating visualizations and discriminant diagrams post-hoc—has potential to rapidly expand our current capabilities to determine the provenance of any given mineral to a potentially hyper-specific degree.

Keywords: Random Forest Classification, CART, Machine Learning, Geochemistry, Colombia, Emeralds, Euclase, LA-ICP-MS, Mineral Origin Determination, Provenance, Gemology

3.2 Introduction

Geographic origin determination is one of the most pressing issues facing the gem industry (e.g. McClure et. al 2019), and it is the responsibility of gemology laboratories to develop methods to better predict where an unknown gemstone is from to ensure public trust. Whether due to the perceived quality, history, lore, geology, or collector's interest—some localities are valued more highly than others. For example, a Burmese (Myanmar) ruby can fetch a higher price than a ruby of equal quality from elsewhere simply due to the fame behind its source locality (Shor and Weldon, 2009). Likewise, Colombian emeralds are generally more highly valued than those from other sources, and even more specifically within Colombia, emeralds from the Muzo mining area hold exceptional value. Each collected mineral has a deep geologic and anthropological history to it, and to the collector, information can be as valuable as the stone. Whether or not the reader agrees that added value should be placed on gemstones based on location, it is an undeniable trend in the gem and mineral industry that location holds a special value in the eyes of many buyers.

Preserving origin information for gemstones is notoriously difficult because original location information may be inadvertently lost due to poor record keeping and poor inventory control (e.g. McClure et. al 2019). Additionally, as in any industry, where there is perceived value, there is also opportunity for unethical practices. Herein lies the importance of gem laboratories to provide and continue to develop quality assurance methods. There is already an established market for origin determination, as is evident by the services offered at gemology laboratories around the world. Previous and current methods of origin determination include the qualitative observation of inclusions, color, and habit of a particular gem mineral, determined by highly skilled gemologists (Gübelin and Koivula, 1986; Renfro et al., 2016; Saeseaw et al., 2019). While undeniably useful, these physical observations are usually coupled with advanced laboratory techniques to geochemically fingerprint the origin of a stone due to the ever-increasing number of producing gem

deposits. The recorded complexities of a mineral's formational environment are left imprinted in the crystal form of a mineral, such as chemical or color zonation, micro-textural features, inclusions, crystal habits, and minerals associations. These differences can often be detected at the trace element level, which is the basis for geochemical provenance determination methods.

Here we present a highly effective approach to origin determination using a machine learning algorithm on trace elemental data from Colombian emeralds at increasing levels of specificity: by mining belt, mining district, and by individual mine. In Colombia, emeralds are mined from two regional mining belts: the Eastern and Western, and 9 mining districts encompassing numerous mines (Fig. 3-1). Emerald mineralization is associated with Lower Cretaceous strata. In the Western belt, emeralds are hosted by the Rosablanca and Muzo Formations; whereas in the Eastern belt the two hosting units are the Santarosa and Chivor Formations (Terraza Melo, 2019).

Colombian emeralds form from the chemical interaction of evaporitic brines and black shales containing chromophore elements such as Cr and V (Ottoway et al., 1994). They are distinct from most emeralds that formed by chemical reaction of magmatic-hydrothermal fluids evolved from granitic melts with mafic-ultramatic host rocks (Giuliani et al, 2019; Alonso-Perez and Day 2021). Thermal reduction of sulfate from brines at 300-330 °C, with organic matter led to extensive albitization, followed by precipitation of carbonates, pyrite, and Be-bearing minerals (e.g., beryl, euclase), which are very low in Fe, and relatively enriched in V and Cr (Giuliani et al., 2000; Alonso-Perez and Day, 2021). Emerald mineralization in both mining belts involved comparable but not identical rock units and took place under similar physicochemical conditions as evidenced by fluid inclusion data and consistent mineral assemblages (Kozlowski et al., 1988; Cheilletz et al., 1994; Banks et al., 2000; Giuliani et al., 2000; Romero Ordoñez et al 2021; Gonzalez-Duran et al., 2021). Although, the structural setting and age of mineralization differ, with the Western belt being

associated with a compressive phase (Branquet et al., 1999) dating at 34-51 Ma, as determined through Ar/Ar dating on micas by Cheilletz et al. (1994) and Th/Pb dating on syngenetic parisite by Altenbergen (2022), and the Eastern belt being linked to extensional events at 65 Ma (Cheilletz et al., 1994; Branquet et al., 1999). The method detailed in this study provides an origin prediction, an accuracy probability, as well as helpful graphs, charts, and tools to provide broader insights into the underlying geochemistry and geologic processes and has potential to serve as a blueprint for future mineral provenance studies.

3.3 Methods

3.3.1 Sample Material

The most critical aspect in developing a database for origin determination is ensuring the samples of interest are actually from their stated location. This is where the collaboration of the Technological Development Centre for the Colombian Emerald (CDTEC) and the Gemological Institute of America (GIA) has proven exceptionally beneficial. Geoscientists at CDTEC have spent years meticulously collecting gem-rough emeralds from active mines with first-hand knowledge of where each stone originated. Likewise, the GIA takes equally careful record of their reference collection in order to ensure location accuracy (Vertiest et al., 2019). The compiled database contains a comprehensive 2284 individual LA-ICP-MS spot analyses, 694 emeralds, from 9 mining districts and 40 individual mines. Of these, 1113 spots from 388 emeralds were from CDTEC collected samples, 458 spots from 77 emeralds in the GIA reference collection, and 527 spots, from 229 emeralds from Jiménez (2017).

3.3.2 LA-ICP-MS trace element data collection at the GIA

New trace elemental data of Colombian emerald samples were acquired at the Gemological Institute of America in Carlsbad, CA by using a Thermo Fisher iCAP Qc ICP-MS, coupled with an Elemental Scientific Lasers NWR213 laser ablation system with a frequency quintupled Nd:YAG laser operated in Q-switched (pulsed) mode at a wavelength of 213nm and pulse duration of 4 ns. Laser sampling was performed in the third generation two-volume cell from ESI (TwoVol2). The laser-generated aerosol was collected by a device (or cup) that is supported evenly throughout the entire range of motion with a specially designed internal movement system. This system minimizes inconsistent gas dynamics and a positional sensitivity dependence. The laser cell is flushed with helium gas, carrying the ablated material to where nebulizer gas (Ar) was mixed with the carrier gas (He) via a wye shaped connector before entering the plasma for ionization and subsequent analysis in the mass spectrometer. Data acquisition was performed in time-resolved mode. The following elements were measured: Li, Be, Na, Mg, Al, Si, Ca, Ti, V, Cr, Fe, Ga, Rb, Cs. Dwell time of each analyte measured was 0.01 seconds except Al, Si and Fe that were measured for 0.005 seconds, and Li, K and Rb that were measured for 0.05 seconds. Dwell time of each laser spot was 40 seconds. Si was used as an internal standard. National Institute of Standards and Technology (NIST) Standard Reference Material (SRM) 610 and 612 were used as external standards. All isotopes were externally standardized using both standards. Concentrations of all isotopes were calculated by Qtegra software (Version 2.10.3324.131). Full LA-ICP-MS parameters can be found in Table 1 in the supplemental data sheet.

3.4 Results

3.4.1 Variable Selection and Database Compilation

In addition to the major elements measured (Be, Al, Si) in Colombian emerald samples, the following elements were present in minor concentrations (1 - 5 wt. %): Na, Mg, V, Cr. The following elements were detected at trace level (<1000 ppm): Li, Ca, Sc, Ti, Fe, Ga, Rb, and Cs. In over 50% of analyses, K, P and Mn were detected in trace amounts, but were not consistently detected. Summary statistics of elemental concentrations can be found in Appendix B (B-2, B-3, B-4, B-5).

Only analytes which were detected in all (or very nearly all, >99%) spot analyses were considered for separation analysis. This included Li, Be, Na, Mg, Al, Si, Ca, Ti, V, Cr, Fe, Ga, Rb, and Cs. The analytes: K, P, and Mn were detected in >50% of analyses, therefore were not used in separation analysis. Additionally, some analytes raised suspicion of having been affected from systematic instrumental drift over time, including the major elements Be and Al and Si. This potential systematic drift between sessions was tested by re-analyzing the same emeralds on different days and comparing the results (Fig. 3-2). Be and Si were determined to be significantly different enough to be excluded from analysis, and Al was determined to be consistent enough between sessions to use in analysis. The analytes which had plausible polyatomic interferences, ^{56}Fe (e.g. $^{40}Ar + {}^{16}O^{+}$), ^{44}Ca (e.g. $^{28}Si + {}^{16}O^{+}$) (May and Wiedmeyer, 1998), were not considered.

A split in data is apparent with ^{24}Mg (Fig. 3-3a). Initially, this was suspected to be a natural split in data by mine, district, or belt—however, none of these attributes explained the separation. It is suspected that ^{24}Mg has an interference with H^{+} and ^{23}Na, and different sessions might have had different levels of hydrous gas present in the system which was then ionized upon contact with the argon plasma. This split is not seen in ^{23}Na vs. ^{25}Mg (Fig. 3-3b). For this reason, ^{24}Mg was not considered for analysis.

Lastly, an effort was made to reconcile the newly collected data with the dataset from Jiménez (2017), as their study includes nearly 500 spot analyses on Colombian emeralds with specific mine information. The standard NIST 610 was used in the Jiménez (2017) study, whereas the newly collected analyses in this study used both NIST 610 and NIST 612. After re-calculating our data using only NIST 610, it was found that our concentrations remained the same, except for Fe, so it was not included in data analysis.

The analytes that our study had in common with Jiménez (2017), and were therefore used in separation analysis included: Li, Na, Al, Sc, Ti, V, Cr, Ga, Rb, and Cs. Each of these elemental concentrations were then divided by each other systematically to determine ratios (e.g. Li/Na, Li/Al, Li/Sc, etc.). A total of 55 variables, both measured and derived, were used in separation analysis.

It should be noted that Fe and Mg showed promise for separation, however, equally effective separations were possible without using these elements, and the decision to exclude Fe and Mg was made to appropriately include the previously published dataset into this new database.

3.4.2 Machine Learning and Data Processing

Attempts were made in the nascency of this study to separate emeralds using more traditional trace elemental discriminant approaches, namely scatterplots and other graphic multivariate diagrams. While there were some encouraging results using these approaches, when working with 55 variables, the possibilities for diagram separation were practically endless, therefore, the feasibility of machine learning algorithms was explored.

Eight different machine learning algorithms were considered for predictive effectiveness on the database: Linear Regression (LR), Linear Discriminant Analysis (LDA), K-Nearest Neighbors (KNN), Gaussian Naïve Bayes (NB), Linear Support Vector Classification (SVM), Quadratic Discriminant Analysis (QDA), Decision Tree Classification (DTC), and Random Forest

Classification (RFC). A training - test data split of 80% - 20% was used, along with stratified K-fold sampling with 5 splits while shuffling. Cross validation accuracy scores were used to determine the model's effectiveness (Fig. 3-4).

Several variables, especially the derived variables, had co-linearity (e.g. Rb:Na:Mg, and Cr:V:Sc), which results in LR, LDA, QDA not having an underlying assumption met. Additionally, homoscedasticity is required for LDA, and not every variable had the similar degrees of variance. The strict assumptions needed for the parametric algorithms lead to the decision to choose a non-parametric option. Of these, NB and KNN had moderately successful performance, and SVM performed poorly.

The DTC and RFC algorithms (both under the classification and regression tree, or "CART", family of algorithms) performed the best, did not violate any assumptions, and was therefore the chosen algorithm for this study.

Figure 3-5 shows an example of a single, simplified, DTC model applied to our data. While effective at handling data of different variances, sizes, and even types (categorical and continuous), one of the shortcomings of a DTC is its tendency to over-fit noisy data, meaning the training accuracy is much higher than the testing accuracy, thereby limiting its predictive ability. This is where an RFC surpasses a single DTC in terms of effective predictive ability. While over-fitting can still occur with very noisy data in RFC, by using hundreds of decision trees with randomized variables, and taking a simple majority vote of all those trees, the RFC algorithm performs exceptionally well in both training and testing accuracy, reducing the chance of an over-fit model. For this reason, an RFC was chosen and performed on the trace element database of Colombian emeralds by mining belt (east vs. west), mining district, and by individual mine. Each RFC model was run independently on these three categories to self-validate the results. For example, if the model predicted a mine that was not in the predicted district or belt, it would alert the analyst to take

caution in interpretation. It was found that a random forest of 100 trees performs equally well to a random forest of 1000 trees, so for computational brevity, a forest of 100 trees was used. Each random forest used an 80-20 training-testing data partition, and the Gini split rule.

This decision tree recursively partitions the data into subsets based on the chemical variables, with the aim of maximizing the homogeneity of the target variable within each subset. Each split is a Boolean True/False question. In this diagram, the green bar represents the number of classifications which fall under “True”, and the red represents those which fall under “False” for each split. For example, the first split (root node) divides the data into those with a V/Cr ratio less than or equal to 0.6781. Training accuracy is improved when more nodes are allowed, and when multiple DTC trees are used in a random forest classification (RFC) analysis. This highlights the simple flow-chart style logic underlying DTC and RFC machine learning algorithms.

3.4.3 Random Forest Classification Predictive Results

The random forest classification (RFC) model was applied to the dataset independently to the following attributes: east or west mining belt (n=2), mining district (n = 9), and individual mine (n = 40). One of the characteristics of a RFC model is that each time it is performed, the results can vary slightly even when the same data is being fit. This is because variables are generated randomly, and each occurrence is slightly different. For this reason, results here are reported as approximations, however, they are still representative of the model’s performance (Table 3-1).

The RFC model successfully separated emeralds by belt with 98% testing accuracy and 99% training accuracy. For mining districts, the RFC model was able to separate the 9 districts with a testing accuracy of 93% accuracy with a 97% training accuracy. For individual mine separation, the model has an 85% testing accuracy, with 92% training accuracy (summarized in Table 3-1).

Throughout the development of this model and the database, accuracy scores improved when more data was added. Full example RFC model summaries are reported in Appendix B (B6, B7, B8).

3.4.4 Probability Heat Maps

One of the most useful features of the RFC model is that in addition to making predictions, it calculates a probability associated with those predictions, as well as probabilities associated with attributes that it did not predict. This proves particularly useful in the case of confused predictions. Fig. 3-6a-c show example probability heat maps that can be created from data produced in the RFC model. Each row is an individual spot analysis, and each grouping of three rows is from one emerald (i.e. rows 0 - 2 is one emerald, 3 - 5 is another, for a total of 9 emeralds - one from each district). This sample set is representative of the model's performance. The lighter the color, the higher the probability of an emerald being from a particular belt (Fig 3-5a), district (Fig 3-5b) or mine (Fig 3-5c). In this sample, the model correctly predicted the belt of origin with 100% accuracy (27/27), the district with 93% accuracy (25/27, missing analyses labeled 14 and 26), and by individual mine with 88% accuracy (24/27, missing analyses labeled 9, 14 and 26).

3.4.5 Variable Importance

In addition to predictions and probabilities, another highly useful feature of a RFC model is that it can calculate the most important variables for separation, which can aid in the creation of graphical visualizations. The top 12 variables for separation of each are reported in table 2. Full results can be found in Appendix B (B6-, B7, B8). Using the variable importance, it is obvious the most significant variable for separation by belt is the V/Cr ratio (Table 2, Fig. 3-7a-c).

3.5 Discussion

3.5.1 Importance of V and Cr in Differentiating East and West Emerald Belts

By far the most important variable in separating an emerald by mining belt is the V/Cr ratio (Fig. 3-7a-c.). These elements are, interestingly, the primary chromophores which give emerald its characteristic color. In fact, running the RFC model using only those two variables, predicts the belt of origin with ~85% testing accuracy (training = ~93%). Meaning, this model can correctly predict whether an emerald is from the Eastern or Western belt based solely on the primary chromophores ~ 85% of the time. Using the other variables as mentioned above, we can fully separate emeralds from Eastern and Western belts with a testing accuracy greater than 98%. Fortaleché et al. (2020) noted the anecdotal color difference in Western vs. Eastern emeralds, with Western emeralds having "light to vivid green to yellowish green color" and Eastern emeralds having "light to vivid bluish green color". Experienced traders of Colombian emeralds claim to know the difference between an Eastern and a Western emerald based solely on color, albeit with some overlap (e.g. Fig. 3-8). The noted qualitative difference in color can now be empirically corroborated with the distinctive difference in V/Cr ratio of emeralds by belt reported here.

A handful of previous studies have touched on the differences in V and Cr concentrations between individual mines in Colombia (Cedeño et al, 2015; Jimenez 2017; Angarita-Sarmiento et al., 2022). Additionally, Cronin and Rendle (2012) determined the chromophores V, Cr, Mg and Ni to be statistically different in the Guali (Eastern belt) vs the Coscuez and Muzo mines (Western belt) of Colombia, and speculated this as a cause of the color difference in these emeralds. The differences in Cr and V were specifically emphasized between the Guali, Coscuez, and Muzo mines. A photoluminescence study of Colombian emeralds found the wavelengths between 683 and 685 nm, which correspond to the Cr^{3+} ion, effective in differentiating emeralds from the Eastern and Western belts of Colombia (García et al., 2019). Data from our study complements this finding well

and takes it a step further to determine that the V and Cr concentrations are significantly different by the entire mining belts – east vs. west, not just localized to specific mines.

3.5.2 Mines vs. Mining Districts

Both mines and mining districts could be separated with moderately high to high accuracy (Table 3-1). Grouping mines into "mining districts" presents key advantages over individual mines. First, it aids with the issue of the proximity of mines. Some mines in Colombia are so close to each other that they have shafts and adits which overlap. This, obviously, renders any sort of geographical separation extremely difficult if not impossible, obfuscating any meaningful potential difference in geochemistry. Second, the apparent trace elemental heterogeneity of Colombian emeralds—even at a localized level—raises the possibility that some emeralds from larger mines could face significant differences in trace element chemistry even within the same mine. By grouping mines at the district regional level, this overcomes these challenges and presents a more accurate prediction, as is seen with the results of this study where the accuracy improved with each broadening group (Mine ~85%, District ~93%, Belt ~98%).

3.5.3 Value Even in Confusion

Valuable information can be ascertained even when predictions are confused. In the case of Colombian emeralds, a common mistake for the RFC algorithm to make is confusing the Maripi with Muzo districts, and occasionally with Coscuez—a mistake which is quite intuitive (see green boxes in Fig. 3-6c). These districts are less than 10 km away from each other and are in the same lithostratigraphic unit (Fig. 3-1). The fact that this algorithm can separate these districts with a moderate degree of confidence is itself, quite remarkable. Even if the algorithm determines an emerald to have a 50-50 chance of being from either Muzo or Maripi, knowing this is not from any

other mining district is itself an important result. As mentioned before, Muzo emeralds have a reputation for being among the world's finest, and where there is inflated value due to a famous locality, there could be fraudulent dealers falsely attaching the Muzo location onto an emerald to fetch a higher price. This method now gives us the ability to say either plausibly whether an emerald is from the Muzo district, or decisively if it is not, with a quantitative probability. Ruling out options is possible because the separation of emerald trace element chemistry between Eastern and Western districts is so conclusive, and separation of districts further away while in the same unit (i.e. Pauna vs. Muzo) and in different lithostratigraphic units (i.e. Muzo vs. Peñas Blancas) is also quite decisive. Despite the geochemical similarities, the RFC model can successfully differentiate these two districts remarkably well, in particular with the RFC model's ability to produce probability heat maps (Fig. 3-6). The RFC provides a list of potential predictions and associated confidence in these predictions. Most of the time, it provides only one district as an option; sometimes it will provide 2-3, and only very rarely will it provide more than 3. If the algorithm cannot place the unknown emerald to a particular mine, it will provide its best guess with a low probability, alerting the analyst to take caution in interpretation. Having a comprehensive database containing samples from each mining district from 40 mines allows us to have confidence in the machine learning's output, and the post-hoc visualizations help aid the analyst's interpretation to ensure that no conclusion is overstated.

3.5.4 Causes of separation

Various authors, including Schwarz (1992), Cedeño et al. (2015), Jimenez (2017), McManus et al. (2018), Fortaleché et al. (2020), and Angarita-Sarmiento et al. (2022), have pointed out differences in trace element concentrations of emeralds from different mining belts. Geochemical variation along the stratigraphy and the paleoenvironment of deposition within the Colombian

Cretaceous basin emerges as a major control influencing the endowment of minor and trace elements for the mineralizing system. Despite emerald mineralization being hosted by comparable rock units (e.g., Muzo, Chivor Formations), emerald pockets are not found at the very same stratigraphic levels, as demonstrated by Cheilletz et al. (1994), Giuliani et al. (2000), Terraza (2019), Romero-Ordoñez et al. (2021), and Gonzalez-Duran et al. (2021). The latter authors documented geochemical variation across the Muzo Formation in the La Pava mine, while Mantilla et al. (2007) and Terraza (2019) reported distinct deposition facies along the mining belts.

This variation is further reflected in the non-homogeneous distribution of V/Cr ratios in the host rocks. The concentration of V in the rock strata is notably higher in the Western Emerald Belt may be attributed to heightened levels of organic matter, coupled with the affinity of V and Cr for sediments abundant in organic content (Breit and Wanty, 1991; Gustafsson, et al., 2014). The measured total organic carbon (TOC) is higher in the Western belt (3-4 % in the Muzo Formation, 2-3 % in the Rosablanca Formation), as opposed to the Eastern Emerald Belt: 1.46 % in the Santa Rosa Formation, 1.06% in Chivor Formation, and 0.34% in Las Juntas Formation (Mantilla et al., 2007).

Consequently, the Western belt has on average 409 ppm of Vanadium and 111 ppm of Chromium (González et al., 2021), while the Eastern Belt has on average 133 ppm of Vanadium and 82 ppm of Chromium (Pignatelli et al., 2017). This trend has also been recorded in other minerals that incorporate chromophore elements. Garcia-Toloza et al. (2022) studied green micas documenting average concentrations of 5368 ppm (V) and 1259 ppm (Cr) in the Western belt, compared to 2278 ppm (V) and 778 ppm (Cr) in the Eastern belt. Additionally, the concentration of Vanadium is higher in euclase from the Western belt, as reported here and corroborated by Garcia-Toloza et al., 2022.

Furthermore, Jimenez (2017) attributed differences in the concentration of Cr/V, and other trace elements, to variations in fluid evolution controlled by tectonic conditions. In the Eastern belt, emerald compositions reflect the signature of evaporite-derived fluids, while the Western belt, influenced by a compressive tectonic regime, involves the input of salt diapirs. The order of precipitation of the mineral assemblage may also play a role in the incorporation of trace elements in emeralds. For instance, Gonzalez-Duran et al. (2021) found different V/Cr ratios in the rocks and emeralds in the La Pava mine, attributing this difference to the crystallization of green mica before emeralds. The early formation of micas and carbonates can deplete the mineralizing fluid in Vanadium, leading to a different V/Cr ratio by the time emeralds precipitate (Garcia-Toloza et al., 2022).

In summary, differences in trace element concentrations, including Vanadium and Chromium, among Colombian emeralds arise from complex interactions involving geochemical variations in stratigraphy, tectonic influences, and nuances during mineralization processes.

3.5.5 Further proof of Concept: Colombian Euclase

To further test the effectiveness of this method, samples of Colombian Euclase. Euclase ($BeAl(SiO_4)(OH)$) has a similar composition to beryl ($Be_3Al_2Si_6O_{18}$) and is found in some of the same mines as emeralds. Euclase lacks the long channels down the c-axis as seen in beryl which can trap fluid inclusions. For this reason, fewer trace elemental substitutions can occur, resulting in a shorter list of detectable trace elements than in emerald.

Gem rough euclase from three of the same Colombian mines (La Marina, Pauna district; La Vega de San Juan, Gachalá district; and Palo Arañado, Chivor district) were analyzed with LA-ICP-MS and an RFC model was applied using the same procedure as detailed above. A total of 360 LA-ICP-MS spot analyses were obtained on 60 euclase crystals (108 spots on 18 euclase from La

Marina; 180 spots on 30 euclase from La Vega de San Juan; 72 spots on 12 euclase from, Palo Arañado). Minor concentrations (<1wt%) of Ca, V, Cr, Ge, and trace concentrations (<100 ppm) of Mg, Sc, Ti, Fe, and Ga, were detected. Using the same methods detailed above, the RFC model was able to predict with 98-99% training-testing accuracy which mine a Colombian euclase is from. The bi-variant discriminant diagrams in Fig. 3-9 were created post-hoc with guidance from the variable importance list.

This further demonstrates the effectiveness and relative ease of use for this method for mineral origin determination studies, which can be summarized as such:

1. Collect a comprehensive database of trace element data
2. Apply the random forest model
3. Create discriminant diagrams after the analysis based on variable importance and probability heat maps, and other visual supplements to the "black box" machine learning algorithm to better understand its classification and predictive ability.

3.5.6 Previous work in Machine Learning Applied to Mineral Origin Determination

The random forest classification (RFC) model has been relatively underutilized in mineral science to date, with the many applications coming from economic geologic prospectively and classification studies (e.g. Rodriguez-Galiano et al. 2015, O'Brian et al, 2015; McKay and Harris, 2016; Hong et al., 2021, Bédard et al., 2022).

Other machine learning algorithms, such as linear discriminant analysis (LDA), have been more commonly applied to mineral science. However as noted previously, using this parametric approach limits the type of variables and data that can be used, needing to satisfy the assumptions of homoscedasticity and collinearity, and for a suite of trace element data such as used in this study, the ability to use as many variables as possible gives a greater chance of determining subtle

differences in mineral chemistry. An additional benefit of the random forest model, however not utilized in this study, is the ability to incorporate categorical information as well as numerical data into the model. This could lead to the inclusion of some of the more traditional qualitative observations (such as phase inclusion shape or composition), or additional instrumental analyses to be incorporated into a random forest model, theoretically improving, and extending the breadth of separational ability.

A study published in Gem Frontiers by Gem Guild (Fortaleché et al., 2020), performed LDA machine learning on a suite of emerald trace element data from the Chivor, Gachala and Muzo mining districts, and reported successful separations from these three districts. While the authors of this present study saw LDA as promising, we ultimately decided against it in favor of RFC as some of the variables we used contained some degree of collinearity. Another study determined it to be possible to differentiate Colombian Emeralds by mine using laser induced breakdown spectroscopy (LIBS) coupled with a statistical algorithm (McManus et al. 2018). Regardless of the differences in approach, previous results support the separability of these emeralds at the district level, and our study is consistent with their conclusion, expounding upon the idea to include the remaining active districts.

3.6 Implications

By coupling the power of machine learning and the uniqueness of each mineral's trace elemental chemistry, it appears hyper-specific origin determination could be possible for many different mineral systems. Machine learning assists in quantifying the otherwise mostly qualitative observation-based gemstone origin determination and could help standardize origin reporting from differing laboratories—which can occasionally provide conflicting origin opinions.

It is suspected that this method will work best on minerals which have more crystallographic sites for trace elemental substitution. The long c-axis channels in emerald can trap primordial fluid, along with the sites in the crystal structure which allow for elemental substitutions, making slight differences in trace element chemistry possible. Minerals such as apatite and tourmaline, with multiple site-substitutions, are predicted to be even more readily separable with this method.

Another benefit of the RFC and the CART class of machine learning is that both quantitative and qualitative observations can be incorporated into the model. While not used in this study, this offers the ability to build a database including different variable types. With Colombian emeralds, previous diagnostic features include the shape and phases of inclusions (Saeseaw et al 2019), and type of mineral included if observable. For example, the rare earth phosphate mineral parisite is diagnostic of Colombian emeralds. A decision tree could be crafted to include these observations. Other types of analytical test, such as UV-Vis and Raman spectroscopy, isotope chemistry etc., could also theoretically be used in conjunction with this model. In this study, LA-ICP-MS data was determined to be effective enough on its own, but in future origin determination studies, these considerations could be taken into account.

With the results of this study, we are now able to confidently determine the belt and mining district of origin from an unknown Colombian emerald by using trace elements analyzed with a random forest classification machine learning algorithm. We are also able to determine the mine of origin of 40 individual mines in Colombia with moderate confidence. More data would be needed in order to increase the confidence in differentiating down to the individual mine, but with the vast number of Colombian emerald mines, along with their geographic proximity, it may not be possible to achieve a better separation using any combination of analytical or machine learning method, nor would it be practical.

The key advantage of this approach is the coupling of a machine learning model, with the prediction score and visualizations to assist the user in understanding why the "black box" arrived at the determinations it did. Even when the algorithm guesses incorrectly, there is ample evidence as to why the model predicted wrong, and what the other possibilities are. This allows the analyst to make an informed prediction and allows this information to be passed along to the client.

Additionally, the empirical probability and corresponding visualizations could give laboratories more confidence in stating their origin opinions, as it is harder for an unethical dealer to claim with certainty that a stone is 100% from a specific location based solely on a report made in good faith. This method has promise for rapidly expanding origin determination capabilities hyper-specifically, well beyond the country of origin.

An issue with country-of-origin reporting when it comes to gemstones is that the geo-political lines drawn over the course of history are completely geologically arbitrary. This results in ready confusion between gems from deposits (or gem-rough alluvium) that cross country boundaries. While it may never be possible to fully connect each unknown gem and mineral back to their mine of origin, the results of this study should provide optimism that there may be ways of continuing to pinpoint origin determinations even better.

3.7 Acknowledgments

The authors would like to thank Alexander Goodsuhm, Research Associate, GIA, for assistance with analyses and sample preparation, and Robert Weldon, Library Director, GIA, for the use of his photographs. Special thanks to the Colombian National Emerald Fund (FEDESMERALDAS) for providing the funds and assistance for fieldwork and sample collection.

3.8 Figures and Tables

Table 3-1. Representative Sample Performance of RFC Model Separations

Belt (East or West)		**Mining District**		**Individual mine**	
Training Accuracy	**Testing Accuracy**	**Training Accuracy**	**Testing Accuracy**	**Training Accuracy**	**Testing Accuracy**
98%	99%	93%	97%	85%	92%

Table 3-2. Top 12 Variables for each RFC separation

Belt (East or West)		**Mining District**		**Individual mine**	
Variable	**Importance (%)**	**Variable**	**Importance (%)**	**Variable**	**Importance (%)**
V/Cr	12.09	V/Ga	4.93	V/Ga	3.57
Li/Na	6.79	Cs	3.87	Li	3.15
Li/Ga	5.46	Sc/Ga	3.54	Ga/Cs	3.01
Li/Al	5.41	Na/Rb	3.53	V/Cr	2.89
Li/Rb	4.95	Ga	3.51	V	2.84
Sc/V	4.03	Ga/Cs	3.49	Ga	2.69
Na/Cs	3.95	Li/Ga	3.35	Al/V	2.67
Rb/Cs	3.63	Rb/Cs	2.85	Li/Al	2.65
Li/V	3.41	V/Cs	2.82	Sc/V	2.40
Cr/Ga	3.15	Al/Ga	2.72	Li/V	2.31
Li	3.11	Na/Cs	2.65	Al	2.29
V/Cs	3.08	Al/Cs	2.61	V/Cs	2.26

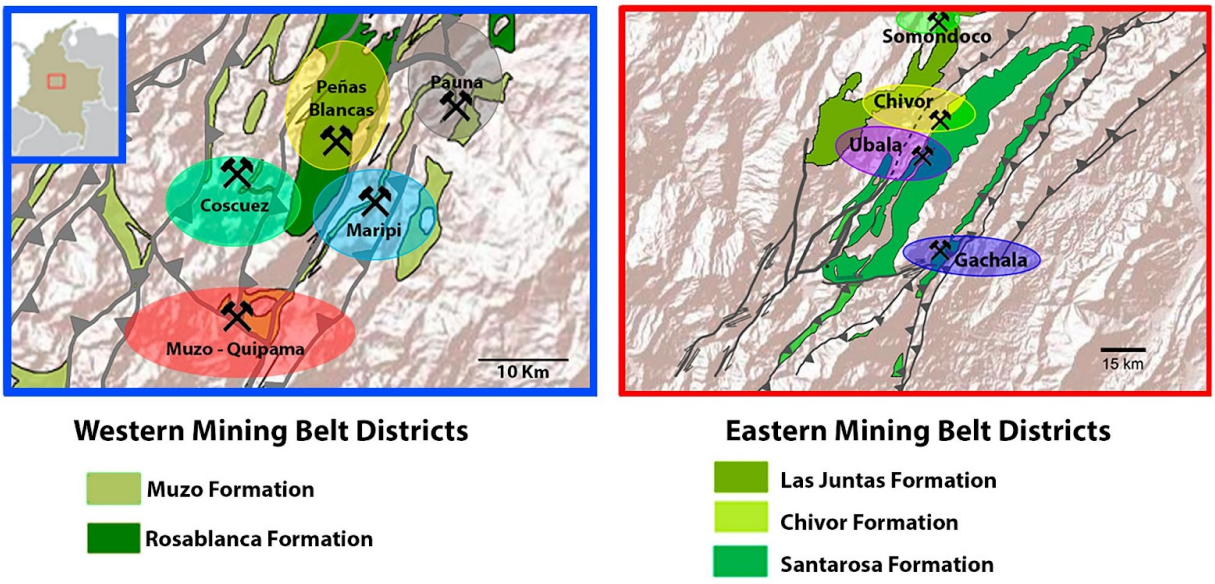

Figure 3-1: Generalized map of the Colombian mining districts showing geographic and geologic proximity

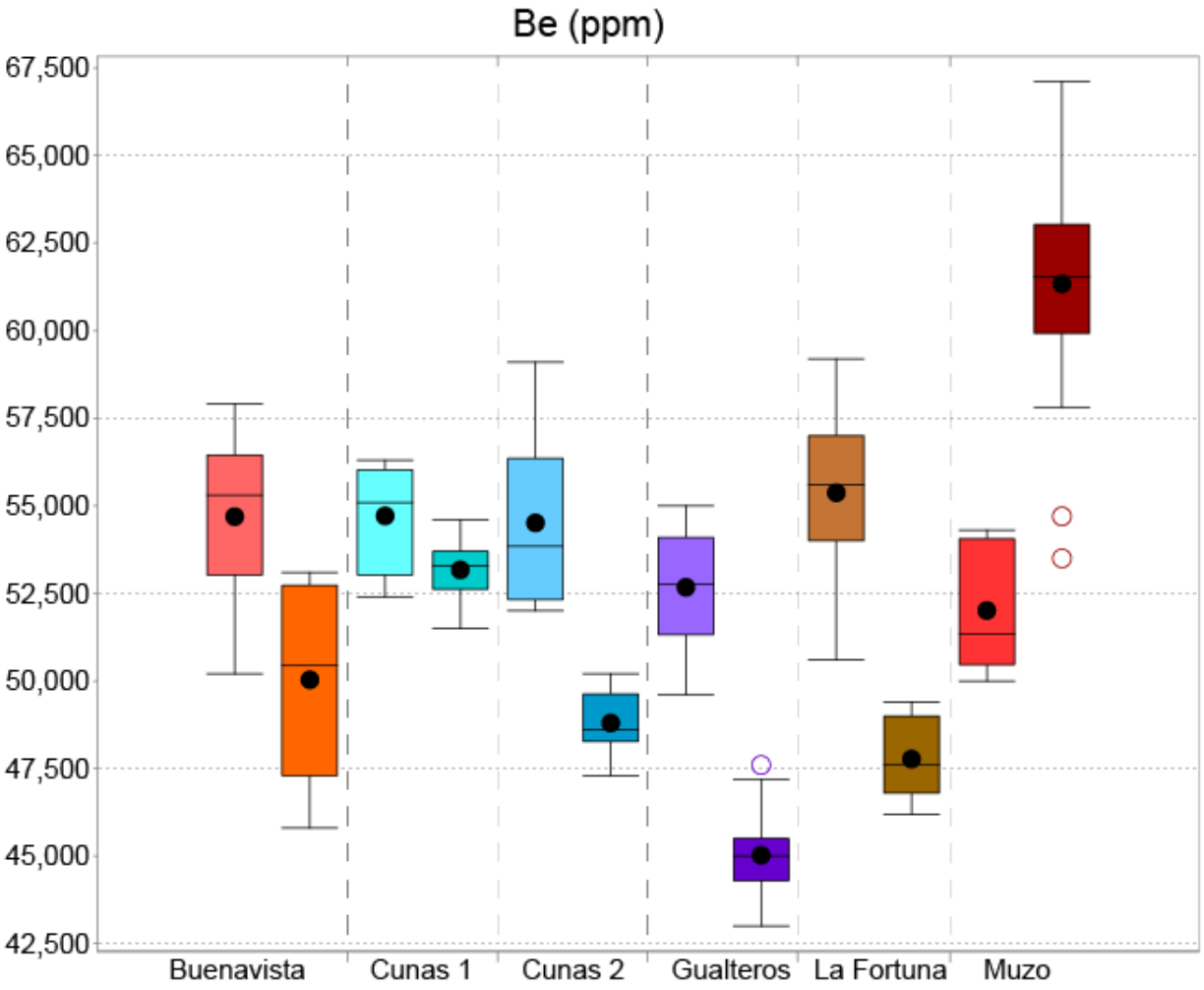
Be (ppm)
67,500
65,000
62,500
60,000
57,500
55,000
52,500
50,000
47,500
45,000
42,500
Buenavista
Cunas 1
Cunas 2
Gualteros
La Fortuna
Muzo

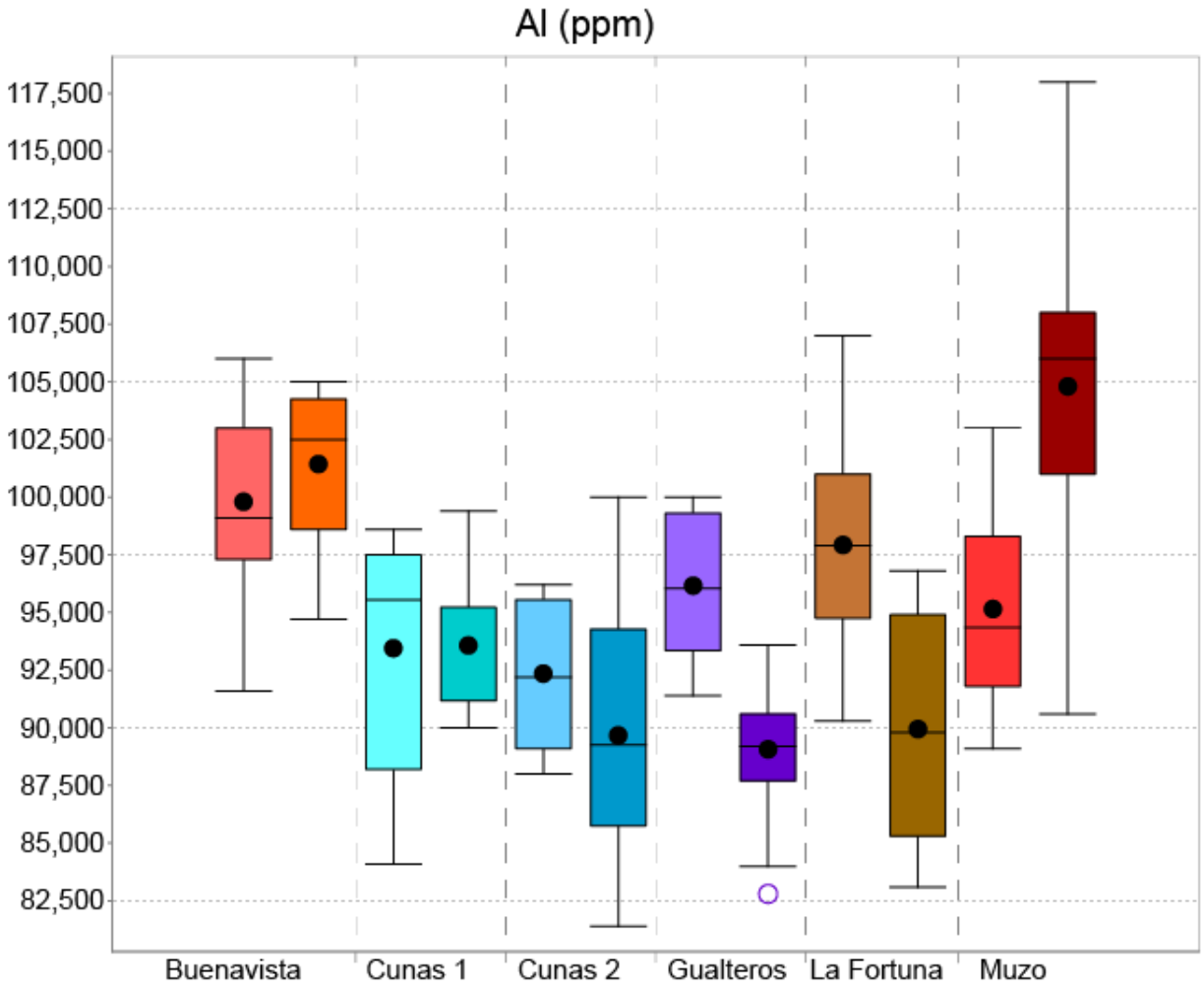

Figure 3-2 (a,b): Example test for systematic instrumental drift by comparing (a) Be and (b) Al, from different LA-ICP-MS sessions. Each dotted section represents emeralds tested from a specific mine—the left box in each is an earlier session, and the right box the same emeralds analyzed in a later session. This shows significant changes in ^{9}Be from session to session, and occurring at each sample location. For this reason, ^{9}Be was not considered for data analysis. Conversely, Al was determined to be consistent between laboratory sessions, and was considered for analysis

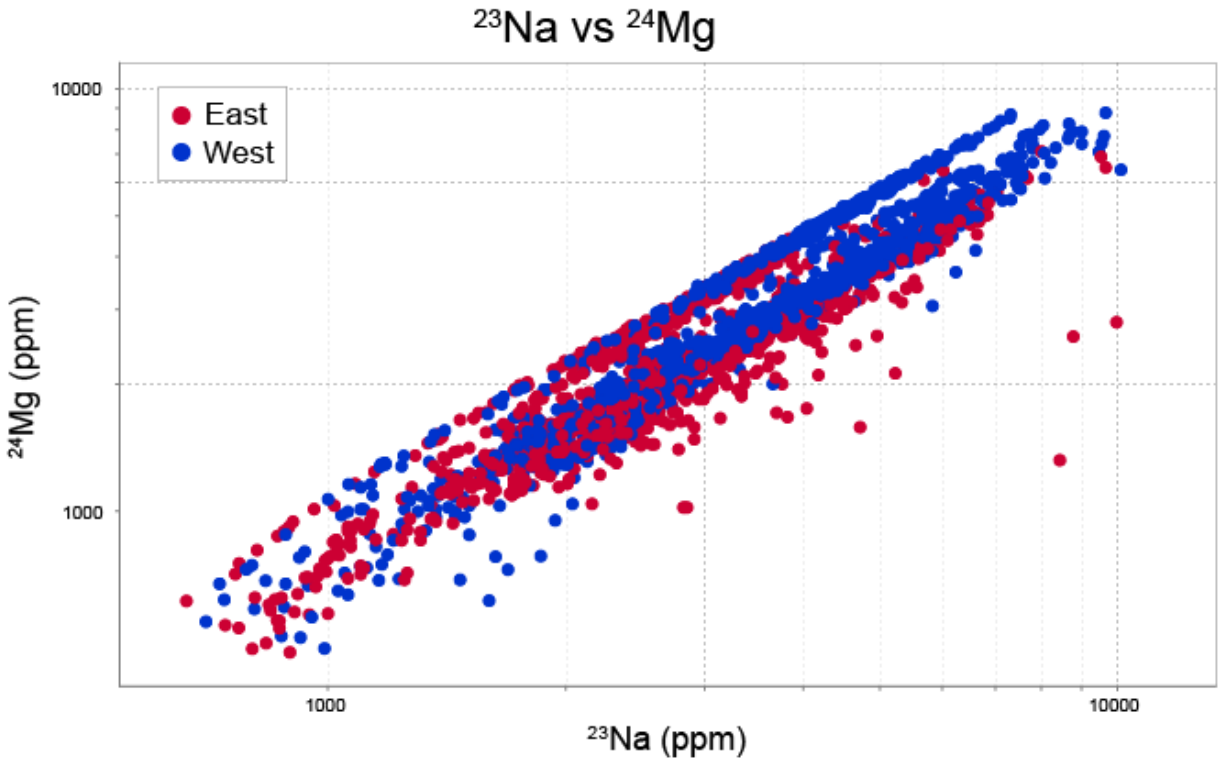

Figure 3-3(a): Scatterplot of ^{24}Mg vs. ^{23}Na from all spot analyses highlighting a possible polyatomic interference varying by laboratory session causing a split in ^{24}Mg. Also note the strong positive correlation between ^{23}Na and ^{24}Mg.

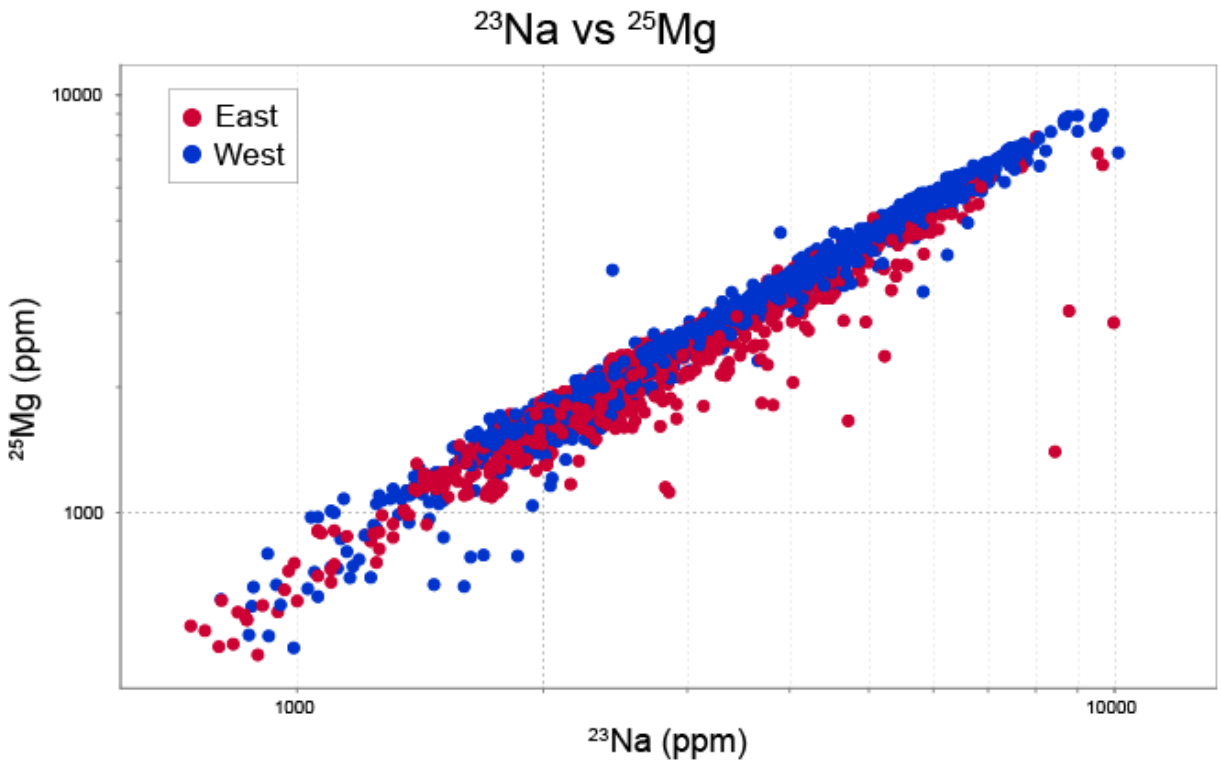

Figure 3-3(b): Scatterplot of ^{25}Mg vs. ^{23}Na from all spot analyses. Note the lack of a split in data as seen in the plot of ^{24}Mg vs. ^{23}Na, still showing a very strong positive correlation

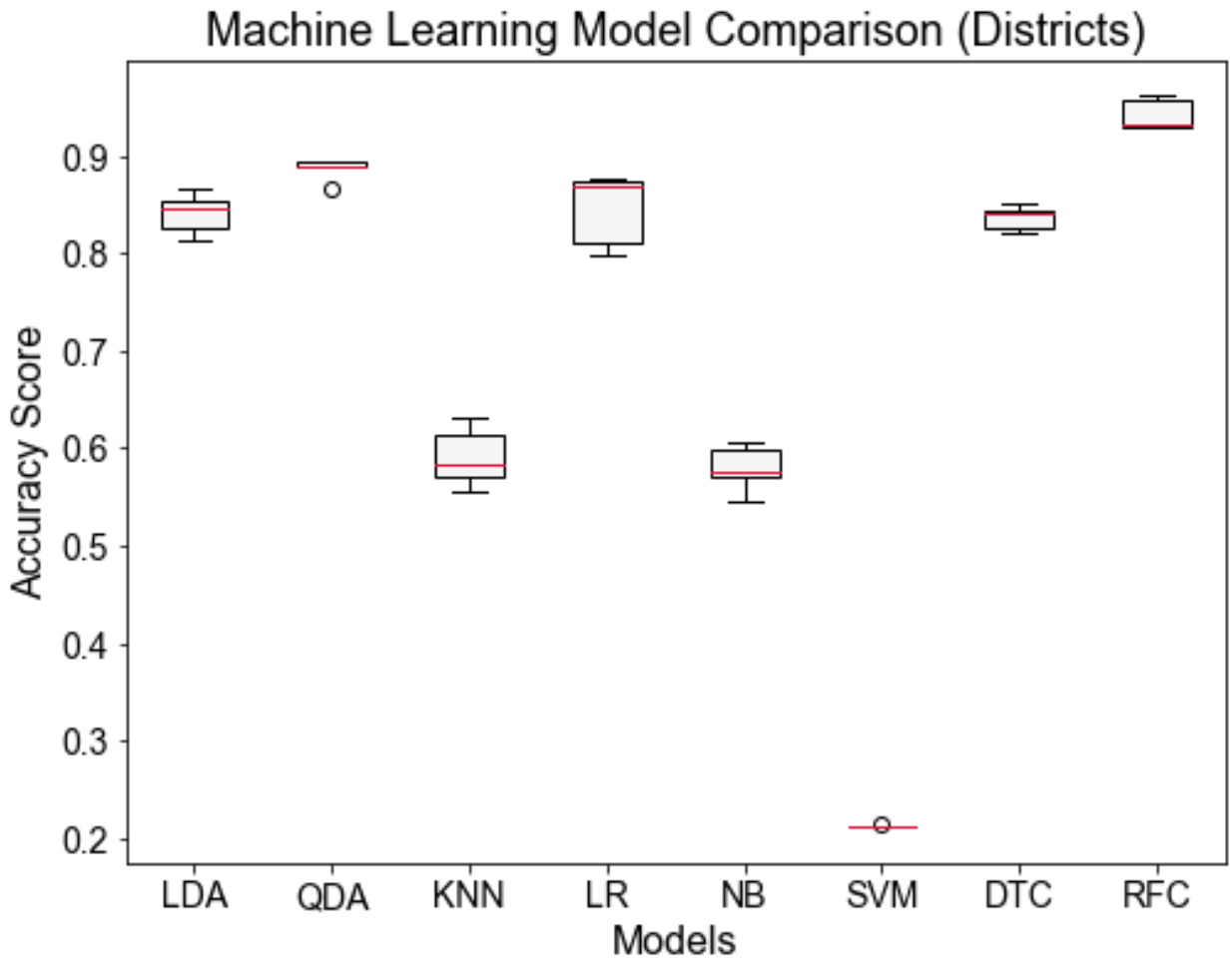

Figure 3-4: Comparison of different machine learning algorithm's effectiveness on the mining belt (east vs. west) dataset. All but the decision tree classification (DTC) and random forest classification (RFC) performed poorly or did not satisfy the underlying assumptions of the model. The RFC model was ultimately chosen for data analysis.

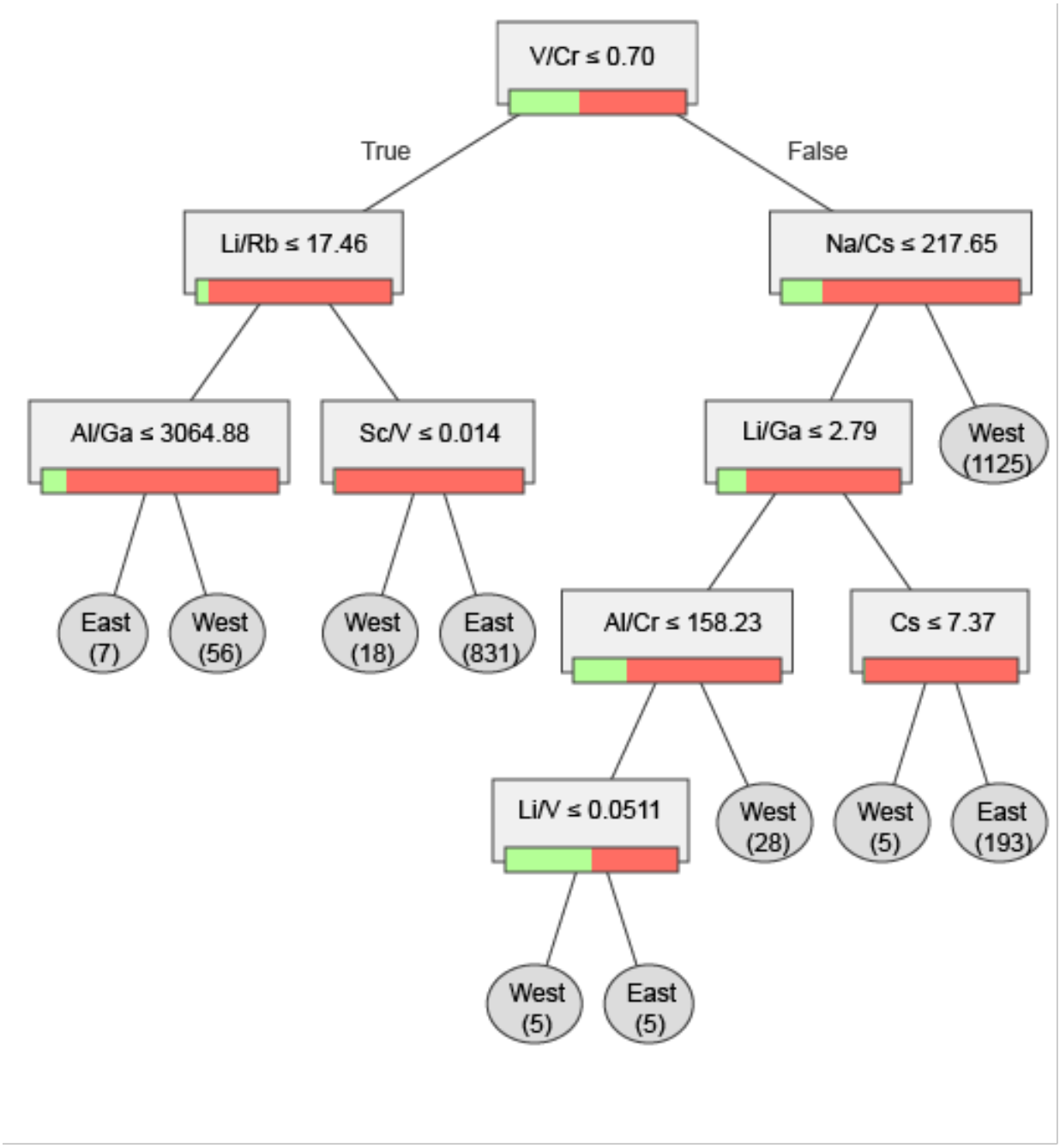

Figure 3-5: An example of a simple 10-node decision tree classification analysis (DTC) performed on the emerald database for separation by mining belt.

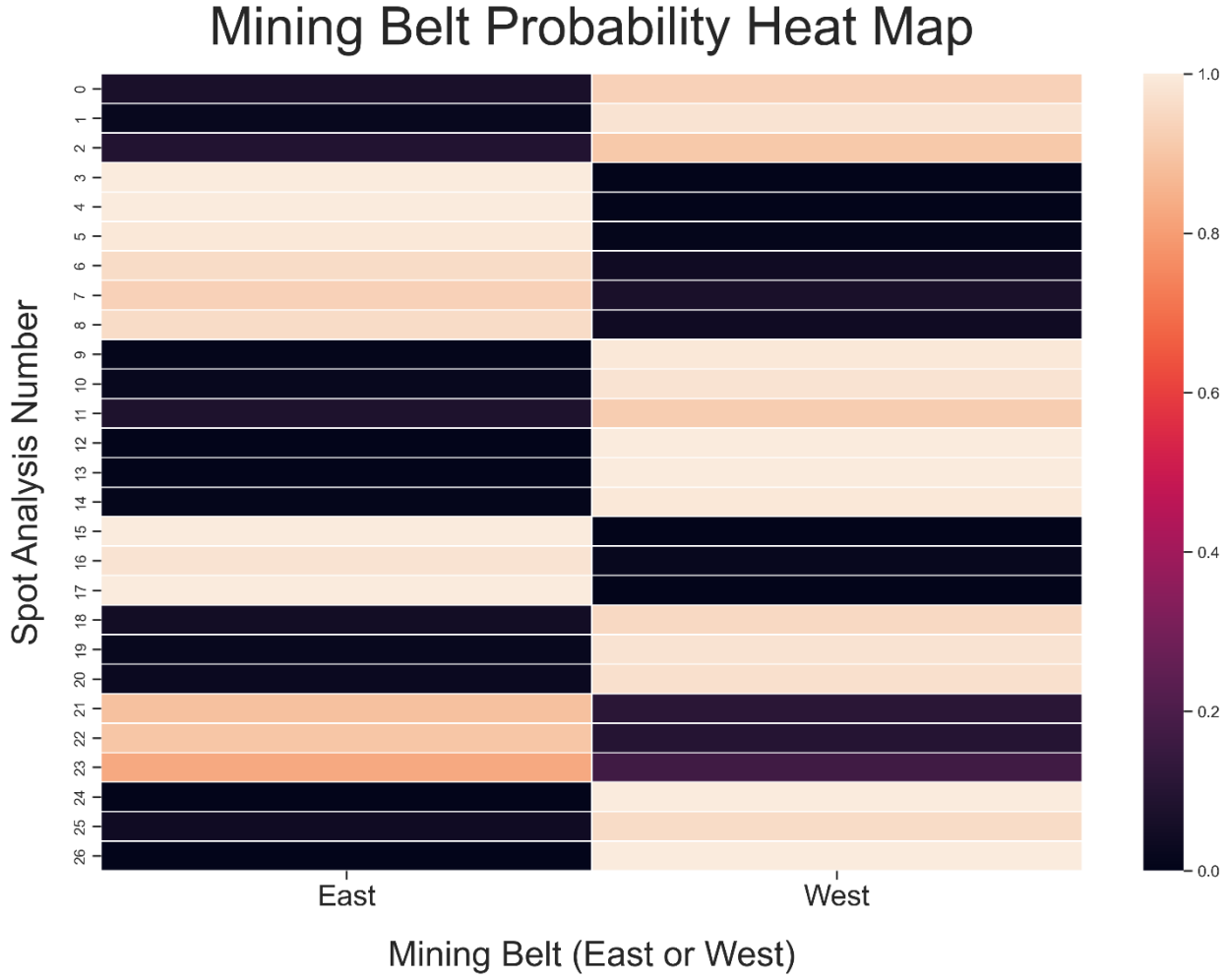
Mining Belt Probability Heat Map
Spot Analysis Number
0
1
2
3
4
5
6
7
8
9
10
11
12
13
14
15
16
17
18
19
20
21
22
23
24
25
26
East
West
Mining Belt (East or West)
1.0
0.8
0.6
0.4
0.2
0.0

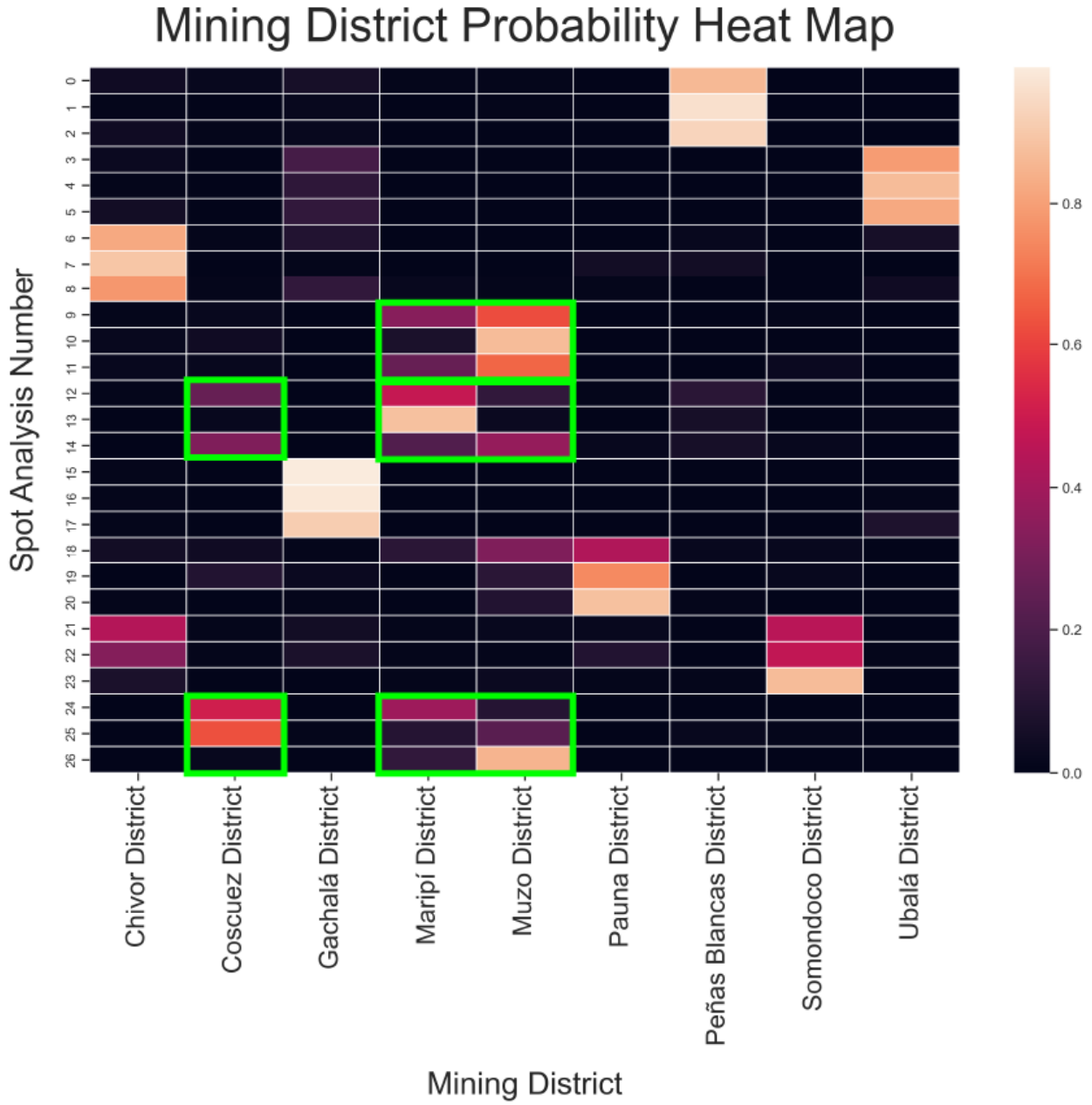
Mining District Probability Heat Map
Spot Analysis Number
0
1
2
3
4
5
6
7
8
9
10
11
12
13
14
15
16
17
18
19
20
21
22
23
24
25
26
Chivor District
Coscuez District
Gachalá District
Maripí District
Muzo District
Pauna District
Peñas Blancas District
Somondoco District
Ubalá District
Mining District
0.0
0.2
0.4
0.6
0.8

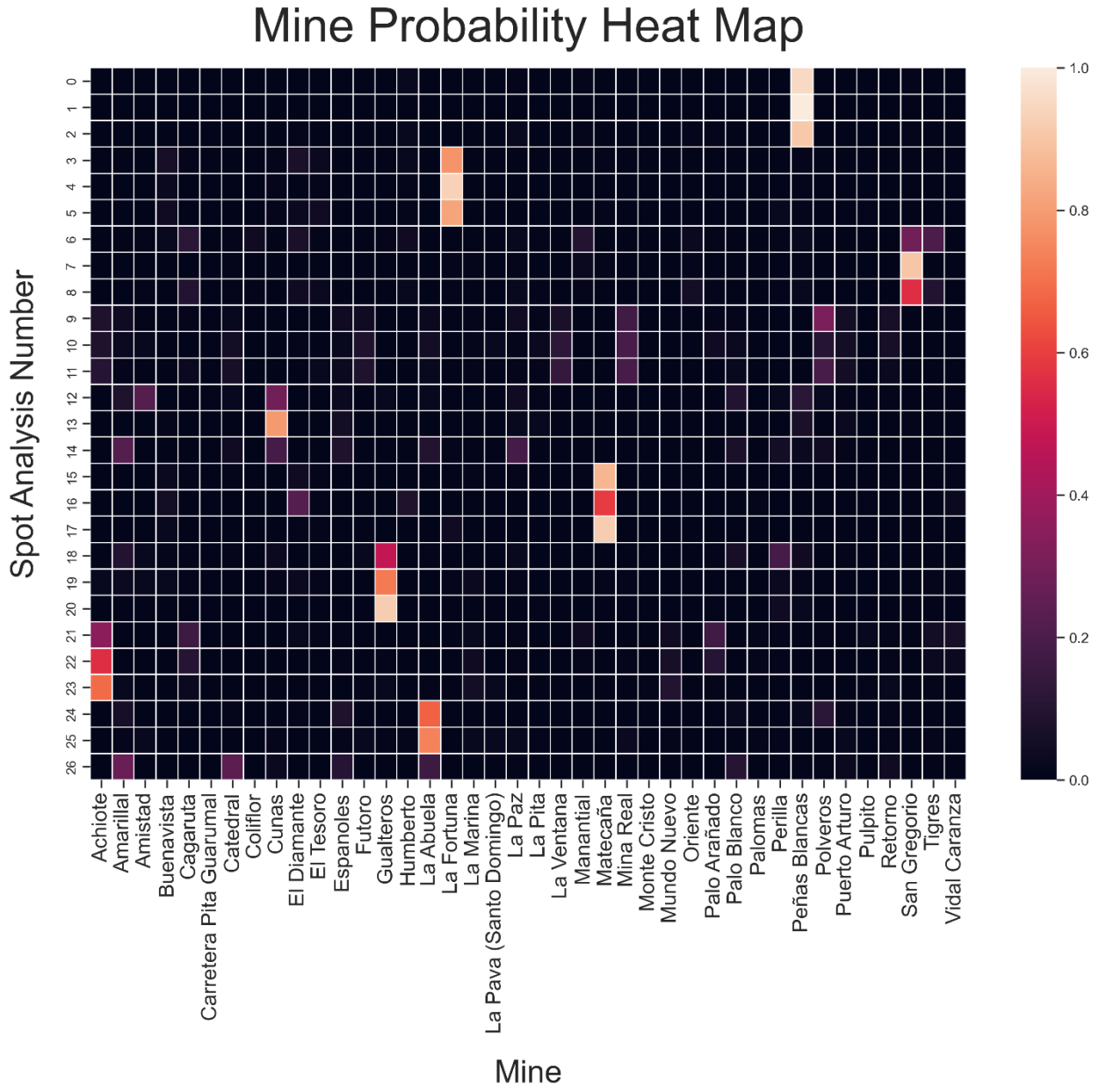

Figure 3-6 (a-c). Probability heat map of sample data by belt (6a), district (6b) and mine (6c). Each grouping of 3 rows are 3 spot analyses on the same emerald, for a total of 9 emeralds—one from each of the 9 mining districts. In this example, the RFC model correctly predicted each mining belt (27/27); correctly predicted mining districts (25/27); and correctly predicted the mine of origin (24/27). In Fig. 3-6b, the most confused districts are highlighted in the green boxes. The correct origins for the 9 sampled emeralds are as followed: Sample 1 (rows 0-2): Peñas Blancas Mine, Peñas Blancas District, Western Belt. Sample 2 (rows 3-5): La Fortuna Mine, Ubalá District, Eastern Belt. Sample 3 (rows 6-8): San Gregorio Mine, Chivor District, Eastern Belt. Sample 4 (rows 9-11): Mina Real, Muzo District, Western Belt. Sample 5 (rows 12-14): Cunas Mine, Maripí District, Western Belt. Sample 6 (rows 15-17): Matecaña Mine, Gachalá District, Eastern Belt. Sample 7 (rows 18-20): Gualteros Mine, Pauna District, Western Belt. Sample 8 (rows 21-23): Achiote Mine, Somondoco District, Eastern District. Sample 9 (rows 24-26): La Abuela Mine, Coscuez District, Western Belt.

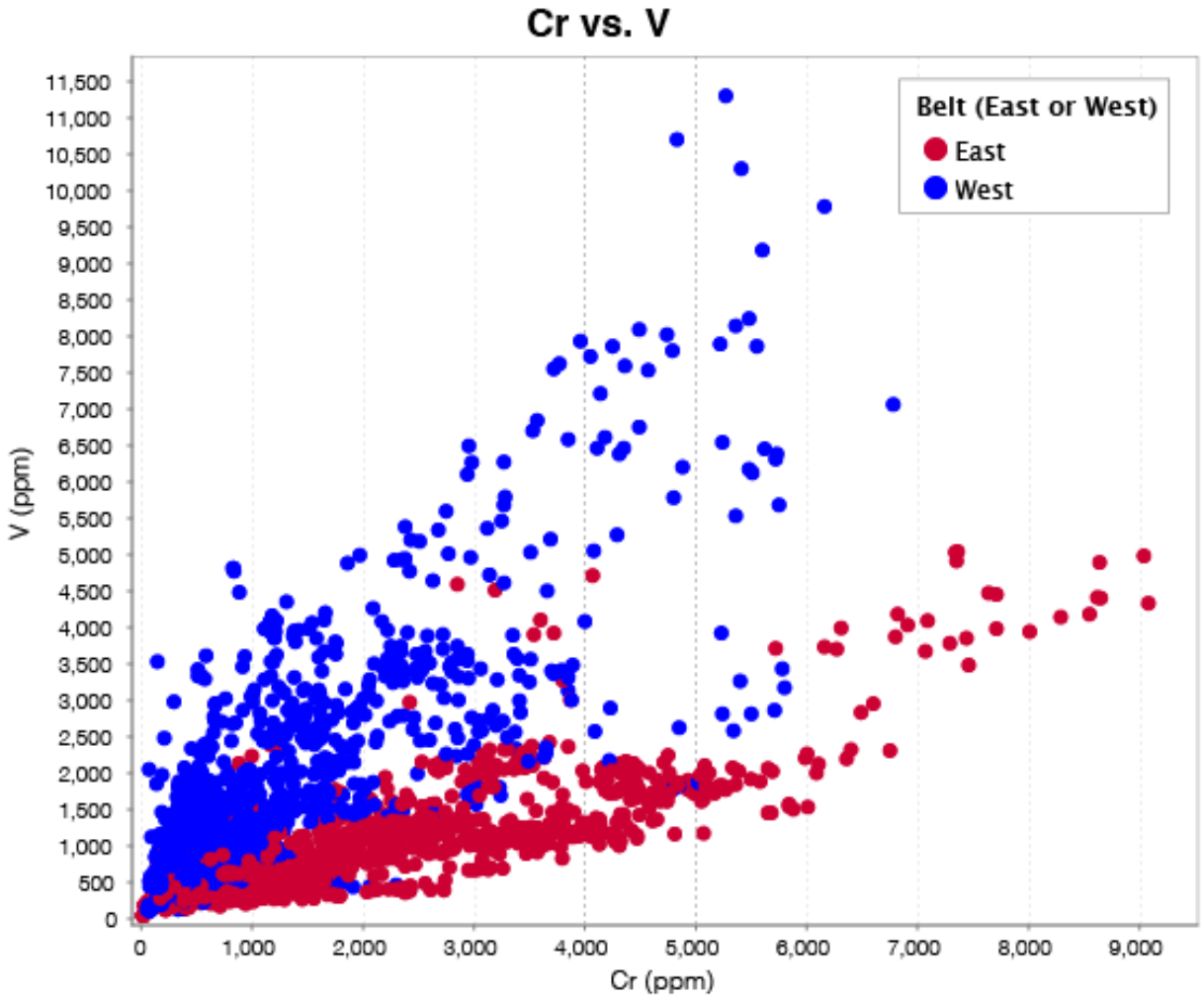

Figure 3-7 (a) Scatter Plot of V vs. Cr in Colombian emeralds highlighting the distinct trends between Eastern and Western belts.

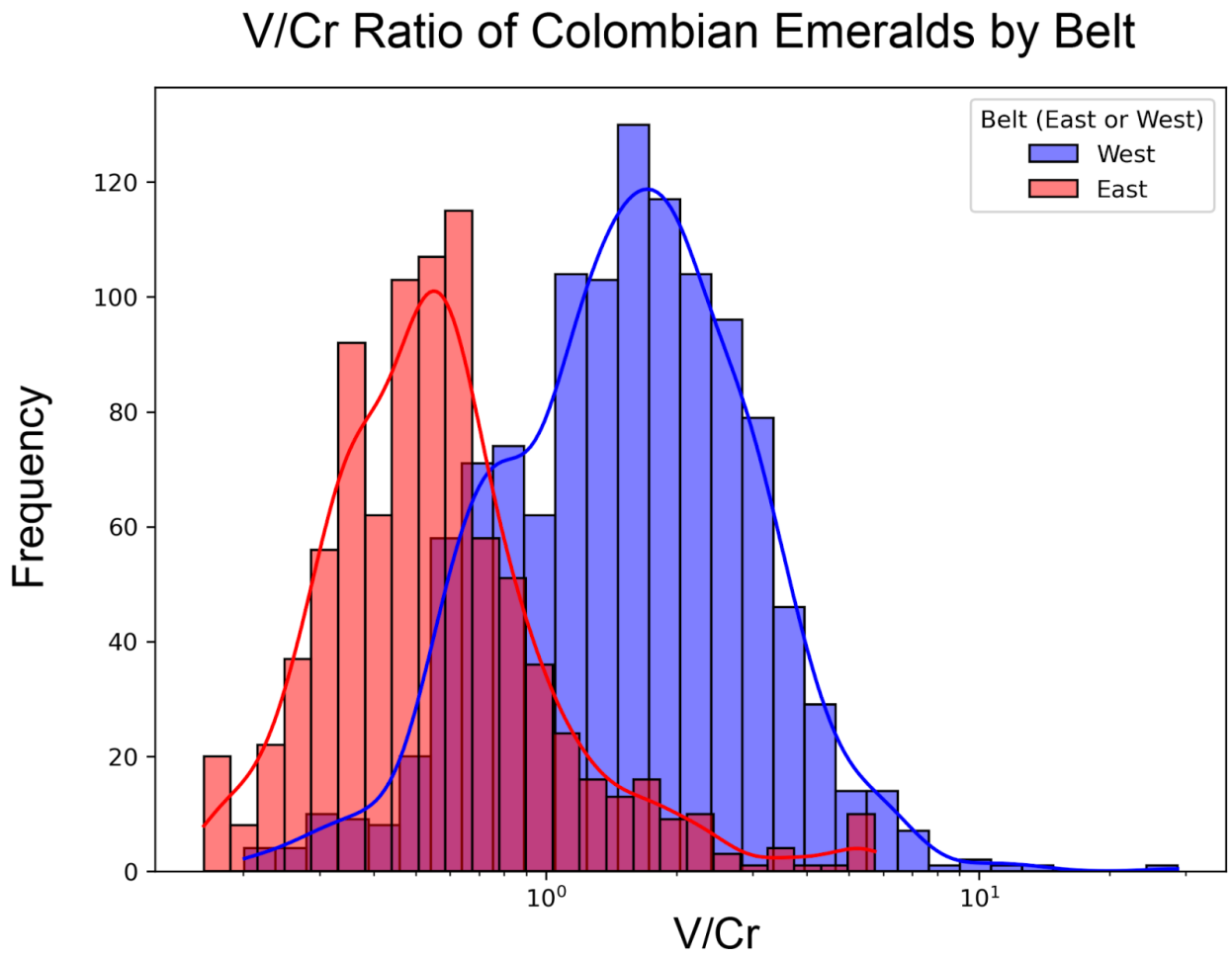

Figure 3-7 (b) Histograms with kernel density estimate (KDE) lines highlighting the bi-modality of the V/Cr ratio in Colombian emeralds between Eastern and Western belts, with some overlap.

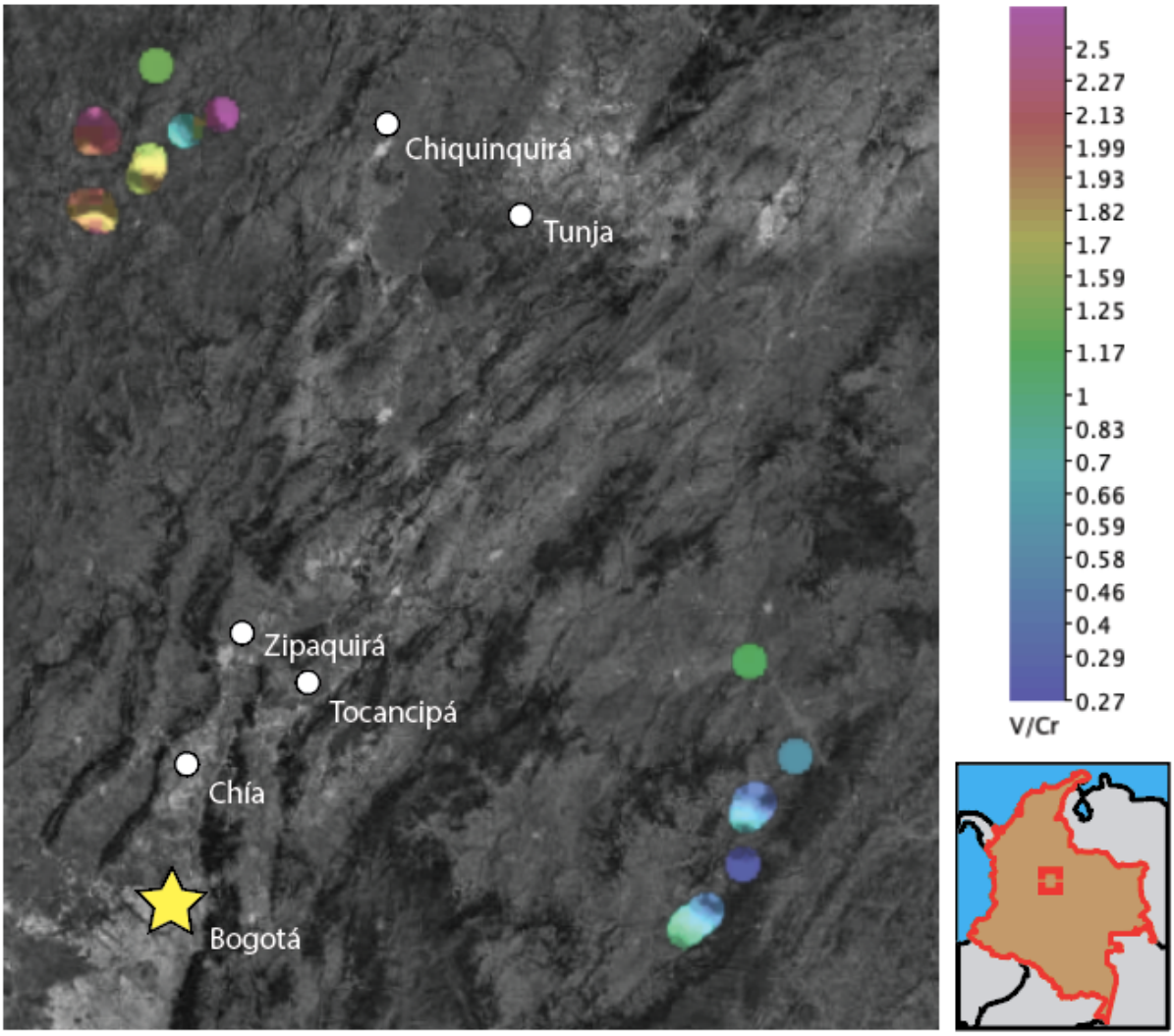

Figure. 3-7 (c) Map of Colombian emerald mines with V/Cr ratios averaged by individual mine and interpolated. Notice the generally higher V/Cr ratio in Western belt, where V/Cr is generally greater than 1, over the Eastern belt emeralds where V/Cr is generally less than 1.

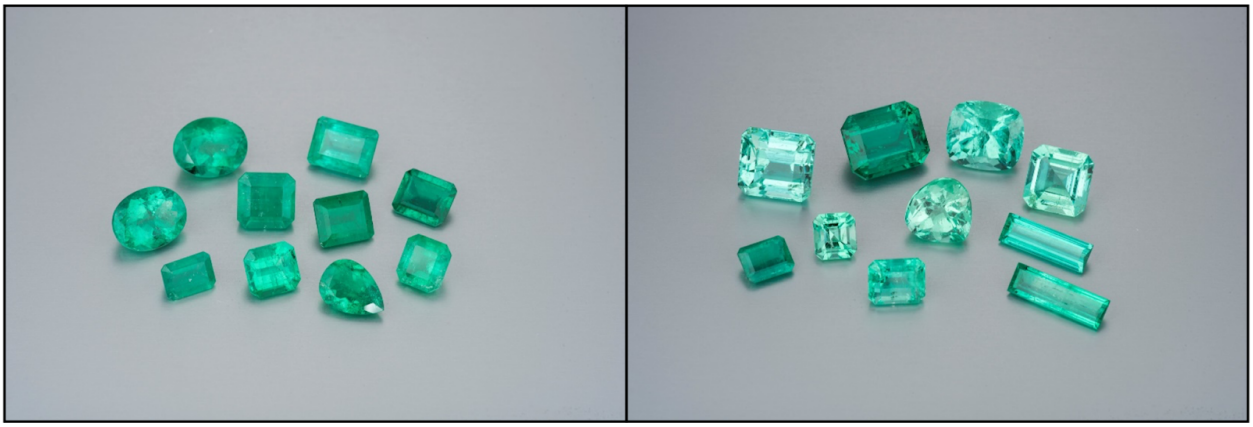

Figure 3-8: Emeralds from the Chivor mining district (east) and the Coscuez mining district (west). Photos by Robert Weldon, GIA. Chivor emeralds (24.90 ct total) and Muzo emeralds (16.20 ct total) are courtesy of Guillermo Ortiz, Colombian Emeralds, Inc.

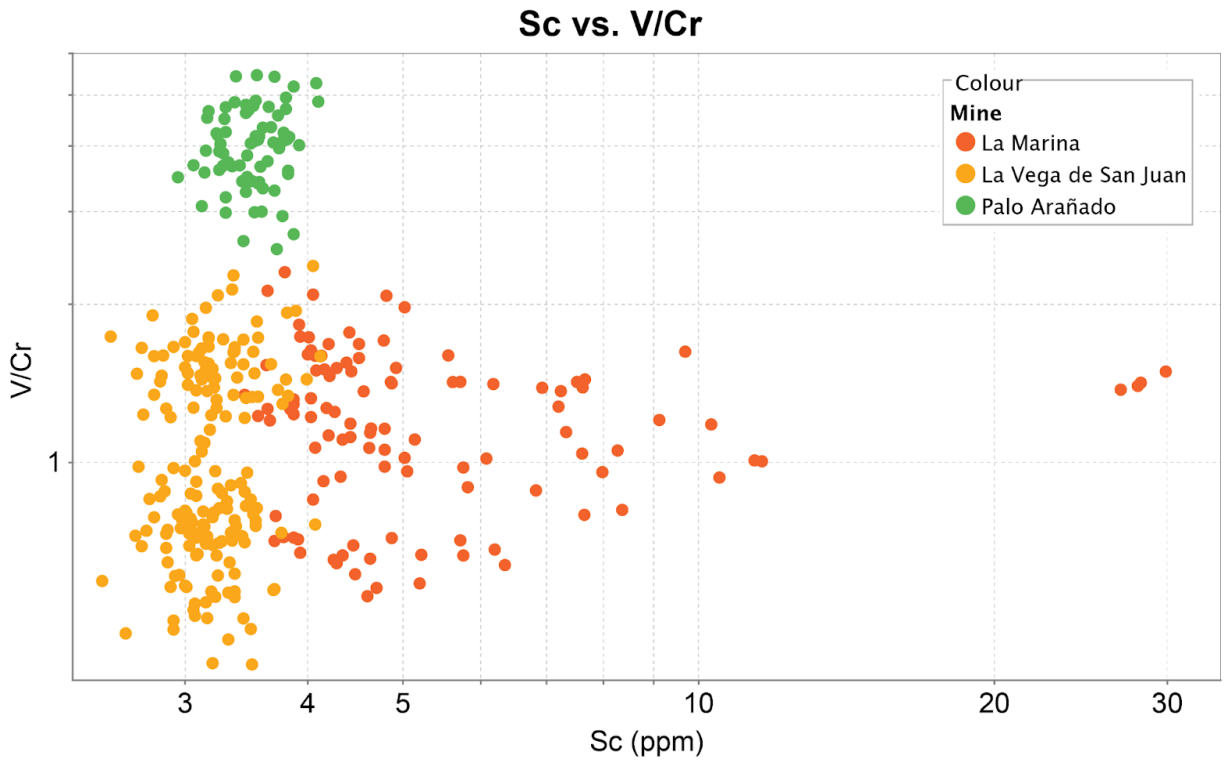

Figure 3-9: Discriminant scatterplot created post-hoc following RFC on LA-ICP-MS Data on Euclase, which effectively separates euclase from each of the 3 mines

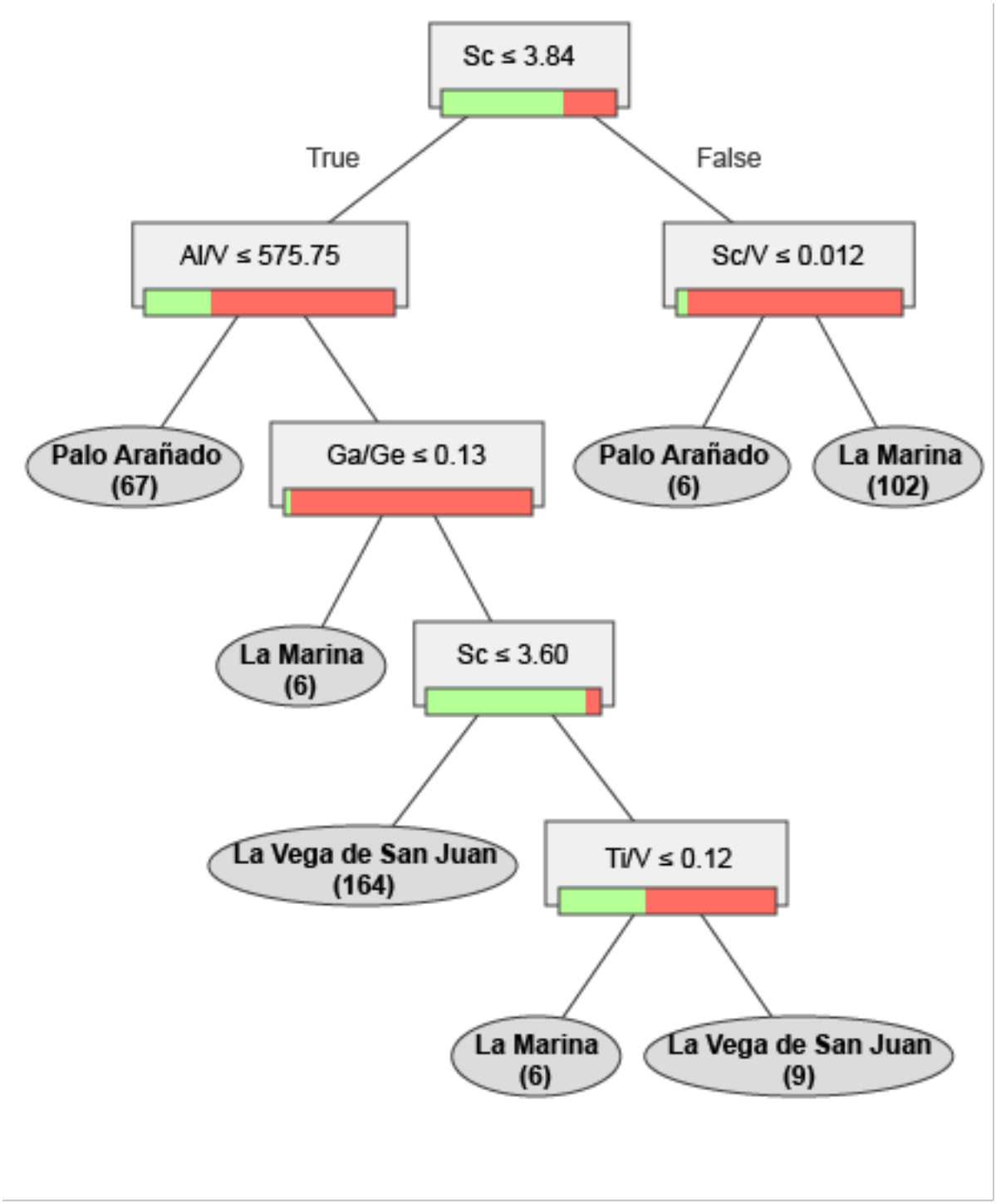

Figure 3-10: A highly effective single decision tree for origin determination of Colombian euclase. Using a random forest containing 100 individual decision trees, overfitting is reduced, and the predictive ability is nearly 100% accurate.

3.9 References Cited

Alonso-Perez, R., Day, J.M.D., Sylvester, P., Cruden, A.R., Antao, S.M., Xu, H., Cook, N.J., Bornhorst, T.J., Kota, H.R., and Kaksonen, A.H. (2021) Rare Earth Element and Incompatible Trace Element Abundances in Emeralds Reveal Their Formation Environments. Minerals (2075-163X), 11, 513.

Altenberger, U., Rojas-Agramonte, Y., Yang, Y., Fernández-Lamus, J., Häger, T., Guenter, C., Gonzalez-Pinzón, A., Charris-Leal, F., and Artel, J. (2022) In Situ U–Th–Pb Dating of Parisite: Implication for the Age of Mineralization of Colombian Emeralds. Minerals, 12, 1232.

Angarita-Sarmiento, L.G., García-Toloza, J., Gonzalez-Duran, A.F., Alvarado-Gonzalez, H.R., Paipa, L., Vargas, H., Morales, A., Zamora, J., and Cedeño-Ochoa, C.J. (2022) Méthodologie pour la détermination de l'origine des émeraudes colombiennes. Émeraudes, tout un monde!, LES ÉDITIONS DU PIAT, 319–328.

Banks, D.A., Giuliani, G., Yardley, B.W.D., and Cheilletz, A. (2000) Emerald mineralisation in Colombia: fluid chemistry and the role of brine mixing. Mineralium Deposita, 35, 699–713.

Bédard, É., De Bronac de Vazelhes, V., and Beaudoin, G. (2022) Performance of predictive supervised classification models of trace elements in magnetite for mineral exploration. Journal of Geochemical Exploration, 236, 106959.

Branquet, Y., Laumonier, B., Cheilletz, A., and Giuliani, G. (1999) Emeralds in the Eastern Cordillera of Colombia: Two tectonic settings for one mineralization. Geology, 27, 597–600.

Breit, G.N., and Wanty, R.B. (1991) Vanadium accumulation in carbonaceous rocks: A review of geochemical controls during deposition and diagenesis. Chemical Geology, 91, 83–97.

Cedeño, C.J., Jiménez, J.F., Herreño, J.H., and Fortaleché, D. (2015) Progress on the study of parameters related to the origin of Colombian emeralds. World Emer, 88–97.

Cheilletz, A., Feraud, G., Giuliani, G., and Rodriguez, C.T. (1994) Time-pressure and temperature constraints on the formation of Colombian emeralds; an 40 Ar/ 39 Ar laser microprobe and fluid inclusion study. Economic Geology, 89, 361–380.

Cronin, D.P., and Rendle, A.M. (2012) Determining the geographical origins of natural emeralds through nondestructive chemical fingerprinting. The Journal of Gemmology, 33, 116.

Fortaleché, D., Li, Q., Shan, M., and Lucas, A. (2020) Specific Mine Determination of Colombian Emeralds from Muzo Formation area, Chivor and Gachala. Gemology Frontier, 1.

García, J., Herreño, M.J., González, A.F., and Cedeño, C.J. (2019) Photoluminescence analysis to determine the origin of emeralds from the Eastern and Western belts in Colombia, 2, 5.

Garcia-Toloza, J., Ramírez-Juya, V., Betancur-Acevedo, C.A., Gonzalez, V., Angarita, G., and Alvarado, H. (2022) Chromium and vanadium from host rock to emerald:tracing differences between the two main emerald zones in Colombia and their gemological implication. In A.B. Christie, Ed., Proceedings of the 16th SGA Biennial Meeting pp. 28–31.

Giuliani, G., France-Lanord, C., Cheilletz, A., Coget, P., Branquet, Y., and Laumomnier, B. (2000) Sulfate Reduction by Organic Matter in Colombian Emerald Deposits: Chemical and Stable Isotope (C, O, H) Evidence. Economic Geology, 95, 1129–1153.

Giuliani, G., Groat, L.A., Marshall, D., Fallick, A.E., and Branquet, Y. (2019) Emerald Deposits: A Review and Enhanced Classification. Minerals, 9, 105.

González-Durán, A.F., García-Toloza, J., Bonilla, G., Cedeño-Ochoa, C.J., Angarita-Sarmiento, L.G., Castañeda-Gómez, A.J., Parra-Bastidas, S.D., Bocanegra-Rodríguez, L.C., Montaña-Cárdenas, J., and López-Castillo, C.L. (2021) Geoquímica y mineralogía de la mina La Pava, Muzo-Quípama: implicaciones en la exploración de esmeraldas en Colombia. Boletín de Geología, 43, 117–142.

Gübelin, E.J., and Koivula, J.I. (1986) Photoatlas of Inclusions in Gemstones, ABC edition., 532 p. Zurich.

Gustafsson, J.P., Persson, I., Oromieh, A.G., van Schaik, J.W.J., Sjöstedt, C., and Kleja, D.B. (2014) Chromium(III) Complexation to Natural Organic Matter: Mechanisms and Modeling. Environmental Science & Technology, 48, 1753–1761.

Hong, S., Zuo, R., Huang, X., and Xiong, Y. (2021) Distinguishing IOCG and IOA deposits via random forest algorithm based on magnetite composition. Journal of Geochemical Exploration, 230, 106859.

Jimenez Guevara, J.F. (2017) Estudio químico, mineralógico y espectroscópico de esmeraldas colombianas de los distritos mineros de Chivor, Muzo y Coscuez y su aplicación en la determinación de origen geográfico.

Kozłowski, A., Metz, P., and Estrada, H. (1988) Emeralds from Somondoco, Colombia: chemical composition, fluid inclusions and origin. Neues Jahrbuch für Mineralogie - Abhandlungen, 159, 23–49.

Mantilla, L.C., Silva, A., Serrano, J.J., Conde, J., Gómez, C., Ramírez, J.C., Meza, J.A., Pelayo, Y., Ortega, L.M., Plata, L.M., and others (2007) Investigación petrográfica y geoquímica de las sedimentitas del Cretácico inferior (K1) y sus manifestaciones hidrotermales asociadas planchas 169, 170, 189, 190 (Cordillera Oriental), implicaciones en la búsqueda de esmeraldas. INGEOMINAS-Universidad Industrial de Santander (UIS), Bogotá.

May, T.W., and Wiedmeyer, R.H. (1998) A Table of Polyatomic Interferences in ICP-MS. Atomic Spectroscopy, 19.

McKay, G., and Harris, J.R. (2016) Comparison of the Data-Driven Random Forests Model and a Knowledge-Driven Method for Mineral Prospectivity Mapping: A Case Study for Gold Deposits Around the Huritz Group and Nueltin Suite, Nunavut, Canada. Natural Resources Research, 25, 125–143.

McManus, C.E., Dowe, J., and McMillan, N.J. (2018) Quantagenetics® analysis of laser-induced breakdown spectroscopic data: Rapid and accurate authentication of materials. Spectrochimica Acta Part B: Atomic Spectroscopy, 145, 79–85.

O'Brien, J.J., Spry, P.G., Nettleton, D., Xu, R., and Teale, G.S. (2015) Using Random Forests to distinguish gahnite compositions as an exploration guide to Broken Hill-type Pb–Zn–Ag deposits in the Broken Hill domain, Australia. Journal of Geochemical Exploration, 149, 74–86.

Ottaway, T.L., Wicks, F.J., Bryndzia, L.T., Kyser, T.K., and Spooner, E.T.C. (1994) Formation of the Muzo hydrothermal emerald deposit in Colombia. Nature, 369, 552–554.

Pignatelli, I., Giuliani, G., Morlot, C., Rouer, O., Claiser, N., Chatagnier, P.-Y., and Goubert, D. (2017) Recent Advances in Understanding the Similarities and Differences of Colombian Euclases. The Canadian Mineralogist, 55, 799–820.

Renfro, N.D., Koivula, J.I., Muyal, J., McClure, S.F., Schumacher, K., and Shigley, J.E. (2016) Chart: Inclusions in Natural, Synthetic, and Treated Emerald | Gems & Gemology. Gems & Gemology, 52, 402–403.

Rodriguez-Galiano, V., Sanchez-Castillo, M., Chica-Olmo, M., and Chica-Rivas, M. (2015) Machine learning predictive models for mineral prospectivity: An evaluation of neural networks, random forest, regression trees and support vector machines. Ore Geology Reviews, 71, 804–818.

Romero-Ordóñez, F.H.R., González-Durán, A.F., García-Toloza, J., Cohen, J.R., Ochoa, C.J.C., González, H.R.A., and Sarmiento, L.G.A. (2021) Mineralogy and Fluid Inclusions of the Cunas Emerald Mine, Maripí, Boyacá, Colombia. Earth Sciences Research Journal, 25, 139–156.

Saeseaw, S., Renfro, N.D., Palke, A.C., Ziyin Sun, and McClure, S.F. (2019) Geographic Origin Determination of Emerald. Gems & Gemology, 55, 614.

Schwarz, D. (1992) The chemical properties of Colombian emeralds. Journal of Gemmology, 23, 225–233.

Shane F. McClure, Moses, T.M., and Shigley, J.E. (2019) The Geographic Origin Dilemma | Gems & Gemology. Gems & Gemology, 55, 457–462.

Shor, R., and Weldon, R. (2009) Ruby and Sapphire Production and Distribution: A Quarter Century of Change. Gems & Gemology, 45, 236–259.

Terraza Melo, R. (2019) Notas sobre el contexto tectonoestratigráfico de formación de las esmeraldas colombianas. Boletín Geológico, 37–48.

Vertriest, W., Palke, A., and Renfro, N. (2019) Field Gemology: Building a Research Collection and Understanding the Development of Gem Deposits | Gems & Gemology. Gems & Gemology, 55, 490–511.

Chapter 4: Promise and Limitations of Provenance Determination of Alluvial Montana Sapphires Using Random Forest Machine Learning on LA-ICP-MS Trace Elemental Data

Co-authors: Aaron Palke, Adam Simon

4.1 Abstract

Geographic origin is an increasingly important factor driving the value of a gemstone and it is a main objective of gemological laboratories to develop methods to better pin-point the provenance of an unknown gemstone. Recent work has shown promise for hyper-specific provenance determination methods utilizing a random forest machine learning model on a comprehensive suite of trace element chemistry on Colombian emeralds. To further test the effectiveness of this method, Montana sapphires were chosen for provenance analysis as provenance studies have not been done before on these sapphires, and their geologic origin has been a subject of debate. Sapphires occur in four localities in Montana: The Yogo Gulch (primary igneous), Rock Creek (alluvial), Missouri River (alluvial) and Dry Cottonwood Creek (alluvial). While Yogo Gulch sapphires have been fairly well characterized and studied, the source of alluvial sapphire deposits of Montana remain poorly understood. The goal of this study is to see if it is possible to determine the provenance of an unknown Montana sapphire given laser ablation inductively coupled plasma mass spectrometry (LA-ICP-MS) data, and to see if the trace elemental chemistry can shed light on their primary geologic origin. 182 sapphires from each deposit were analyzed with LA-ICP-MS for trace element chemistry (total of 750 individual spot analyses), and a random forest machine learning model was applied to the dataset. It was determined that the

provenance of an alluvial Montana sapphire could be predicted correctly with 90% accuracy, with the most important variable for separation being the Mg/Ti ratio. Yogo Gulch sapphires are confirmed to be chemically distinct from the alluvial sapphires, demonstrating a 99% separability accuracy. Mg/Ti was also determined to have a strong positive correlation (r = 0.84), and is the most effective bi-variate diagram for visualizing geographic separation. This trend in Mg/Ti is interpreted to be a result of differences in oxygen fugacity during formation in the upper mantle, possibly as a result of forming at different depths. This study adds support to the hypothesis that the famous alluvial Montana sapphires have differing primary geologic formational environments, and their geographic provenance can be determined with a high degree of accuracy.

4.2 Introduction

Improving mineral origin determination methods is one of the primary goals of researchers in the gemstone industry (e.g. McClure et al., 2019, Krebs et al., 2020), and has broad reaching implications for quality assurance and promoting ethical trade practice. Recent work detailed a highly effective method of provenance determination at varying degrees of locality specificity using a random forest machine learning algorithm on a suite of trace element data on Colombian emeralds (Chapter 3 of this dissertation: Blakemore et al. *in review*). This study aims to build upon this previous provenance determination work by using a random forest machine learning methodology on an entirely different, and in some ways more challenging set of trace elemental data to test the effectiveness and limitations on a different mineralization system. Sapphires from Montana are an intriguing mineral system and locality to study with this method because (1) there is previous work proving the effectiveness of using trace elements to separate gem corundum broadly by country of origin (e.g. Sutherland et al., 1998; Zaw et al., 2006; Peucat et al., 2007; Simonet et al., 2008; Sutherland and Abduriyim, 2009) (2) much work has been done by gemological laboratories to build up collections of well documented sapphires (e.g. Hsu et al. 2016), (3) corundum has few

crystallographic sites for trace element substitution so the limitations of the method from Blakemore et al. (*in review*) will be tested, and (4) the source of Montana's famous alluvial sapphires remains elusive, and studies have suggested that while they are close in geographic proximity (Fig. 4-1), the wide array of mineral inclusions observed in alluvial Montana sapphires may suggest differing geologic origins, requiring the need of a origin determination study of these gems (Berger and Breg, 2006, Zwaan, 2015). Adding to the body of geochemical work performed on Montana sapphires has the potential to discover insights into their formation by testing to see if alluvial sapphires from Montana are chemically and statistically distinct from each other.

Sapphire is a variety of the mineral corundum (Al_2O_3), and although it is colloquially thought of as blue, it in fact more broadly refers to any non-red colored corundum, with red corundum famously known as ruby. Non blue or red corundum is sometimes referred to as "fancy sapphires", much like a colored diamond is called a "fancy diamond". Its high hardness (Mohs = 9) and durability make it a useful mineral for use as an abrasive, in addition to its ornamental use as a gemstone. Corundum is allochromatic, meaning that its color is determined by trace elemental impurities. Ruby is colored by Cr^{3+}, and blue sapphire is colored by varying amounts of Fe^{3+} and Ti^{3+}, and V^{3+}. The color of corundum can be artificially enhanced using a Be diffusion heat treatment, which is one of the key treatments gem laboratories test for to determine if color is natural or artificial (Emmet et al., 2003). Elemental substitutions occur predominantly in the Al site. Common substituents include Mg, Ti, Cr, Fe, V, and Ga. The limited number of sites for substitution is in part what makes provenance determination in corundum utilizing trace elements challenging (e.g. Palke et al., 2018; Krebs et al 2020).

Sapphires occur in four mining locations in Montana: Yogo Gulch (primary igneous), Missouri River (alluvial), Dry Cottonwood Creek (alluvial), and Rock Creek (alluvial) (Fig. 4-1). One formational model of Yogo Gulch sapphires suggests from garnet inclusion evidence that Yogo

sapphires formed from a mantle eclogite and were then transported as xenocrysts to the surface (Cade and Groat, 2006). Plagioclase inclusions are a relatively common occurrence in Montana sapphires, which is inconsistent with mantle eclogite formation, and surficial etching on the crystal faces of Yogo sapphires indicate disequilibrium with the host rock lamprophyre (Renfro et al. 2018). A possible formational model to reconcile these observations proposes that Yogo sapphires were created through a peritectic melting reaction which occurred when the lamprophyre intruded into the lower crust and partially melted in place aluminum-rich rock (Dahy, 1991, Palke et al., 2015, Renfro et al. 2018).

Sapphires from Missouri River, Dry Cottonwood Creek, and Rock Creek (also called Gem Mountain) are all secondary alluvial deposits, with gemstones being extracted from riverbeds and poorly sorted mudflows (Hsu et al., 2016). This intrinsically obfuscates geologic study on the sapphires from these localities since their primary origin and context to their formation is unknown, especially in contrast to Yogo sapphires, which can be studied in situ. The underlying bedrock at these localities consists of Eocene rhyolite flows along with other volcanics (Breg, 2014). Textual evidence on the surface of these sapphires suggests that these alluvial sapphires are the result of weathered xenocrysts from alkali basaltic magmas (Breg, 2007). Inclusions and geochemical evidence suggest a metasomatic origin (Zwaan et al. 2015; Palke et al., 2023).

The geology of western Montana is defined by basin development and degradation caused by the subducting Pacific plate during the Cenozoic (e.g. Garland 2002, Fuentes et al. 2012). Sediments accumulated fairly rapidly in the Proterozoic basin between 1470 Ga and 1400 Ma (Evans et al. 2000) and these sediments are locally exposed in the Rock Creek area. Several periods of glaciation over North America during the Pleistocene eroded and carved away underlying bedrock. Garland (2002) postulated that alluvial sapphires were distributed post-glacially from a pre-existing paleoplacer deposit from the Pliocene.

One of the motivations behind performing a provenance determination study on Montana sapphires is to gain insight into whether or not alluvial sapphires share a common source material, or are chemically distinct. Krebs et al., 2020 notes the potential and pitfalls of using LA-ICP-MS as a tool for gem-corundum provenance determination, citing the need for additional discrimination tools as it has few sites for trace elemental substitution and can form under a variety of different geologic conditions. Our study proposes utilizing a random forest machine learning model that has previously successfully determined origin from trace elements, with a comprehensive suite of trace element data of sapphires as a potential solution to this problem, to make more accurate sapphire discrimination possible. In addition to a more accurate provenance determination, an added benefit is the potential to gain deeper insight into the formational environment using trace elements. This trace element study aims to shed light on the formation of Montana sapphires and determine geochemical differences between localities in order to see if a successful provenance determination is possible.

4.3 Methods

Sapphire samples were collected by and curated at the Gemological institute of America (GIA). Trace elemental data of Montana samples were acquired at the GIA in Carlsbad, CA by using a Thermo Fisher iCAP Qc ICP-MS, coupled with an Elemental Scientific Lasers NWR213 laser ablation system with a frequency quintupled Nd:YAG laser operated in Q-switched (pulsed) mode at a wavelength of 213nm and pulse duration of 4 ns. Laser sampling was performed in the third generation two-volume cell from ESI (TwoVol2). The laser-generated aerosol was collected by a device (or cup) that is supported evenly throughout the entire range of motion with a specially designed internal movement system. This system minimizes inconsistent gas dynamics and a positional sensitivity dependence. The laser cell is flushed with helium gas, carrying the ablated

material to where nebulizer gas (Ar) was mixed with the carrier gas (He) via a wye shaped connector before entering the plasma for ionization and subsequent analysis in the mass spectrometer. Data acquisition was performed in time-resolved mode. The following elements were measured: Be, Li, Mg, Al, Si, Ti, V, Cr, Mn, Fe, Co, Ni, Cu, Zn, Ga, Ge, Y, Zr, Nb, Sn, La, Ce, Nd, Hf, Ta, W, Pb to observe what elements were and were not present in concentrations above detection. Dwell time of each analyte measured was 0.01 seconds except Be, Mg, Al, Ti, V, Cr, Fe and Ga that were measured for 0.05 seconds. Dwell time of each laser spot was 40 seconds. A laser spot size of 55 um was used for each analysis (3 spots per sapphire), with a 20 Hz repetition rate, and 10 J/cm2 fluence. The internal standard used was Al at 529200 ppm. National Institute of Standards and Technology (NIST) Standard Reference Material (SRM) 610 and 612 were used as external standards. All isotopes were externally standardized using both standards. Concentrations of all isotopes were calculated by Qtegra software (Version 2.10.3324.131).

Additional trace elements were also collected using a ESI NWR193 excimer laser system and Agilent 7900 ICP-MS at the University of Colorado Boulder (CU Boulder), TRaIL laboratory, using the same parameters as the GIA laboratory, with the addition of external standards NIST 616, and corundum standards 07-0687-15, 02-1267-30 and Y-A19 (Stone-Sundberg et al., 2021) were used to validate results. Elemental concentrations were processed with Iolite software (v. 4.9).

4.4 Results

In total, a total of 750 individual spot analyses were collected on 182 sapphires were analyzed: 39 from Dry Cottonwood creek (156 total LA-ICP-MS spots), 61 from Missouri River (215 total LA-ICP-MS spots), 61 from Rock Creek (317 total LA-ICP-MS spots), and 21 from Yogo Gulch (62 total LA-ICP-MS spots). Trace element data collected from Montana sapphires had the following elements above detection limits: Cr, Ga, Mg, Fe, Ti, and V. 10% of samples contained

Cr below detection so it was excluded from provenance determination analysis. A compilation of summary statistics can be found in Table 4-1.

In combining data collected from separate laboratories, it was found that Ga had a significant difference in chemistry between sessions at the GIA and CU Boulder (Fig. 4-2). This difference is further highlighted with probability plots showing a bimodality to the data, between sessions (Fig. 4-3). This probability plot also shows Cr to not have normal distribution. Due to this systematic uncertainty, Ga was also removed from separation analysis in this study although it should be noted that it shows promise for separation in future corundum provenance determination work.

Yogo Gulch sapphires have reasonably distinct chemistry in comparison to the alluvial deposits, having higher concentrations of Mg, and Ti, and generally higher V and Cr (Fig. 4-4). Figure 4-4 also highlights how Rock Creek alluvial sapphires generally have lower trace elemental concentrations of the four groups. A correlation matrix analysis was performed in order to test for collinearity and to discover any elemental relationships (Table 4-2). Only Mg and Ti showed significant positive correlation ($r = 0.84$).

A Random Forest Classification (RFC) machine learning model proved most effective and appropriate considering the data, yielding a 90% testing accuracy (96% training accuracy) in separability. Parameters for the random forest model are 10 k-fold cross validation for training data, a 20% – 80% testing–training data split, with stratified sampling using the methods detailed in Blakemore et al. (*in review*) (chapter 3 of this dissertation). The most important variable for separation was determined to be the Ti/Mg (Table 4-3). The variable importance ranking assisted in deriving useful visual diagrams to aid in separation (e.g. Fig. 4-5). Confusion matrices provide an example of the model's performance, highlighting which classes are more frequently confused with

each other. Taken together, the training and testing confusion matrices provide an effective visual evaluation of the model's performance (Figure 4-6 a and b).

The RFC model was also performed considering only the 2 classes: alluvial Montana sapphires and primary igneous (Yogo Gulch) Montana sapphires. The results of this test show that Yogo Gulch primary igneous sapphires have distinct enough chemistry to be separated with 99% accuracy (both training and testing). The confusion matrix from this test can be seen in Figure 4-7.

4.5 Discussion

4.5.1 Provenance Determination

The results of this study confirm that sapphires from Yogo Gulch have significantly different chemistry from the alluvial Montana sapphires, and can be separated with 99% effectiveness (both training and testing) when the model is used on alluvial vs. Yogo sapphires. In fact, Yogo sapphires can essentially be effectively separated on a simple bi-variate plot of Mg vs. Ti (Fig. 4-5). Even at the gemological level, Yogo sapphires are not as commonly heat treated to enhance their color as alluvial Montana sapphires, as their color is naturally more intense, alluding to intrinsic geochemical difference.

Alluvial Montana sapphires can be separated from each other with 90% testing accuracy (96% training accuracy). The gap between testing and training accuracy, while not too wide, does indicate a degree of overfitting with this model due to the noisy nature of this dataset. However, 90% separation still should be considered successful, and to date, the most effective separation of Montana alluvial sapphires. This provides evidence to support the hypothesis that Montana alluvial sapphires have differing geologic origins. While this is indeed a high degree of separability, the

10% inaccuracy in the test model suggests there is some inseparable overlap in trace element chemistry between the alluvial sapphires.

Some studies have utilized isotopic analysis in hopes of determining provenance, or gaining deeper insight into the formational origin of gem corundum (e.g. Giuliani et al., 2007; Turnier et al., 2020; Krebs et al., 2020). While undeniably useful and potentially successful, precise isotopic work was not considered with this study as the intention is to develop a practical and widely accessible means of provenance determination, without a high financial cost or major destruction to the sample.

4.5.2 Comparison with Colombian Emerald Separation

Recent work demonstrated the effectiveness of applying a random forest machine learning model to a suite of trace element data from Colombian emeralds for hyper-specific provenance determination (Blakemore et al. *in review*, chapter 3 of this dissertation). In that study, minute differences in emerald trace element chemistry was enough to discriminate between mining belts (98% accuracy), mining districts (~93% accuracy) and individual mines (~85% accuracy). This same method was applied in this study to attempt to demonstrate chemical separability in Montana sapphires. Emeralds have a key advantage over sapphires in utilizing this method, in that they have more sites available for elemental substitution, namely the Be^{2+}, Al^{3+}, Si^{4+} cation sites, in addition to long interstitial channels parallel to the c-axis which is shown to trap primordial fluid inclusions (Giuliani et al., 1995). These allowed emeralds to record slight fluctuations in chemistry of the hydrothermal fluids and in the parent rock (organic rich, black shales). Certain elemental ratios, in the case of Columbian emeralds it was V/Cr ratio, appear to be the best indicators for separation across a large geographic area, and was indicative of a documented heterogeneity of V and Cr in the emerald host rock, indicating these geochemical differences can imply formation conditions and

host rock composition. (Breit and Wanty, 1991; Gustafsson, et al., 2014, Mantilla et al., 2007, González et al., 2021, Pignatelli et al., 2017).

Another key difference in the former Colombian emerald study and this Montana sapphire study is that three of the four sapphire deposits are alluvial, meaning the original source is lost. The emerald study had the advantage of knowing precisely where each emerald was found *in situ*. While geographically alluvial sapphires are distinct to their mining areas, considering their age, the tectonic, volcanic, and glacial history of the area it is an unknown question whether they shared a common source.

The RFC model had a 90% testing accuracy in determining the alluvial deposit of origin of Montana sapphires. This falls right in between the accuracies of the individual mine of origin (~85%) and mining district of origin (~93%) with the Colombian emerald study. The alluvial sapphire deposits can be thought of comparably as mining districts, since the area for extraction extends for miles up and down river valleys (e.g. Hsu et al., 2016). By comparing the chemistry of an unknown alluvial sapphire to this dataset, likewise with the Colombian emerald study, probabilities can be calculated for more holistic and realistic origin reporting. The 90% testing accuracy highlights the repeatability of this method yet again showing success on a previously unseparated set of mineral locations. This study adds a piece to a broader puzzle of origin determination, and with more data from more localities, the better and more practical the results will be.

4.5.3 Mg vs Ti: A possible cause of separation and insights into formation

The most striking trend in this data discovered after applying the RFC model to this data to determine variable importance analysis (Table 4-2), is the strong positive correlation ($r = 0.84$;

Table 4-2), and gradational trend of Mg vs. Ti (Fig. 4-5). In fact, the most important variable for separation is the Ti/Mg ratio (Table 4-3), meaning that the processes driving Ti and Mg substitution are a major cause for the separability in geography.

This correlation is also noted in (Oliveira et al., 2021) who reported that the slope of regression changes with Ti content in volcanic corundum from Mt. Carmel, Israel. The Oliveira (2021) study also notes correlations between Sc and Ti and Zr vs Ti. Ti^{3+} is shown to substitute for Al^{3+} under reducing conditions (Oliveira et al. 2021), indicating that oxygen fugacity of the evolving magma controls Ti^{3+} content in corundum. Sapphires measured in this study had much lower concentrations of Ti^{3+} (mean of ~ 40 ppm vs. ~7000 ppm) however maintained the same strong positive correlation between Ti and Mg as observed in Oliveira et al. (2021). Griffin et al. 2021 also demonstrated Cr^{3+} to be higher in Mt. Carmel corundum as well due to the highly reduced conditions, indicating fO_2 is also an important factor controlling the concentration of other trace elements in corundum.

In fact, Yogo Sapphires can be almost entirely separated on the Mg vs. Ti bi-variate plot alone (Fig. 4-5), indicating the source of their formation had more reduced fO_2 conditions than those of alluvial sapphires. This is an observation noted by Renfro et al. (2018) as a distinguishing chemical difference of Yogo Sapphires from alluvial Montana sapphires. Dry Cottonwood Creek and Missouri River sapphires showed consistently lower Ti concentrations than Yogo, with Rock Creek having intermediate concentrations. This observation suggests that there is evidence to suggest a different source for alluvial sapphires, possibly coming from different depths as fO_2 generally decreases with depth.

Additionally, Yogo Gulch sapphires are consistently higher in trace elements (Mg, Ti, Cr, Fe) than alluvial sapphires (Fig. 4-4), yielding to support the idea that Yogo Sapphires were formed under more reduced conditions than their alluvial counterparts. This trend is likewise seen in

somewhat of a gradient in comparing the alluvial sapphires as well, with Rock Creek sapphires having generally higher concentrations of trace elements than Missouri River and Dry Cottonwood Creek sapphires. Rutile (TiO_2) is a common mineral inclusion in Rock Creek sapphires and has been suggested to be characteristic of this deposit (Zwaan, 2015). This is in agreement with the results of our study, where Ti is generally elevated in Rock Creek sapphires than in Missouri River and Dry Cottonwood Creek sapphires.

4.5.4 Implications and future work with gemstone provenance determination

The results of this study show promising results for the random forest machine learning LA-ICP-MS trace elemental method of provenance determination, being able to separate sapphires from each location with 90% accuracy. Additionally, this method is useful in making discoveries in geochemical data post-analysis, using the variable importance list. In this study, the correlation and class separability between Ti and Mg was discovered this way, adding evidence to support the hypothesis of multiple geologic sources of formation for alluvial Montana sapphires. This study should be taken within the broader context of adding to the body of knowledge regarding origin determination, with the goal of making granular improvements which are building towards a more comprehensive way of determining the origin of a gemstone from any source. Having the ability to determine not only an origin opinion on an unknown mineral, but also a probability associated with said prediction presents a more transparent way of representing the geochemical fingerprint for use in origin determination. The success of this method on a new and famously enigmatic mineral system, albeit with some geochemical overlap, should provide optimism in moving forward with expanding this method to new systems.

4.6 Acknowledgments

The authors would like to thank Dr. Liam Courtney-Davis at the University of Colorado, Boulder for his assistance with LA-ICP-MS data collection, and to Julisan Street for her assistance in data processing.

4.7. Figures and Tables

Table 4-1: Summary Statistics of chemistry (ppm)

Summary Statistics of Montana Sapphire Trace Elements (ppm)						
	Mg	Ti	V	Cr	Fe	Ga
Total Montana Sapphires: Count	747	747	747	673	747	747
Total Montana Sapphires: Minimum	3.4	1.9	0.4	0.5	465.9	9.1
Total Montana Sapphires: Maximum	146.0	143.5	19.2	607.9	3999.2	83.3
Total Montana Sapphires: Mean	41.3	41.4	4.6	26.5	1692.4	28.9
Total Montana Sapphires: Median	37.5	34.6	3.5	8.4	1632.0	16.0
Total Montana Sapphires: Range	142.6	141.6	18.8	607.5	3533.3	74.2
Total Montana Sapphires: Interquartile Range	25.7	30.8	4.4	17.3	697.5	32.4
Total Montana Sapphires: Standard Deviation	24.8	29.1	3.5	67.2	573.7	18.6
Dry Cottonwood Creek : Count	152	152	152	152	152	152
Dry Cottonwood Creek : Minimum	3.4	1.9	0.4	0.6	845.0	11.3
Dry Cottonwood Creek : Maximum	123.4	87.2	15.9	115.9	3999.2	66.6
Dry Cottonwood Creek : Mean	28.6	23.4	4.3	12.2	1951.8	33.9
Dry Cottonwood Creek : Median	24.6	17.7	3.3	6.5	1755.0	39.0
Dry Cottonwood Creek : Range	120.0	85.3	15.5	115.3	3154.2	55.3
Dry Cottonwood Creek : Interquartile Range	32.8	32.5	4.8	14.0	861.8	32.8
Dry Cottonwood Creek : Standard Deviation	23.4	20.1	3.6	16.6	676.1	17.1
Missouri River : Count	217	217	217	203	217	217
Missouri River : Minimum	7.1	3.5	0.9	1.2	465.9	9.1
Missouri River : Maximum	110.0	75.1	14.3	173.6	2318.0	83.3
Missouri River : Mean	32.3	24.5	5.1	22.9	1378.5	33.1
Missouri River : Median	31.0	22.0	4.4	11.1	1321.0	15.7

Missouri River : Range	102.9	71.6	13.4	172.4	1852.1	74.2
Missouri River : Interquartile Range	25.8	14.7	5.0	16.7	570.8	43.3
Missouri River : Standard Deviation	16.1	11.5	3.1	31.1	354.9	23.5
Rock Creek : Count	315	315	315	255	315	315
Rock Creek : Minimum	7.1	4.1	0.9	0.5	594.6	11.6
Rock Creek : Maximum	92.4	143.5	15.5	607.9	3598.4	58.3
Rock Creek : Mean	42.1	49.7	3.6	30.7	1834.0	26.7
Rock Creek : Median	40.8	40.3	2.7	5.2	1781.0	15.9
Rock Creek : Range	85.3	139.4	14.6	607.5	3003.8	46.7
Rock Creek : Interquartile Range	16.5	29.9	2.4	13.7	643.0	28.4
Rock Creek : Standard Deviation	13.3	23.2	2.6	90.0	559.6	15.0
Yogo Gulch : Count	63	63	63	63	63	63
Yogo Gulch : Minimum	72.7	76.7	3.4	2.7	1060.0	11.0
Yogo Gulch : Maximum	146.0	131.0	19.2	470.0	3110.0	20.6
Yogo Gulch : Mean	99.0	101.2	9.1	55.7	1439.4	13.7
Yogo Gulch : Median	97.1	100.0	8.0	17.9	1370.0	12.9
Yogo Gulch : Range	73.3	54.3	15.8	467.3	2050.0	9.6
Yogo Gulch : Interquartile Range	17.8	22.2	5.7	37.7	360.0	3.8
Yogo Gulch : Standard Deviation	14.0	15.1	4.5	102.6	381.3	2.6

Table 4-2: Correlation Matrix

	Mg	Ti	V	Cr	Fe	Ga
Mg	1	0.84	0.5	0.21	0.043	0.1
Ti	0.84	1	0.49	0.21	0.21	0.11
V	0.5	0.49	1	0.37	0.06	0.48
Cr	0.21	0.21	0.37	1	-0.11	0.15
Fe	0.043	0.21	0.06	-0.11	1	0.15
Ga	0.1	0.11	0.48	0.15	0.15	1

Table 4-3: List of variable importance for RFC separation

Variable Importance	
Mg/Ti	495.7
Mg	470.8
Ti/Fe	456.7
Fe	425.6
Ti	424.4
Mg/Fe	383.0
Ti/V	375.2
V/Fe	365.7
Mg/V	277.0
V	275.2

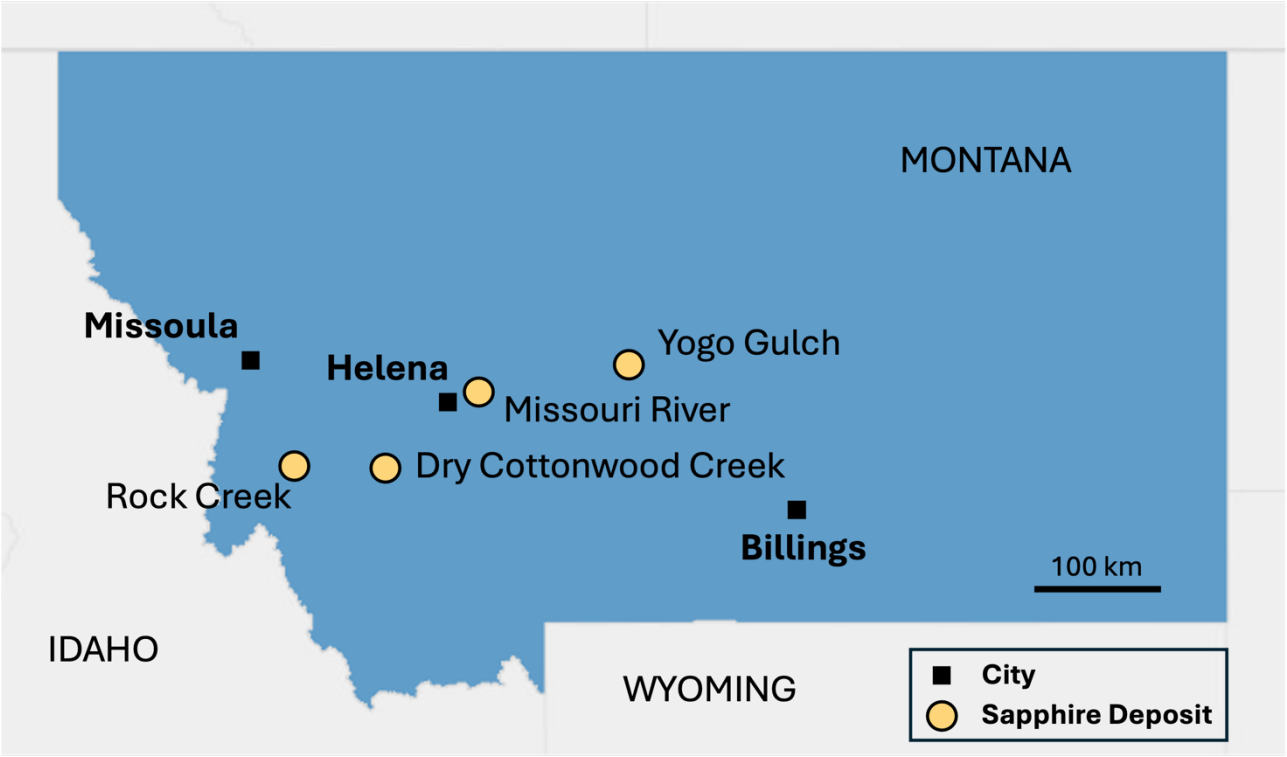

Figure 4-1. Map of Montana Sapphire deposits (Modified after Zwaan et al. 2015). Rock Creek, Dry Cottonwood Creek, and Missouri River deposits are alluvial, and Yogo Gulch is primary igneous.

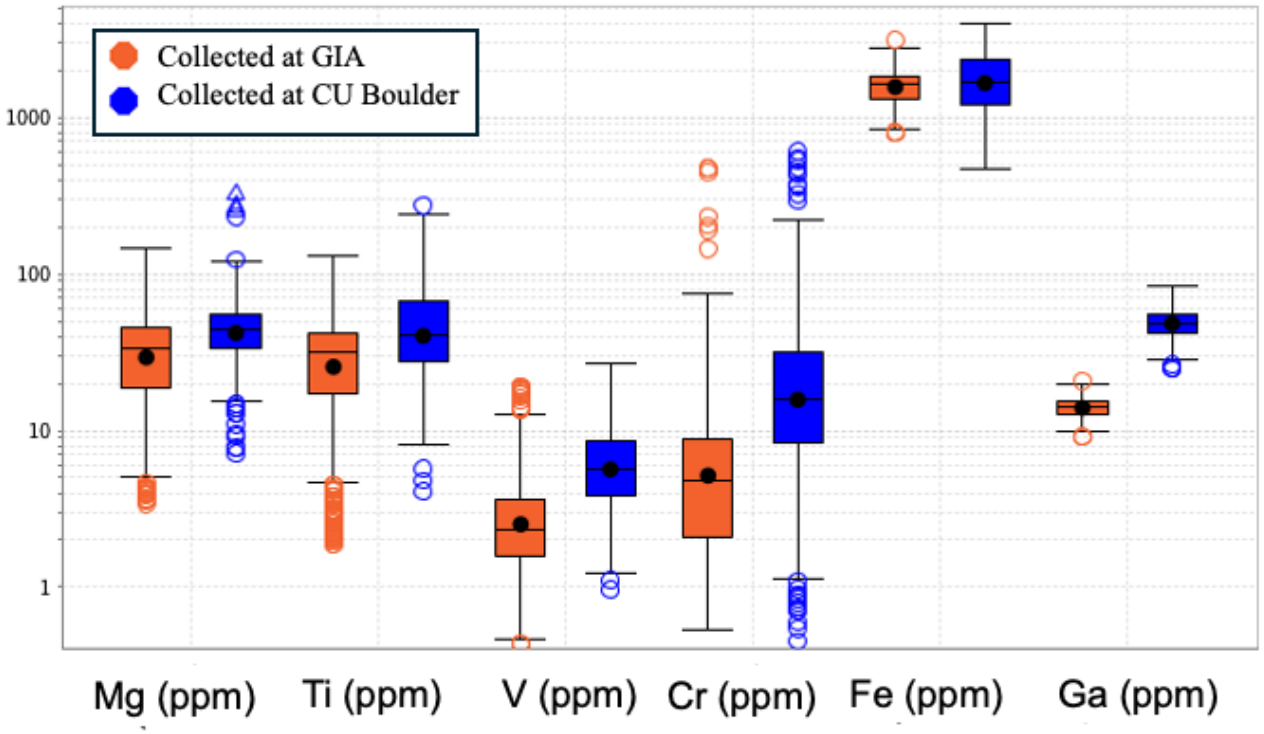

Figure 4-2: Comparison of elemental concentrations collected at different laboratories as a visual test for consistency. Each element except for Ga was shown to be consistent, so Ga was excluded from discrimination analysis to avoid incorporating any artificial breaks in data caused by any systematic error.

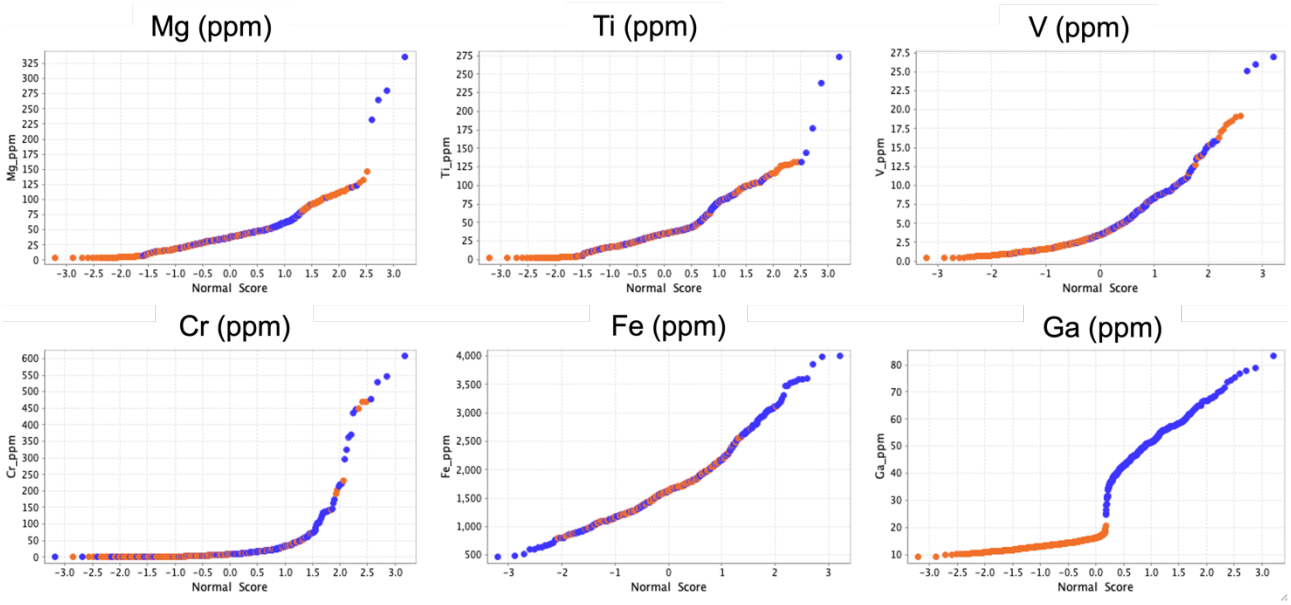

Figure 4-3. Probability plots of sapphire trace elements. Notice how Ga and Cr show non-normal distribution. For this reason, these elements were excluded from separation analysis. Orange data points were collected at the GIA, and blue were collected at the University of Colorado Boulder.

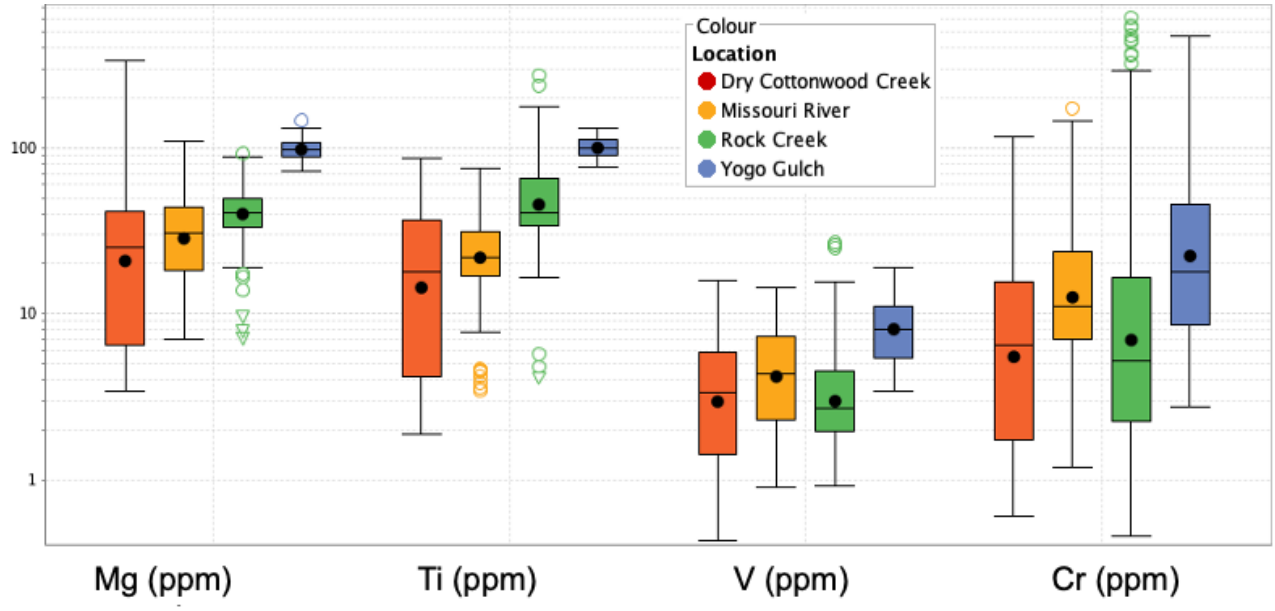

Figure 4-4. Box plots of Mg, Ti, V, and Cr highlighting the unique chemistry of Yogo Gulch sapphires, compared to the alluvial deposits, with generally elevated trace element concentrations. Notice also how dry cottonwood creek generally has the lowest median trace element concentrations.

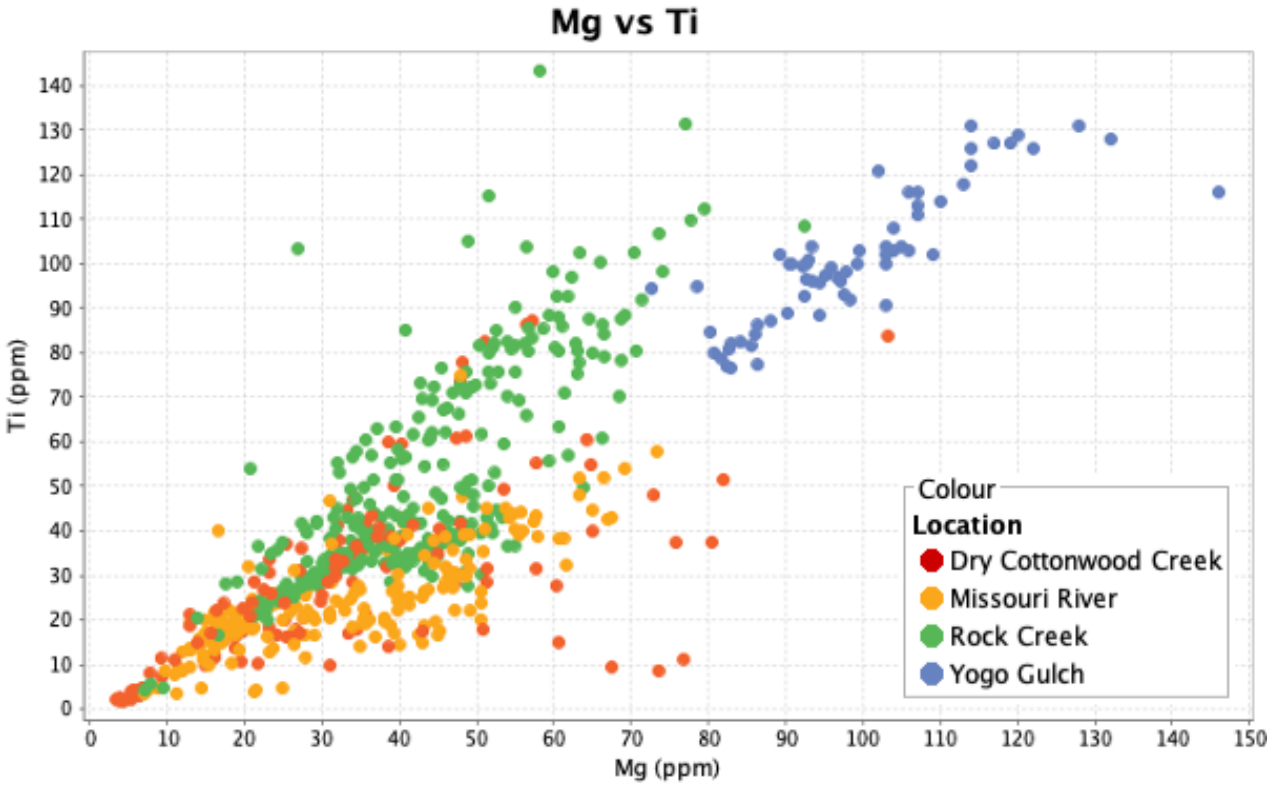

Figure 4-5. Mg vs. Ti. Note the strong positive correlation, and gradation of location, with Yogo Gulch sapphires having higher concentrations of Mg and Ti, Rock creek having intermediate, and Dry Cottonwood and Missouri River having similarly lower concentrations.

Training Data (80%)	Dry Cottonwood Creek	Missouri River	Rock Creek	Yogo Gulch	Count
Dry Cottonwood Creek	115	1	5		121
Missouri River	1	159	2		162
Rock Creek	2	1	200	1	204
Yogo Gulch			1	49	50
Count	118	161	208	50	537

Test Data (20%)	Dry Cottonwood Creek	Missouri River	Rock Creek	Yogo Gulch	Count
Dry Cottonwood Creek	23	4	4		31
Missouri River	3	38			41
Rock Creek	1		50		51
Yogo Gulch				13	13
Count	27	42	54	13	136

Figure 4-6: Example confusion diagrams from the training set and testing set of data during the RFC model analysis for the entire data set. Data was partitioned 80% training and 20% testing.

Training Data (80%)	Alluvial Sapphires	Yogo Gulch	Count
Alluvial Sapphires	487	1	488
Yogo Gulch	1	49	50
Count	488	50	538

Test Data (20%)	Alluvial Sapphires	Yogo Gulch	Count
Alluvial Sapphires	122		122
Yogo Gulch		13	13
Count	122	13	135

Figure 4-7: Confusion matrix showing near perfect separation of alluvial Montana sapphires versus primary igneous Yogo Gulch Montana sapphires.

4.8 References

Berg, B. (2007) Sapphires in the Butte-Deer Lodge Area, Montana. Montana Bureau of Mines and Geology, Bulletin, 134.

Berger, A.L., and Berg, R.B. (2006) The Silver Bow Sapphire Occurrence, Montana: Evidence for a volcanic bedrock source for Montana's alluvial sapphire deposits. Economic Geology, 101, 679–684.

Blakemore, D.R., Palke, A., Gonzalez-Duran, A., Sun, Z., Toloza, J.G., Betancur-Acevedo, C.A., and Simon, A.C. (n.d.) Application of Random Forest Classification Machine Learning for Hyper-Specific Mineral Origin Determination Studies: Insights from Colombian Emerald and Euclase. (In Review, Submitted to American Mineralogist, Chapter 3 of this dissertation).

Breit, G.N., and Wanty, R.B. (1991) Vanadium accumulation in carbonaceous rocks: A review of geochemical controls during deposition and diagenesis. Chemical Geology, 91, 83–97.

Cade, A., and Groat, L.A. (2006) Garnet inclusions from Yogo Sapphires. Gems & Gemology, 42, 106.

Chulapakorn, T., Intarasiri, S., Bootkul, D., and Singkarat, S. (2014) Identification of deposit types of natural corundum by PIXE. Nuclear Instruments and Methods in Physics Research Section B: Beam Interactions with Materials and Atoms, 331, 108–112.

Dahy, J.P. (1991) Geology and igneous rocks of the Yogo sapphire deposit, Little Belt Mountains, Montana. In D.W. Baker and R.B. Berg, Eds., *Guidebook of the Central Montana Alkalic Province*. Montana Bureau of Mines and Geology Special Publication 100, pp. 45–54.

Emmett, J.L., Scarratt, K., McClure, S., Moses, T., Douthit, T., Hughes, R., Novak, S., Shigley, J.E., Wang, W., Bordelon, O., and others (2003) Beryllium Diffusion of Ruby and Sapphire. Gems & Gemology, 39, 84–135.

Evans, K.V., Aleinikoff, J.N., Obradovich, J.D., and Fanning, C.M. (2000) SHRIMP U-Pb geochronology of volcanic rocks, Belt Supergroup, western Montana: evidence for rapid deposition of sedimentary strata. Canadian Journal of Earth Sciences, 37, 1287–1300.

Fuentes, F., DeCelles, P.G., and Constenius, K.N. (2012) Regional structure and kinematic history of the Cordilleran fold-thrust belt in northwestern Montana, USA. Geosphere, 8, 1104–1128.

Garland, M.I. (2002) The alluvial sapphire deposits of western Montana. Thesis.

Giuliani, G., Cheilletz, A., Arboleda, C., Carrillo, V., Rueda, F., and Baker, J.H. (1995) An evaporitic origin of the parent brines of Colombian emeralds; fluid inclusion and sulphur isotope evidence. European Journal of Mineralogy, 7, 151–165.

Giuliani, G., Fallick, A., Rakotondrazafy, M., Ohnenstetter, D., Andriamamonjy, A., Ralantoarison, T., Rakotosamizanany, S., Razanatseheno, M., Offant, Y., Garnier, V., and others (2007) Oxygen isotope systematics of gem corundum deposits in Madagascar: relevance for their geological origin. Mineralium Deposita, 42, 251–270.

González-Durán, A.F., García-Toloza, J., Bonilla, G., Cedeño-Ochoa, C.J., Angarita-Sarmiento, L.G., Castañeda-Gómez, A.J., Parra-Bastidas, S.D., Bocanegra-Rodríguez, L.C., Montaña-Cárdenas, J., and López-Castillo, C.L. (2021) Geoquímica y mineralogía de la mina La Pava, Muzo-Quípama: implicaciones en la exploración de esmeraldas en Colombia. Boletín de Geología, 43, 117–142.

Gustafsson, J.P., Persson, I., Oromieh, A.G., van Schaik, J.W.J., Sjöstedt, C., and Kleja, D.B. (2014) Chromium(III) Complexation to Natural Organic Matter: Mechanisms and Modeling. Environmental Science & Technology, 48, 1753–1761.

Hsu, T., Lucas, A., McClure, S., Renfro, N., and Schumacher, K. (2016) Rock Creek Montana Sapphires: A New Age of Mining Begins. GIA.

Kanouo, N.S., Ekomane, E., Yongue, R.F., Njonfang, E., Zaw, K., Changqian, M., Ghogomu, T.R., Lentz, D.R., and Venkatesh, A.S. (2016) Trace elements in corundum, chrysoberyl, and zircon: Application to mineral exploration and provenance study of the western Mamfe gem clastic deposits (SW Cameroon, Central Africa). Journal of African Earth Sciences, 113, 35–50.

Krebs, M.Y., Hardman, M.F., Pearson, D.G., Luo, Y., Fagan, A.J., and Sarkar, C. (2020) An Evaluation of the Potential for Determination of the Geographic Origin of Ruby and Sapphire Using an Expanded Trace Element Suite Plus Sr–Pb Isotope Compositions. Minerals (2075-163X), 10, 447.

Lin Sutherland, F., Hoskin, P.W.O., Fanning, C.M., and Coenraads, R.R. (1998) Models of corundum origin from alkali basaltic terrains: a reappraisal. Contributions to Mineralogy and Petrology, 133, 356–372.

Mantilla, L.C., Silva, A., Serrano, J.J., Conde, J., Gómez, C., Ramírez, J.C., Meza, J.A., Pelayo, Y., Ortega, L.M., Plata, L.M., and others (2007) Investigación petrográfica y geoquímica de las sedimentitas del Cretácico inferior (K1) y sus manifestaciones hidrotermales asociadas planchas 169, 170, 189, 190 (Cordillera Oriental), implicaciones en la búsqueda de esmeraldas. INGEOMINAS-Universidad Industrial de Santander (UIS), Bogotá.

McClure, S.F., Moses, T.M., and Shigley, J.E. (2019) The Geographic Origin Dilemma | Gems & Gemology, 55, 457–462.

Oliveira, B., Griffin, W.L., Gain, S.E.M., Saunders, M., Shaw, J., Toledo, V., Afonso, J.C., and O'Reilly, S.Y. (2021) Ti3+ in corundum traces crystal growth in a highly reduced magma. Scientific Reports, 11, 2439.

Palke, A.C., and Breeding, C.M. (2017) The origin of needle-like rutile inclusions in natural gem corundum: A combined EPMA, LA-ICP-MS, and nanoSIMS investigation. American Mineralogist, 102, 1451–1461.

Palke, A.C., Renfro, N.D., Hapeman, J.R., and Berg, R.B. (2023) Gemological Characterization of Montana Sapphire from the Secondary Deposits at Rock Creek, Missouri River, and Dry Cottonwood Creek. Gems & Gemology, 59, 2–45.

Palke, A.C., Wong, J., Verdel, C., and Ávila, J.N. (2018) A common origin for Thai/Cambodian rubies and blue and violet sapphires from Yogo Gulch, Montana, U.S.A.? American Mineralogist, 103, 469–479.

Peucat, J.J., Ruffault, P., Fritsch, E., Bouhnik-Le Coz, M., Simonet, C., and Lasnier, B. (2007) Ga/Mg ratio as a new geochemical tool to differentiate magmatic from metamorphic blue sapphires. Lithos, 98, 261–274.

Pignatelli, I., Giuliani, G., Morlot, C., Rouer, O., Claiser, N., Chatagnier, P.-Y., and Goubert, D. (2017) Recent Advances in Understanding the Similarities and Differences of Colombian Euclases. The Canadian Mineralogist, 55, 799–820.

Renfro, N.D., Palke, A.C., and Berg, R.B. (2018) Gemological Characterization of Sapphires from Yogo Gulch, Montana | Gems & Gemology. Gems & Gemology, 54, 184–201.

Simonet, C., Fritsch, E., and Lasnier, B. (2008) A classification of gem corundum deposits aimed towards gem exploration. Ore Geology Reviews, 34, 127–133.

Sorokina, E.S., Hofmeister, W., Häger, T., Mertz-Kraus, R., Buhre, S., and Saul, J.M. (2016) Morphological and chemical evolution of corundum (ruby and sapphire): Crystal ontogeny reconstructed by EMPA, LA-ICP-MS, and Cr3+ Raman mapping. American Mineralogist, 101, 2716–2722.

Stone-Sundberg, J.L., Guan, Y., Sun, Z., and Ardon, T. (2021) Accurate Trace Element Reporting in Corundum: Development of Secondary Ion Mass Spectrometry Relative Sensitivity Factors. Geostandards & Geoanalytical Research, 45, 207–221.

Sutherland, F.L., Zaw, K., Meffre, S., Giuliani, G., Fallick, A.E., Graham, I.T., and Webb, G.B. (2009) Gem-corundum megacrysts from east Australian basalt fields: trace elements, oxygen isotopes and origins∗. Australian Journal of Earth Sciences, 56, 1003–1022.

Sutherland, F.L., Zaw, K., Meffre, S., Tzen-Fui Yui, and Kyaw Thu (2015) Advances in Trace Element "Fingerprinting" of Gem Corundum, Ruby and Sapphire, Mogok Area, Myanmar. Minerals (2075-163X), 5, 61–79.

Turnier, R.B., Katzir, Y., Kitajima, K., Orland, I.J., Spicuzza, M.J., and Valley, J.W. (2020) Calibration of oxygen isotope fractionation and calcite-corundum thermometry in emery at Naxos, Greece. Journal of Metamorphic Geology, 38, 53–70.

Wong, J., Verdel, C., and Allen, C.M. (2017) Trace-element compositions of sapphire and ruby from the eastern Australian gemstone belt. Mineralogical Magazine, 81, 1551–1576.

Zaw, K., Sutherland, F.L., Dellapasqua, F., Ryan, C.G., Yui, T.-F., Mernagh, T.P., and Duncan, D. (2006) Contrasts in gem corundum characteristics, eastern Australian basaltic fields: trace elements, fluid/melt inclusions and oxygen isotopes. Mineralogical Magazine, 70, 669–687.

Zwaan, J.C. (Hanco), Butler, E., Mertz-Kraus, R., and Kane, R.E. (2015) Alluvial Sapphires from Montana: Inclusions, Geochemistry, and Indications of a Metasomatic Origin | Gems & Gemology. Gems & Gemology, 51.

Chapter 5: Conclusion

The results from this dissertation unequivocally demonstrate the utility of the LA-ICP-MS for geochemical studies in mineral resource geology. In chapter 2, the LA-ICP-MS was used to add to the body of geochronology work done on the Candelaria IOCG deposit. Most of the new apatite and titanite dates reported here are consistent with previously reported ages of sulfide mineralization (Re–Os, Molybdenite) at c. 115 Ma. Actinolite-hornblende and four titanite samples record other hydrothermal events at 118 Ma, 121 Ma, and 126 Ma. It was determined that these dates have no meaningful correlation with depth. The new dates presented in chapter 2 present evidence supporting an episodic, multi-pulse model of formation for the Candelaria IOCG deposit. Magnetite U–Pb dates are less precise due to low U/Pb ratios, but still geologically useful and broadly consistent with the other dates reported here. Our results support a multi-phase hydrothermal model of formation of the Candelaria deposit, where an IOA style mineralization (magnetite-actinolite) is overprinted by the Cu-rich IOCG style mineralization. These results have broader reaching implications for adding to the body of knowledge on the formation of IOCG deposits which could aid in the exploration for new IOCG deposits, and also shows promise for the possible future development of magnetite U–Pb dating.

In chapter 3, a large suite of elemental data was collected with LA-ICP-MS and was used to develop a provenance determination machine learning model for Colombian Emeralds. With the results of this study, we are now able to confidently determine the belt (98% accuracy) and mining district (93% accuracy) of origin from an unknown Colombian emerald by using trace elements analyzed with a random forest classification machine learning algorithm. We are also able to determine the mine of origin of 40 individual mines in Colombia with moderate confidence (85% accuracy). More data would be needed in order to increase the confidence in differentiating down to the individual mine, but with the vast number of Colombian emerald mines, along with their geographic proximity, it may not be possible to achieve a better separation using any combination of analytical or machine learning method, nor would it be practical.

The key advantage of this approach is the coupling of a machine learning model, with the prediction score and visualizations to assist the user in understanding why the “black box” arrived

at the determinations it did. Even when the algorithm guesses incorrectly, there is ample evidence as to why the model predicted wrong, and what the other possibilities are. This allows the analyst to make an informed prediction and allows this information to be passed along to the client. Additionally, the empirical probability and corresponding visualizations could give laboratories more confidence in stating their origin opinions, as it is harder for an unethical dealer to claim with certainty that a stone is 100% from a specific location based solely on a report made in good faith. This method has promise for rapidly expanding origin determination capabilities hyper-specifically, well beyond the country of origin.

In addition to provenance determination, this method allows for the ability to make impartial observations about data after analyses to discover insights into the underlying geologic process. In the case of the emerald study, it was discovered that V/Cr is the most important variable for separation and alludes to a natural heterogeneity in the host rock shale between the eastern and western mining belts, likely controlled by total organic carbon concentration at deposition.

Chapter 4 followed up this provenance determination model on an entirely different mineral system: Montana Sapphires. This was the first time an attempt has been made at determining if there is a way to geochemically fingerprint alluvial sapphires from Montana, and the results show a great deal of potential, with RFC model having ~90% accuracy in separating the alluvial sapphires form each other, and over 99% accuracy in separating the only primary igneous sapphire deposit from the other Montana localities. The broader implications of this study are a confirmation that the method developed in chapter 3 can be applied to different mineral systems successfully, and will continue to be a useful method in future provenance studies. Another important takeaway from this study is the correlation between Ti and Mg, suggesting a change in oxygen fugacity in the original formational environment of alluvial sapphires. This highlights the added benefit of uncovering geologic insights after applying the provenance RFC machine learning model to a suite of LA-ICP-MS data.

This dissertation highlights the dual applications of the LA-ICP-MS in application to mineral resource geology and paves the way for future work in mineral provenance method development.

Appendices

Appendix A: Chapter 2 Supplemental

Extended methods used in chapter 2

Scanning Electron Microscopy

A JEOL JSM-7800F field emission scanning electron microscope coupled with an Oxford Instruments X-Max energy dispersive X-ray spectrometer (EDS) detector at the University of Michigan's EMAL facility was used to identify and document minerals in preparation for isotopic and trace element analysis. EDS spectra were processed with AZtec EDS software by Oxford Instruments. Images of selected minerals were collected in backscattered electron spectroscopy (BSE) mode to document textural context. All EDS spectra and BSE images were taken at variable magnifications with an accelerating voltage of 20 KeV and a working distance of 10 mm. Usage of the SEM allowed for non-destructive identification of apatite, titanite, and magnetite for this study.

Laser Ablation Multi-Collector ICP-MS (University of California Santa Barbara)

Laser ablation multi-collector inductively coupled plasma mass spectrometry (LA-MC-ICP-MS) analyses were performed at the University of California, Santa Barbara to measure U-Pb ratios. A Photon Machines 193 nm excimer Excitelaser with a HelExII cell was used for mineral ablation. Ablated material was measured with a Nu Instruments Plasma HR-ES multi-collector

ICP-MS. Spots were ablated at a repetition rate of 5 Hz, for 15 s, with a fluence of ~1 J/cm^2. Spot diameters were 35 μm for titanite and apatite, and 65 μm for magnetite.

Data were processed using the commercially available software Iolite v3.5. A series of reference materials were run at the beginning and end of each analytical session, and in between every 8-12 unknown analyses. The primary Titanite reference material (RM) for U–Pb was MKED (Spandler et al., 2016). Secondary RMs BLR (Aleinikoff et al., 2007), Y1710C5 (Spencer et al., 2013), P5701G (Kylander-Clark et al., 2008), and FCT (Schmitz and Bowring, 2001) were used as quality control and yielded ages within 2% of their accepted values; the 91500 zircon RM (Weidenbeck et al., 1995) was used as an additional check on 207Pb/206Pb. The primary apatite RM for U–Pb was the Madagascar apatite (467 Ma; Apen et al. 2022); Durango (32.3 Ma; Paul et al., 2021), McClure (Krestianinov et al., 2021), and BRZ-1 (Apen et al., 2022) . Titanite and apatite trace-element data was processed using NIST612 and BHVO glass reference materials assuming stoichiometric Ca as an internal standard. No matrix-matched magnetite standard exists yet, so Mud Tank zircon (Black and Gulson, 1978) was used as the primary RM, and NIST and BHVO were used as a secondary check on 207Pb/206Pb. Dates were calculated using the $^{207}Pb/^{206}Pb$ vs $^{238}U/^{206}Pb$ Tera-Wasserburg diagram using Isoplot-R (Vermeesch, 2018; Parameters: discordia model-1 age, no correction for common lead or disequilibrium). Data presented in the manuscript first show the 2σ analytical uncertainty, followed by that uncertainty propagated with the long-term reproducibility (2% for titanite and apatite, but unknown for magnetite) in brackets.

Laser Ablation ICP-MS (University of Maine)

U-Pb isotopes were collected on titanite at the University of Maine MicroAnalytical Geochemistry and Isotope Characterization (MAGIC) laboratory using an ESL NWR193^{UC}

excimer laser ablation system equipped with a TV2 large format cell coupled to an Agilent 8900 ICP-MS. Titanite was ablated using a 25 μm round spot at 6 Hz and 3 J/cm2. Each spot analysis consisted of 15 s of background collection during laser warmup, 30 s of ablation, and 10 s of washout. Isotope ratios were determined in iolite 4 (Paton et al., 2011; Woodhead et al., 2007; Paton et al., 2010) relative to titanite reference material MKED (Spandler et al., 2016). Secondary titanite RM BLR gave a weighted mean age of 151±15 Ma (2s) with a correction for common Pb based on Stacey and Kramers (1965), which is consistent with the TIMS age of 147.1±0.4 Ma (Aleinikoff et al., 2007). Titanite dates based on 206Pb/238U were calculated using discordia model 1 in IsoplotR (Vermeesch, 2018).

Argon-Argon (Auburn University)

Argon-Argon dating was performed on an actinolite at Auburn University's Noble Isotope Mass Analysis Lab (ANIMAL).The GLM-110 mass spectrometer was used for the analyses, that is a 10-cm radius 90° sector instrument with double focusing geometry, a Nier-type source, and a single detector (an ATP discrete dynode-style electron multiplier). Samples fused for gas extraction with a CO_2 laser. Operation of the laser, extraction line and mass spectrometer were fully automated. The time required for one complete analysis cycle is 20 minutes (4 minutes gettering, followed by generally 10 measurements per peak and baseline, 30 measurements of m/e=36). Sample inlet and equilibration time is 5 s for a half-split of a sample and 20 s for an entire sample. Blanks were measured following every 5^{th} analysis. Blank corrections to 36 Ar measurements are based on an average or regression of several blanks measured for a given day of analysis. Air aliquots are typically analyzed 3 times per day (generally at the beginning of the day). Data were reduced using an Excel spreadsheet and Isoplot (Ludwig, 2012, Sp. Pub. BGC,

75 p.). Samples were irradiated for 16 hours with Cd shielding in the CLICIT facility of the Oregon State University TRIGA reactor. Unless indicated otherwise, the data are in volts and errors are the standard deviation of measurement and do not include the error in estimating the J-Value (0.15% at the 95% confidence level). P = Laser Power Level (10 = 100%), t = laser heating time (s). Data are corrected for blank, mass discrimination, and interfering nuclear reactions. The rubric for irradiation filenames is: 'AU + package"+ "layer, radial position" + "phase" + "planchet hole # and sequence", saved as a text file. All samples for this study were in radial positions of a single irradiation layer, with positions labeled as in sketch, and the monitor data for this layer are included in the dataset.

Irradiation parameters, analysis standards, and correction factors for $^{40}Ar/^{39}Ar$ data

Irradiation package: AU-36

Median date of Irradiation: 12/28/2019

Median dates of analyses: ~1/29/2020 (monitors and K-feldspars); ~5/28/2020 (actinolite)

GA-1550 Biotite age used: 9.944E+07 (Jordan and Renne, 2007) (age of GA-1550 Biotite is recalculated to FCS=28.201 Ma, see Schaen et al., 2020)

FC Sanidine age used: 28.201E+07 (Kuiper et al., 2016)

λ total: 5.463E-10 (Min et al., 2000)

$(^{40}Ar/^{36}Ar)_{air}$: 295.5 (Nier, 1950)

Air $^{40}Ar/^{36}Ar$ (based on daily measurements): 291.5 +/- 0.5

(36/37)Ca: 0.0003046± 0.000008

(39/37)Ca: 0.0007380± 0.000037

(40/39)K: 0± 0.00040

(38/39)Cl: 0.01± 0.01

References

Aleinikoff, J.N., Wintsch, R.P., Tollo, R.P., Unruh, D.M., Fanning, C.M., and Schmitz, M.D., 2007, Ages and origins of rocks of the Killingworth dome, south-central Connecticut: Implications for the tectonic evolution of southern New England: American Journal of Science, v. 307, no. 1, p. 63–118.

Apen, F.E., Wall, C.J., Cottle, J.M., Schmitz, M.D., Kylander-Clark, A.R.C., and Seward, G.G.E., 2022, Apatites for destruction: Reference apatites from Morocco and Brazil for U-Pb petrochronology and Nd and Sr isotope geochemistry: Chemical Geology, v. 590, p. 120689.

Black, L., and Gulson, B., 1978, The Age of the Mud Tank Carbonatite, Strangways Range, Northern Territory: B.M.R.J. AUSTRAL. GEOL. GEOPHYS.; AUS; DA. 1978; VOL. 3; NO 3; PP. 227-232; BIBL. 1 P.; 6 ILL.

Jourdan, F. and Renne, P., 2007, Age Calibration of the Fish Canyon sanidine $^{40}Ar/^{39}Ar$ dating standards using primary K-Ar standards: Geochimica et Cosmochimica Acta, v. 71, no. 2, p. 387-402.

Krestianinov, E., Amelin, Y., Neymark, L.A., and Aleinikoff, J.N., 2021, U-Pb systematics of uranium-rich apatite from Adirondacks: Inferences about regional geological and geochemical evolution, and evaluation of apatite reference materials for in situ dating: Chemical Geology, v. 581, p. 120417.

Kuiper, K.F., Deino, A., Hilgen, F.J., Krijgsman, W., Renne, P.R., and Wijbrans, J.R., 2008, Synchronizing Rock Clocks of Earth History: Science, v.320, no. 5875, p. 500-504.

Kylander-Clark, A.R.C., Hacker, B.R., and Mattinson, J.M., 2008, Slow exhumation of UHP terranes: Titanite and rutile ages of the Western Gneiss Region, Norway: Earth and Planetary Science Letters, v. 272, no. 3, p. 531–540.

Ludwig, K.,2012, User's Manual for ISOPLOT version 3.75-4.15. *A geochronological toolkit for Microsoft Excel. Berkeley Geochronology Center Special Publication*, *5*, p. 75.

Min, K., Mundil, R., Renne, P.R., and Ludwig, K.R., 2000, A test for systematic errors in $^{40}Ar/^{39}Ar$ geochronology through comparison with U/Pb analysis of a 1.1-Ga rhyolite, v. 64, no. 1, p. 73-98.

Nier, A.O., 1950, A Redetermination of the Relative Abundances of the Isotopes of Carbon, Nitrogen, Oxygen, Argon, and Potassium, Physical Review, v. 77, 789.

Paton, C., Woodhead, J.D., Hellstrom, J.C., Hergt, J.M., Greig, A., and Maas, R., 2010, Improved laser ablation U-Pb zircon geochronology through robust downhole fractionation correction: Geochemistry, Geophysics, Geosystems, v. 11, no. 3.

Paton, C., Hellstrom, J., Paul, B., Woodhead, J., and Hergt, J., 2011, Iolite: Freeware for the visualisation and processing of mass spectrometric data: Journal of Analytical Atomic Spectrometry, v. 26, no. 12, p. 2508–2518.

Schaen, A. J., Jicha, B.R., Hodges, K.V., Vermeesch, P., Stelten, M.E., Mercer, C.M., Phillips, D., Rivera, T.A., Jourdan, F., Matchan, E.L., and Hemming, S.R, 2020, Interpreting and reporting $^{40}Ar/^{39}Ar$ geochronologic data: GSA Bulletin.

Schmitz, M.D., and Bowring, S.A., 2001, U-Pb zircon and titanite systematics of the Fish Canyon Tuff: an assessment of high-precision U-Pb geochronology and its application to young volcanic rocks: Geochimica et Cosmochimica Acta, v. 65, no. 15, p. 2571–2587.

Spandler, C., Hammerli, J., Sha, P., Hilbert-Wolf, H., Hu, Y., Roberts, E., and Schmitz, M., 2016, MKED1: A new titanite standard for in situ analysis of Sm–Nd isotopes and U–Pb geochronology: Chemical Geology, v. 425, p. 110–126.

Spencer, K.J., Hacker, B.R., Kylander-Clark, A.R.C., Andersen, T.B., Cottle, J.M., Stearns, M.A., Poletti, J.E., and Seward, G.G.E., 2013, Campaign-style titanite U–Pb dating by laser-ablation ICP: Implications for crustal flow, phase transformations and titanite closure: Chemical Geology, v. 341, p. 84–101.

Vermeesch, P., 2018, IsoplotR: a free and open toolbox for geochronology. *Geoscience Frontiers*, v.9, p.1479-1493, doi: 10.1016/j.gsf.2018.04.001.

Woodhead, J.D., Hellstrom, J., Hergt, J.M., Greig, A., and Maas, R., 2007, Isotopic and Elemental Imaging of Geological Materials by Laser Ablation Inductively Coupled Plasma-Mass Spectrometry: Geostandards and Geoanalytical Research, v. 31, no. 4, p. 331–343.

Table A-1: Sample Descriptions and data from Rodriguez-Mustafa et al., 2020 and del Real et al., 2021. These thin sections are from a 1000 m drill core (LD1687B) of the Candelaria mine.

Thin Section Label	Drill Core-sample number	Vertical Depth from Collar (m)	Description
C11	LD1687B-11	148	Sample with straight edge vein containing K-feldspar and bladed, colorful actinolite. The vein has pyrite-magnetite and minor chalcopyrite in the middle and some large titanite cristals with it. The host rock presents a fine grained pervasive biotite alteration with minor dark grean fine patches and fine grains magnetite.
C12	LD1687B-12	133	Undifferentiated matrix with magnetite fragments; sulfides present in their borders and fractures
C34	LD1687B-34	486	Abundant sulfides (py, cpy, po) in magnetite breccia with clasts pervasively altered to chlorite
C43	LD1687B-43	618	Breccia with sodic-calcic–altered groundmass with few disseminated sulfides and massive magnetite clasts
C52	LD1687B-52	731	Mushketovite and potassic feldspar veins in fine, undifferentiated matrix
C58	LD1687B-58	817	Massive mushketovite and minor actinolite in altered volcanic matrix
C61	LD1687B-61	840	Albitized volcanic rock with a massive magnetite vein crosscut by a chlorite vein; posterior K-feldspar veins contain sulfides
C62	LD1687B-62	871	Porphyritic rock with K-feldspar veins cutting magnetite veins
C65	LD1687B-65	1030.4	Volcanic rock with patches albite-chlorite-actinolite and titanite alteration and disseminated magnetite-pyrite-epidote-feldspar-actinolite
C70	LD1687B-70	1109.5	Andesite with disseminated magnetite and actinolite aggregates
C73	LD1687B-73	1132.1	Andesite with disseminated magnetite and minor actinolite. Actinolite-magnetite veins with minor sulfides.

Table A-2: Titanite sample information and associated depth at which the titanite originated, U-Pb ages and associated error, rho values, the textural relationship of the titanite within the overall sample, and whether samples fell off the discordia line and therefore omitted from further calculation, data taken at USCB. Parameters used in Isoplot-R (Vermeesch, 2018) discordia model-1 age, no correction for common lead or disequilibrium.

Sample Label	Depth (m)	$^{238}U/^{206}Pb$	2se	$^{207}Pb/^{206}Pb$	2se	rho	Textural Relationship	Omitted point (x)
C52_01	731	53.0223	1.4855	0.0731	0.0034	0.1562	Matrix, in contact with mag	
C52_03_1	731	54.2594	1.3452	0.0788	0.0066	0.1696	Matrix	
C52_03_2	731	53.7634	1.4184	0.0690	0.0034	0.1624	Matrix	
C52_04	731	54.1419	1.3075	0.0624	0.0029	0.3677	Matrix	
C58_01_1	817	50.7614	3.0107	0.1030	0.0112	0.1861	Matrix	
C58_01_2	817	52.8541	1.7295	0.1140	0.0152	0.1678	Matrix	
C58_02_01	817	38.0228	6.6937	0.2180	0.0582	0.2704	Matrix	
C58_02_2	817	27.1739	3.1486	0.4360	0.0351	0.4779	Matrix	
C58_03	817	29.9401	2.2332	0.3930	0.0291	0.4203	Matrix	
C58_04_1	817	64.6412	2.0154	0.0899	0.0083	0.2924	In a cross-cutting K-spar vein	x
C58_04_2	817	65.2316	1.6568	0.1132	0.0063	0.4175	In a cross-cutting K-spar vein	x
C58_04_3	817	46.3392	1.6934	0.2900	0.0180	0.2602	In a cross-cutting K-spar vein	x
C58_05	817	49.6524	1.3484	0.1340	0.0104	0.1913	Matrix	
C58_06	817	44.0917	1.2285	0.2120	0.0146	0.2136	Matrix	
C61_02	840	21.9780	2.6452	0.5010	0.0403	0.5343	Undifferentia-ted	
C61_01	840	17.0068	2.5392	0.5770	0.0407	0.5524	Undifferentia-ted	

Figure A-1: Titanite C52 Tera-Wasserburg Diagram (UCSB)

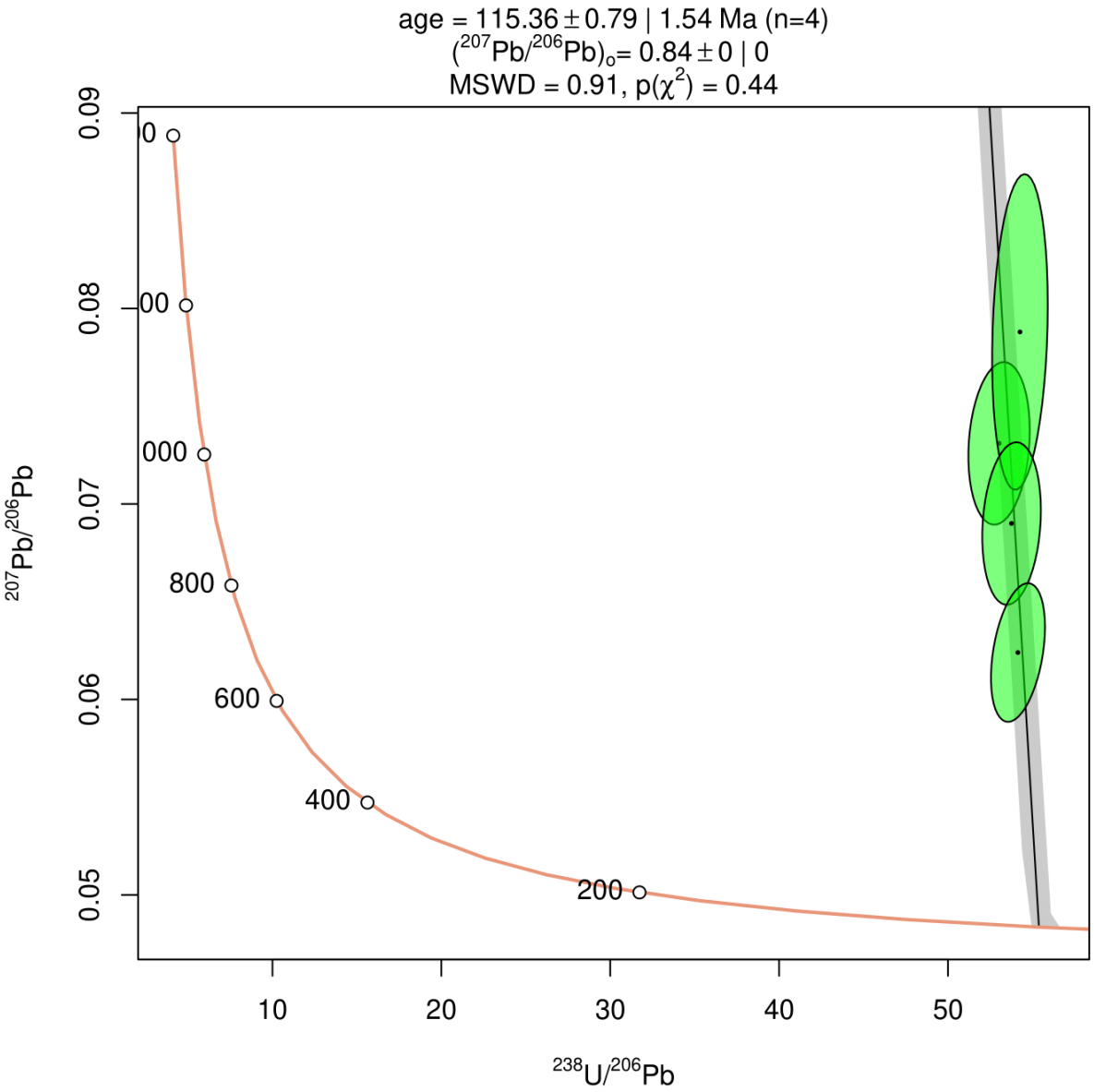

Figure A-2: Titanite C58, Tera-Wasserburg Diagram Omit C58_04 (UCSB)

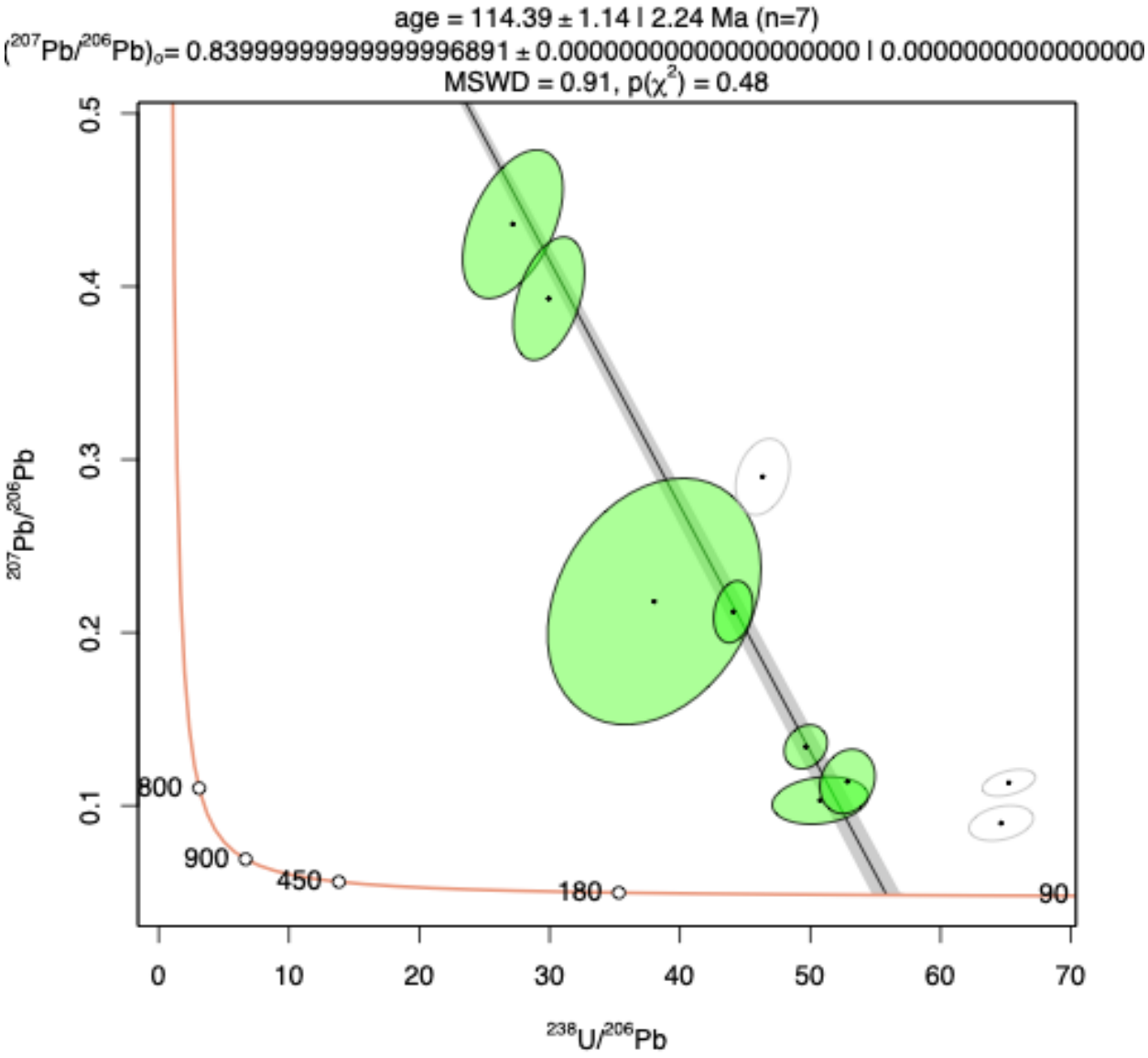

Table A-3: Titanite sample ID information, $^{207}Pb/^{235}U$ ratios and error, $^{206}Pb/^{238}U$ ratios and error, and $^{207}Pb/^{206}Pb$ ratios and error, data taken at University of Maine.

Sample ID	Final ^{207}Pb $/^{235}U$ mean	Final ^{207}Pb $/^{235}U$ 2SE (prop)	Final ^{206}Pb $/^{238}U$ mean	Final ^{206}Pb $/^{238}U$ 2SE (prop)	Final ^{207}Pb $/^{206}Pb$ mean	Final ^{207}Pb $/^{206}Pb$ 2SE (prop)
11ttn						
11ttn_1.d	0.173336	0.019067	0.020021	0.001324	0.062687	0.006163
11ttn_2.d	0.180778	0.026101	0.020508	0.001522	0.060353	0.008464
11ttn_3.d	3.509307	0.537072	0.0475	0.00521	0.497069	0.060519
11ttn_4.d	0.483907	0.098627	0.021842	0.002121	0.154043	0.031504
11ttn_6.d	0.196364	0.027444	0.019846	0.001408	0.072173	0.009407
11ttn_31.d	0.162396	0.046022	0.02166	0.00218	0.063316	0.020113
11ttn_32.d	0.206034	0.042843	0.021426	0.001777	0.068245	0.0144
11ttn_35.d	1.730713	0.202919	0.032267	0.00269	0.375678	0.039177
11ttn_36.d	0.827276	0.126254	0.025861	0.002163	0.22339	0.030541
11ttn_39.d	0.535377	0.104022	0.022379	0.001982	0.18102	0.033567
11ttn_41.d	1.552159	0.276607	0.034097	0.003903	0.390435	0.073725
11ttn_42.d	1.644613	0.257993	0.033144	0.003927	0.451517	0.089989
11ttn_43.d	1.82681	0.356765	0.031841	0.003536	0.413285	0.05865
11ttn_44.d	2.032748	0.266434	0.036879	0.003268	0.391843	0.044464
11ttn_45.d	1.053233	0.113297	0.028239	0.002411	0.257051	0.026275
11ttn_46.d	0.625064	0.1384	0.025687	0.003091	0.214654	0.056979
11ttn_47.d	0.142656	0.034178	0.019883	0.001699	0.05554	0.013942
11ttn_48.d	0.705996	0.140299	0.023972	0.002314	0.188307	0.033559
11ttn_49.d	0.357158	0.05729	0.022259	0.001896	0.125076	0.01954
11ttn_50.d	0.831104	0.117157	0.023354	0.002428	0.293657	0.047715
11ttn_51.d	2.63631	0.368094	0.04118	0.004165	0.449139	0.051806
11ttnvein						
11ttnvein_4.d	88.17616	20.40227	0.286224	0.069352	0.816476	0.095088
11ttnvein_6.d	4.617864	0.899022	0.069863	0.012234	0.570995	0.100531
11ttnvein_7.d	6.0104	0.821919	0.074392	0.008841	0.670256	0.097416
65ttn						
65ttn_1.d	1.023187	0.182103	0.029484	0.002958	0.27556	0.043597
65ttn_2.d	0.320098	0.069236	0.022235	0.002227	0.134651	0.032568
65ttn_3.d	0.477251	0.092089	0.02276	0.002206	0.186186	0.039593
65ttn_4.d	0.977335	0.228579	0.029854	0.003917	0.276824	0.048743
65ttn_5.d	1.987495	0.255872	0.039041	0.003938	0.430012	0.057676
65ttn_6.d	2.143988	0.531303	0.037267	0.005545	0.409394	0.063999
65ttn_7.d	2.958418	0.473749	0.041855	0.004644	0.500525	0.060169
65ttn_8.d	2.446534	0.250614	0.039871	0.004034	0.491149	0.049404
65ttn_9.d	0.338677	0.073201	0.02198	0.002247	0.153997	0.039325
65ttn_10.d	2.387072	0.447256	0.039579	0.004651	0.413764	0.048266
65ttn_13.d	0.458937	0.095261	0.023443	0.00234	0.149951	0.034824
65ttn_14.d	0.495765	0.088821	0.023995	0.002761	0.202888	0.043911
65ttn_15.d	0.974695	0.222484	0.025454	0.00284	0.290831	0.057691
65ttn_16.d	0.302328	0.054318	0.019031	0.001924	0.121173	0.026738
65ttn_19.d	1.127214	0.240921	0.028144	0.003012	0.273054	0.042012
65ttn_20.d	0.570245	0.097109	0.022842	0.002147	0.180737	0.029552
65ttn_21.d	0.361989	0.076367	0.024586	0.002384	0.136491	0.034216
65ttn_22.d	0.576651	0.122638	0.02455	0.002876	0.163671	0.036583
65ttn_23.d	0.701653	0.157934	0.025373	0.002681	0.213291	0.049691

65ttn_26.d	0.615593	0.116174	0.0236	0.002998	0.254902	0.059495
65ttn_27.d	0.442064	0.092197	0.022864	0.002105	0.149547	0.03255
65ttn_28.d	0.409531	0.101223	0.022724	0.002322	0.153179	0.042378
65ttn_30.d	0.478285	0.098203	0.022107	0.002148	0.191676	0.041777
70area3ttn						
70area3ttn2_1.d	1.599479392	0.359878811	0.035205093	0.004399927	0.35161004	0.092502252
70area3ttn2_2.d	1.402894121	0.360586521	0.028283174	0.003742813	0.290370925	0.066506208
70area3ttn2_3.d	0.24982714	0.092899366	0.021521383	0.002634367	0.10992567	0.047926054
70area3ttn2_4.d	0.251545415	0.068951139	0.021898494	0.00220155	0.088701134	0.026637169
70area3ttn2_5.d	0.227704449	0.058044586	0.021123576	0.001925761	0.087618327	0.022839857
70area3ttn2_6.d	0.292538189	0.092700486	0.020615937	0.002393774	0.143250136	0.04621212
70area3ttn2_7.d	0.907591307	0.130217778	0.027489292	0.002415354	0.253413933	0.036488029
70area3ttn2_8.d	1.19822737	0.316453479	0.027869473	0.003688417	0.301376842	0.062554218
70area3ttn2_9.d	0.224199432	0.050182756	0.023230086	0.001770916	0.072777418	0.016061712
70area3ttn2_10.d	0.248918778	0.04120564	0.020266172	0.001558966	0.095212576	0.015680618
70area3ttn2_11.d	0.272948201	0.089156001	0.019383106	0.002535816	0.126603612	0.044845305
70area3ttn2_12.d	0.801089703	0.144662145	0.026641019	0.002307037	0.231138165	0.035304544
70area3ttn2_13.d	0.659313686	0.144867011	0.027488303	0.002619019	0.17371	0.034601141
70area3ttn2_14.d	0.146664089	0.041144762	0.019770442	0.002212245	0.051652011	0.01664262
70area3ttn2_15.d	0.385073789	0.066850925	0.024000526	0.002622217	0.117585617	0.019917503
70area3ttn2_16.d	0.210611747	0.040291693	0.021444883	0.001616121	0.068952549	0.01298895
70area3ttn2_17.d	0.254154541	0.054476144	0.022503907	0.001870183	0.08492588	0.018031059
70area3ttn2_18.d	0.268148825	0.051307866	0.021995083	0.001692605	0.088733213	0.01722135
70area3ttn2_19.d	0.231392193	0.048764154	0.023236715	0.001804431	0.077486512	0.016018197
70area3ttn2_20.d	0.159417529	0.028991342	0.019806139	0.001599916	0.063404813	0.011419397
70area3ttn2_21.d	0.209999927	0.042139022	0.021866259	0.00158496	0.066750752	0.013197476
70area3ttn2_22.d	0.24236008	0.047938786	0.022961451	0.00184279	0.084804054	0.017629818
70area3ttn2_23.d	0.256552877	0.055381424	0.022343413	0.001794272	0.083294982	0.01744865
70area3ttn2_24.d	0.186956141	0.040241342	0.020895928	0.001726957	0.071417068	0.014557811
70area3ttn2_25.d	0.188540061	0.034906269	0.021970053	0.001602725	0.064445134	0.011571484
70area3ttn2_26.d	0.135539639	0.019756144	0.019054566	0.001202827	0.050229032	0.006733289
70area3ttn2_27.d	0.290081613	0.066541766	0.021088062	0.001949874	0.090698399	0.013696045
70area3ttn2_28.d	0.219278187	0.050494613	0.020878365	0.001598315	0.075157252	0.016881739
70area3ttn2_29.d	0.136824538	0.020462631	0.019361204	0.001207178	0.049304482	0.006748384
70area3ttn2_30.d with links	0.311962947	0.05986873	0.020062474	0.002352963	0.124216066	0.026124425
73area2						
73area2ttn1_1.d	0.135321193	0.019816007	0.018272431	0.001276696	0.05468503	0.007306493
73area2ttn1_2.d	0.129986093	0.01555176	0.018737275	0.001115509	0.050131348	0.005099829
73area2ttn1_3.d	0.123205332	0.015206807	0.018489454	0.001156538	0.050286485	0.005764023
73area2ttn1_4.d	0.298911834	0.025466616	0.020393889	0.001175921	0.105873568	0.006847654
73area2ttn1_5.d	0.1174413	0.01510867	0.018819889	0.001171699	0.046253329	0.005350242
73area2ttn1_6.d	0.110462878	0.014031312	0.018425351	0.001102209	0.044074737	0.005156564
73area2ttn1_7.d	0.112974176	0.021889869	0.017872866	0.001165274	0.044703939	0.008549229
73area2ttn1_8.d	0.141977848	0.01756888	0.018416727	0.001366511	0.055901868	0.005730836
73area2ttn1_9.d	0.124909221	0.016145176	0.018638304	0.001119598	0.048352129	0.006014641
73area2ttn1_10.d	0.123907956	0.014394275	0.018701506	0.001139888	0.048866961	0.004617509
73area2ttn1_11.d	0.130028649	0.016682155	0.0181778	0.001066147	0.054602641	0.006482747
73area2ttn1_12.d	0.126089089	0.014604073	0.018710522	0.001109831	0.047419073	0.004639258
73area2ttn1_13.d	0.147982143	0.021330806	0.018277518	0.001183232	0.055139162	0.00784721
73area2ttn1_14.d	0.12365758	0.013296404	0.018343494	0.001098105	0.04917826	0.004731915
73area2ttn1_15.d	0.119185448	0.015118316	0.018553912	0.001162418	0.04590435	0.005202021
73area2ttn1_16.d	0.127133801	0.013266116	0.019487858	0.001221834	0.047161028	0.004250521
73area2ttn1_17.d	0.129184424	0.013596357	0.01870914	0.001162583	0.051220274	0.004559313

73area2ttn1_18.d	0.192981359	0.027193796	0.01902795	0.00128877	0.076080814	0.010790969
73area2ttn1_19.d	0.120979498	0.009903672	0.018075637	0.001072772	0.049803955	0.002807753
73area2ttn1_20.d	0.09116582	0.019437691	0.017381781	0.001153627	0.040751526	0.009068495
73area2ttn1_21.d	0.121906899	0.012287069	0.019589475	0.001207073	0.045912503	0.004147419
73area2ttn1_22.d	0.130097379	0.014069353	0.018798257	0.001139022	0.051972505	0.004811244
73area2ttn1_23.d	0.131495148	0.013457112	0.019164128	0.00116498	0.049417337	0.003961331
73area2ttn1_24.d	0.129666295	0.01260081	0.018839547	0.001197172	0.049214675	0.004209042
73area2ttn1_25.d	0.131593556	0.017891819	0.019573218	0.001271049	0.049136198	0.006021622
73area2ttn1_26.d	0.164948647	0.018831722	0.019780259	0.001228733	0.05872666	0.005092993
73area2ttn1_27.d	0.132786223	0.014373292	0.018404439	0.0011315	0.051409615	0.004563203
73area2ttn1_28.d	0.137479193	0.014555872	0.019146653	0.001209806	0.053484257	0.005054992
73area2ttn1_29.d	0.139432652	0.025710563	0.017863059	0.001159464	0.057322039	0.01076814
73area2ttn1_30.d	0.138537753	0.013143294	0.018922353	0.001172116	0.052542885	0.004241413

Figure A-3: Titanite C11 Tera-Wasserburg Diagram (Maine)

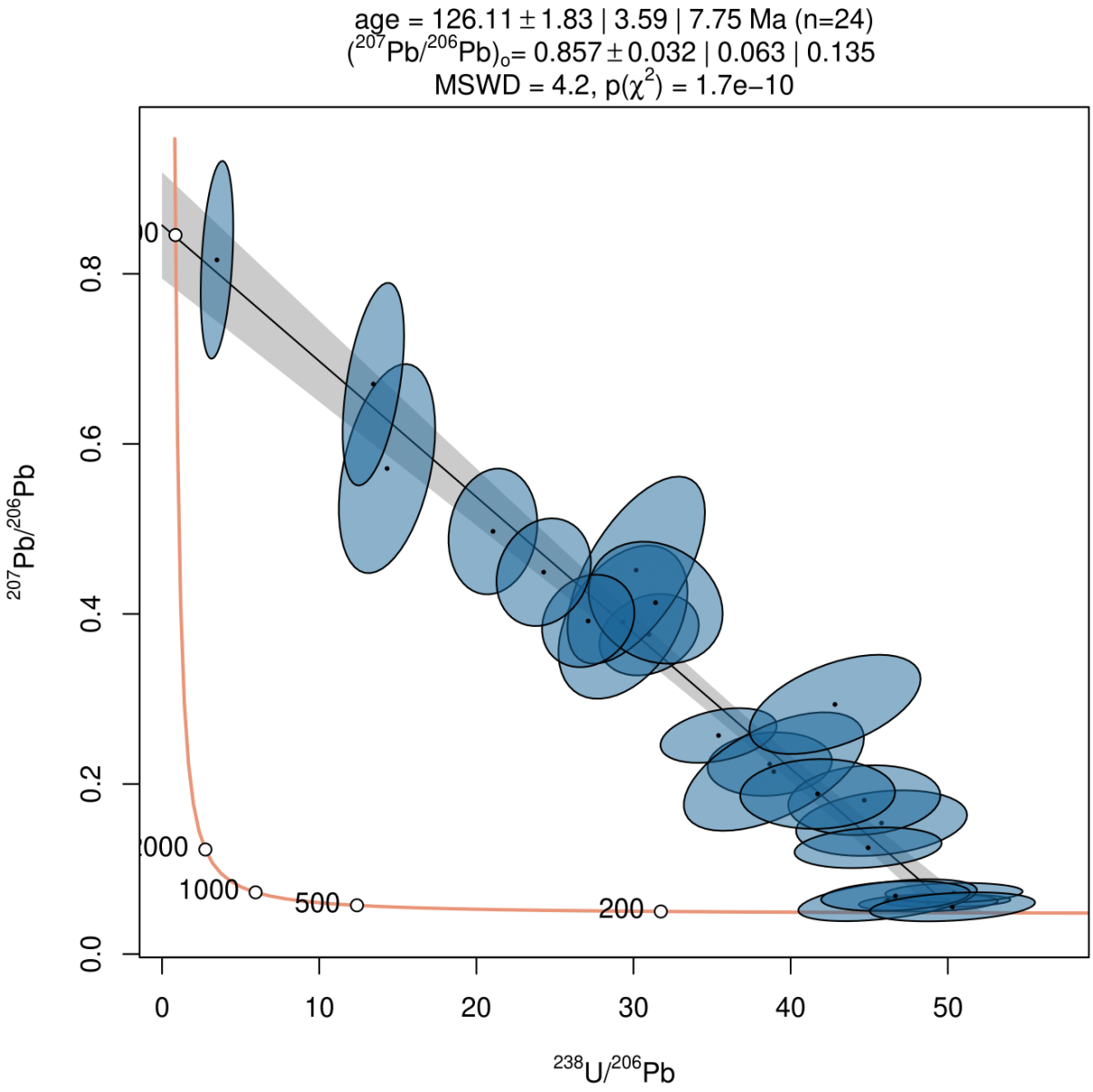

Figure A-4: Titanite C65 Tera-Wasserburg Diagram (Maine)

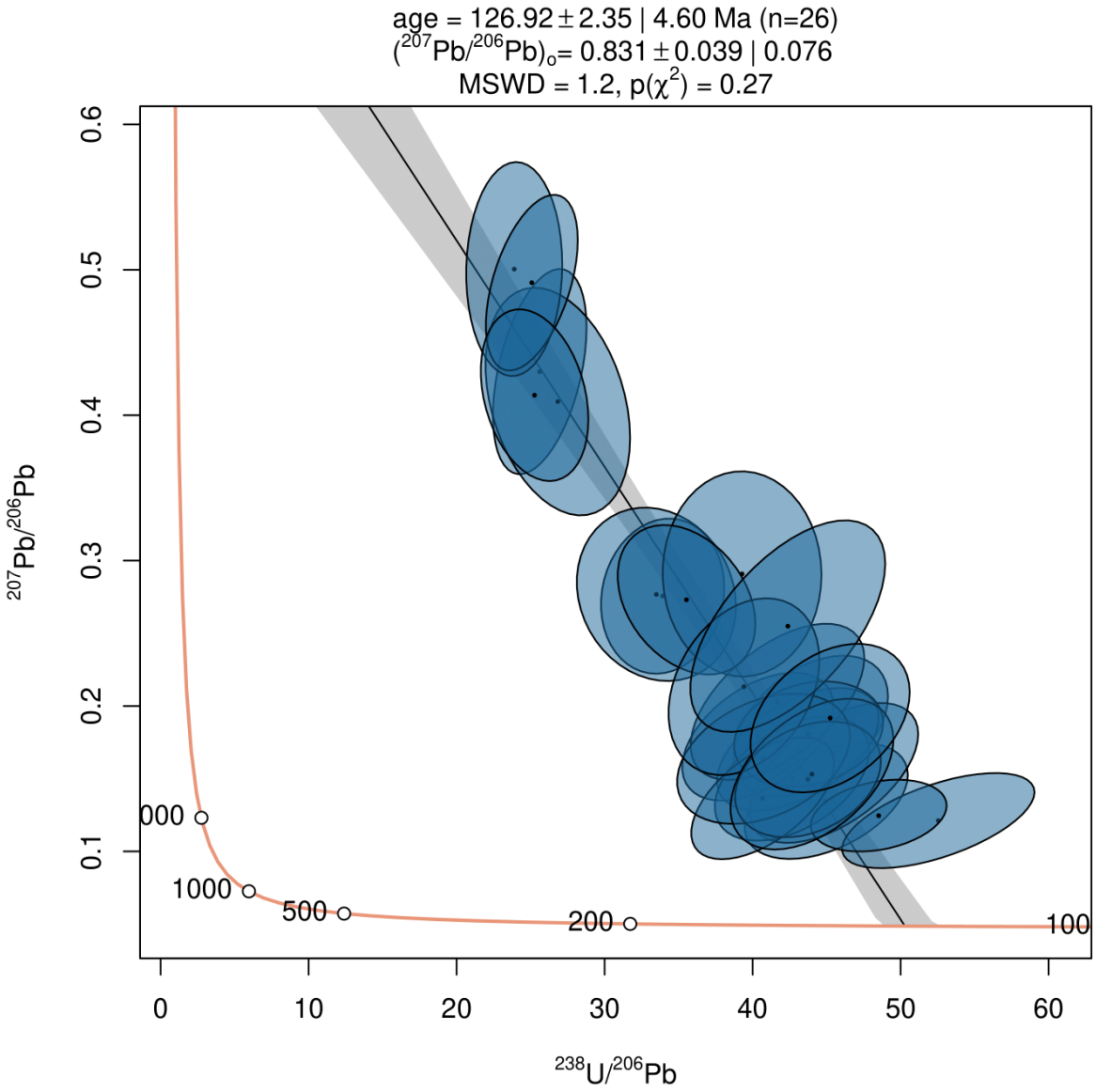

Figure A-5: C70

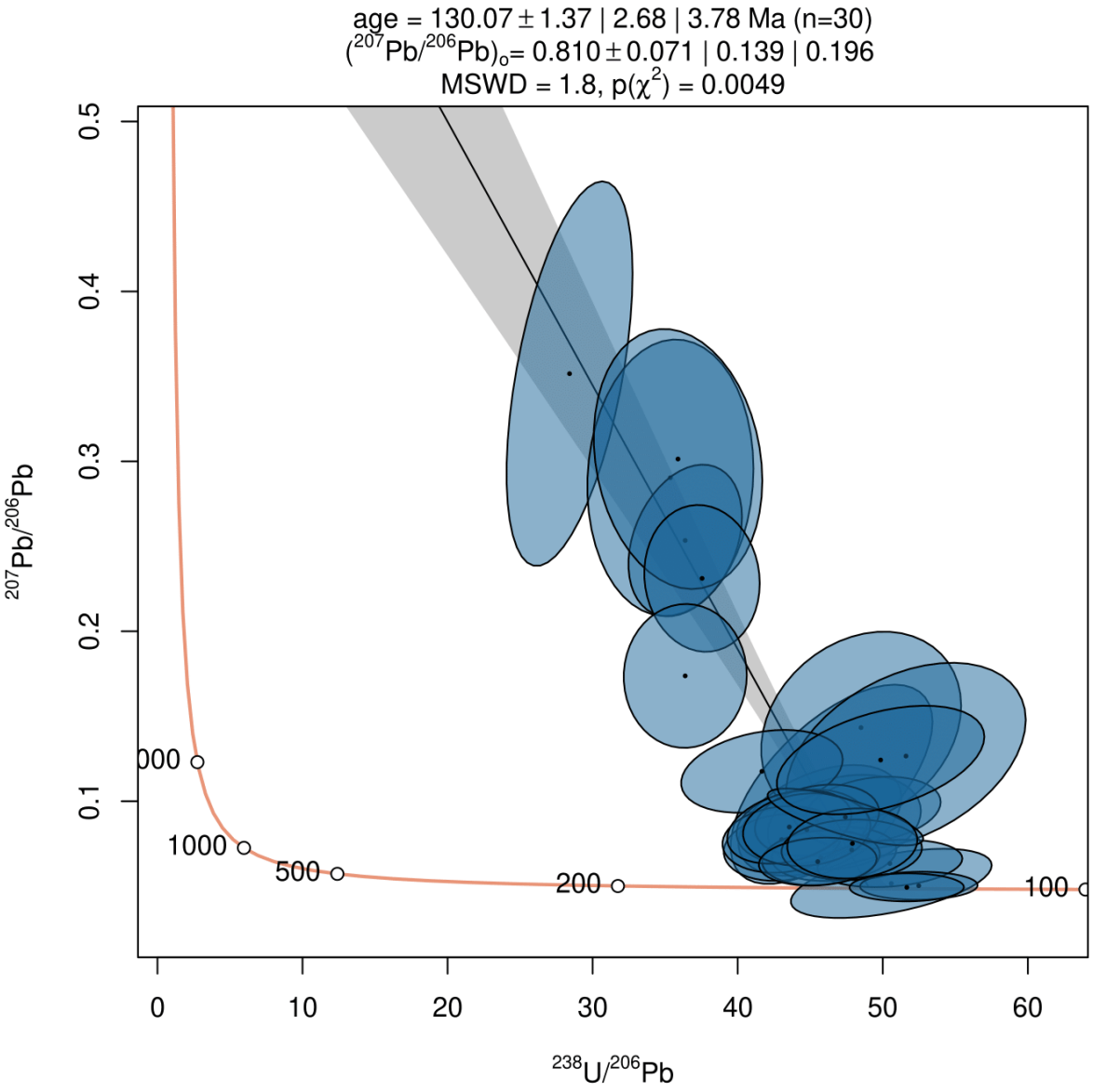

Figure A-6: Titanite C73 Tera-Wasserburg Diagram (Maine)

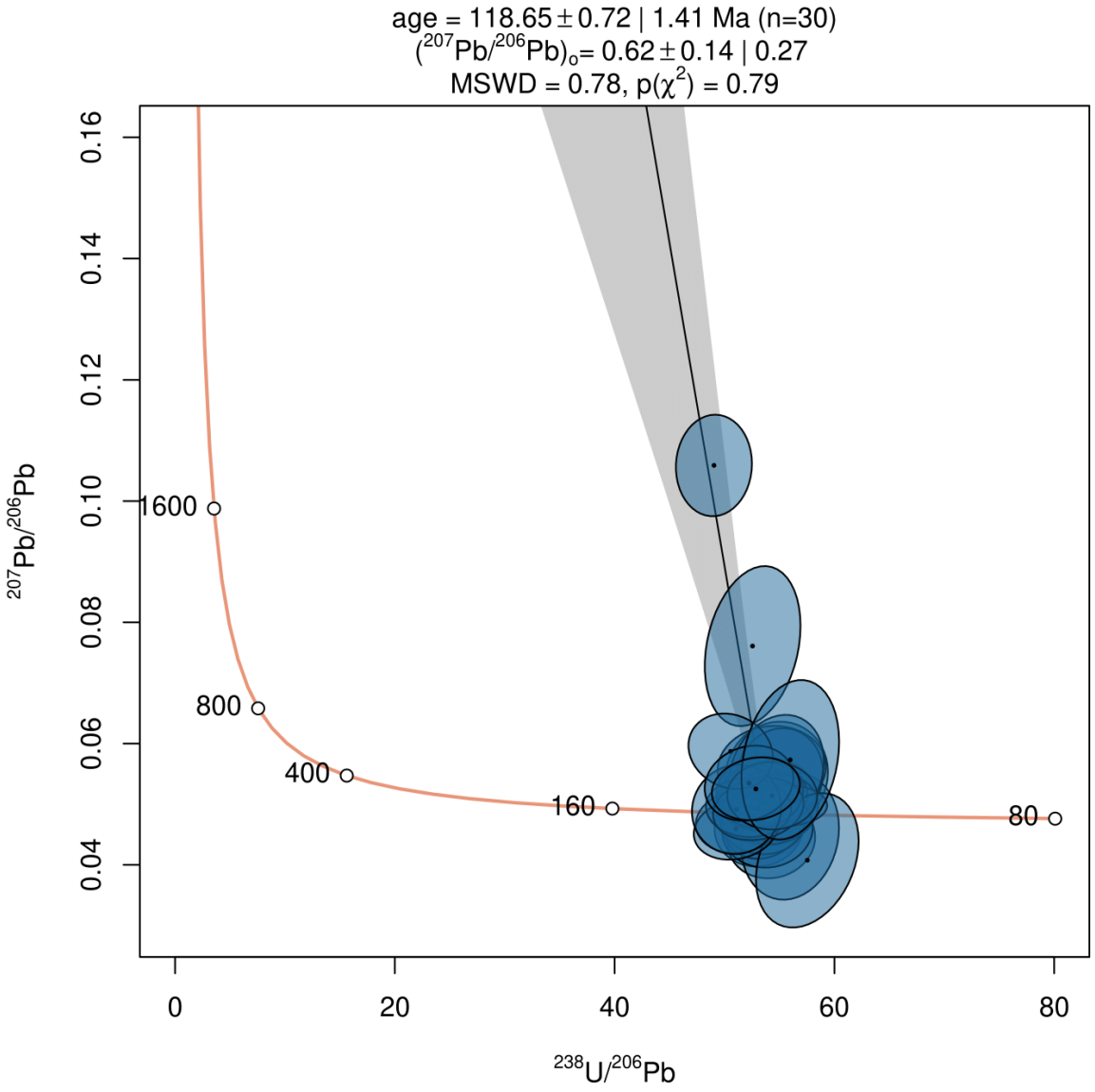

Table A-4: Apatite sample ID information and associated depth at which the titanite originated, $^{238}U/^{206}Pb$ ratios and error, $^{207}Pb/^{206}Pb$ ratios and error, rho, the textural relationship of the titanite within the overall sample, and whether samples fell off the discordia line and therefore omitted from further calculation, data taken at UCSB.

Sample Label	Depth (m)	$^{238}U/^{206}Pb$	2se	$^{207}Pb/^{206}Pb$	2se	rho	Textural relationship	Omitted point? (x)
C12_05_1	133	26.12	2.57	0.497	0.025	0.35	Undifferentiated	
C12_05_2	133	26.81	2.42	0.449	0.035	0.24	Undifferentiated	
C12_05_3	133	25.26	2.46	0.51	0.021	0.21	Undifferentiated	
C12_05_4	133	25.47	2.24	0.479	0.028	0.21	Undifferentiated	
C12_05_5	133	33.06	3.03	0.41	0.036	0.46	Undifferentiated	
C12_04	133	22.98	1.83	0.533	0.029	0.13	Undifferentiated	
C12_06_1	133	23.6	1.93	0.492	0.02	0.32	Undifferentiated	
C12_06_2	133	21.11	1.38	0.497	0.022	0.18	Undifferentiated	
C12_06_3	133	19.27	1.54	0.547	0.025	0.27	Undifferentiated	
C12_06_4	133	24.3	2.33	0.494	0.026	0.28	Undifferentiated	
C12_06_5	133	29.61	3.5	0.378	0.02	0.12	Undifferentiated	
C12_06_6	133	23.87	1.61	0.489	0.022	0.22	Undifferentiated	
C12_06_7	133	20.4	2.66	0.524	0.021	0.1	Undifferentiated	
C12_06_8	133	20.44	1.99	0.521	0.019	0.12	Undifferentiated	
C12_06_9	133	22.68	2.36	0.51	0.023	0.14	Undifferentiated	
C12_06_10	133	22.93	2.29	0.468	0.028	0.12	Undifferentiated	
C12_07_1	133	23.83	2.56	0.556	0.037	0.22	Undifferentiated	
C12_07_2	133	18.05	1.98	0.589	0.019	0.47	Undifferentiated	
C12_07_3	133	25.63	1.54	0.491	0.026	0.09	Undifferentiated	
C12_07_4	133	26.24	2.98	0.48	0.038	0.43	Undifferentiated	
C12_08	133	19.61	1.38	0.58	0.021	0.3	Undifferentiated	
C12_09_1	133	25.05	2.32	0.501	0.025	0.12	Undifferentiated	
C12_09_2	133	28.18	1.48	0.478	0.024	0.17	Undifferentiated	
C12_09_3	133	24.75	1.68	0.491	0.02	0.1	Undifferentiated	
C12_09_4	133	25.42	1.77	0.477	0.018	0.38	Undifferentiated	
C12_09_5	133	28.57	2.15	0.504	0.026	0.44	Undifferentiated	
C12_09_6	133	24.3	2	0.486	0.028	0.27	Undifferentiated	
C12_10	133	19.12	2.16	0.572	0.031	0.51	Undifferentiated	
C12_11_1	133	23.64	2.12	0.499	0.022	0.16	Undifferentiated	
C12_11_2	133	23.87	2.06	0.48	0.028	0.13	Undifferentiated	
C12_11_3	133	26.01	2.17	0.447	0.037	0.23	Undifferentiated	
C12_12	133	26.18	3.19	0.446	0.03	0.34	Undifferentiated	
C12_13_1	133	21.07	1.34	0.551	0.025	0.24	Undifferentiated	
C12_13_2	133	10.25	2.94	0.665	0.037	0.6	Undifferentiated	
C12_25_1	133	21.52	1.43	0.553	0.021	0.13	Undifferentiated	
C12_25_2	133	20.68	1.43	0.568	0.026	0.34	Undifferentiated	
C12_25_3	133	25.42	1.72	0.505	0.024	0.21	Undifferentiated	
C12_26_1	133	24.8	1.08	0.509	0.024	0.34	Undifferentiated	

C12_26_2	133	24.8	2.96	0.471	0.029	0.08	Undifferentiated	
C12_26_3	133	27.98	1.94	0.48	0.03	0.17	Undifferentiated	
C12_27_1	133	23.42	2.52	0.514	0.023	0.2	Undifferentiated	
C12_27_2	133	22.1	1.86	0.529	0.023	0.19	Undifferentiated	
C12_27_3	133	19.15	1.32	0.551	0.023	0.2	Undifferentiated	
C12_27_4	133	25.21	1.64	0.514	0.022	0.13	Undifferentiated	
C12_27_5	133	22.39	1.62	0.541	0.025	0.25	Undifferentiated	
C12_27_6	133	22.89	2.11	0.486	0.029	0.24	Undifferentiated	
C12_27_7	133	25.26	2.36	0.501	0.024	0.15	Undifferentiated	
C12_27_8	133	22.76	1.64	0.505	0.026	0.17	Undifferentiated	
C12_28_1	133	19.27	1.99	0.547	0.019	0.07	Undifferentiated	
C12_28_2	133	20.23	1.5	0.534	0.024	0.24	Undifferentiated	
C12_28_3	133	14.22	1.03	0.614	0.02	0.26	Undifferentiated	
C12_29_1	133	23.92	2.3	0.483	0.032	0.46	Undifferentiated	
C12_29_2	133	24.65	1.62	0.504	0.022	0.35	Undifferentiated	
C12_30_1	133	22.22	1.52	0.551	0.023	0.32	Undifferentiated	
C12_30_2	133	25.47	1.83	0.501	0.022	0.37	Undifferentiated	
C12_30_3	133	25.1	1.53	0.485	0.02	0.31	Undifferentiated	
C12_31_2	133	42.51	2.24	0.374	0.031	0.38	Undifferentiated	x
C12_36	133	23.51	1.52	0.514	0.023	0.33	Undifferentiated	
C12_32_1	133	26.46	1.75	0.502	0.028	0.25	Undifferentiated	
C12_32_2	133	24.9	1	0.508	0.024	0.49	Undifferentiated	
C12_32_3	133	26.12	2.03	0.503	0.024	0.25	Undifferentiated	
C12_33_1	133	19.33	1.76	0.557	0.017	0.13	Undifferentiated	
C12_33_2	133	17.91	1.82	0.569	0.025	0.13	Undifferentiated	
C12_34	133	21.48	2.2	0.54	0.024	0.22	Undifferentiated	
C12_35_1	133	23.24	2.13	0.527	0.023	0.18	Undifferentiated	
C12_35_2	133	21.59	2.07	0.528	0.028	0.15	Undifferentiated	
C12_37_1	133	3.38	0.74	0.749	0.019	0.67	Undifferentiated	
C12_37_2	133	19.65	1.94	0.584	0.028	0.39	Undifferentiated	
C12_37_3	133	27.98	2.44	0.436	0.026	0.19	Undifferentiated	
C12_38_1	133	27.48	1.64	0.446	0.017	0.28	Undifferentiated	
C12_38_2	133	26.12	1.23	0.434	0.014	0.31	Undifferentiated	
C12_39_1	133	36.53	3.36	0.431	0.021	0.26	Undifferentiated	x
C12_39_2	133	27.54	1.89	0.462	0.029	0.09	Undifferentiated	
C12_39_3	133	27.6	2.25	0.458	0.021	0.3	Undifferentiated	
C12_39_4	133	21.94	2.14	0.538	0.019	0.33	Undifferentiated	
C12_39_5	133	26.52	2.31	0.499	0.025	0.23	Undifferentiated	
C12_39_6	133	27.35	2.22	0.416	0.028	0.26	Undifferentiated	
C12_39_7	133	27.11	2.53	0.455	0.025	0.23	Undifferentiated	
C12_50_1	133	26.75	1.45	0.454	0.019	0.16	Undifferentiated	
C12_50_2	133	25.1	2.83	0.454	0.029	0.16	Undifferentiated	
C12_50_3	133	23.92	2.12	0.497	0.023	0.2	Undifferentiated	
C12_50_4	133	22.02	1.92	0.489	0.023	0.25	Undifferentiated	
C12_50_5	133	28.11	2.21	0.44	0.033	0.42	Undifferentiated	

C12_50_6	133	23.15	1.82	0.503	0.024	0.43	Undifferentiated	
C12_50_7	133	24.4	1.87	0.486	0.034	0.26	Undifferentiated	
C12_50_8	133	22.3	2.17	0.558	0.029	0.12	Undifferentiated	
C12_50_9	133	24.55	1.89	0.507	0.027	0.26	Undifferentiated	
C12_49_1	133	8.78	0.78	0.725	0.021	0.41	Undifferentiated	
C12_49_2	133	24.55	2.96	0.503	0.026	0.33	Undifferentiated	
C12_49_3	133	21.37	1.45	0.608	0.031	0.34	Undifferentiated	
C12_49_4	133	20.5	1.41	0.554	0.024	0.2	Undifferentiated	
C12_49_5	133	18.6	1.58	0.596	0.033	0.2	Undifferentiated	
C12_49_6	133	23.11	2.36	0.495	0.021	0.17	Undifferentiated	
C34_35_2	486	0.63	0.03	0.837	0.017	0.36	Undifferentiated	
C34_35_3	486	0.55	0.03	0.832	0.017	0.21	Undifferentiated	
C34_35_4	486	0.51	0.03	0.837	0.017	0.37	Undifferentiated	
C34_35_5	486	0.61	0.03	0.839	0.017	0.36	Undifferentiated	
C34_35_6	486	0.65	0.12	0.837	0.018	0.09	Undifferentiated	
C34_34_2	486	0.54	0.04	0.834	0.017	0.41	Undifferentiated	
C34_34_3	486	1.21	0.05	0.827	0.017	0.24	Undifferentiated	
C34_34_4	486	0.78	0.06	0.834	0.017	0.24	Undifferentiated	
C34_32_1	486	0.29	0.04	0.842	0.017	0.26	Undifferentiated	
C34_32_2	486	0.93	0.07	0.828	0.017	0.18	Undifferentiated	
C34_32_3	486	0.48	0.06	0.838	0.017	0.48	Undifferentiated	
C34_32_4	486	0.38	0.04	0.838	0.018	0.12	Undifferentiated	
C34_32_5	486	0.87	0.05	0.833	0.017	0.22	Undifferentiated	
C34_32_6	486	0.77	0.03	0.835	0.017	0.52	Undifferentiated	
C34_32_7	486	0.78	0.05	0.834	0.017	0.32	Undifferentiated	
C34_32_8	486	0.98	0.05	0.829	0.018	0.35	Undifferentiated	
C34_32_9	486	1.07	0.04	0.828	0.017	0.4	Undifferentiated	
C34_36_1	486	0.63	0.07	0.834	0.017	0.13	Undifferentiated	
C34_36_2	486	0.49	0.04	0.835	0.017	0.15	Undifferentiated	
C34_36_3	486	1.39	0.21	0.821	0.018	0.14	Undifferentiated	
C34_36_4	486	0.63	0.06	0.833	0.018	0.15	Undifferentiated	
C34_36_5	486	0.85	0.03	0.831	0.017	0.31	Undifferentiated	
C34_37_1	486	0.82	0.04	0.833	0.017	0.24	Undifferentiated	
C34_37_2	486	0.84	0.12	0.829	0.017	0.31	Undifferentiated	
C34_37_4	486	1.3	0.15	0.821	0.017	0.13	Undifferentiated	
C34_37_5	486	0.76	0.16	0.834	0.021	0.03	Undifferentiated	
C34_37_6	486	0.45	0.14	0.833	0.019	0.04	Undifferentiated	
C34_37_7	486	2.69	0.46	0.796	0.019	0.15	Undifferentiated	
C34_10_1	486	0.84	0.06	0.834	0.017	0.37	Undifferentiated	
C34_10_2	486	0.68	0.04	0.833	0.017	0.44	Undifferentiated	
C34_10_3	486	0.81	0.08	0.836	0.018	0.37	Undifferentiated	
C34_10_4	486	0.53	0.04	0.836	0.018	0.24	Undifferentiated	
C34_10_5	486	2.34	0.14	0.817	0.017	0.27	Undifferentiated	
C34_10_6	486	0.45	0.04	0.836	0.017	0.39	Undifferentiated	
C34_10_7	486	1.05	0.15	0.828	0.017	0.47	Undifferentiated	

C34_10_8	486	0.51	0.04	0.836	0.017	0.34	Undifferentiated	
C34_10_9	486	0.46	0.04	0.836	0.017	0.21	Undifferentiated	
C34_10_10	486	0.6	0.05	0.84	0.017	0.34	Undifferentiated	
C34_10_11	486	0.55	0.03	0.838	0.017	0.5	Undifferentiated	
C34_10_12	486	0.88	0.1	0.831	0.018	0.49	Undifferentiated	
C34_10_13	486	0.97	0.08	0.829	0.017	0.15	Undifferentiated	
C34_10_14	486	0.32	0.02	0.839	0.017	0.24	Undifferentiated	
C34_10_15	486	0.81	0.06	0.832	0.017	0.14	Undifferentiated	
C34_10_16	486	0.88	0.04	0.832	0.018	0.53	Undifferentiated	
C34_10_17	486	0.91	0.05	0.828	0.017	0.21	Undifferentiated	
C34_10_18	486	0.79	0.03	0.832	0.017	0.43	Undifferentiated	
C34_10_19	486	0.91	0.06	0.836	0.018	0.15	Undifferentiated	
C34_10_20	486	0.94	0.07	0.832	0.018	0.22	Undifferentiated	
C34_10_21	486	1.05	0.2	0.827	0.019	0.23	Undifferentiated	
C34_22_1	486	0.63	0.08	0.832	0.018	0.44	Undifferentiated	
C34_22_2	486	0.8	0.04	0.834	0.018	0.18	Undifferentiated	
C34_22_3	486	0.87	0.11	0.831	0.018	0.17	Undifferentiated	
C34_22_4	486	0.84	0.11	0.83	0.018	0.36	Undifferentiated	
C34_22_5	486	0.64	0.04	0.836	0.017	0.22	Undifferentiated	
C34_22_6	486	0.92	0.04	0.832	0.017	0.46	Undifferentiated	
C34_22_7	486	0.65	0.03	0.835	0.017	0.23	Undifferentiated	
C34_22_8	486	0.6	0.06	0.839	0.017	0.13	Undifferentiated	
C34_22_9	486	1.28	0.19	0.826	0.017	0.32	Undifferentiated	
C34_29_1	486	1.27	0.07	0.826	0.017	0.37	Undifferentiated	
C34_29_2	486	0.84	0.04	0.829	0.017	0.42	Undifferentiated	
C34_29_3	486	1.3	0.26	0.822	0.018	0.04	Undifferentiated	
C34_29_4	486	1.14	0.06	0.829	0.017	0.49	Undifferentiated	
C34_29_5	486	0.93	0.07	0.827	0.018	0.35	Undifferentiated	
C34_29_6	486	1.27	0.07	0.832	0.017	0.33	Undifferentiated	
C34_29_7	486	0.6	0.07	0.834	0.018	0.13	Undifferentiated	
C34_29_8	486	0.79	0.11	0.84	0.018	0.38	Undifferentiated	
C34_31_1	486	0.54	0.02	0.837	0.017	0.29	Undifferentiated	
C34_31_2	486	0.97	0.04	0.832	0.017	0.24	Undifferentiated	
C34_31_3	486	0.87	0.06	0.834	0.017	0.25	Undifferentiated	
C34_31_4	486	0.65	0.03	0.837	0.017	0.27	Undifferentiated	
C34_31_5	486	0.8	0.04	0.832	0.017	0.48	Undifferentiated	
C34_11_8	486	0.72	0.03	0.832	0.017	0.34	Undifferentiated	
C34_11_9	486	0.72	0.03	0.83	0.017	0.34	Undifferentiated	
C34_11_10	486	0.53	0.03	0.837	0.017	0.2	Undifferentiated	
C34_11_11	486	0.97	0.03	0.832	0.017	0.36	Undifferentiated	
C34_11_12	486	0.74	0.08	0.839	0.017	0.51	Undifferentiated	
C34_11_13	486	0.75	0.04	0.834	0.017	0.17	Undifferentiated	
C34_11_14	486	0.57	0.04	0.84	0.017	0.32	Undifferentiated	
C34_11_15	486	0.64	0.03	0.84	0.017	0.3	Undifferentiated	
C34_11_16	486	0.66	0.04	0.834	0.017	0.42	Undifferentiated	

C34_11_17	486	0.52	0.06	0.841	0.017	0.34	Undifferentiated	
C34_11_18	486	0.47	0.02	0.839	0.017	0.17	Undifferentiated	
C34_11_19	486	0.97	0.04	0.832	0.017	0.44	Undifferentiated	
C34_11_20	486	0.69	0.03	0.84	0.017	0.35	Undifferentiated	
C34_12_1	486	1.03	0.21	0.829	0.018	0.05	Undifferentiated	
C34_12_2	486	0.44	0.11	0.838	0.018	0.03	Undifferentiated	
C34_12_3	486	0.94	0.12	0.829	0.018	0.19	Undifferentiated	
C43_01_1	618	41.08	4.91	0.303	0.047	0.08	Brecciated Matrix	
C43_01_2	618	27.11	7.85	0.447	0.036	0.05	Brecciated Matrix	
C43_01_4	618	53.74	14.01	0.264	0.089	0.11	Brecciated Matrix	
C43_04_1	618	43.26	8.79	0.233	0.054	0.08	Brecciated Matrix	
C43_04_2	618	28.77	4.11	0.482	0.03	0.15	Brecciated Matrix	
C43_04_3	618	34.17	7.12	0.296	0.035	0.2	Brecciated Matrix	
C43_04_4	618	45.35	12	0.195	0.031	0.26	Brecciated Matrix	
C43_04_5	618	26.52	16.73	0.51	0.22	0.06	Brecciated Matrix	
C52_03_1	731	30.93	4.59	0.329	0.028	0.23	Matrix	
C52_03_2	731	37.15	4.43	0.331	0.015	0.1	Matrix	
C52_03_3	731	38.59	3.2	0.266	0.022	0.23	Matrix	
C52_05	731	40.82	10.31	0.203	0.054	0.18	Matrix	
C52_06	731	33.33	2.41	0.267	0.023	0.16	Matrix	
C52_07_1	731	46.88	5.93	0.198	0.04	0.27	Matrix	
C52_07_2	731	47.17	2.01	0.141	0.011	0.2	Matrix	
C52_08_1	731	45.63	2.59	0.171	0.013	0.2	Matrix	
C52_09_1	731	44.94	1.91	0.204	0.011	0.34	Matrix	
C52_09_2	731	42.11	2.51	0.238	0.016	0.22	Matrix	
C52_10	731	45.63	2.27	0.213	0.018	0.13	Matrix	
C52_11	731	43.96	3.96	0.343	0.029	0.2	Matrix	x
C52_12_1	731	40.82	2.24	0.265	0.019	0.38	Matrix	
C52_15	731	38.83	3.73	0.296	0.035	0.14	Matrix	
C52_16_1	731	47.06	3.99	0.198	0.022	0.43	Matrix	
C52_16_2	731	40.27	4.4	0.264	0.036	0.46	Matrix	
C52_17_1	731	45.28	2.09	0.187	0.018	0.21	Mag Vein	
C52_17_2	731	43.8	2.85	0.17	0.014	0.28	Mag Vein	
C52_17_3	731	44.28	2.76	0.198	0.015	0.12	Mag Vein	
C52_17_4	731	32.17	3.76	0.347	0.029	0.2	Mag Vein	
C52_24_1	731	48.06	1.4	0.135	0.009	0.21	Mag Vein	
C52_24_2	731	46.15	2.82	0.177	0.011	0.3	Mag Vein	

C52_24_3	731	43.48	2.37	0.174	0.012	0.12	Mag Vein	
C52_24_4	731	37.74	3.06	0.277	0.021	0.25	Mag Vein	
C52_24_5	731	48.06	1.52	0.165	0.02	0.11	Mag Vein	
C52_24_6	731	45.8	2.94	0.164	0.011	0.19	Mag Vein	
C52_26_1	731	50.42	2.35	0.125	0.006	0.27	Mag Vein	
C52_26_2	731	48.17	2.07	0.136	0.008	0.23	Mag Vein	
C52_26_3	731	49.5	2.05	0.128	0.006	0.38	Mag Vein	
C52_26_4	731	49.69	1.45	0.123	0.006	0.25	Mag Vein	
C52_26_5	731	48.86	1.65	0.14	0.009	0.19	Mag Vein	
C52_26_6	731	48.94	1.52	0.127	0.008	0.23	Mag Vein	
C52_26_7	731	49.5	1.61	0.138	0.008	0.14	Mag Vein	
C52_26_8	731	48.13	1.85	0.141	0.008	0.4	Mag Vein	
C52_26_9	731	47.87	1.71	0.126	0.008	0.14	Mag Vein	
C52_27_1	731	39.09	4.27	0.33	0.038	0.04	Mag Vein	
C52_27_2	731	43.8	3.62	0.267	0.026	0.25	Mag Vein	
C52_27_3	731	45.45	3.73	0.187	0.022	0.38	Mag Vein	
C52_27_4	731	41.67	5.13	0.166	0.028	0.61	Mag Vein	
C52_27_5	731	35.19	6.64	0.202	0.038	0.13	Mag Vein	
C52_27_6	731	44.94	7.8	0.247	0.024	0.11	Mag Vein	
C52_27_7	731	48.19	9.34	0.191	0.027	0.3	Mag Vein	
C52_27_9	731	30.3	7.29	0.212	0.033	0.13	Mag Vein	x
C52_28_1	731	27.27	8.08	0.497	0.071	0.11	Mag Vein	
C52_28_10	731	47.71	1.99	0.164	0.011	0.29	Mag Vein	
C52_28_3	731	44.61	2.8	0.186	0.017	0.16	Mag Vein	
C52_28_4	731	48	2.5	0.148	0.015	0.23	Mag Vein	
C52_28_5	731	42.86	18.39	0.17	0.093	0.07	Mag Vein	
C52_28_8	731	37.15	7.28	0.192	0.066	0.11	Mag Vein	
C52_28_9	731	36.25	3.79	0.302	0.021	0.2	Mag Vein	
C52_29_2	731	45.63	2.59	0.183	0.015	0.22	Mag Vein	
C52_29_3	731	46.33	2.67	0.182	0.01	0.34	Mag Vein	
C52_29_4	731	48.9	2.2	0.167	0.011	0.1	Mag Vein	
C52_30_1	731	37.27	6.18	0.243	0.035	0.18	Mag Vein	
C52_30_2	731	38.22	4.69	0.23	0.021	0.2	Mag Vein	
C52_30_3	731	35.4	3.42	0.318	0.034	0.08	Mag Vein	
C52_30_4	731	39.47	2.59	0.254	0.015	0.31	Mag Vein	
C52_30_5	731	37.27	5.72	0.283	0.017	0.29	Mag Vein	
C52_30_6	731	40.54	2.21	0.233	0.018	0.27	Mag Vein	
C52_30_7	731	38.22	3.49	0.223	0.02	0.13	Mag Vein	
C52_30_8	731	40.68	3.54	0.235	0.024	0.2	Mag Vein	
C52_31_1	731	45.8	3.95	0.227	0.021	0.38	Mag Vein	
C52_31_2	731	48.54	1.97	0.186	0.016	0.39	Mag Vein	
C52_31_3	731	43.96	2.87	0.171	0.014	0.24	Mag Vein	
C52_32_1	731	49.48	2.1	0.137	0.009	0.27	Mag Vein	
C52_32_2	731	47.36	1.72	0.143	0.008	0.41	Mag Vein	
C52_33_1	731	38.83	2.99	0.254	0.019	0.22	Mag Vein	

C52_33_2	731	45.45	2.42	0.171	0.016	0.12	Mag Vein	
C52_33_3	731	45.98	2.31	0.171	0.011	0.21	Mag Vein	
C52_33_4	731	43.64	2.39	0.192	0.006	0.44	Mag Vein	
C52_33_5	731	43.32	2.5	0.187	0.017	0.07	Mag Vein	
C52_34_2	731	28.78	4.52	0.335	0.038	0.4	Mag Vein	
C52_34_4	731	33.99	4.2	0.288	0.022	0.2	Mag Vein	
C52_34_5	731	40.4	3.36	0.216	0.008	0.35	Mag Vein	
C52_34_6	731	37.97	2.87	0.281	0.025	0.29	Mag Vein	
C52_35_1	731	50.21	5.55	0.203	0.027	0.26	Mag Vein	
C52_35_2	731	44.44	7.13	0.226	0.034	0.07	Mag Vein	
C52_35_3	731	33.61	2.81	0.378	0.033	0.12	Mag Vein	
C52_36_1	731	42.84	1.71	0.218	0.017	0.2	Mag Vein	
C52_36_2	731	47.06	2.41	0.169	0.01	0.21	Mag Vein	
C61_01_1	840	3.47	0.66	0.78	0.022	0.29	Vein 3	
C61_01_2	840	14.12	6.48	0.556	0.07	0.12	Vein 3	
C61_02	840	40.13	1.68	0.329	0.025	0.25	Vein 3	
C61_03	840	22.22	11.12	0.46	0.13	0.35	Vein 3	
C61_04	840	30.77	8.7	0.282	0.072	0.49	Vein 3	
C61_05_2	840	30	9.02	0.34	0.17	0.13	Vein 3	
C61_06	840	6.49	0.71	0.768	0.024	0.24	Matrix	
C61_07	840	34.88	1.49	0.368	0.025	0.4	Vein 3	
C61_08	840	44.94	2.52	0.237	0.019	0.25	Vein 3	
C61_09_1	840	49.75	2.16	0.182	0.013	0.49	Vein 3	
C61_09_2	840	45.11	1.39	0.169	0.007	0.26	Vein 3	
C61_10	840	62.5	10.49	0.67	0.32	0.17	Matrix	x
C61_11	840	25.53	14.13	0.5	0.25	0.08	Matrix	
C61_12_2	840	12.12	5.76	0.47	0.1	0.1	Matrix	x
C61_13	840	29.13	4.42	0.443	0.035	0.2	Vein 3	
C61_14	840	23.3	2.35	0.476	0.027	0.25	Vein 3	
C61_15	840	67.42	4.02	0.081	0.014	0.66	Vein 3	x
C61_16	840	35.29	3.4	0.36	0.034	0.13	Matrix	
C61_18_2	840	20	13.01	0.305	0.095	0.07	Vein 1	
C61_19_1	840	17.65	8.57	0.287	0.046	0.17	Vein 1	x
C61_19_10	840	37.38	10.97	0.3	0.11	0.04	Vein 1	
C61_19_2	840	29.27	15.72	0.237	0.073	0.1	Vein 1	
C61_19_3	840	29.27	8.59	0.273	0.048	0.11	Vein 1	
C61_19_5	840	37.15	7.63	0.33	0.089	0.07	Vein 1	
C61_19_7	840	44.61	11.48	0.313	0.068	0.03	Vein 1	
C61_19_9	840	15.58	10.53	0.53	0.12	0.09	Vein 1	
C61_22	840	31.09	2.26	0.365	0.017	0.1	Matrix	
C61_23	840	23.9	1.55	0.461	0.021	0.2	Matrix	
C62_05_1	871	47.58	2.04	0.209	0.021	0.36	Vein 1	
C62_05_2	871	41.5	2.14	0.271	0.028	0.37	Vein 2	
C62_01	871	40.53	2.68	0.276	0.021	0.18	Vein 3	
C62_03_1	871	47.25	1.49	0.179	0.007	0.41	Vein 4	

C62_03_2	871	48.05	1.61	0.156	0.007	0.22	Vein 5	
C62_03_3	871	47.96	1.38	0.178	0.009	0.23	Vein 6	
C62_02	871	9.24	1.07	0.703	0.021	0.41	Vein 7	
C62_04	871	39.14	1.34	0.288	0.015	0.5	Brecciated Matrix	

Figure A-7: Apatite C12 Tera-Wasserburg Diagram (UCSB)

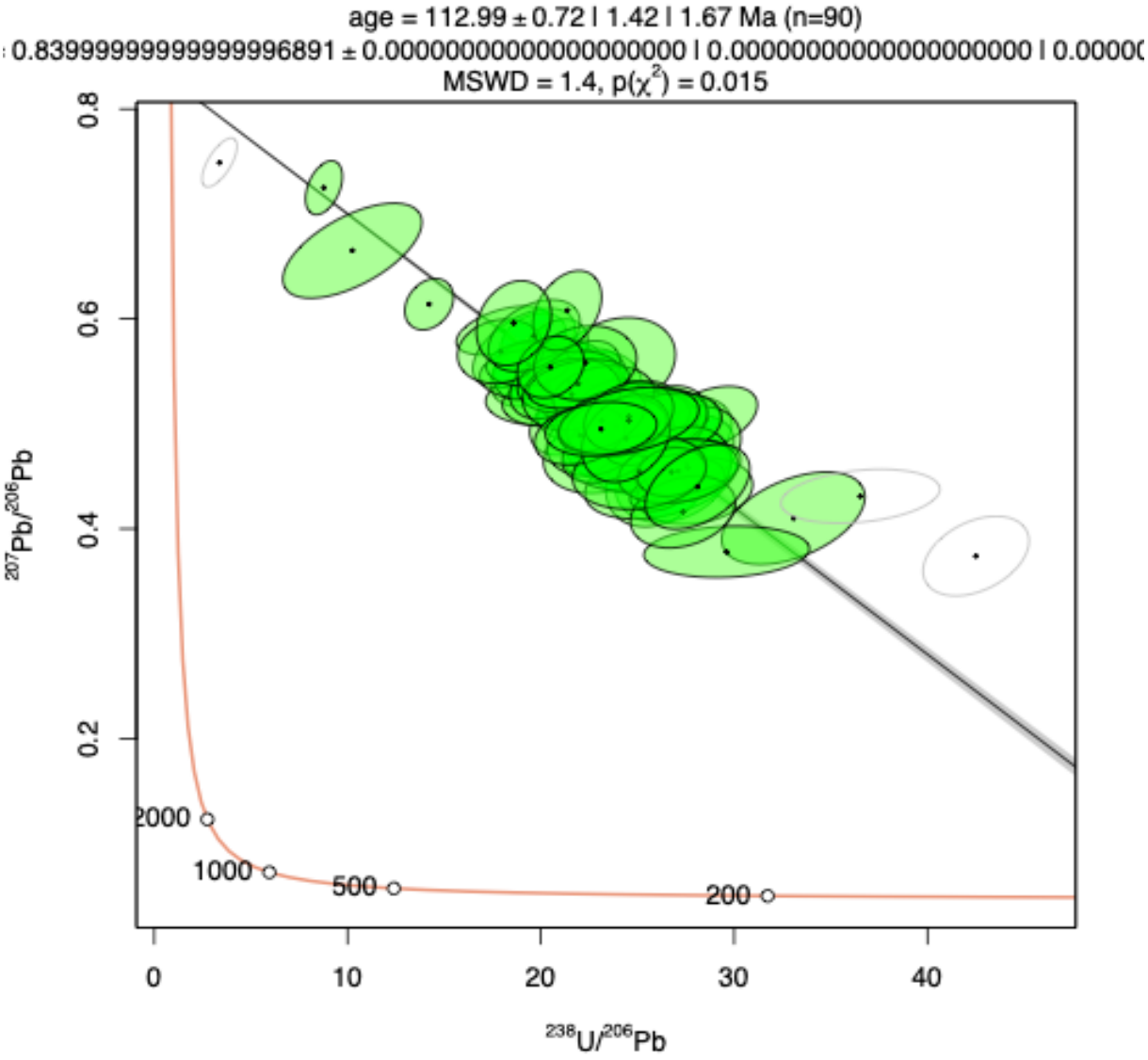

Figure A-8: Apatite C34 (Low U) Tera-Wasserburg Diagram (UCSB)

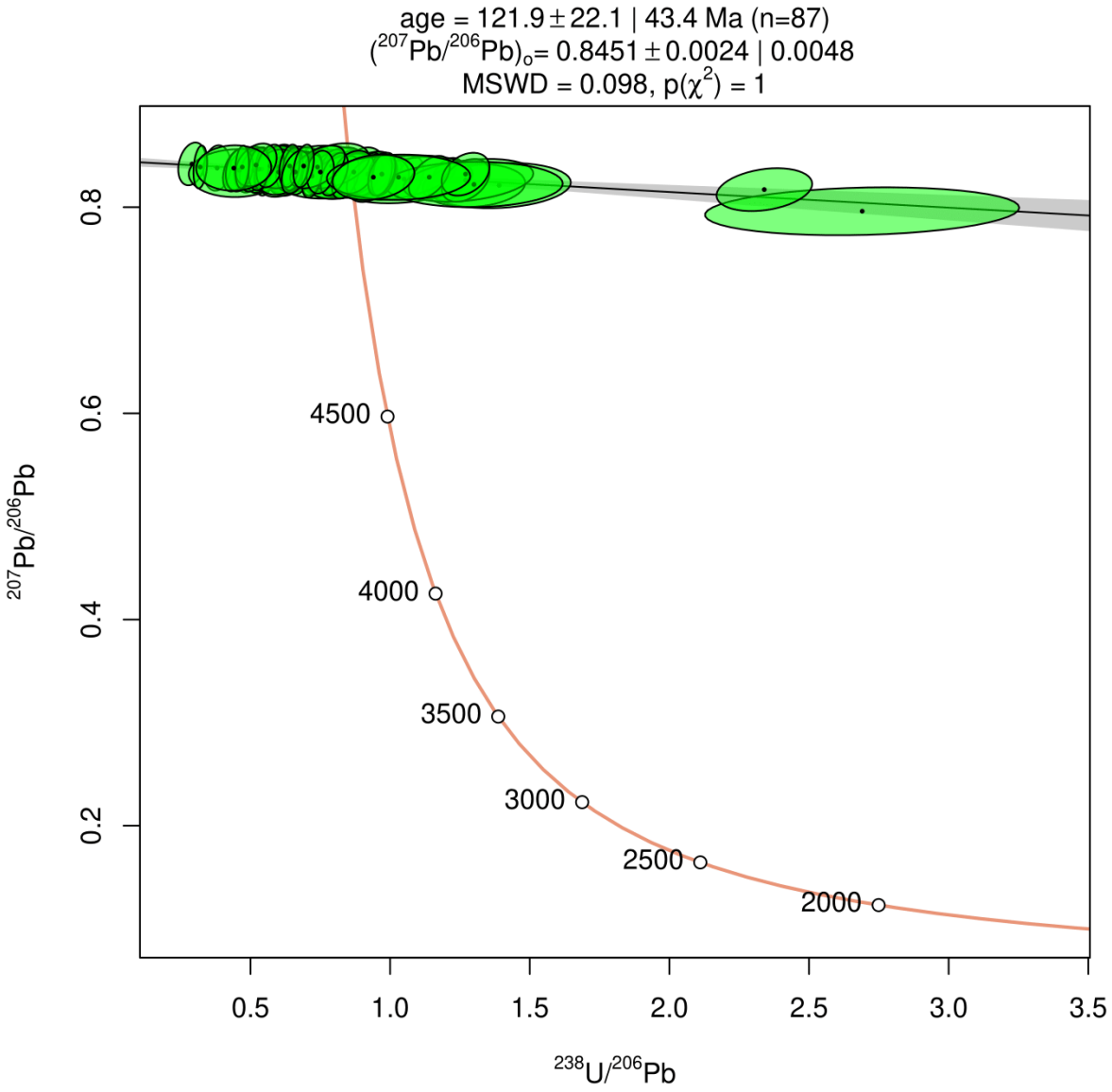

Figure A-9: Apatite C43 Tera-Wasserburg Diagram (UCSB)

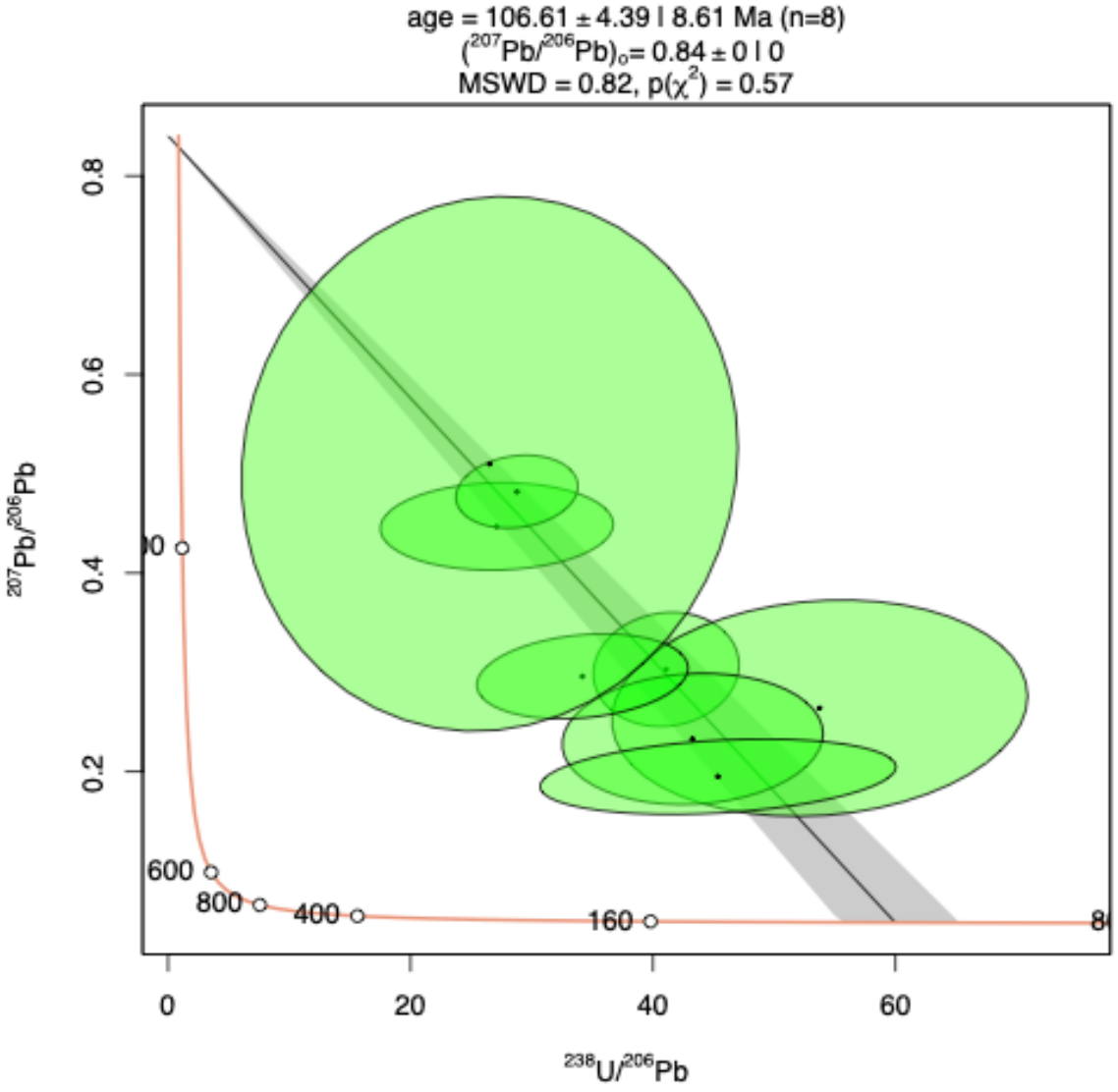

Figure A-10: Apatite C52 in Mushketovite vein Tera-Wasserburg Diagram (UCSB)

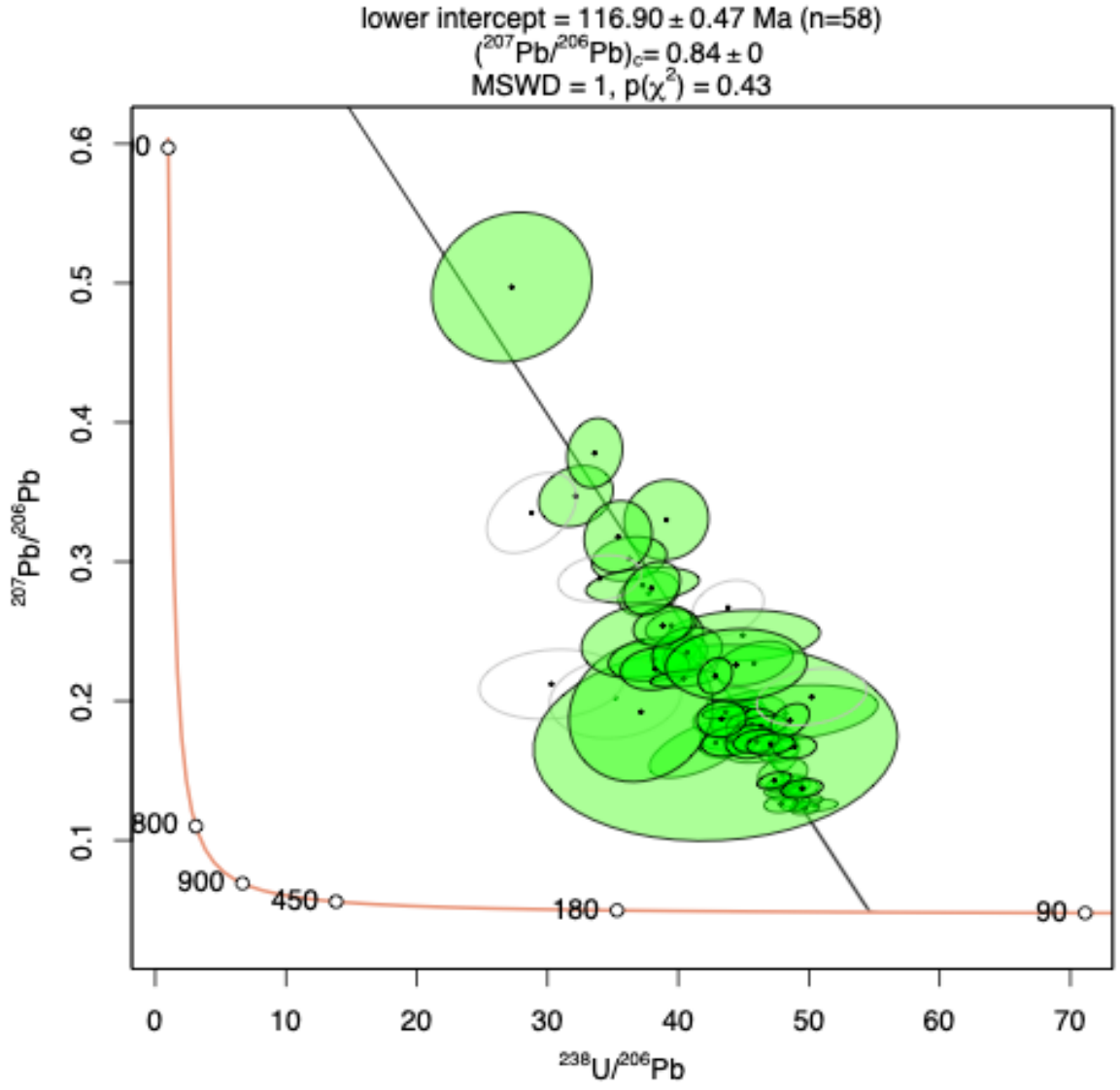

Figure A-11: Apatite C52 in Volcanic Groundmass Tera-Wasserburg Diagram (UCSB)

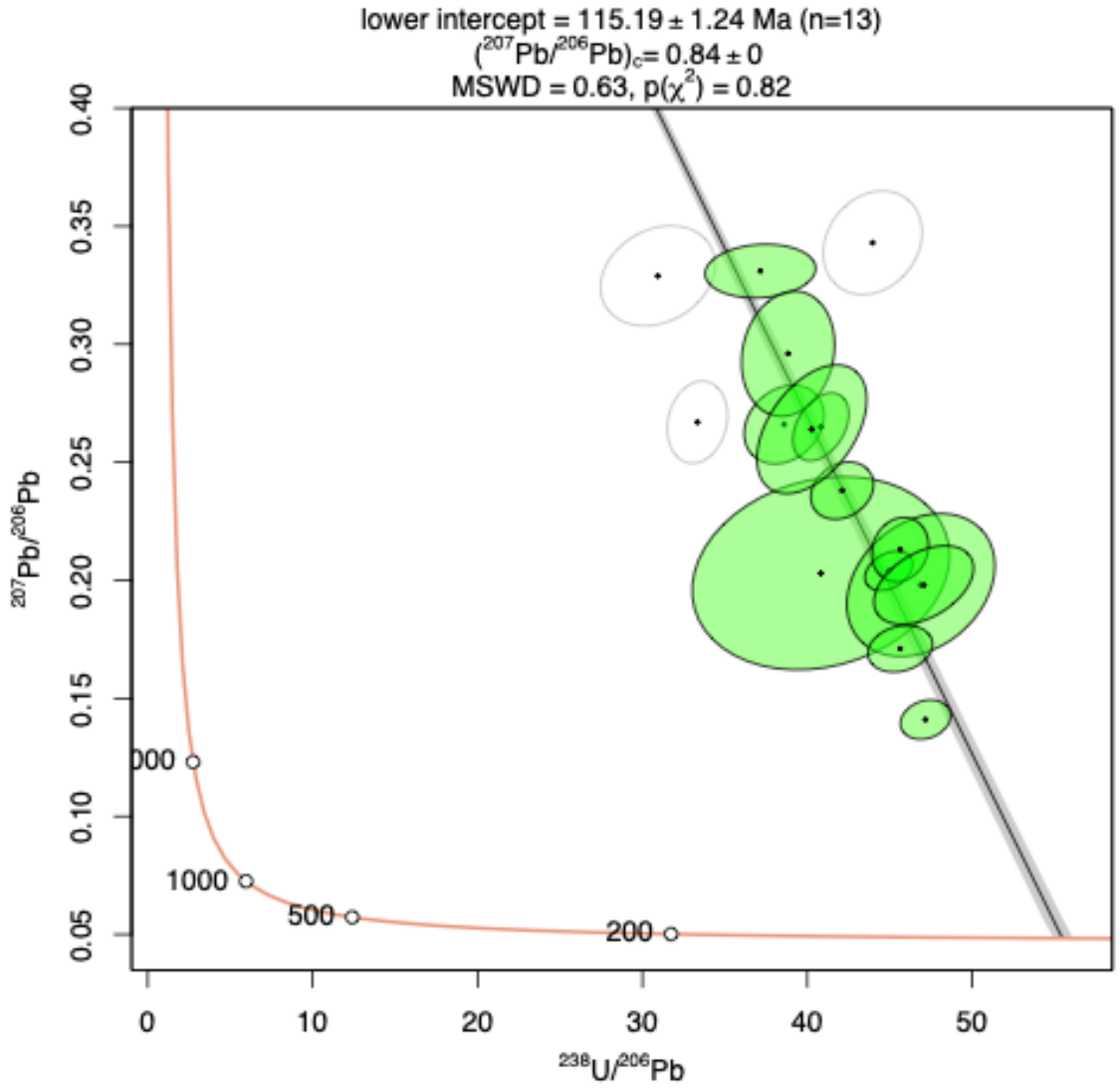

Figure A-12: Apatite C61 Tera-Wasserburg Diagram (UCSB)

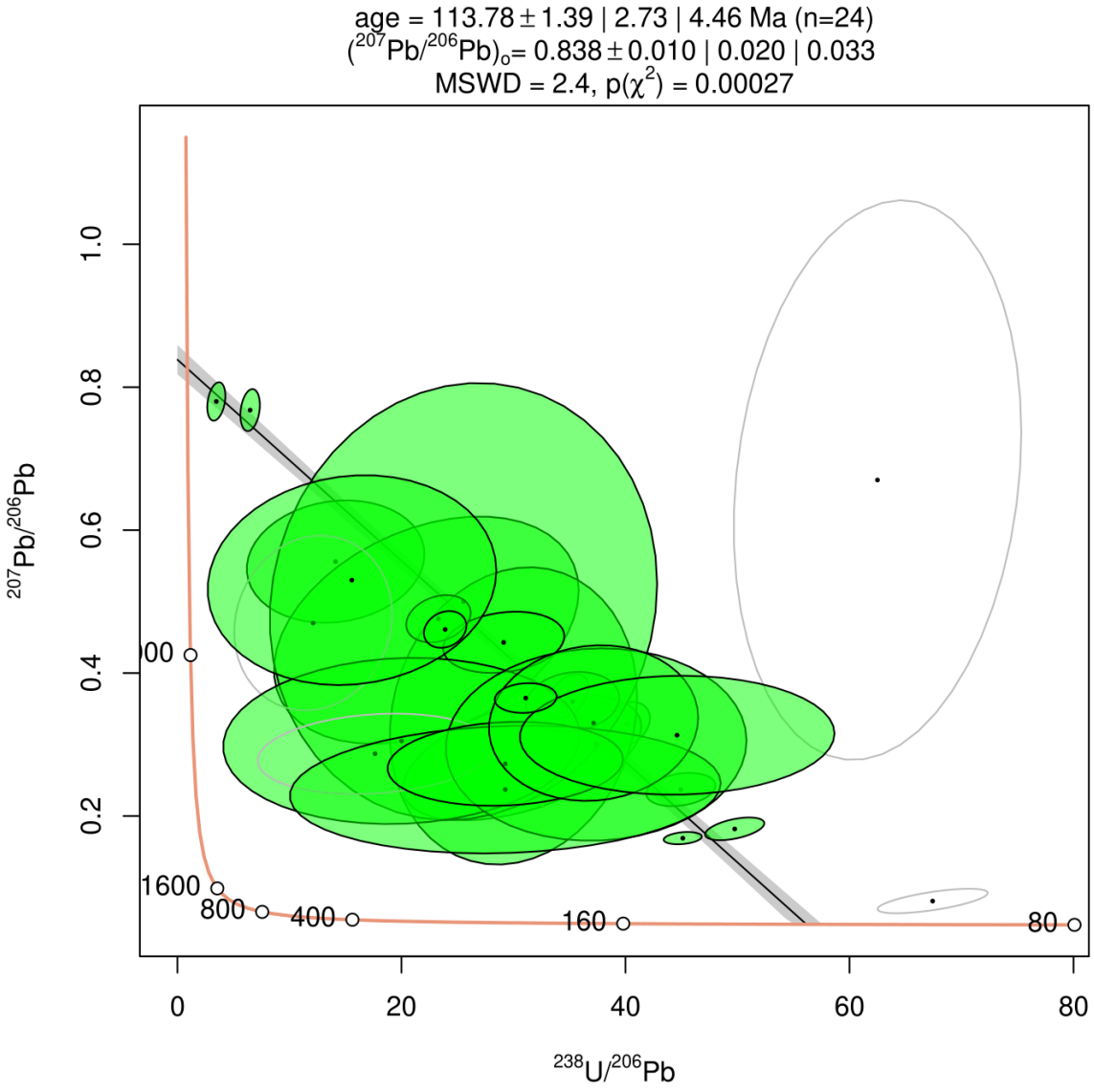

Figure A-13: Apatite C62 Tera-Wasserburg Diagram (UCSB)

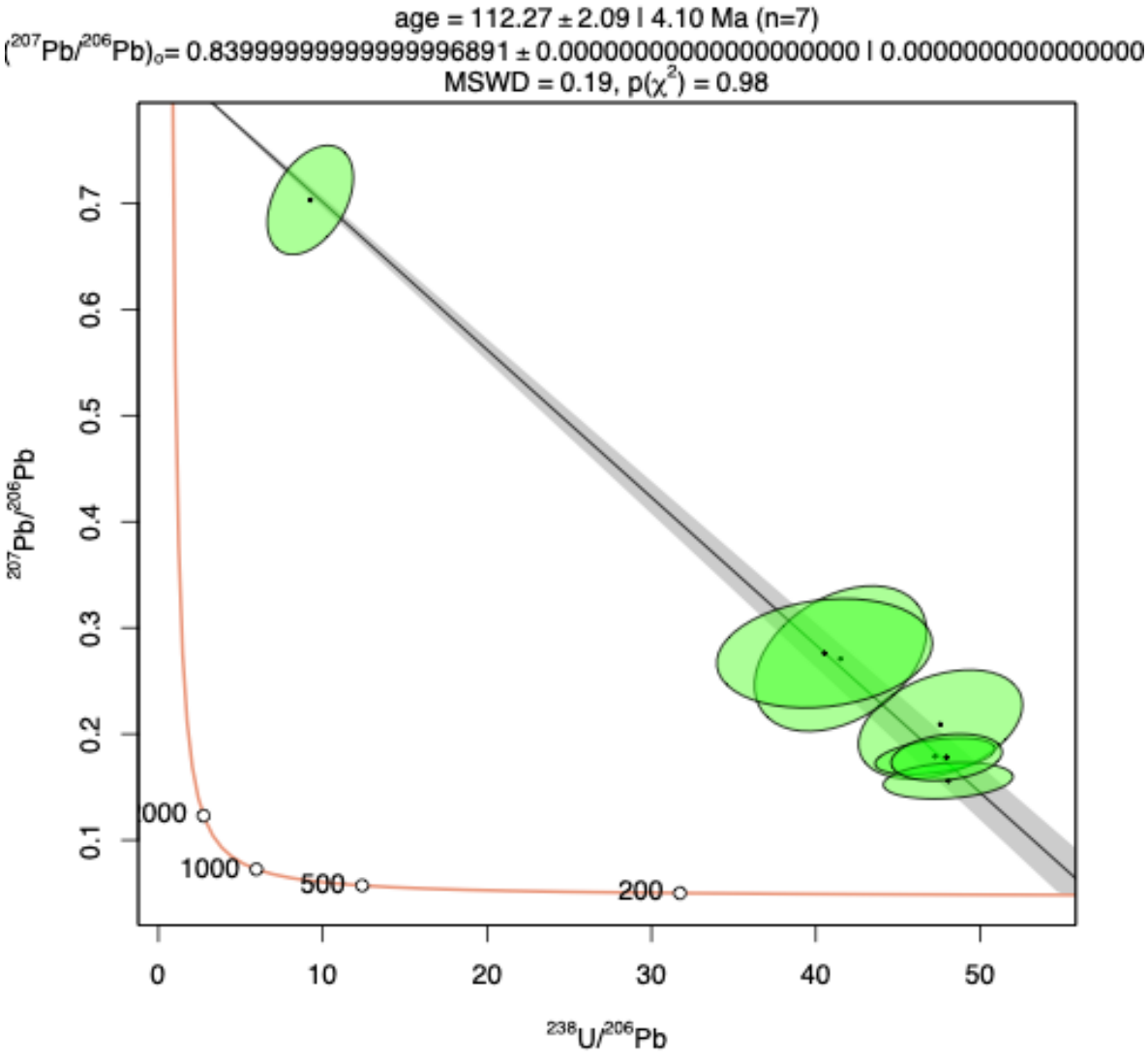

Table A-5: $^{40}Ar/^{39}Ar$ representative air and representative blank

Representative Air or Blank	P	t	40 V	40 V error	39 V	39 V error	38 V	38 V error	37 V	37 V error	36 V	36 V error	Moles 40Ar*	40/36	40/38
air.5.29.20.b.txt	0	0	13.65275	0.00697			0.00886	0.00006			0.0468769	0.0001163	9.29E-14	**291.2**	**1540**
air.5.29.20.c.txt	0	0	13.76888	0.00804			0.00894	0.00005			0.0472995	0.0000973	9.37E-14	**291.1**	**1540**
blank.5.29.20.m.txt	0	0	0.00598	0.000093	0.00022	0.000012	0.00005	0.000005	0.00012	0.000008	0.0000459	0.000004	4.07E-17	130	5.1
blank.5.29.20.n.txt	0	0	0.00563	0.000100	0.00020	0.000028	0.00006	0.000008	0.00011	0.000007	0.0000447	0.000004	3.83E-17	126	3.2

Table A-6: Monitor Data (GA-1550 Biotite, ca. 200 μm diameter flakes provided by M. Cosca of USGS)

Irradiation Filename	P	t	40 V	39 V	38 V	37 V	36 V	Moles 40Ar*	% Rad	R	J ± 1s	% s.d.
au36.1a.bio.4a.txt	2.2	10	4.35175 ± 0.001562	0.32421 ± 0.000326	0.00517 ± 0.000031	0.00086 ± 0.000019	0.000569 ± 0.000008	2.96E-14	96.14%	12.90439	0.00432618 ± 0.000005	0.1%
au36.1a.bio.6a.txt	2.2	10	3.22746 ± 0.002015	0.24206 ± 0.000306	0.00360 ± 0.000013	0.00057 ± 0.000018	0.000331 ± 0.000009	2.20E-14	96.97%	12.92906	0.00431792 ± 0.000007	0.2%
au36.1a.bio.3a.txt	2.2	10	3.51508 ± 0.001262	0.26712 ± 0.000420	0.00410 ± 0.000022	0.00137 ± 0.000015	0.000194 ± 0.000006	2.39E-14	98.37%	12.94486	0.00431265 ± 0.000007	0.2%
au36.1a.bio.7a.txt	2.2	10	2.89165 ± 0.001543	0.19935 ± 0.000417	0.00327 ± 0.000016	0.00088 ± 0.000009	0.001050 ± 0.000016	1.97E-14	89.27%	12.94944	0.00431113 ± 0.000013	0.3%
au36.1a.bio.5a.txt	2.2	10	2.14265 ± 0.000731	0.15813 ± 0.000195	0.00252 ± 0.000024	0.00048 ± 0.000017	0.000241 ± 0.000009	1.46E-14	96.67%	13.09904	0.00426189 ± 0.000008	0.2%
								Mean: 0.0043199±0.0000072 [0.17%] 2σ				
								Wtd by data-pt errs only, 0 of 4 rej.				
								MSWD = 0.95, probability = 0.41				
au36.1e.bio.12a.txt	2.2	10	1.28331 ± 0.000897	0.09313 ± 0.000194	0.00151 ± 0.000014	0.00075 ± 0.000018	0.000246 ± 0.000007	8.73E-15	94.33%	12.99831	0.00429492 ± 0.000012	0.3%

au36.1e.bio.13a.txt	2.2	10	8.38807 ± 0.003961	0.61255 ± 0.000233	0.00946 ± 0.000070	0.00849 ± 0.000083	0.001460 ± 0.000012	5.71E-14	94.85%	12.99050	0.00429750 ± 0.000003	0.1%
au36.1e.bio.14a.txt	2.2	10	7.25783 ± 0.006947	0.52592 ± 0.000787	0.00876 ± 0.000102	0.00642 ± 0.000059	0.001378 ± 0.000014	4.94E-14	94.39%	13.02741	0.00428533 ± 0.000008	0.2%
au36.1e.bio.8a.txt	2.2	10	2.55864 ± 0.001269	0.18925 ± 0.000201	0.00309 ± 0.000030	0.00490 ± 0.000040	0.000335 ± 0.000006	1.74E-14	96.14%	12.99985	0.00429441 ± 0.000006	0.1%
								Mean = 0.0042955±0.0000054 [0.13%] 2σ				
								Wtd by data-pt errs only, 0 of 4 rej.				
								MSWD = 0.61, probability = 0.61				
au36.1i.bio.15a.txt	2.2	10	2.59444 ± 0.001039	0.18945 ± 0.000398	0.00294 ± 0.000021	0.00077 ± 0.000013	0.000488 ± 0.000013	1.77E-14	94.44%	12.93304	0.00431660 ± 0.000012	0.3%
au36.1i.bio.16a.txt	2.2	10	2.77727 ± 0.000421	0.20899 ± 0.000229	0.00330 ± 0.000046	0.00118 ± 0.000012	0.000269 ± 0.000006	1.89E-14	97.14%	12.90888	0.00432467 ± 0.000006	0.1%
au36.1i.bio.17a.txt	2.2	10	2.32549 ± 0.001268	0.16984 ± 0.000273	0.00274 ± 0.000019	0.00110 ± 0.000015	0.000460 ± 0.000014	1.58E-14	94.16%	12.89343	0.00432986 ± 0.000011	0.3%
au36.1i.bio.18a.txt	2.2	10	4.49204 ± 0.003640	0.33214 ± 0.000446	0.00538 ± 0.000042	0.00207 ± 0.000033	0.000740 ± 0.000010	3.06E-14	95.13%	12.86651	0.00433892 ± 0.000008	0.2%
au36.1i.bio.19a.txt	2.2	10	2.42395 ± 0.001378	0.17692 ± 0.000314	0.00286 ± 0.000019	0.00199 ± 0.000022	0.000474 ± 0.000011	1.65E-14	94.23%	12.91056	0.00432411 ± 0.000011	0.2%
								Mean = 0.0043283±0.0000080 [0.19%] 2σ				
								Wtd by data-pt errs only, 0 of 4 rej.				
								MSWD = 1.09, probability = 0.35				
au36.1s.bio.22a.txt	2.2	10	3.25711 ± 0.003851	0.24457 ± 0.000364	0.00385 ± 0.000021	0.00067 ± 0.000018	0.000337 ± 0.000012	2.22E-14	96.94%	12.91005	0.00432428 ± 0.000010	0.2%
au36.1s.bio.20a.txt	2.2	10	8.33497 ± 0.003399	0.63185 ± 0.000527	0.01036 ± 0.000041	0.02805 ± 0.000129	0.000589 ± 0.000015	5.67E-14	97.91%	12.92021	0.00432088 ± 0.000005	0.1%
au36.1s.bio.24a.txt	2.2	10	1.19394 ± 0.001238	0.08991 ± 0.000163	0.00141 ± 0.000012	0.00019 ± 0.000015	0.000080 ± 0.000006	8.12E-15	98.03%	13.01787	0.00428847 ± 0.000011	0.3%

au36.1s.bio.21a.txt	2.2	10	4.45157 ± 0.002837	0.32077 ± 0.000401	0.00496 ± 0.000034	0.00037 ± 0.000013	0.000927 ± 0.000016	3.03E-14	93.85%	13.02416	0.00428640 ± 0.000008	0.2%
au36.1s.bio.23a.txt	2.2	10	2.56169 ± 0.001869	0.17544 ± 0.000493	0.00270 ± 0.000034	0.00014 ± 0.000013	0.000717 ± 0.000006	1.74E-14	91.73%	13.39382	0.00416809 ± 0.000014	0.3%
								Mean = 0.004311±0.000029 [0.67%] 95% conf.				
								Wtd by data-pt errs only, 0 of 4 rej.				
								MSWD = 6.5, probability = 0.000				

Irradiation Filename	P	t	40 V	39 V	38 V	37 V	36 V	Moles 40Ar*	% Rad	R	J ± 1s	% s.d.
au36.1c.act.1a.txt	0.5	30	0.00411 ± 0.000144	0.00002 ± 0.000031	-0.00002 ± 0.000009	-0.00001 ± 0.000168	0.000013 ± 0.000006	2.80E-17	3.9%	6.6790	52.7 ± 2493.5	4732%
au36.1c.act.1b.txt	0.6	30	0.05363 ± 0.000289	0.00010 ± 0.000030	0.00008 ± 0.000010	0.00101 ± 0.000321	0.000150 ± 0.000012	3.65E-16	17.4%	94.6974	634.2 ± 1468.7	232%
au36.1c.act.1c.txt	0.7	30	0.05474 ± 0.000245	0.00028 ± 0.000033	0.00008 ± 0.000010	0.00030 ± 0.000150	0.000134 ± 0.000011	3.72E-16	27.6%	54.7187	392.7 ± 224.8	57%
au36.1c.act.1d.txt	0.8	30	0.03704 ± 0.000242	0.00043 ± 0.000040	0.00005 ± 0.000011	0.00123 ± 0.000156	0.000102 ± 0.000006	2.52E-16	18.7%	16.2809	125.9 ± 88.2	70%
au36.1c.act.1e.txt	0.9	30	0.05044 ± 0.000308	0.00049 ± 0.000035	0.00004 ± 0.000010	0.00071 ± 0.000141	0.000133 ± 0.000009	3.43E-16	22.1%	22.6348	172.8 ± 83.0	48%
au36.1c.act.1f.txt	1	30	0.01505 ± 0.000167	0.00032 ± 0.000043	0.00000 ± 0.000021	0.00036 ± 0.000174	0.000031 ± 0.000008	1.02E-16	38.9%	18.3336	141.2 ± 80.3	57%
au36.1c.act.1g.txt	1.1	30	0.02053 ± 0.000223	0.00045 ± 0.000039	0.00003 ± 0.000008	0.00132 ± 0.000204	0.000042 ± 0.000006	1.40E-16	39.5%	17.9760	138.5 ± 47.3	34%
au36.1c.act.1h.txt	1.2	30	0.04411 ± 0.000279	0.00071 ± 0.000040	0.00002 ± 0.000009	0.00594 ± 0.000246	0.000101 ± 0.000011	3.00E-16	32.1%	20.0234	153.6 ± 48.9	32%
au36.1c.act.1i.txt	1.3	30	0.02369	0.00094	0.00002	0.00754	0.000027	1.61E-	65.9%	16.5581	128.0	20%

			± 0.000216	± 0.000038	± 0.000007	± 0.000273	± 0.000009	16			± 25.7	
au36.1c.act.1j.txt	1.4	30	0.24641 ± 0.000496	0.00948 ± 0.000067	0.00033 ± 0.000011	0.26587 ± 0.002118	0.000313 ± 0.000010	1.68E-15	62.4%	16.2284	125.49 ± 3.46	2.8%
au36.1c.act.1k.txt	1.5	30	0.10000 ± 0.000323	0.00362 ± 0.000037	0.00011 ± 0.000011	0.07261 ± 0.000872	0.000145 ± 0.000009	6.80E-16	57.1%	15.7735	122.09 ± 7.15	5.9%
au36.1c.act.1l.txt	1.6	30	0.44029 ± 0.000749	0.01645 ± 0.000062	0.00065 ± 0.000012	0.51442 ± 0.004886	0.000628 ± 0.000017	3.00E-15	57.9%	15.4873	119.94 ± 3.07	2.6%
au36.1c.act.1m.txt	1.7	30	0.73503 ± 0.000795	0.03889 ± 0.000249	0.00138 ± 0.000043	1.26311 ± 0.007281	0.000367 ± 0.000010	5.00E-15	85.2%	16.1063	124.58 ± 1.58	1.3%
au36.1c.act.1n.txt	1.8	30	0.40567 ± 0.000875	0.02225 ± 0.000087	0.00063 ± 0.000009	0.69014 ± 0.002626	0.000200 ± 0.000005	2.76E-15	85.5%	15.5833	120.66 ± 1.14	0.9%
au36.1c.act.1o.txt	1.9	30	0.31315 ± 0.000449	0.01640 ± 0.000102	0.00051 ± 0.000013	0.46296 ± 0.002118	0.000169 ± 0.000008	2.13E-15	84.0%	16.0395	124.08 ± 2.28	1.8%
au36.1c.act.1p.txt	2	30	0.46928 ± 0.000643	0.02762 ± 0.000077	0.00082 ± 0.000015	0.81579 ± 0.004025	0.000104 ± 0.000003	3.19E-15	93.5%	15.8809	122.89 ± 1.04	0.8%
au36.1c.act.1q.txt	2.2	30	0.30645 ± 0.000336	0.01879 ± 0.000107	0.00045 ± 0.000013	0.49219 ± 0.003413	0.000037 ± 0.000002	2.08E-15	96.5%	15.7337	121.79 ± 1.40	1.2%
au36.1c.act.1r.txt	2.4	30	0.12324 ± 0.000617	0.00775 ± 0.000045	0.00010 ± 0.000004	0.08649 ± 0.000541	0.000010 ± 0.000002	8.38E-16	97.6%	15.5285	120.25 ± 2.27	1.9%
au36.1c.act.1s.txt	2.5	30	0.14019 ± 0.000510	0.00920 ± 0.000067	0.00009 ± 0.000005	0.06072 ± 0.000663	-0.000043 ± 0.000018	9.54E-16	109.0%	15.8265	122.48 ± 2.76	2.3%
au36.1c.act.1t.txt	2.6	30	0.10884 ± 0.000691	0.00709 ± 0.000048	0.00006 ± 0.000005	0.02865 ± 0.000324	-0.000001 -± 0.000001	7.40E-16	100.3%	15.3803	119.14 ± 2.50	2.1%
			Total 39ArK = 0.18128					Age = 120.51 ± 0.54 Ma				
			J = 0.00437 ± 0.000009					(1σ, including J-error of .1%)				
			100% of the 39Ar, steps 1 through 20					MSWD = 0.61, probability = 0.90				

au36.1f.act.2a.txt	0.5	30	0.01136 ± 0.000142	0.00001 ± 0.000032	0.00001 ± 0.000008	0.00020 ± 0.000178	0.000031 ± 0.000008	7.73E-17	19.1%	241.1535	1304 ± 30596	2346%
au36.1f.act.2b.txt	0.6	30	0.07456 ± 0.000389	0.00009 ± 0.000040	0.00008 ± 0.000012	0.00040 ± 0.000153	0.000219 ± 0.000013	5.07E-16	13.2%	106.5756	692 ± 2988	432%
au36.1f.act.2c.txt	0.7	30	0.03059 ± 0.000275	0.00015 ± 0.000030	0.00005 ± 0.000009	0.00017 ± 0.000142	0.000102 ± 0.000006	2.08E-16	1.7%	3.4406	27 ± 468	1739%
au36.1f.act.2d.txt	0.8	30	0.15944 ± 0.000377	0.00025 ± 0.000043	0.00017 ± 0.000012	0.00139 ± 0.000239	0.000531 ± 0.000009	1.08E-15	1.5%	9.7241	75 ± 1229	1637%
au36.1f.act.2e.txt	0.9	30	0.07106 ± 0.000276	0.00036 ± 0.000030	0.00007 ± 0.000007	0.00175 ± 0.000305	0.000229 ± 0.000007	4.83E-16	4.9%	9.6942	75 ± 186	249%
au36.1f.act.2f.txt	1	30	0.03481 ± 0.000283	0.00028 ± 0.000043	0.00004 ± 0.000008	0.00246 ± 0.000368	0.000107 ± 0.000008	2.37E-16	8.8%	10.9106	84 ± 208	247%
au36.1f.act.2g.txt	1.1	30	0.07899 ± 0.000254	0.00242 ± 0.000037	0.00011 ± 0.000007	0.07977 ± 0.001165	0.000151 ± 0.000005	5.37E-16	43.5%	14.2020	109 ± 7	6.8%
au36.1f.act.2h.txt	1.2	30	0.09743 ± 0.000317	0.00117 ± 0.000042	0.00010 ± 0.000008	0.02167 ± 0.000304	0.000275 ± 0.000008	6.63E-16	16.7%	13.8803	106 ± 33	31.4%
au36.1f.act.2i.txt	1.3	30	0.56304 ± 0.000644	0.01391 ± 0.000060	0.00079 ± 0.000013	0.45706 ± 0.001982	0.001144 ± 0.000021	3.83E-15	39.9%	16.1665	123.23 ± 4.05	3.3%
au36.1f.act.2j.txt	1.4	30	0.53577 ± 0.000652	0.02426 ± 0.000097	0.00089 ± 0.000016	0.83084 ± 0.003120	0.000497 ± 0.000006	3.64E-15	72.6%	16.0231	122.18 ± 1.15	0.9%
au36.1f.act.2k.txt	1.5	30	0.33339 ± 0.000668	0.01594 ± 0.000066	0.00055 ± 0.000009	0.56597 ± 0.001853	0.000251 ± 0.000010	2.27E-15	77.7%	16.2630	123.95 ± 2.39	1.9%
au36.1f.act.2l.txt	1.6	30	0.63729 ± 0.000679	0.02881 ± 0.000159	0.00103 ± 0.000013	0.99614 ± 0.002997	0.000605 ± 0.000015	4.34E-15	71.9%	15.9148	121.38 ± 1.97	1.6%
au36.1f.act.2m.txt	1.7	30	0.46093 ± 0.000451	0.02339 ± 0.000139	0.00077 ± 0.000013	0.82501 ± 0.004437	0.000319 ± 0.000005	3.14E-15	79.5%	15.6736	119.60 ± 1.23	1.0%
au36.1f.act.2n.txt	1.8	30	0.37207	0.02111	0.00067	0.73760	0.000113	2.53E-	91.0%	16.0411	122.31	1.1%

			± 0.000331	± 0.000072	± 0.000014	± 0.003667	± 0.000004	15			± 1.35	
au36.1f.act.2o.txt	1.85	30	0.11390 ± 0.000455	0.00591 ± 0.000045	0.00019 ± 0.000010	0.19366 ± 0.001689	0.000076 ± 0.000004	7.75E-16	80.2%	15.4670	118.07 ± 2.76	2.3%
au36.1f.act.2p.txt	2	30	0.08143 ± 0.000273	0.00476 ± 0.000055	0.00014 ± 0.000007	0.15268 ± 0.001200	0.000016 ± 0.000003	5.54E-16	94.1%	16.1054	122.78 ± 5.23	4.3%
au36.1f.act.2q.txt	2.2	30	0.06613 ± 0.000298	0.00378 ± 0.000041	0.00010 ± 0.000008	0.11197 ± 0.001661	0.000032 ± 0.000003	4.50E-16	85.5%	14.9504	114.25 ± 4.16	3.6%
au36.1f.act.2r.txt	2.4	30	0.05460 ± 0.000218	0.00313 ± 0.000034	0.00013 ± 0.000007	0.09605 ± 0.000686	0.000012 ± 0.000003	3.71E-16	93.5%	16.3263	124.41 ± 6.56	5.3%
au36.1f.act.2s.txt	2.6	30	0.04975 ± 0.000210	0.00295 ± 0.000030	0.00011 ± 0.000009	0.09436 ± 0.000740	0.000021 ± 0.000003	3.38E-16	87.8%	14.7869	113.04 ± 4.72	4.2%
au36.1f.act.2t.txt	2.7	30	0.03585 ± 0.000203	0.00200 ± 0.000047	0.00007 ± 0.000009	0.06319 ± 0.000564	0.000018 ± 0.000003	2.44E-16	85.0%	15.2304	116.32 ± 8.16	7.0%
			Total 39ArK = 0.15466					Age = 121.05 ± 0.61 Ma				
			J = 0.0043077 ± 0.000009					(1σ, including J-error of .1%)				
			100% of the 39Ar, steps 1 through 20					MSWD = 0.82, probability = 0.68				
au36.1f.act.3a.txt	0.5	30	0.01131 ± 0.000169	0.00000 ± 0.000031	0.00002 ± 0.000008	0.00006 ± 0.000166	0.000016 ± 0.000009	7.70E-17	57.8%	5824.6750	5970 ± 293430	4915%
au36.1f.act.3b.txt	0.6	30	0.03373 ± 0.000192	0.00005 ± 0.000034	0.00006 ± 0.000012	-0.00007 ± 0.000170	0.000113 ± 0.000008	2.29E-16	1.0%	6.6512	52 ± 5245	10144%
au36.1f.act.3c.txt	0.7	30	0.08527 ± 0.000211	0.00016 ± 0.000033	0.00011 ± 0.000009	0.00054 ± 0.000086	0.000266 ± 0.000007	5.80E-16	8.0%	41.6108	302 ± 1035	343%
au36.1f.act.3d.txt	0.8	30	0.05272 ± 0.000342	0.00022 ± 0.000033	0.00008 ± 0.000008	0.00112 ± 0.000110	0.000139 ± 0.000010	3.59E-16	22.0%	52.5005	373 ± 330	88%
au36.1f.act.3e.txt	0.9	30	0.06398 ± 0.000239	0.00022 ± 0.000042	0.00009 ± 0.000007	0.00108 ± 0.000123	0.000200 ± 0.000007	4.35E-16	7.6%	21.9122	165 ± 553	335%
au36.1f.act.3f.txt	1	30	0.03732	0.00030	0.00004	0.00145	0.000120	2.54E-	4.8%	5.9352	46	356%

			± 0.000227	± 0.000035	± 0.000008	± 0.000116	± 0.000006	16			± 165	
au36.1f.act.3g.txt	1.1	30	0.04519 ± 0.000268	0.00035 ± 0.000036	0.00006 ± 0.000008	0.00276 ± 0.000208	0.000148 ± 0.000008	3.07E-16	3.2%	4.1615	33 ± 157	484%
au36.1f.act.3h.txt	1.2	30	0.05121 ± 0.000258	0.00100 ± 0.000030	0.00006 ± 0.000006	0.02407 ± 0.000317	0.000142 ± 0.000006	3.48E-16	17.9%	9.1724	71 ± 21	30%
au36.1f.act.3i.txt	1.3	30	0.22094 ± 0.000357	0.00642 ± 0.000034	0.00034 ± 0.000009	0.20948 ± 0.001576	0.000401 ± 0.000006	1.50E-15	46.3%	15.9366	121.54 ± 2.95	2.4%
au36.1f.act.3j.txt	1.4	30	0.39720 ± 0.000358	0.01513 ± 0.000058	0.00067 ± 0.000012	0.54082 ± 0.002896	0.000512 ± 0.000007	2.70E-15	61.9%	16.2445	123.81 ± 1.63	1.3%
au36.1f.act.3k.txt	1.5	30	0.49289 ± 0.000612	0.02108 ± 0.000061	0.00080 ± 0.000011	0.73731 ± 0.003959	0.000538 ± 0.000011	3.35E-15	67.7%	15.8374	120.81 ± 1.68	1.4%
au36.1f.act.3l.txt	1.6	30	0.38120 ± 0.000700	0.01930 ± 0.000096	0.00067 ± 0.000009	0.67807 ± 0.003550	0.000244 ± 0.000005	2.59E-15	81.1%	16.0089	122.07 ± 1.39	1.1%
au36.1f.act.3m.txt	1.7	30	0.35039 ± 0.000283	0.01434 ± 0.000104	0.00058 ± 0.000016	0.53015 ± 0.003735	0.000401 ± 0.000006	2.38E-15	66.2%	16.1703	123.26 ± 1.92	1.6%
au36.1f.act.3n.txt	1.8	30	0.58044 ± 0.000463	0.02749 ± 0.000085	0.00096 ± 0.000013	0.99812 ± 0.003976	0.000460 ± 0.000009	3.95E-15	76.6%	16.1651	123.22 ± 1.36	1.1%
au36.1f.act.3o.txt	1.9	30	0.55640 ± 0.000673	0.03137 ± 0.000082	0.00100 ± 0.000014	1.09478 ± 0.003461	0.000196 ± 0.000003	3.79E-15	89.6%	15.8883	121.18 ± 0.76	0.6%
au36.1f.act.3p.txt	2	30	0.24763 ± 0.000280	0.01345 ± 0.000064	0.00041 ± 0.000011	0.46147 ± 0.002130	0.000120 ± 0.000004	1.68E-15	85.6%	15.7647	120.27 ± 1.70	1.4%
au36.1f.act.3q.txt	2.2	30	0.07952 ± 0.000294	0.00393 ± 0.000033	0.00015 ± 0.000011	0.13805 ± 0.000959	0.000065 ± 0.000007	5.41E-16	75.7%	15.3012	116.84 ± 6.20	5.3%
au36.1f.act.3r.txt	2.4	30	0.07555 ± 0.000285	0.00405 ± 0.000037	0.00015 ± 0.000010	0.14160 ± 0.001390	0.000032 ± 0.000004	5.14E-16	87.4%	16.3084	124.28 ± 5.53	4.5%
au36.1f.act.3s.txt	2.5	30	0.03769 ±	0.00207 ±	0.00009 ±	0.07493 ±	0.000019 ±	2.56E-16	85.0%	15.4737	118.12 ± 7.70	6.5%

			0.000223	0.000031	0.000008	0.000822	0.000003					
au36.1f.act.3t.txt	2.6	30	0.01789 ± 0.000243	0.00081 ± 0.000029	0.00004 ± 0.000008	0.02979 ± 0.000393	0.000022 ± 0.000005	1.22E-16	64.2%	14.2455	109.02 ± 18.97	17%
			Total 39ArK = 0.16175					Age = 121.76 ± 0.50 Ma				
			J = 0.0043077 ± 0.000009					(1σ, including J-error of .1%)				
			100% of the 39Ar, steps 1 through 20					MSWD = 0.71, probability = 0.81				
Data summary of all sample sets			7B-52 Actinolite (1st aliquot) (au36.1f.act.2)					Age = 121.05 ± 0.61 Ma				
			7B-52 Actinolite (1st aliquot duplicate) (au36.1f.act.3)					Age = 121.76 ± 0.50 Ma				
			7B-52 Actinolite (2nd aliquot) (au36.1c.act)					Age = 120.51 ± 0.54 Ma				
Average across all samples combined								Mean = 121.15 ± 0.63 [0.52%] 2σ				
								Wtd by data-pt errs only, 0 of 3 rej.				
								MSWD = 1.5, probability = 0.23				

Table A-7: Magnetite sample ID information and associated depth at which the magnetite originated, $^{238}U/^{206}Pb$ ratios and error, $^{207}Pb/^{206}Pb$ ratios and error, rho, the textural relationship of the magnetite within the overall sample, and whether samples fell off the discordia line discordant and therefore omitted from further calculation, data taken at UCSB.

Sample Label	Depth (m)	$^{238}U/^{206}Pb$	2se	$^{207}Pb/^{206}Pb$	2se	rho	Textural Relationship	Omitted point? (x)
C12_49_m1_1	133	8.99	0.62	0.705	0.022	0.52	Undifferentiated	
C12_49_m1_3	133	5.24	0.32	0.762	0.018	0.44	Undifferentiated	
C12_49_m1_4	133	2.24	0.31	0.802	0.018	0.62	Undifferentiated	
C12_49_m1_5	133	8.06	0.67	0.720	0.021	0.45	Undifferentiated	
C12_49_m1_6	133	23.64	2.45	0.467	0.030	0.24	Undifferentiated	
C12_50_m2	133	1.53	0.10	0.816	0.017	0.39	Undifferentiated	
C12_39_m3_1	133	1.00	0.12	0.827	0.018	0.28	Undifferentiated	
C12_39_m3_2	133	7.58	1.21	0.737	0.021	0.59	Undifferentiated	
C12_39_m3_3	133	1.48	0.17	0.820	0.017	0.25	Undifferentiated	
C12_39_m3_4	133	7.35	2.11	0.701	0.041	0.19	Undifferentiated	
C12_33_m4_1	133	1.54	0.19	0.819	0.017	0.22	Undifferentiated	
C12_33_m4_2	133	3.93	0.16	0.781	0.017	0.56	Undifferentiated	
C12_33_m4_3	133	1.19	0.05	0.821	0.017	0.41	Undifferentiated	
C12_33_m4_4	133	2.78	0.11	0.798	0.016	0.60	Undifferentiated	
C12_33_m4_5	133	2.22	0.42	0.806	0.020	0.10	Undifferentiated	
C12_33_m4_6	133	1.65	0.12	0.808	0.018	0.29	Undifferentiated	
C12_33_m4_7	133	2.83	0.46	0.797	0.016	0.12	Undifferentiated	
C12_36_m5_1	133	1.49	0.19	0.823	0.019	0.23	Undifferentiated	
C12_36_m5_2	133	2.36	0.27	0.809	0.018	0.60	Undifferentiated	
C12_36_m5_3	133	2.62	0.15	0.793	0.017	0.28	Undifferentiated	
C12_25_m6_1	133	3.26	0.42	0.804	0.018	0.34	Undifferentiated	
C12_25_m6_2	133	4.46	0.27	0.775	0.017	0.49	Undifferentiated	
C12_25_m6_3	133	3.42	0.22	0.791	0.017	0.44	Undifferentiated	
C12_25_m6_4	133	5.35	0.69	0.762	0.019	0.57	Undifferentiated	
C12_25_m6_5	133	6.06	0.64	0.748	0.021	0.38	Undifferentiated	
C12_25_m6_6	133	7.58	0.65	0.717	0.017	0.35	Undifferentiated	
C34_12_m1_1	486	0.17	0.09	0.835	0.018	0.31	Undifferentiated	
C34_12_m1_2	486	0.12	0.03	0.840	0.018	0.60	Undifferentiated	
C34_12_m2_4	486	0.09	0.02	0.839	0.017	0.43	Undifferentiated	
C34_12_m2_5	486	0.08	0.01	0.840	0.017	0.61	Undifferentiated	
C34_12_m2_6	486	0.14	0.06	0.845	0.017	0.17	Undifferentiated	
C34_12_m2_7	486	0.03	0.02	0.842	0.018	0.61	Undifferentiated	
C34_12_m2_8	486	0.23	0.04	0.836	0.017	0.39	Undifferentiated	
C34_12_m2_9	486	0.16	0.03	0.837	0.017	0.52	Undifferentiated	
C34_12_m2_10	486	0.18	0.03	0.839	0.017	0.36	Undifferentiated	
C34_12_m2_11	486	0.33	0.11	0.838	0.019	0.64	Undifferentiated	
C34_12_m3_1	486	3.16	0.64	0.787	0.021	0.44	Undifferentiated	

C34_12_m3_2	486	0.24	0.04	0.833	0.018	0.50	Undifferentiated	
C34_37_m5_1	486	0.07	0.02	0.842	0.017	0.29	Undifferentiated	
C34_37_m5_2	486	0.01	0.00	0.843	0.017	0.19	Undifferentiated	
C34_37_m5_3	486	0.08	0.02	0.842	0.017	0.70	Undifferentiated	
C34_37_m5_5	486	3.05	0.61	0.808	0.019	0.50	Undifferentiated	
C34_37_m5_6	486	0.59	0.24	0.833	0.019	0.18	Undifferentiated	
C34_37_m5_7	486	0.07	0.04	0.841	0.018	0.30	Undifferentiated	
C34_36_m6_1	486	0.67	0.24	0.823	0.019	0.67	Undifferentiated	
C34_36_m6_2	486	0.15	0.04	0.843	0.017	0.42	Undifferentiated	
C34_36_m6_3	486	0.40	0.05	0.836	0.017	0.66	Undifferentiated	
C34_36_m6_4	486	1.05	0.09	0.834	0.017	0.64	Undifferentiated	
C34_36_m6_5	486	0.34	0.06	0.838	0.017	0.39	Undifferentiated	
C34_32_m7_1	486	0.27	0.05	0.840	0.018	0.36	Undifferentiated	
C34_32_m7_2	486	0.49	0.08	0.841	0.018	0.20	Undifferentiated	
C34_32_m7_4	486	0.35	0.12	0.833	0.018	0.46	Undifferentiated	
C34_32_m7_5	486	0.24	0.14	0.842	0.018	0.31	Undifferentiated	
C34_32_m7_6	486	0.30	0.10	0.837	0.017	0.54	Undifferentiated	
C34_35_m8_1	486	0.10	0.03	0.839	0.018	0.36	Undifferentiated	
C34_35_m8_2	486	1.11	0.28	0.830	0.021	0.37	Undifferentiated	
C34_35_m8_3	486	0.05	0.01	0.842	0.017	0.40	Undifferentiated	
C43_01_m1_1	618	4.44	1.21	0.775	0.045	0.13	Undifferentiated	
C43_01_m1_2	618	3.27	0.82	0.781	0.027	0.44	Undifferentiated	
C43_01_m2_1	618	3.28	0.45	0.815	0.026	0.14	Undifferentiated	
C43_01_m2_2	618	0.91	0.83	0.817	0.047	0.16	Undifferentiated	
C43_01_m2_3	618	3.52	1.03	0.820	0.027	0.23	Undifferentiated	
C43_01_m2_4	618	5.15	0.36	0.759	0.019	0.46	Undifferentiated	
C52_17_m05	731	6.17	0.44	0.731	0.024	0.56	Mag Vein	
C52_24_m11	731	1.32	0.54	0.812	0.026	0.48	Mag Vein	
C52_24_m15	731	8.70	1.75	0.676	0.026	0.41	Mag Vein	
C52_17_m08	731	4.31	0.79	0.774	0.026	0.53	Mag Vein	
C52_24_m18	731	20.41	3.07	0.511	0.027	0.27	Mag Vein	
C52_24_m17	731	14.71	2.61	0.655	0.027	0.48	Mag Vein	
C52_24_m20	731	12.99	2.38	0.598	0.028	0.49	Mag Vein	
C52_17_m09	731	8.62	2.16	0.683	0.032	0.34	Mag Vein	
C52_17_m07	731	6.90	1.15	0.743	0.034	0.33	Mag Vein	
C52_24_m12	731	12.17	1.17	0.652	0.035	0.52	Mag Vein	
C52_24_m16	731	24.57	2.52	0.462	0.036	0.16	Mag Vein	
C52_17_m01	731	19.57	3.74	0.563	0.037	0.30	Mag Vein	
C52_24_m14	731	9.09	3.97	0.679	0.053	0.35	Mag Vein	
C52_24_m13	731	12.50	2.82	0.626	0.054	0.24	Mag Vein	
C52_24_m19	731	20.83	4.79	0.574	0.055	0.18	Mag Vein	
C52_17_06	731	8.93	4.71	0.760	0.111	0.15	Mag Vein	
C58_10_m11	817	4.24	0.67	0.763	0.021	0.17	Undifferentiated	
C58_03_m03	817	34.01	1.76	0.308	0.023	0.52	Undifferentiated	
C58_31_m17	817	35.34	4.18	0.243	0.027	0.54	Undifferentiated	

C58_31_m20	817	0.81	0.61	0.820	0.028	0.11	Undifferentiated	
C58_03_m04	817	2.94	0.55	0.756	0.034	0.03	Undifferentiated	
C58_31_m18	817	8.47	2.09	0.713	0.040	0.29	Undifferentiated	
C58_26_m14	817	7.69	0.84	0.722	0.041	0.33	Undifferentiated	
C58_26_m15	817	3.70	2.47	0.825	0.045	0.11	Undifferentiated	
C58_31_m16	817	24.51	4.11	0.426	0.068	0.52	Undifferentiated	
C61_17_m06	840	0.29	0.13	0.830	0.018	0.15	Vein 1	
C61_17_m07	840	0.82	0.35	0.823	0.019	0.45	Vein 1	
C61_05_m03	840	2.47	0.20	0.790	0.020	0.41	Vein 3	
C61_18_m20	840	2.28	0.26	0.801	0.020	0.58	Vein 1	
C61_17_m11	840	0.38	0.30	0.831	0.021	0.35	Vein 1	
C61_17_m08	840	6.71	0.40	0.734	0.022	0.35	Vein 1	
C61_18_m16	840	5.88	0.63	0.736	0.022	0.64	Vein 1	
C61_17_m13	840	2.47	0.36	0.792	0.023	0.35	Vein 1	
C61_18_m19	840	2.70	0.54	0.799	0.023	0.58	Vein 1	
C61_17_m10	840	0.16	0.26	0.819	0.024	0.34	Vein 1	
C61_05_m02	840	12.33	1.35	0.637	0.025	0.50	Vein 3	
C61_18_m15	840	6.25	0.64	0.743	0.026	0.27	Vein 1	
C61_18_m18	840	12.35	1.85	0.638	0.026	0.40	Vein 1	
C61_17_m09	840	3.34	0.76	0.775	0.029	0.64	Vein 1	
C61_14_m04	840	9.71	1.71	0.686	0.030	0.28	Vein 3	
C61_17_m12	840	1.19	0.65	0.798	0.036	0.20	Vein 1	
C61_14_m05	840	6.37	1.43	0.715	0.039	0.29	Vein 3	
C61_18_m14	840	0.82	0.65	0.809	0.046	0.32	Vein 1	
C61_18_m17	840	6.54	0.70	0.770	0.076	0.31	Vein 1	
C61_01_m01	840	0.26	0.26	0.820	0.820	0.25	Vein 3	
C62_01_m1_1	871	11.63	5.95	0.690	0.101	0.09	Magnetite Breccia	
C62_01_m1_2	871	3.23	1.25	0.807	0.042	0.42	Magnetite Breccia	
C62_01_m1_3	871	0.70	0.26	0.834	0.018	0.42	Magnetite Breccia	
C62_01_m1_4	871	1.22	0.58	0.820	0.027	0.47	Magnetite Breccia	
C62_03_m2_1	871	2.08	0.65	0.797	0.026	0.52	Magnetite Breccia	
C62_03_m2_2	871	1.82	0.40	0.788	0.031	0.36	Magnetite Breccia	
C62_03_m2_3	871	4.02	0.78	0.771	0.027	0.28	Magnetite Breccia	
C62_03_m2_5	871	0.71	0.71	0.814	0.030	0.22	Magnetite Breccia	
C62_03_m2_6	871	2.04	1.29	0.840	0.067	0.45	Magnetite Breccia	
C62_03_m2_11	871	5.05	0.77	0.766	0.018	0.39	Magnetite	

							Breccia	
C62_03_m2_12	871	4.39	0.95	0.783	0.031	0.21	Magnetite Breccia	
C62_03_m2_13	871	0.30	0.23	0.832	0.022	0.14	Magnetite Breccia	
C62_03_m2_14	871	1.47	1.21	0.755	0.035	0.57	Magnetite Breccia	x
C62_03_m2_15	871	0.22	0.13	0.798	0.020	0.13	Magnetite Breccia	
C62_03_m2_16	871	1.75	0.59	0.808	0.023	0.50	Magnetite Breccia	

Figure A-14: Magnetite C12 Tera-Wasserburg Diagram (UCSB)

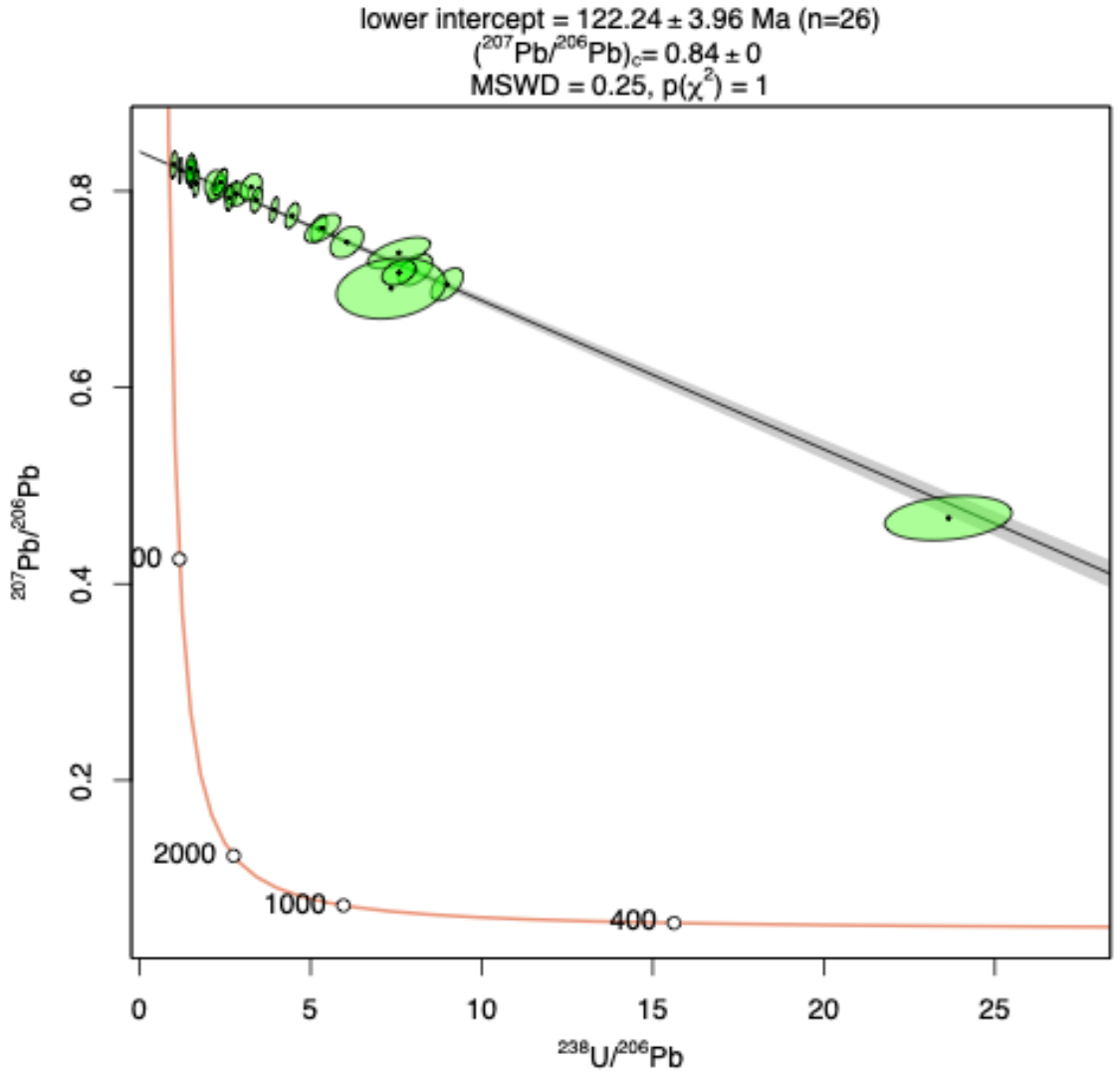

Figure A-15: Magnetite C34 (Low U) Tera-Wasserburg Diagram (UCSB)

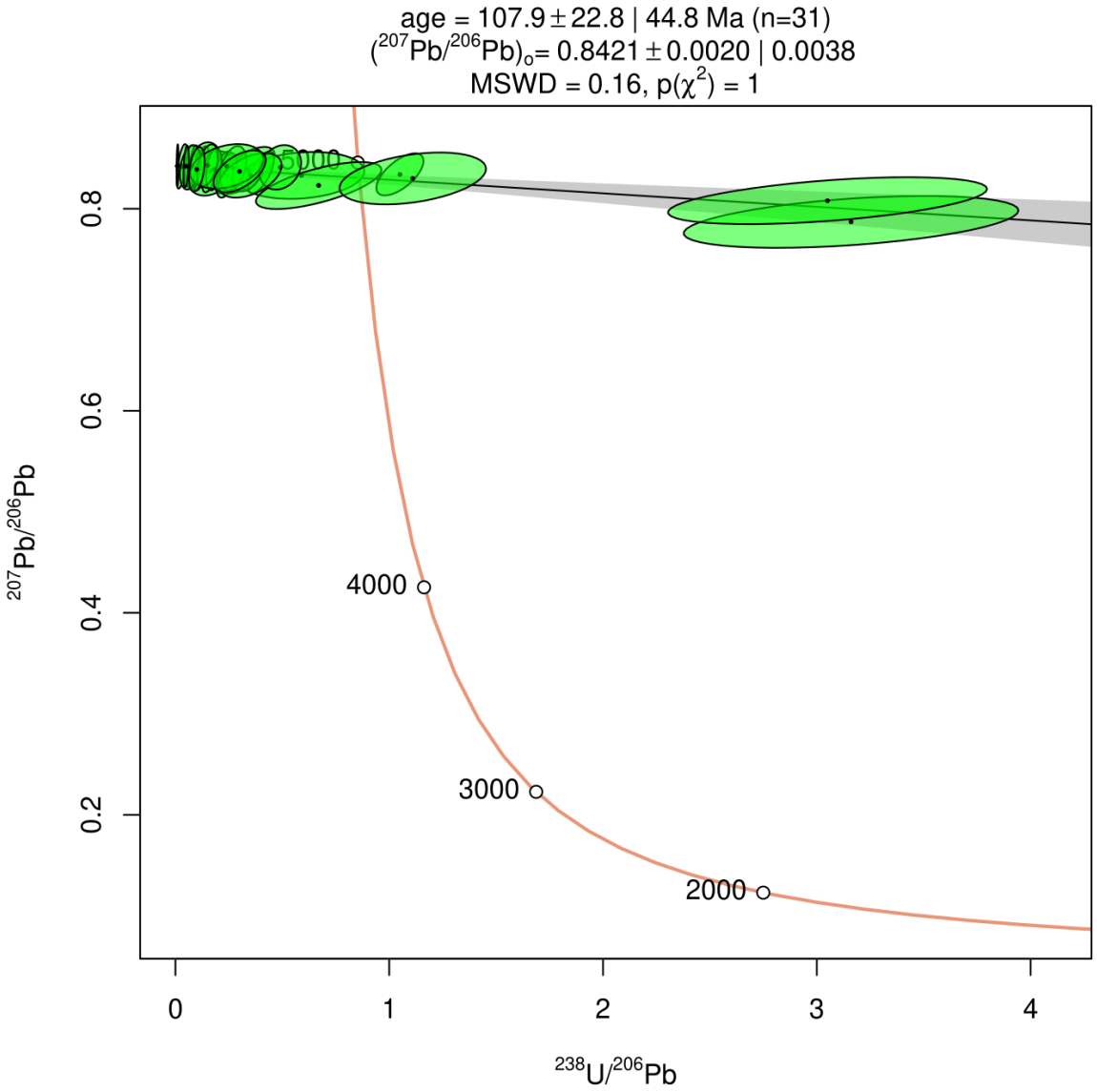

Figure A-16: Magnetite C43 Tera-Wasserburg Diagram (UCSB)

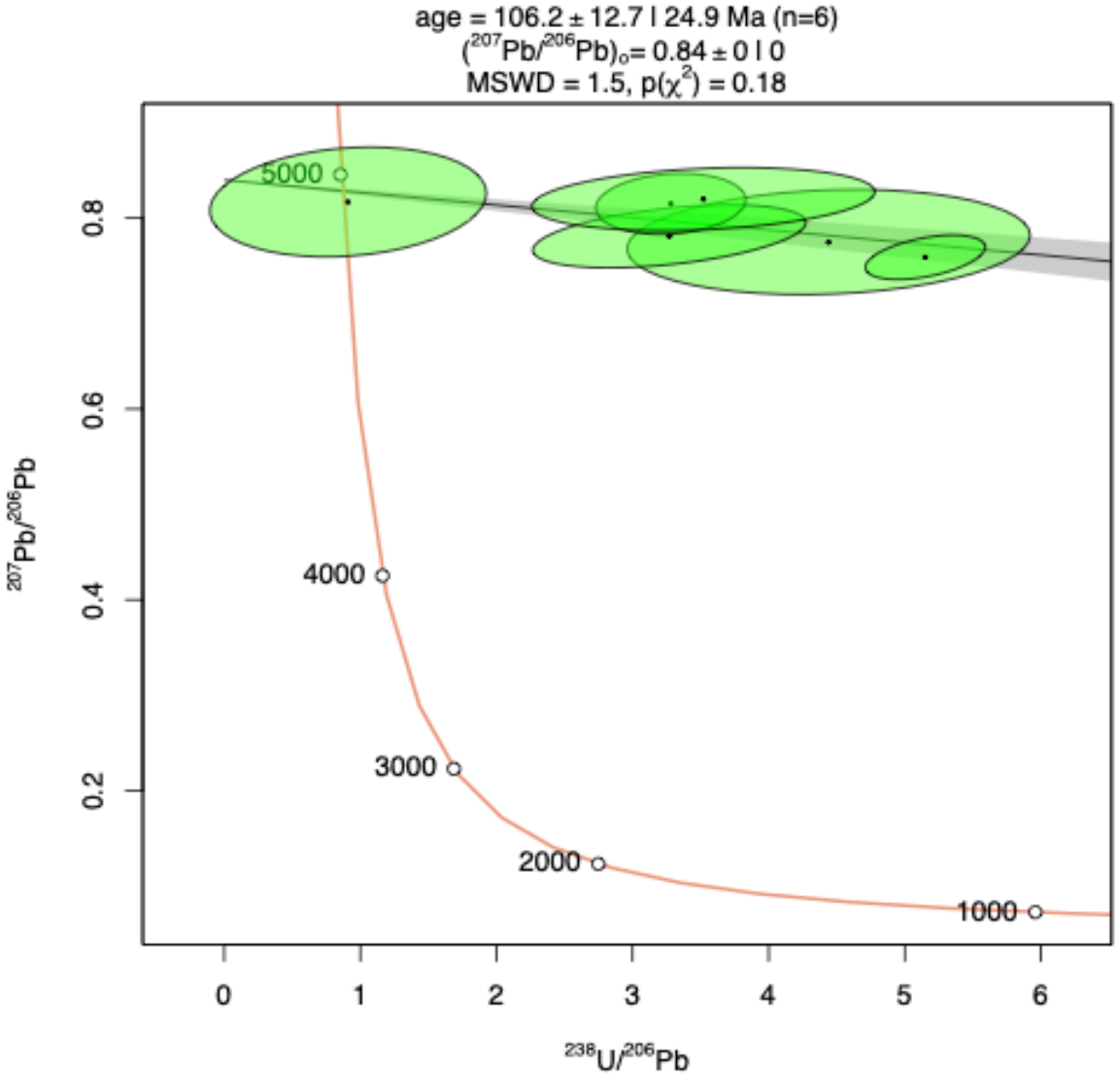

Figure A-17: Magnetite C52 Tera-Wasserburg Diagram (UCSB)

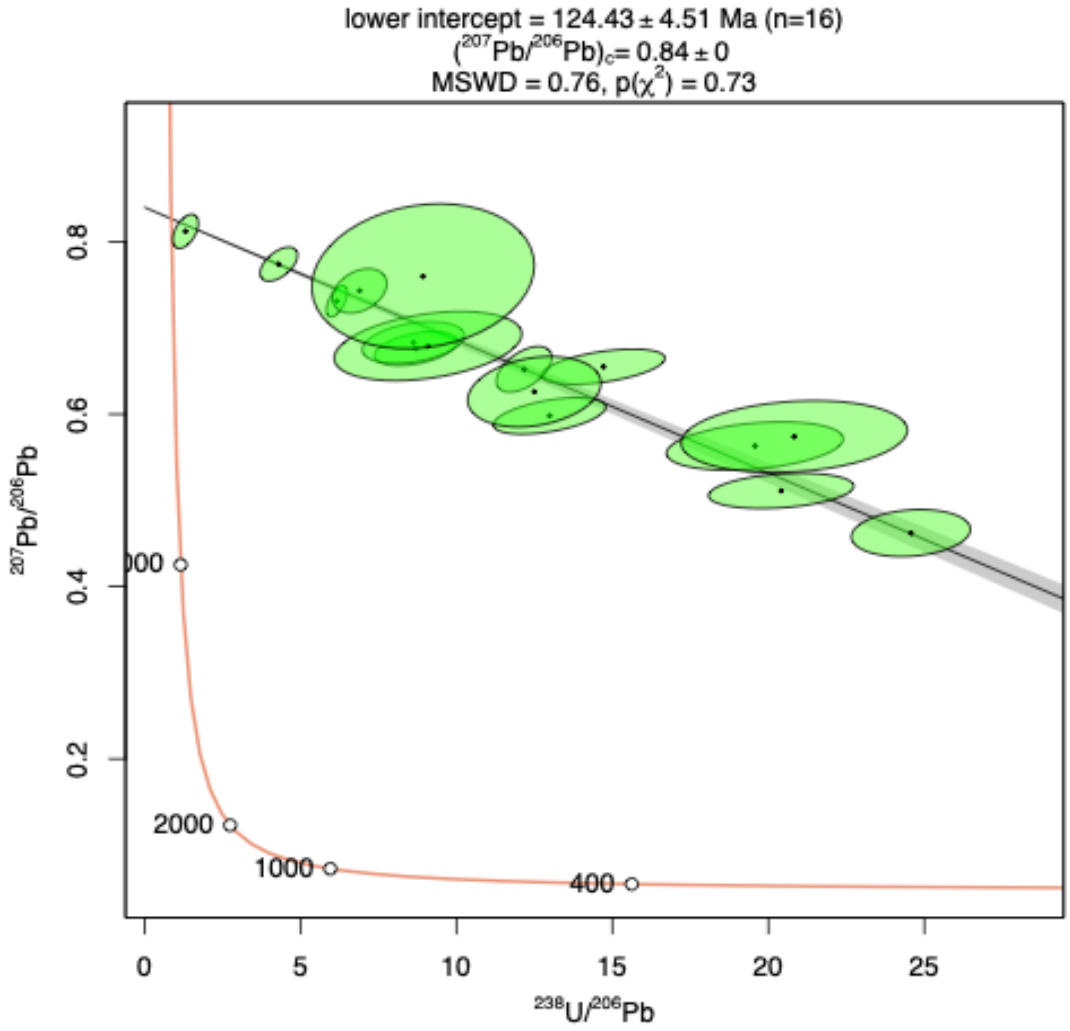

Figure A-18: Magnetite C58 Groundmass Tera-Wasserburg Diagram (UCSB)

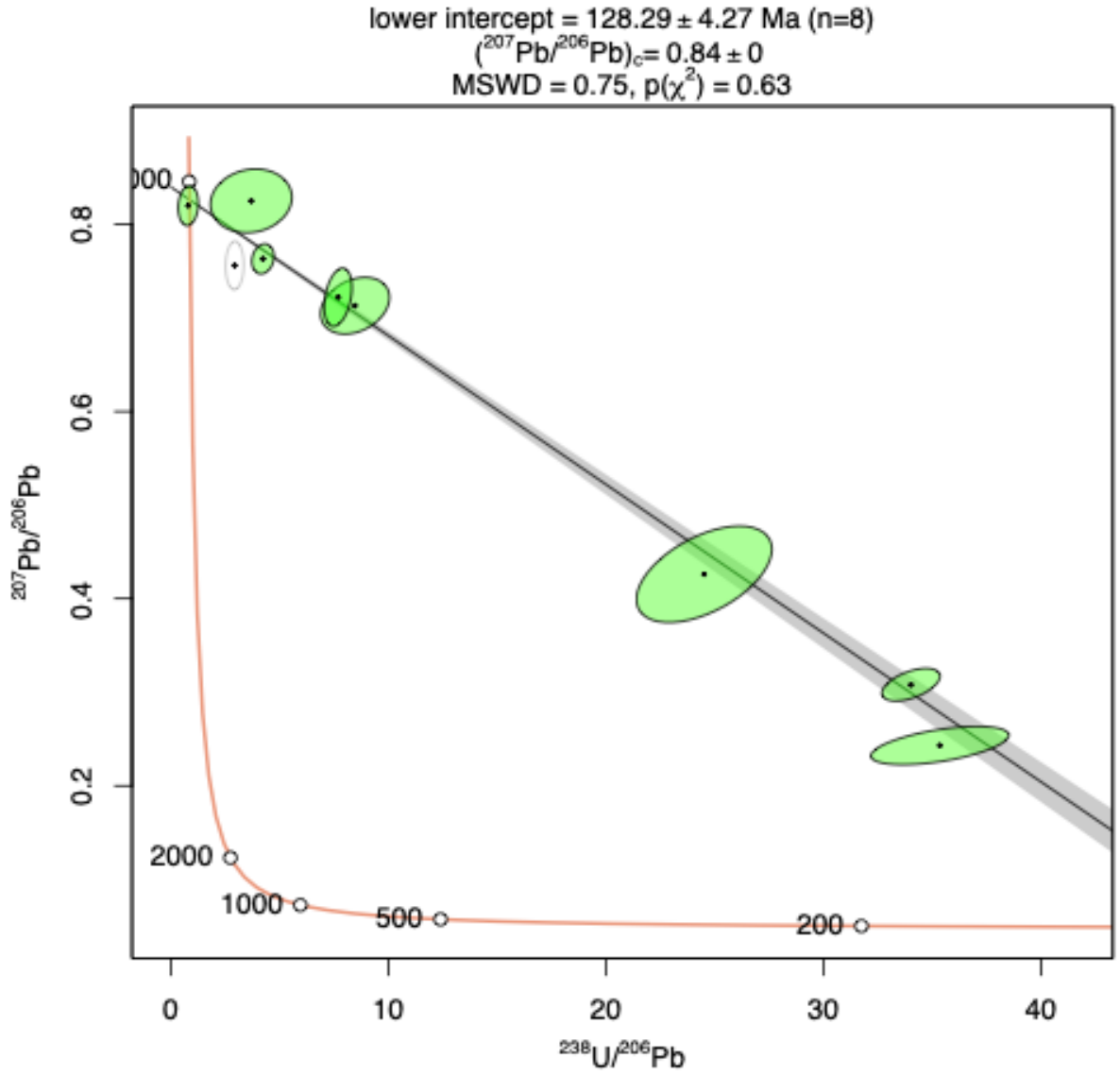

Figure A-19: Magnetite C61 Tera-Wasserburg Diagram (UCSB)

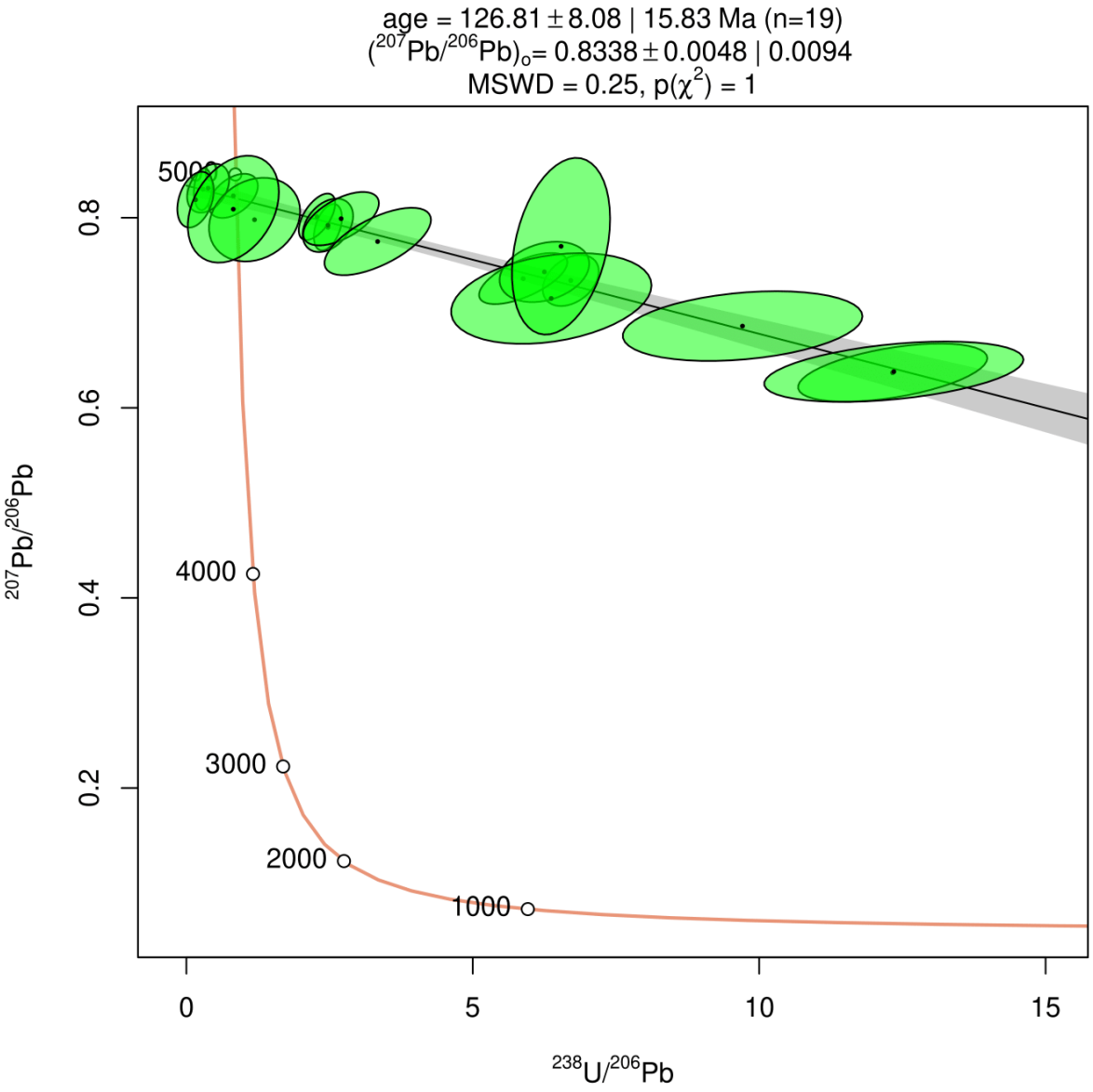

Figure A-20: Magnetite C62 Tera-Wasserburg Diagram (UCSB)

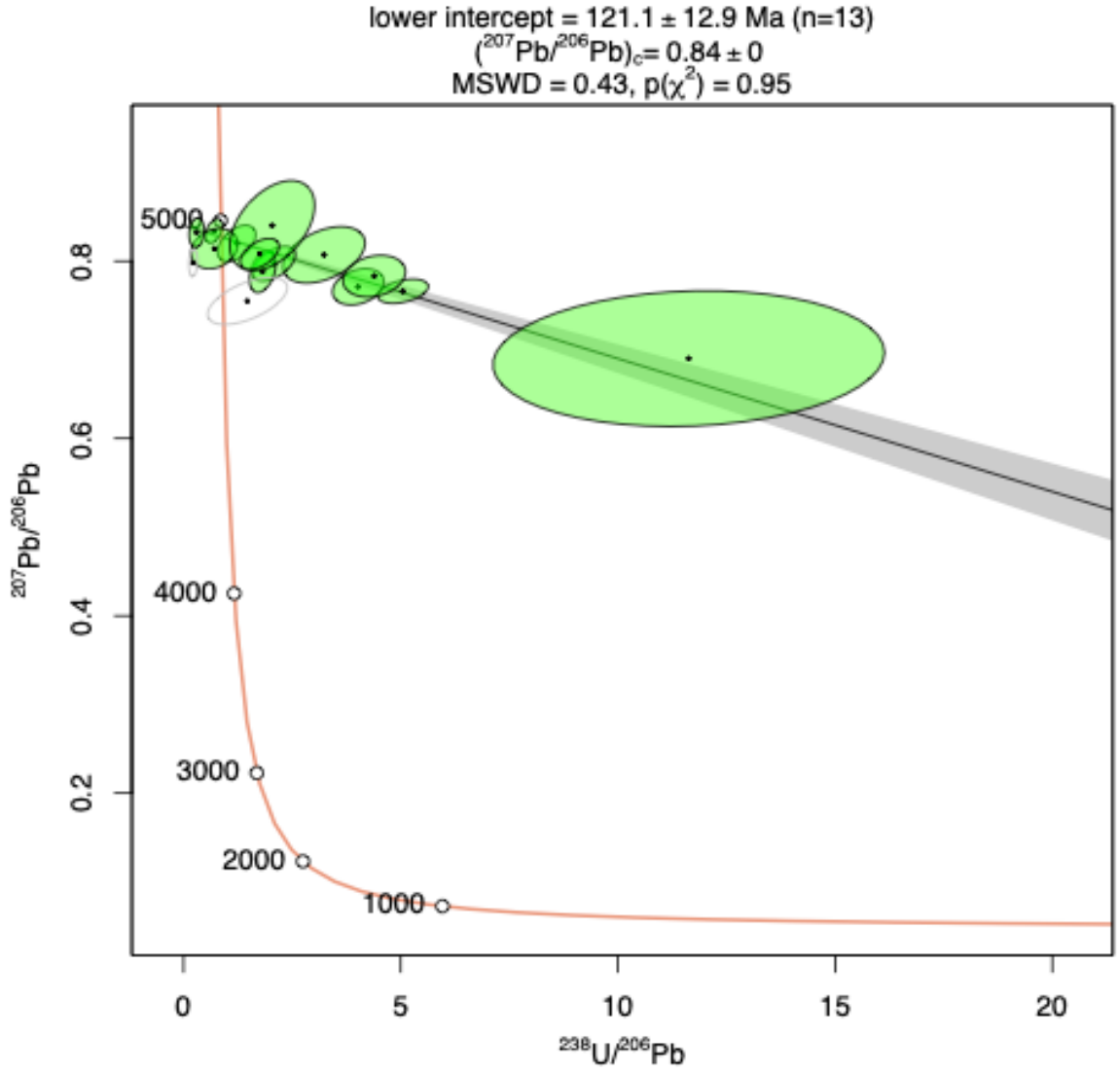

Table A-8: Magnetite sample ID information and associated depth at which the magnetite originated, $^{238}U/^{206}Pb$ ratios and error, $^{207}Pb/^{206}Pb$ ratios and error, rho, the textural relationship of the magnetite within the overall sample and whether samples fell off the discordia line and therefore omitted from further calculation, data taken at UCSB.

Sample Label	Depth (m)	$^{238}U/^{206}Pb$	2se	$^{207}Pb/^{206}Pb$	2se	rho	Textural Relationship	Omitted point? (x)
C34_Mag_Rim-1	486	1.5826	0.3823	0.7916	0.0273	0.4503	Magnetite Breccia	
C34_Mag_Core-2	486	0.0986	0.0493	0.8474	0.0172	0.4876	Magnetite Breccia	
C34_Mag_Rim-3	486	1.9133	0.4727	0.8139	0.0311	0.4251	Magnetite Breccia	
C34_Mag_Core-3	486	0.5962	0.1668	0.8290	0.0174	0.3083	Magnetite Breccia	
C34_Mag_Rim-4	486	0.7699	0.1143	0.8406	0.0177	0.6159	Magnetite Breccia	
C34_Mag_Rim-5	486	14.6506	2.9447	0.5595	0.0377	0.1722	Magnetite Breccia	
C34_Mag_Core-4	486	0.0610	0.0175	0.8445	0.0172	0.1434	Magnetite Breccia	
C34_Mag_Core-5	486	0.0817	0.0248	0.8411	0.0170	0.5467	Magnetite Breccia	
C34_Mag_Rim-6	486	0.4578	0.0985	0.8372	0.0198	0.3828	Magnetite Breccia	
C34_Mag_Rim-7	486	0.2817	0.0499	0.8271	0.0179	0.4435	Magnetite Breccia	
C34_Mag_Core-6	486	0.0625	0.0168	0.8423	0.0171	0.3676	Magnetite Breccia	
C34_Mag_Core-7	486	0.1654	0.0609	0.8382	0.0187	0.1587	Magnetite Breccia	
C34_Mag_Rim-9	486	1.1981	0.1807	0.8244	0.0187	0.6431	Magnetite Breccia	
C34_Mag_Rim-11	486	2.0844	1.0515	0.7503	0.0390	0.2580	Magnetite Breccia	
C34_Mag_Core-11	486	0.0541	0.0081	0.8609	0.0177	0.5332	Magnetite Breccia	
C34_Mag_Core-12	486	0.1349	0.0853	0.8495	0.0176	0.6186	Magnetite Breccia	
C34_Mag_Core-14	486	0.0466	0.0153	0.8461	0.0171	0.6225	Magnetite Breccia	
C34_Mag_Rim-16	486	0.4662	0.4578	0.8086	0.0258	0.1147	Magnetite Breccia	
C34_Mag_Core-15	486	0.0722	0.0091	0.8496	0.0171	0.4542	Magnetite Breccia	
C34_Mag_	486	0.8379	0.1842	0.8087	0.0186	0.5153	Magnetite	

Rim-17							Breccia	
C34_Mag_ Core-16	486	0.9461	0.1825	0.8271	0.0170	0.2289	Magnetite Breccia	
C34_Mag_ Rim-18	486	4.0696	0.6511	0.7669	0.0180	0.5914	Magnetite Breccia	
C34_Mag_ Core-17	486	0.1592	0.0466	0.8431	0.0177	0.1622	Magnetite Breccia	
C34_Mag_ Rim-19	486	0.1942	0.0239	0.8409	0.0174	0.6472	Magnetite Breccia	
C34_Mag_ Core-18	486	0.0741	0.0053	0.8570	0.0176	0.6046	Magnetite Breccia	
C34_Mag_ Rim-20	486	0.8841	0.1716	0.8282	0.0182	0.6679	Magnetite Breccia	
C34_Mag_ Core-19	486	0.0759	0.0056	0.8594	0.0173	0.6052	Magnetite Breccia	
C34_Mag_ Core-20	486	0.0200	0.0049	0.8767	0.0182	0.5493	Magnetite Breccia	
C34_Mag_ Core-21	486	0.0099	0.0038	0.8459	0.0179	0.4317	Magnetite Breccia	
C34_Mag_ Rim-22	486	0.4273	0.0717	0.8196	0.0181	0.4861	Magnetite Breccia	
C34_Mag_ Core-22	486	0.3016	0.0818	0.8300	0.0170	0.2961	Magnetite Breccia	
C34_Mag_ Rim-23	486	0.5232	0.1179	0.8297	0.0209	0.4183	Magnetite Breccia	
C34_Mag_ Core-23	486	0.0583	0.0173	0.8428	0.0171	0.4315	Magnetite Breccia	
C34_Mag_ Rim-24	486	1.3494	0.7817	0.7948	0.0655	0.0596	Magnetite Breccia	
C34_Mag_ Rim-25	486	1.6435	0.4332	0.8011	0.0233	0.3354	Magnetite Breccia	
C34_Mag_ Core-24	486	0.2084	0.0764	0.8676	0.0196	0.3626	Magnetite Breccia	
C34_Mag_ Core-25	486	0.0122	0.0033	0.8673	0.0176	0.1763	Magnetite Breccia	
C34_Mag_ Rim-27	486	0.6855	0.1017	0.8287	0.0203	0.3432	Magnetite Breccia	
C34_Mag_ Core-26	486	0.0325	0.0042	0.8512	0.0171	0.4960	Magnetite Breccia	
C34_Mag_ Core-27	486	0.1831	0.1439	0.8611	0.0174	0.5056	Magnetite Breccia	
C34_Mag_ Core-28	486	0.0777	0.0330	0.8619	0.0180	0.4807	Magnetite Breccia	
C34_Mag_ Core-29	486	0.3827	0.1202	0.8428	0.0182	0.2255	Magnetite Breccia	
C34_Mag_	486	14.087	4.8072	0.6581	0.0847	0.4140	Magnetite	

Rim-30		1					Breccia	
C43_Mag-1	618	1.1761	0.2439	0.8117	0.0194	0.4113	Undifferentiated	
C43_Mag-2	618	0.6410	0.1927	0.8160	0.0201	0.6666	Undifferentiated	
C43_Mag-3	618	1.2209	0.6981	0.8117	0.0250	0.6598	Undifferentiated	
C43_Mag-4	618	3.8266	0.7464	0.7640	0.0270	0.4993	Undifferentiated	
C43_Mag-5	618	0.4662	0.2206	0.8255	0.0208	0.6615	Undifferentiated	
C43_Mag-6	618	3.0522	0.4043	0.8086	0.0258	0.4858	Undifferentiated	
C43_Mag-7	618	5.9486	0.7820	0.7280	0.0208	0.3938	Undifferentiated	
C43_Mag-8	618	10.7725	1.8682	0.6655	0.0444	0.4786	Undifferentiated	
C43_Mag-9	618	6.5740	1.6908	0.7492	0.0314	0.5627	Undifferentiated	
C43_Mag-10	618	6.3777	0.8348	0.7810	0.0326	0.4466	Undifferentiated	
C43_Mag-11	618	4.8374	1.2815	0.7429	0.0520	0.2068	Undifferentiated	
C43_Mag-12	618	1.4906	0.1844	0.8241	0.0181	0.5889	Undifferentiated	
C43_Mag-13	618	5.3976	0.6454	0.7397	0.0233	0.5429	Undifferentiated	
C43_Mag-14	618	15.3524	1.1451	0.5680	0.0231	0.4444	Undifferentiated	
C43_Mag-15	618	0.1756	0.1167	0.8357	0.0196	0.4285	Undifferentiated	
C43_Mag-16	618	2.1545	1.1957	0.6888	0.0476	0.1519	Undifferentiated	
C43_Mag-17	618	5.9624	1.5299	0.7376	0.0419	0.2309	Undifferentiated	
C43_Mag-18	618	29.1346	4.0154	0.3274	0.0492	0.3884	Undifferentiated	
C43_Mag-19	618	1.2692	0.3027	0.8315	0.0194	0.3379	Undifferentiated	
C43_Mag-20	618	4.4128	0.6441	0.7715	0.0271	0.3678	Undifferentiated	
C43_Mag-21	618	0.6442	0.1608	0.8353	0.0181	0.6530	Undifferentiated	
C43_Mag-23	618	12.6298	1.0874	0.6316	0.0172	0.6290	Undifferentiated	
C43_Mag-	618	4.8835	0.7505	0.7609	0.0236	0.5590	Undifferentia	

24							ted	
C43_Mag-25	618	11.4971	1.2079	0.6305	0.0265	0.5063	Undifferentiated	
C43_Mag-26	618	11.6011	1.2810	0.6379	0.0247	0.5864	Undifferentiated	
C43_Mag-27	618	2.9812	0.3860	0.7831	0.0195	0.6265	Undifferentiated	
C43_Mag-28	618	10.2966	1.5028	0.6475	0.0276	0.6259	Undifferentiated	
C43_Mag-29	618	0.7987	0.1923	0.8361	0.0224	0.3953	Undifferentiated	
C43_Mag-30	618	6.5238	0.6442	0.7354	0.0209	0.5992	Undifferentiated	
C43_Mag-31	618	2.6431	0.4392	0.8096	0.0227	0.5276	Undifferentiated	
C43_Mag-32	618	2.8487	0.7618	0.7874	0.0364	0.4829	Undifferentiated	
C61_Mag-1	840	4.9210	0.6685	0.7407	0.0189	0.4761	Matrix zone 1	
C61_Mag-2	840	7.0825	1.3379	0.7153	0.0349	0.3307	Matrix zone 1	
C61_Mag-3	840	2.3739	0.2249	0.8096	0.0227	0.4154	Matrix zone 1	
C61_Mag-4	840	9.6749	2.1263	0.6379	0.0494	0.1203	Matrix zone 1	
C61_Mag-5	840	10.5076	2.3349	0.5934	0.0349	0.3958	Matrix zone 1	
C61_Mag-6	840	16.3302	1.7982	0.5765	0.0318	0.4544	Matrix zone 1	
C61_Mag-7	840	3.8096	0.4369	0.7609	0.0185	0.3841	Matrix zone 1	
C61_Mag-8	840	4.6615	0.8527	0.7397	0.0233	0.5737	Matrix - dissemenated	
C61_Mag-9	840	21.8386	1.1640	0.5034	0.0254	0.4378	Matrix - dissemenated	
C61_Mag-10	840	12.6923	1.1591	0.6083	0.0263	0.4890	Matrix - dissemenated	
C61_Mag-11	840	2.2891	0.6353	0.7874	0.0308	0.3849	Matrix - dissemenated	
C61_Mag-12	840	4.2030	1.5870	0.7206	0.0339	0.1448	Vein 3	
C61_Mag-13	840	3.1652	1.1740	0.7630	0.0334	0.1349	Vein 3	
C61_Mag-14	840	1.4404	0.4137	0.7982	0.0180	0.1779	Vein 3	
C61_Mag-	840	4.6279	0.8073	0.7545	0.0243	0.1799	Matrix -	

15							dissemenated	
C61_Mag-16	840	7.4530	0.8580	0.6909	0.0262	0.5819	Vein 2	
C61_Mag-17	840	7.8405	0.7597	0.6952	0.0196	0.6333	Vein 2	
C61_Mag-18	840	12.1509	0.7871	0.6379	0.0204	0.5144	Matrix - dissemenated	
C61_Mag-19	840	9.7115	0.9399	0.6454	0.0257	0.6182	Matrix - dissemenated	
C61_Mag-20	840	2.7045	0.1822	0.6485	0.0164	0.5189	Matrix - dissemenated	x
C61_Mag-21	840	6.8552	0.4433	0.7139	0.0177	0.4563	Matrix - dissemenated	
C61_Mag-22	840	1.3784	0.3420	0.7969	0.0225	0.5969	Vein 2	
C61_Mag-23	840	5.1900	0.3519	0.7515	0.0174	0.4729	Vein 2	
C61_Mag-24	840	11.8150	0.6438	0.6252	0.0178	0.6126	Vein 2	
C61_Mag-25	840	14.1259	0.5931	0.5807	0.0206	0.5288	Vein 2	
C61_Mag-26	840	5.0272	1.5803	0.7015	0.0387	0.2629	Vein 3	
C61_Mag-27	840	2.3098	0.6052	0.7989	0.0189	0.5416	Vein 3	
C61_Mag-28	840	4.9305	1.5203	0.7227	0.0378	0.5904	Matrix zone 1	
C61_Mag-29	840	10.8638	1.5345	0.6464	0.0295	0.5762	Matrix zone 1	
C61_Mag-30	840	9.3914	1.1507	0.6613	0.0250	0.5826	Matrix zone 1	
C61_Mag-31	840	6.2839	0.7347	0.7280	0.0266	0.5649	Matrix zone 1	
C61_Mag_V-32	840	1.5538	0.2281	0.8027	0.0176	0.4397	Vein 1	
C61_Mag_V-33	840	7.8646	1.5760	0.6983	0.0328	0.2863	Vein 1	
C61_Mag_V-34	840	12.3262	3.6233	0.5818	0.0553	0.2705	Vein 1	
C61_Mag_V-35	840	1.8714	0.9706	0.7757	0.0354	0.5772	Vein 1	
C61_Mag_V-36	840	19.5714	2.5698	0.4779	0.0435	0.2969	Vein 1	
C61_Mag_V-37	840	1.3148	0.3852	0.8255	0.0252	0.1788	Vein 1	
C61_Mag_	840	5.6225	0.3748	0.7422	0.0164	0.6326	Vein 1	

V-38								
C61_Mag_V-39	840	2.5385	0.5302	0.8022	0.0257	0.4753	Vein 1	
C61_Mag_V-40	840	8.3786	0.7047	0.7111	0.0213	0.4647	Vein 1	
C61_Mag_V-41	840	9.2558	0.4416	0.6814	0.0201	0.5323	Vein 1	
C61_Mag_V-42	840	6.4581	1.0007	0.7460	0.0313	0.4850	Vein 1	
C62_Mag_Vein-3	871	4.4204	1.5268	0.7524	0.0420	0.3058	Undifferentiated	
C62_Mag_Vein-4	871	1.1497	0.2024	0.8064	0.0250	0.3730	Undifferentiated	
C62_Mag_Vein-5	871	4.2030	1.9999	0.6846	0.0376	0.3398	Undifferentiated	
C62_Mag_Vein-6	871	2.6162	0.8559	0.7831	0.0264	0.5245	Undifferentiated	
C62_Mag_Vein-7	871	0.7063	0.1118	0.8262	0.0182	0.5782	Undifferentiated	
C62_Mag_Vein-8	871	7.3253	2.7248	0.7323	0.0479	0.6087	Undifferentiated	
C62_Mag_Vein-9	871	11.1958	1.4354	0.5998	0.0262	0.1974	Undifferentiated	
C62_Mag_Vein-10	871	7.9376	1.8010	0.7227	0.0378	0.2065	Undifferentiated	
C62_Mag_Vein-11	871	6.1631	1.0002	0.7312	0.0350	0.4281	Undifferentiated	
C62_Mag_Vein-12	871	6.8369	0.8317	0.7259	0.0248	0.5526	Undifferentiated	
C62_Mag_Vein-13	871	20.6762	4.8532	0.5299	0.1593	0.1379	Undifferentiated	
C62_Mag_Vein-14	871	11.2945	0.6851	0.6528	0.0231	0.5521	Undifferentiated	
C62_Mag_Vein-15	871	1.7092	0.6390	0.7948	0.0240	0.2664	Undifferentiated	
C62_Mag-1	871	6.5404	1.6570	0.6655	0.0384	0.5326	Undifferentiated	
C62_Mag-3	871	3.7704	1.7205	0.7513	0.0410	0.3711	Undifferentiated	
C62_Mag-4	871	3.6626	0.7883	0.7725	0.0402	0.4963	Undifferentiated	
C62-mush-1	871	14.6506	0.8870	0.5892	0.0189	0.6237	Undifferentiated	
C62-mush-2	871	4.5620	0.3923	0.7556	0.0197	0.5981	Undifferentiated	
C62-mush-	871	4.8928	0.5963	0.7545	0.0269	0.6382	Undifferentia	

3							ted	
C62-mush-4	871	11.6011	0.8714	0.6697	0.0251	0.5083	Undifferentiated	
C62-mush-5	871	5.9624	0.7445	0.7450	0.0196	0.6045	Undifferentiated	
C62-mush-6	871	26.3499	1.3776	0.4101	0.0257	0.4190	Undifferentiated	
C62-mush-7	871	2.5897	0.6821	0.7958	0.0211	0.5514	Undifferentiated	
C62-mush-8	871	4.2030	1.1056	0.7630	0.0244	0.5717	Undifferentiated	
C62_Mag-5	871	7.3253	4.6068	0.6824	0.0723	0.0759	Undifferentiated	
C62_Mag-6	871	5.0669	0.7975	0.7354	0.0249	0.6355	Undifferentiated	
C62_Mag-7	871	7.7458	0.7876	0.6708	0.0251	0.4450	Undifferentiated	
C62_Mag-8	871	3.5609	0.6960	0.7778	0.0208	0.6223	Undifferentiated	
C62_Mag-9	871	41.7565	4.2317	0.2077	0.0279	0.3751	Undifferentiated	

Figure A-21: Magnetite C34 All Spots Tera-Wasserburg Diagram (UCSB)

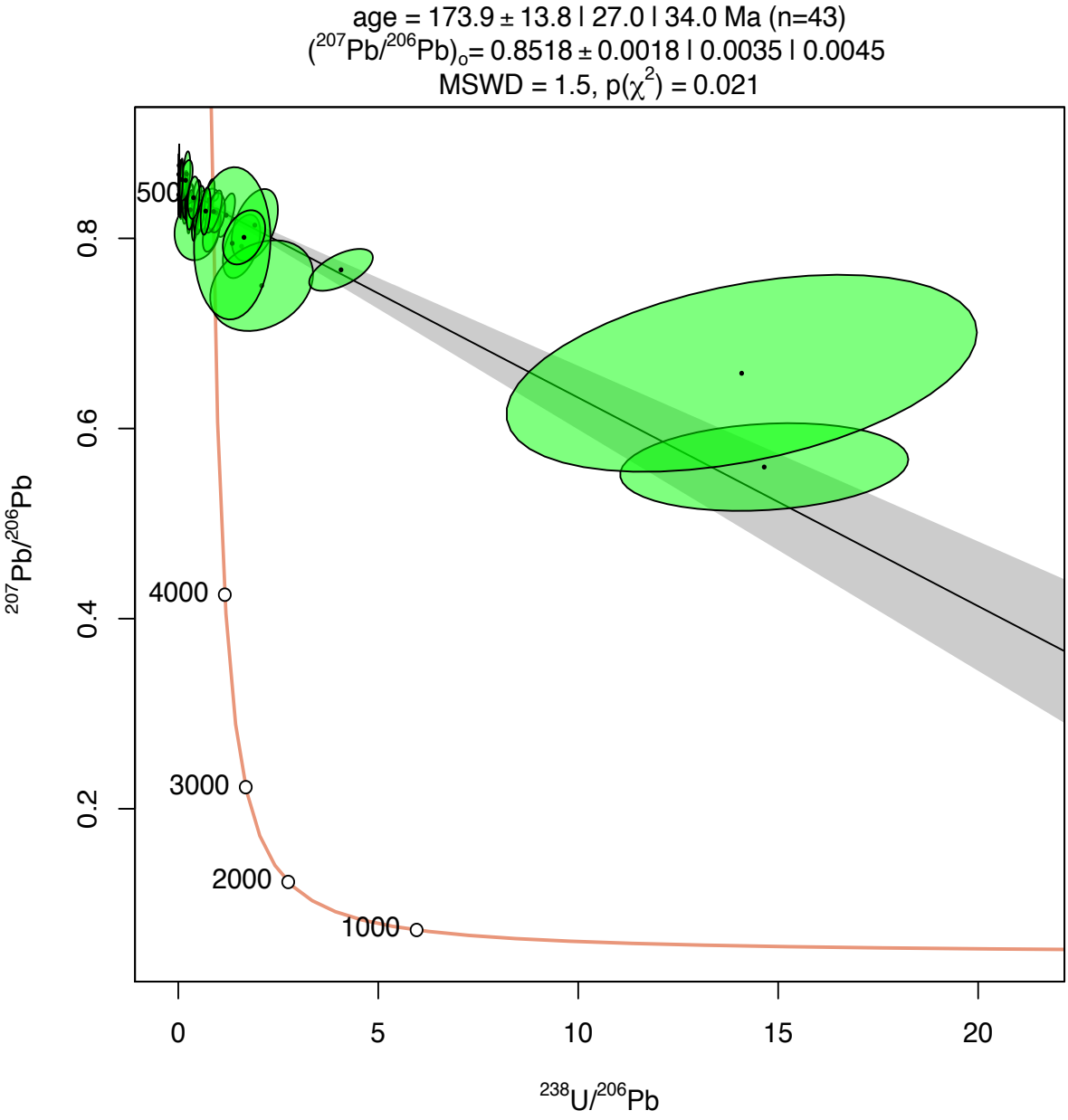

Figure A-22: Magnetite C34 “Rims” Tera-Wasserburg Diagram (UCSB)

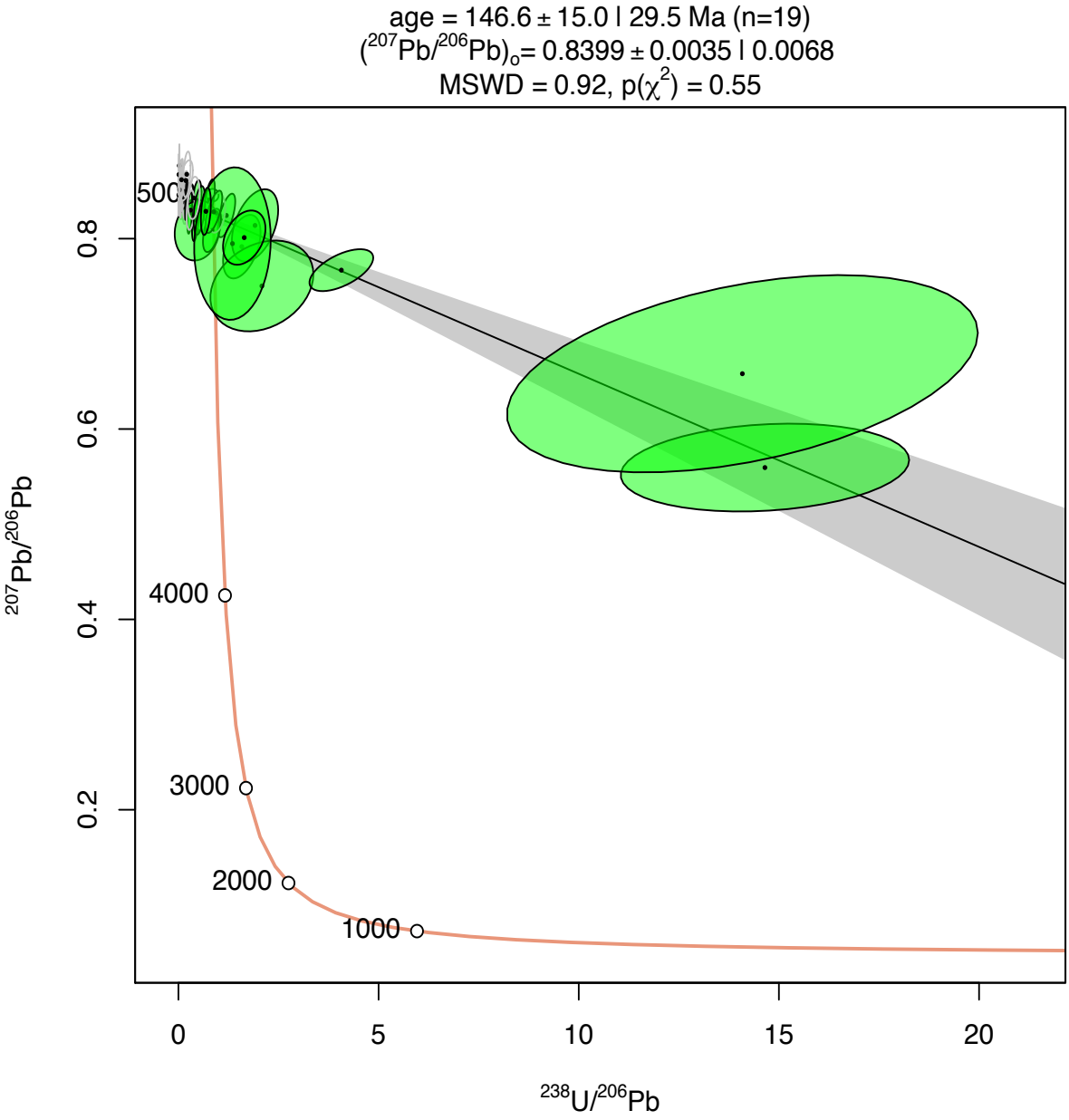

Figure A-23: Magnetite C34 “Cores” Tera-Wasserburg Diagram (UCSB)

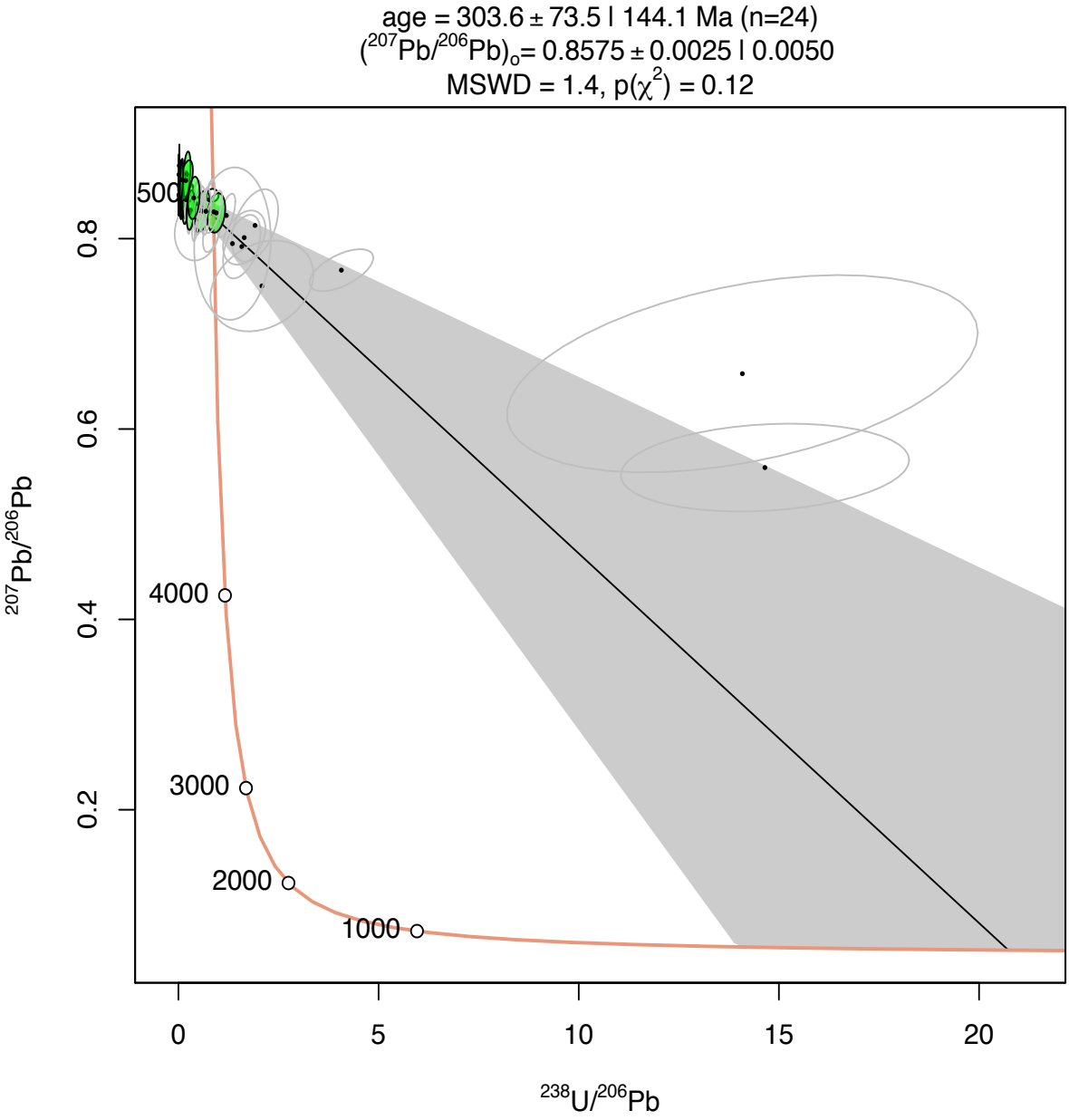

Figure A-24: Magnetite C43 Tera-Wasserburg Diagram (UCSB)

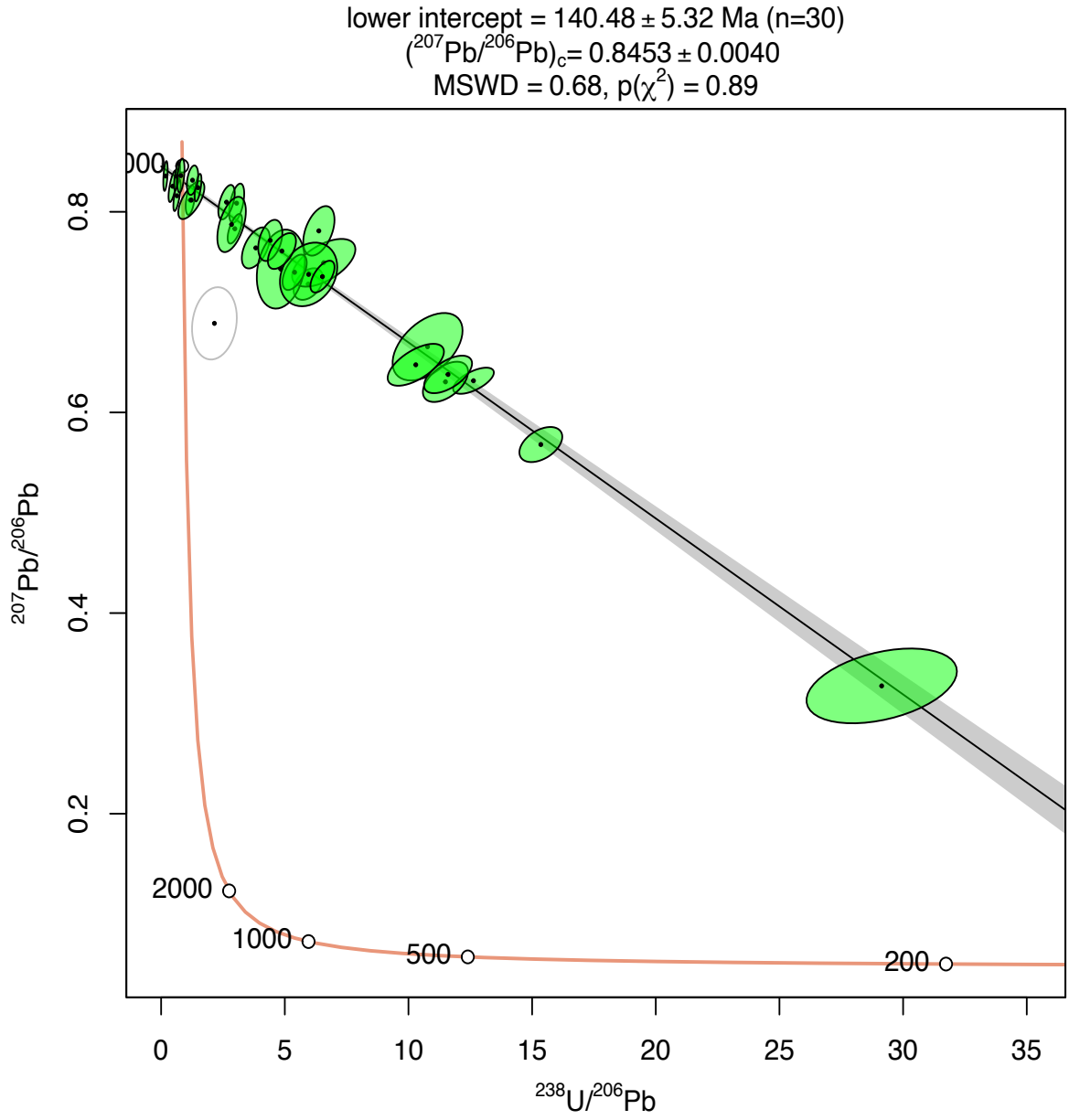

Figure A-25: Magnetite C61 All Spots Tera-Wasserburg Diagram (UCSB)

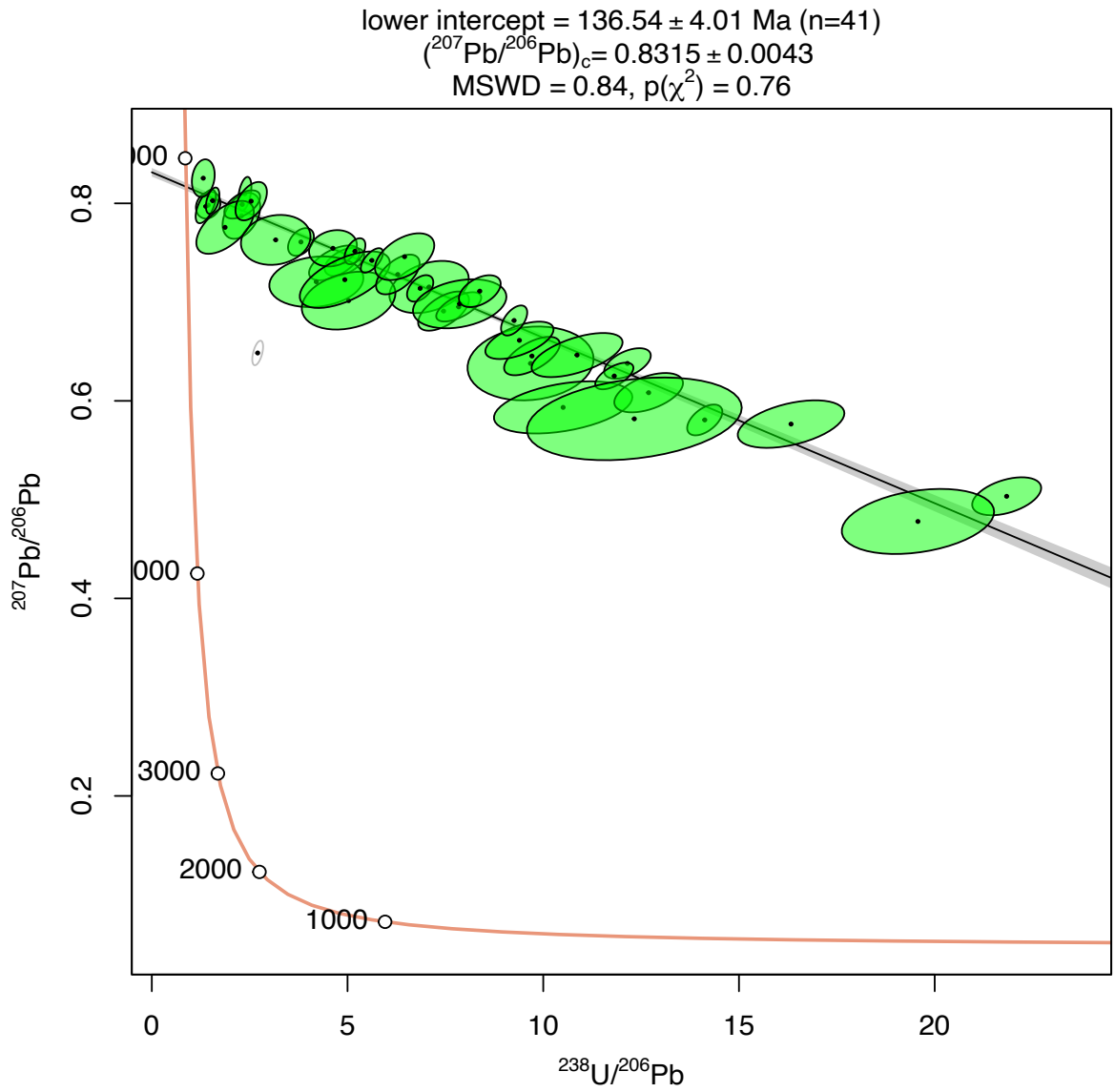

Figure A-26: Magnetite C61 In Matrix Tera-Wasserburg Diagram (UCSB)

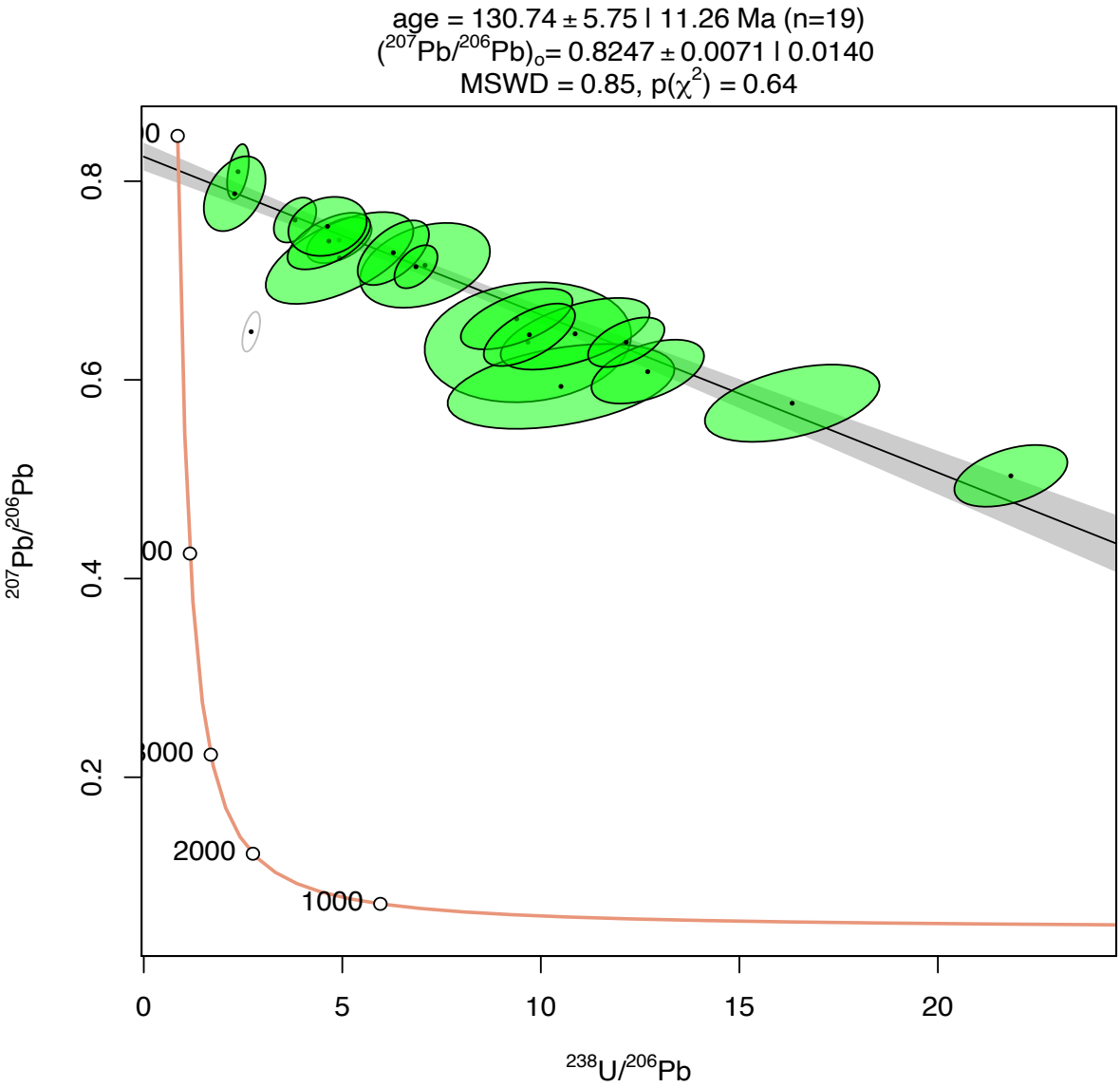

Figure A-27: Magnetite C61 Vein 1 Tera-Wasserburg Diagram (UCSB)

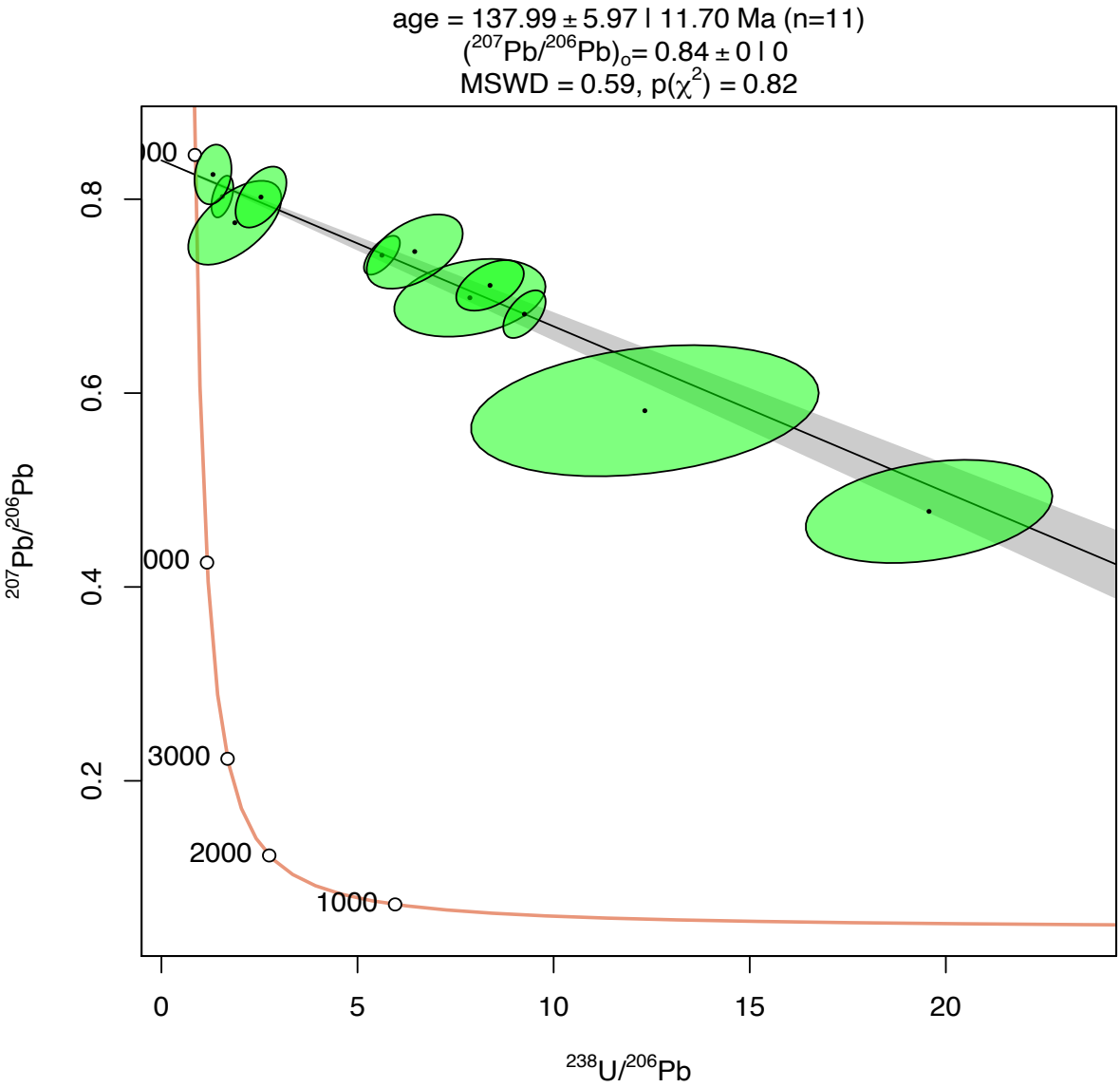

Figure A-28: Magnetite C61 Vein 2 Tera-Wasserburg Diagram (UCSB)

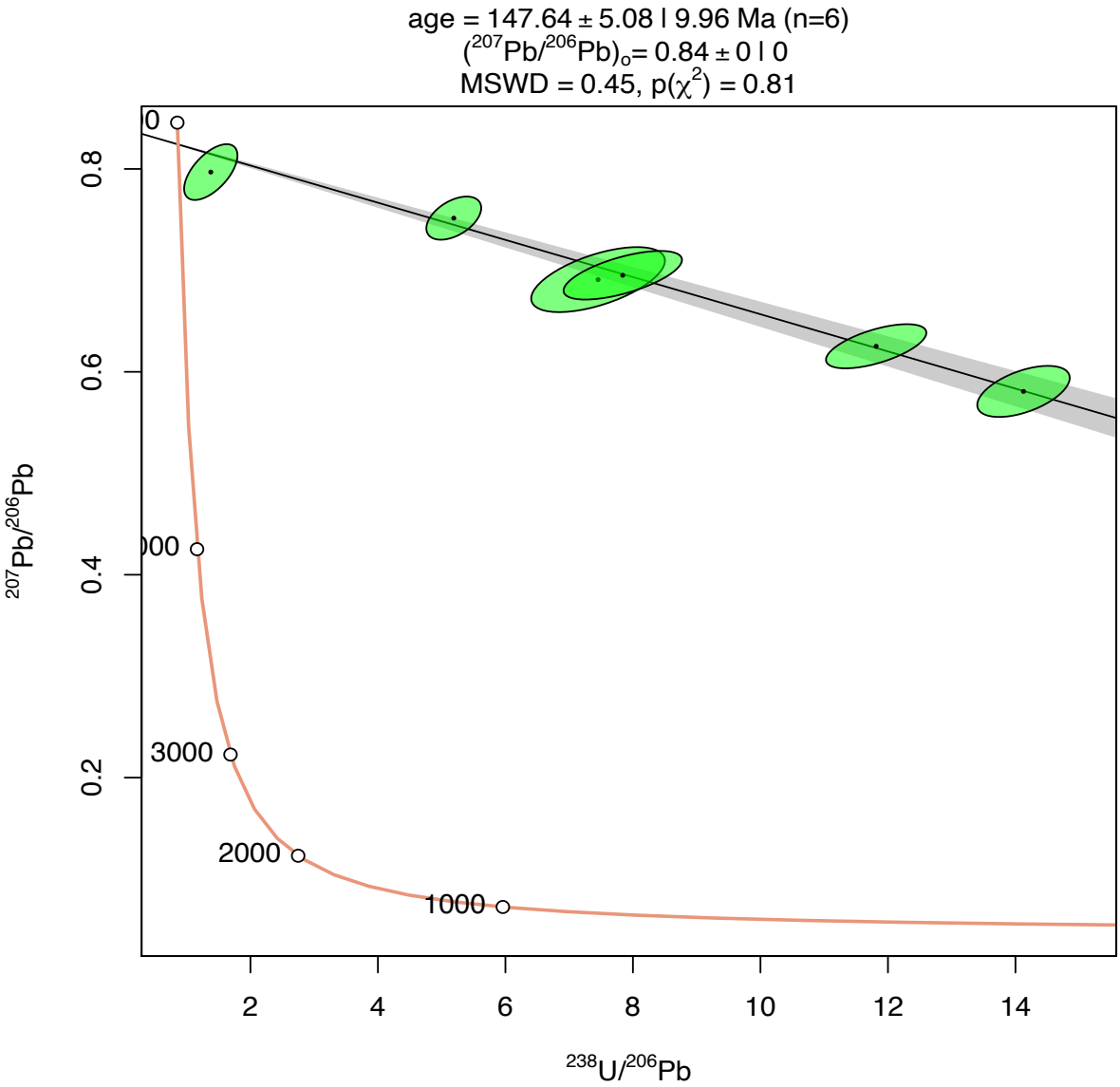

Figure A-29: Magnetite C62 All Spots Tera-Wasserburg Diagram (UCSB)

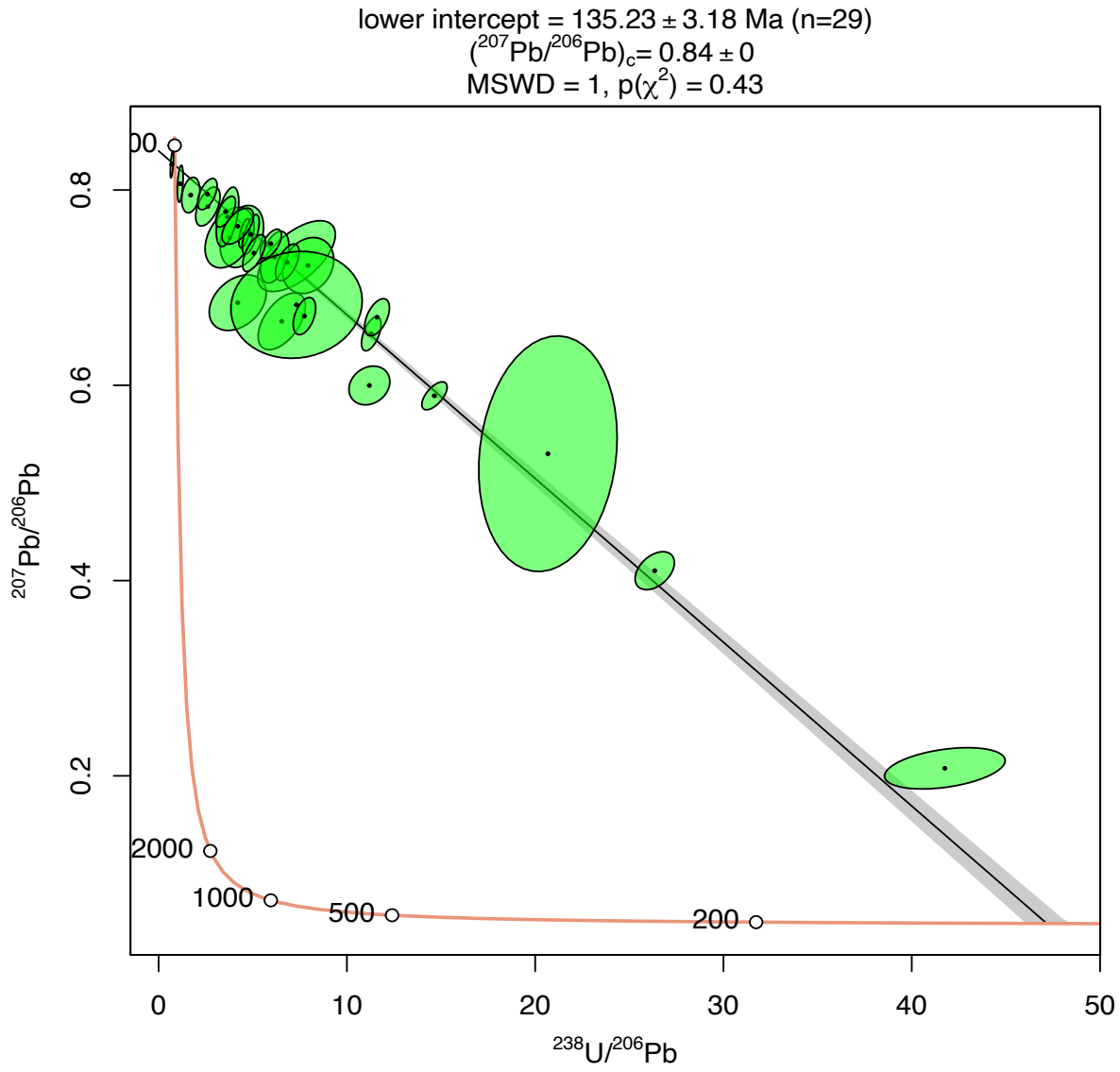

Figure A-30: Magnetite C62 In Matrix Tera-Wasserburg Diagram (UCSB)

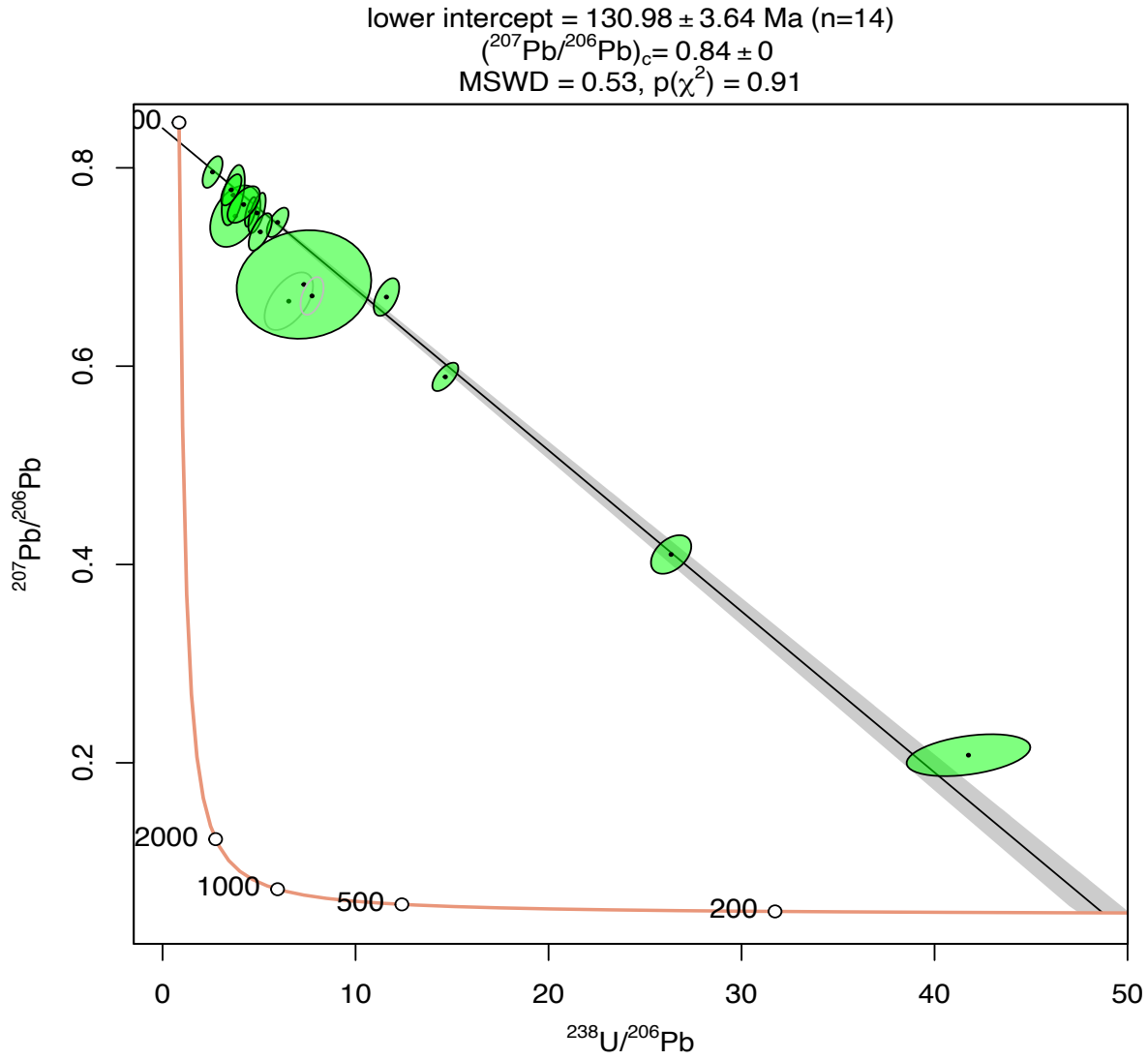

Figure A-31: Magnetite C62 Vein Tera-Wasserburg Diagram (UCSB)

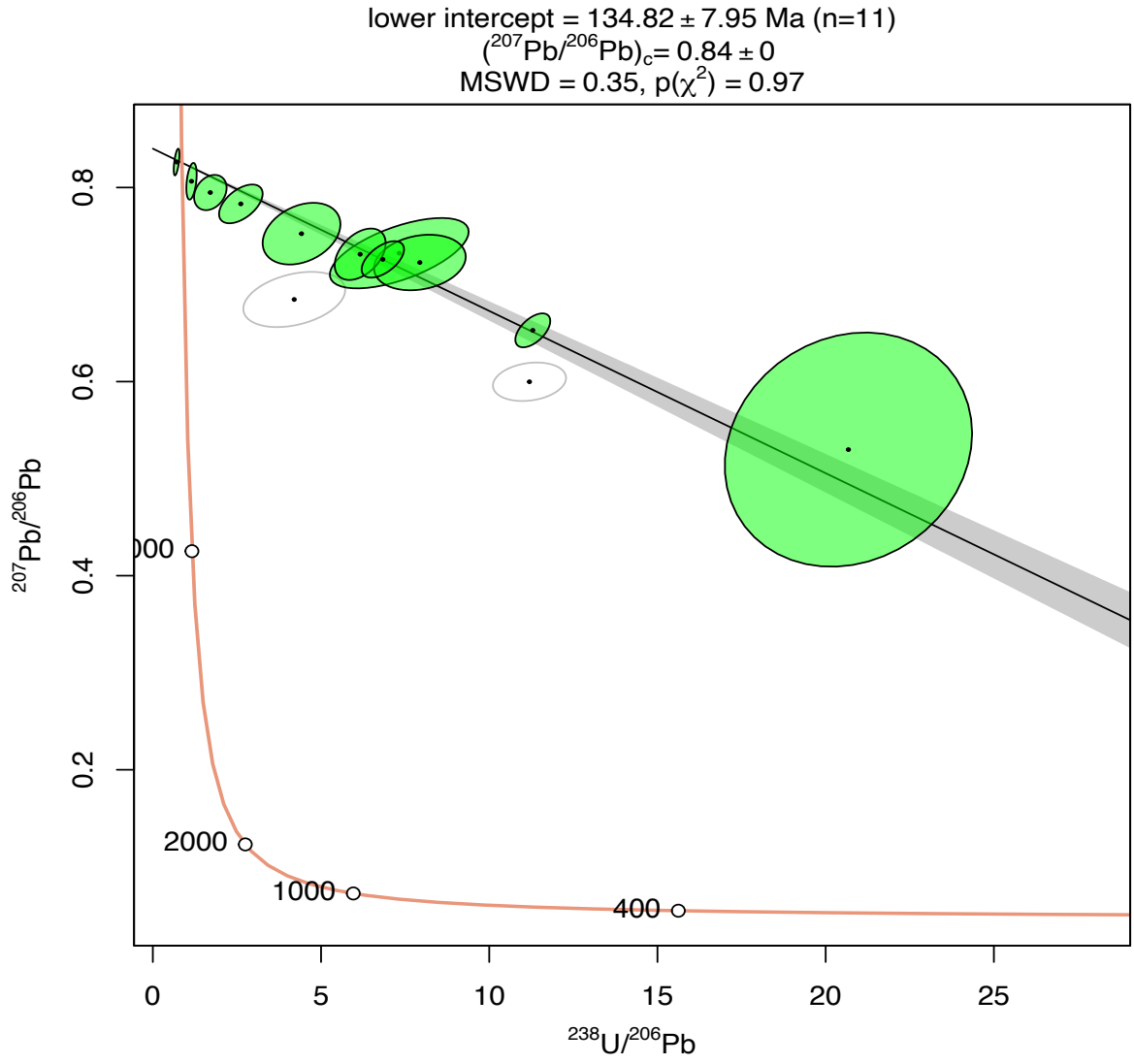

Appendix B: Chapter 3 Supplemental

Table B-1: Operating conditions for LA-ICP-MS analysis at the Gemological Institute of America

Operation conditions for LA-ICP-MS analysis	
Material	Emerald
ICP-MS conditions	
Plasma power	1550 W
Cool gas flow	14 L/min Argon
Auxiliary gas flow	0.8 L/min Argon
Nebulizer gas flow (argon gas)	1.01 L/min Argon
Sampling depth	5 mm
Extraction Lens 2	-172 V
CCT Focus Lens	0.24 V
Detector type	Dual (analog and pulse counting)
Laser parameters	
Wavelength	213 nm
Fluence (energy density)	8-10 J/cm^2
Repetition rate	10 Hz
Ablation style	Single circular spot
Ablation spot size	55 μm diameter
Carrier gas flow (helium gas)	0.8 L/min Helium

Note: Argon and helium gas flow rate, torch position, sampling depth and lens voltage were optimized to achieve maximum sensitivity (counts per concentration) and low oxide production rates (232Th16O/232Th < 1%).

Table B-2: Summary Stats for the full Colombian emerald geochemical database

	7Li	9Be	23Na	25Mg	28Si	39K	43Ca	45Sc	46Ti
East : Count Numeric	1044	1044	1044	798	798	960	791	1044	798
East : Minimum	24.77834	40500	545	358	291000	0.640423	110	5.31	3.16
East : Maximum	356	64900	54400	17300	373000	1090	34000	2020	166
East : Mean	78.25891	52631.67	3033.389	2555.125	316809.5	20.5291	325.7598	162.1952	10.1131
East : Median	71.55	52800	2630	2290	316000	8.87	199	113	8.13
East : Range	331.2217	24400	53855	16942	82000	1089.36	33890	2014.69	162.84
East : Interquartile Range	28.425	5942.586	1542.301	1495	9000	16.61411	88	136.8733	2.29
East : Standard Deviation	37.93142	3543.19	2372.758	1381.236	7412.987	44.89352	1241.125	180.9885	10.06205
East : 1 percentile	30.78297	44045	804.7	553.82	300990	0.997749	123.92	7.0245	5.259
East : 5 percentile	39.18191	46700	1073.129	1009.1	306000	1.942394	142	12.15	6.1295
East : 10 percentile	44.06676	47900	1509.497	1280	308000	2.707	151.4	23.65677	6.578
East : 25 percentile	58.525	50000	2041.261	1670	312000	4.46089	171	60.7	7.27
East : 75 percentile	86.95	55942.59	3583.562	3165	321000	21.075	259	197.5733	9.56
East : 90 percentile	111	56749.27	4790	4243	326000	48.38	454.2	335	13.1
East : 95 percentile	127	57043.98	5732.5	5162	330000	79.5	727	493.5	18.61
East : 99 percentile	266.55	60865	8637	6800.9	336000	163.56	1891.2	1004.15	63.224
West : Count Numeric	1240	1240	1240	959	959	1208	931	1236	959
West : Minimum	20.9	40800	546	273	294000	1.220894	92.9	2.738814	3.45
West : Maximum	421	67100	41600	10700	342000	270	61800	1480	144
West : Mean	46.84693	52944.66	3885.593	3422.827	318597.5	22.63852	369.7142	102.374	12.24342
West : Median	39.06416	52800	3710	3150	318000	19.1	184	59.03575	8.82
West : Range	400.1	26300	41054	10427	48000	268.7791	61707.1	1477.261	140.55
West : Interquartile Range	24.175	6300	2487.5	2580	9000	23.98514	46	79.83696	3.16
West : Standard Deviation	25.14421	4144.177	2024.451	1776.212	7052.194	21.43585	2466.719	145.1851	12.03458
West : 1 percentile	23.8	44141	883.9632	646.8	304000	1.69175	117.32	4.659106	5.074
West : 5 percentile	27.4	45800	1370	1100	308000	2.8845	135.6	10.385	6.1
West : 10 percentile	29.6	47700	1760	1420	310000	4.145478	146.2	14.27	6.71

West : 25 percentile	32.9	50000	2472.5	1970	314000	7.78958	162	30	7.54
West : 75 percentile	57.075	56300	4960	4550	323000	31.77472	208	109.837	10.7
West : 90 percentile	68.99	57538.59	6164	5920	328000	44.60343	268	219	18.9
West : 95 percentile	82.76364	59197.89	6929.5	6780	332000	51.2	413.2	364.6	36
West : 99 percentile	134.59	62636	8685.9	8556	338000	90.356	1707.2	772.26	74.18

	47Ti	51V	52Cr	53Cr	55Mn	57Fe	69Ga	71Ga	85Rb	133Cs
East : Count Numeric	1042	1044	798	1044	731	1044	1044	1044	1042	1044
East : Minimum	0.070583	37.5	16.2	15.4	0.032124	44.8	2.81	2.79	0.13	2.66
East : Maximum	166	5040	8480	9080	638	7500	47.9	49.1	12.7	41.6
East : Mean	4.971517	1120.442	2215.25	2309.857	4.681771	455.8384	18.726	19.16175	1.332818	12.97815
East : Median	3.075	982.966	1795	1926.604	0.67	377	18.56366	19	1.23	11.6
East : Range	165.9294	5002.5	8463.8	9064.6	637.9679	7455.2	45.09	46.31	12.57	38.94
East : Interquartile Range	1.9725	687.9291	2276	2247.5	3.495841	327.7999	6.8	6.809903	0.887238	8.43
East : Standard Deviation	11.44851	777.3125	1587.387	1636.706	25.90265	385.8585	6.032815	6.197062	0.907663	6.48966
East : 1 percentile	0.168605	120.35	32.991	34.045	0.036443	95.17007	8.181642	8.246513	0.184792	3.951332
East : 5 percentile	0.351141	271.676	290.55	310.25	0.053576	134.8817	9.62302	9.690351	0.31	5.286627
East : 10 percentile	0.524864	361.3128	484.9	551.6482	0.065711	162	10.59943	10.7	0.401323	6.05
East : 25 percentile	2.2075	642.9973	986.5	1052.5	0.194159	242.2001	15.1	15.6	0.795262	7.97
East : 75 percentile	4.18	1330.926	3262.5	3300	3.69	570	21.9	22.4099	1.6825	16.4
East : 90 percentile	7.101	2029.7	4211	4449.141	10.68	774.7637	26.16312	26.8	2.17	21
East : 95 percentile	13.38	2240	4881	5207.5	16.2	1050	29.6	30.6	2.69	25.775
East : 99 percentile	58.727	4432	7305.4	7678.5	36.224	1772.18	36.04	36.775	4.3821	33.91
West : Count Numeric	1238	1240	959	1240	895	1240	1240	1240	1239	1240
West : Minimum	0.273505	91.56541	56.4	45.96175	0.046514	53.7	4.533194	4.519671	0.051	0.4
West : Maximum	227	11300	6150	6780	217	2680	91.7	61.57172	11.5	32.5
West : Mean	7.038639	1691.715	1192.056	1163.639	1.850976	420.2553	23.60317	24.06822	2.223855	9.33832
West : Median	3.58	1240	808	786.4167	0.42	364.5953	21.9	22.2	2.02	9.087381
West : Range	226.7265	11208.43	6093.6	6734.038	216.9535	2626.3	87.16681	57.05205	11.449	32.1
West : Interquartile Range	3.085	1694.87	1265	1183	0.498185	274.7896	19.075	19.4	2.34	5.266329

West : Standard Deviation	12.42979	1585.245	1164	1179.441	9.348681	262.6584	11.72244	11.73145	1.561621	4.040221
West : 1 percentile	0.49845	130	74.4	73.051	0.071327	102.41	6.4305	6.34	0.17	2.0664
West : 5 percentile	0.883581	251.1614	141	128	0.136663	145.0238	8.074984	8.2515	0.41	3.7005
West : 10 percentile	1.398044	331.2075	166	162	0.2	184.8635	9.411	9.787	0.52	4.384
West : 25 percentile	2.5175	572.6301	365	367	0.281815	241.25	13.725	14	0.88	6.433671
West : 75 percentile	5.6025	2267.5	1630	1550	0.78	516.0396	32.8	33.4	3.22	11.7
West : 90 percentile	14.52	3570	2830	2854.054	3.118	692.8	40.39	41.09	4.29	14.4
West : 95 percentile	28.625	4918	3760	3717.906	5.588	897.5354	44.1	44.995	5.16	16.495
West : 99 percentile	65.381	7860	5120	5505.9	32.736	1390	50.259	50.913	6.646	20.69048

Table B-3: Table B-3: Summary Stats for mining district Colombian emerald geochemistry

	7Li	9Be	23Na	25Mg	27Al	28Si	39K	43Ca	45Sc	46Ti
Chivor District : Count Numeric	484	484	484	370	484	370	454	367	484	370
Chivor District : Minimum	24.77834	41200	545	358	75800	291000	0.640423	124	8.436106	5.08
Chivor District : Maximum	351	58800	21500	9200	111000	341000	1090	4450	624	166
Chivor District : Mean	66.10426	52373.54	2611.388	2099.276	94614.61	316708.1	27.44233	332.1744	111.6998	10.05586
Chivor District : Median	62.05	52800	2422.265	1945	94300	316000	10.14702	217	99.45	7.92
Chivor District : Range	326.2217	17600	20955	8842	35200	50000	1089.36	4326	615.5639	160.92
Chivor District : Interquartile Range	30.325	6132.06	1013.851	825	5200	9000	26.2425	140	88.225	2.13
Chivor District : Standard Deviation	34.00089	3579.323	1471.204	997.8675	5158.453	7259.883	60.65192	383.8667	79.69926	12.03913
Chivor District : 1 percentile	28.52497	43470	729.1331	503.15	81785	297420	1.094475	133	10.525	5.3978
Chivor District : 5 percentile	34.21023	46025	998.714	892.2	84500	306000	2.205	152.6	15.425	6.031
Chivor District : 10 percentile	38.46827	47300	1415	1260	87900	308000	3.094604	167.8	23.80991	6.36
Chivor District : 25 percentile	46.55	49700	1996.149	1625	92500	312000	5.6575	186	58.525	6.975
Chivor District : 75 percentile	76.875	55832.06	3010	2450	97700	321000	31.9	326	146.75	9.105
Chivor District : 90 percentile	88.3	56611.19	3620	2908	101000	326000	71.7	576.8	202.5	11.48
Chivor District : 95 percentile	104	56865.02	4145	3273.5	103000	330000	93.75	849.2	239.1342	15.735
Chivor District : 99 percentile	270.9	57515	9706.5	7770.7	108000	336580	191.4	2308.8	432.061	75.326
Coscuez District : Count Numeric	255	255	255	182	255	182	253	173	254	182
Coscuez District : Minimum	22.9	45000	833.84	664	78400	297000	1.2208	105	6.5592	5.48

			66				94		37	
Coscuez District : Maximum	180	59900	41600	8980	111000	334000	82.6	8680	1040	61
Coscuez District : Mean	58.2095	53497.96	4229.337	3899.418	94983.98	316192.3	13.86618	243.2081	106.2989	11.13038
Coscuez District : Median	59.05178	53400	3715.223	3340	94220.1	316000	7.591052	172	62.9	8.49
Coscuez District : Range	157.1	14900	40766.15	8316	32600	37000	81.37911	8575	1033.441	55.52
Coscuez District : Interquartile Range	20.1	5640.166	2268.316	2392.5	6100	7500	17.87735	38	88.02135	2.9
Coscuez District : Standard Deviation	24.19439	3074.314	2829.019	1536.522	5364.197	6024.934	13.12409	662.5943	157.6185	8.893204
Coscuez District : 1 percentile	23.268	47112	983.7226	1009.28	81856	300320	2.00383	109.44	7.962	5.7041
Coscuez District : 5 percentile	28.1	48300	1624	1990.5	86520	305000	3.057877	129.4	10.64494	6.22
Coscuez District : 10 percentile	31.13526	49500	2345.811	2400	89260	308300	3.854	140	13.8	6.656
Coscuez District : 25 percentile	44.3	50900	2950	2740	91800	312750	5.025519	154	30	7.425
Coscuez District : 75 percentile	64.4	56540.17	5218.316	5132.5	97900	320250	22.90286	192	118.0213	10.325
Coscuez District : 90 percentile	71.94	57351.37	6374	6197	102000	324000	31.46	206.6	203	15.4
Coscuez District : 95 percentile	111.4	57613.54	6946	6758.5	105000	326000	40.74	293.2	299.25	30.55
Coscuez District : 99 percentile	161	58542.79	8624	7735	110440	329850	58.396	3574	965.55	59.34
Gachalá District : Count Numeric	383	383	383	251	383	251	331	249	383	251
Gachalá District : Minimum	56.3	44500	802	478	77800	294000	0.851902	110	5.31	3.16
Gachalá District : Maximum	356	64900	9618.446	6100	109000	338000	214	3090	794.1274	116
Gachalá District : Mean	94.17556	53745.62	3102.762	2842.303	94544.37	315784.9	11.28655	268.9116	139.1009	10.02418

Gachalá District : Median	84.93485	53600	2787.966	2930	94119.87	315000	5.014149	196	119	8.5
Gachalá District : Range	299.7	20400	8816.446	5622	31200	44000	213.1481	2980	788.8174	112.84
Gachalá District : Interquartile Range	32.99705	5361.275	1870	2010	3900	9000	6.915245	64.5	152.3	2.56
Gachalá District : Standard Deviation	36.57985	3364.481	1397.688	1241.56	4723.237	7687.492	20.96524	312.3489	108.7578	7.765332
Gachalá District : 1 percentile	58.452	45268	854.594	552.6	79188	298640	0.913147	115.5	5.6888	4.6408
Gachalá District : 5 percentile	64.75395	48420	1038.876	1096	87800	305000	1.253589	137	9.85	5.924
Gachalá District : 10 percentile	67.04073	49300	1394.777	1204	89200	307000	1.961338	149	14.31748	6.564
Gachalá District : 25 percentile	72.00295	51200	2130	1750	92200	311000	3.584755	167	58.7	7.44
Gachalá District : 75 percentile	105	56561.28	4000	3760	96100	320000	10.5	231.5	211	10
Gachalá District : 90 percentile	124	57043.44	5046	4562	102000	327000	25.7	364	278.4755	14.5
Gachalá District : 95 percentile	151	57859.09	5634	4874	104000	331000	36.98	715.5	317.9786	19.3
Gachalá District : 99 percentile	310.16	61780	6816.4	5739.2	107160	336480	114.8	2150	465.0262	28.408
Maripí District : Count Numeric	213	213	213	213	213	213	213	207	213	213
Maripí District : Minimum	20.9	43300	1780	1530	78100	303000	4.3	92.9	11.4	5.43
Maripí District : Maximum	69.4	59100	10100	8920	106000	341000	228	1280	957	89.6
Maripí District : Mean	35.23192	52530.99	4813.897	4428.545	95184.51	318375.6	27.3554	194.956	189.2549	10.97413
Maripí District : Median	33.3	52600	4500	3940	96000	318000	23.7	185	117	8.12
Maripí District : Range	48.5	15800	8320	7390	27900	38000	223.7	1187.1	945.6	84.17
Maripí District : Interquartile Range	8.55	4100	2385	2550	8350	7000	16.9	42	192.85	2.595
Maripí District : Standard Deviation	8.469608	3095.246	1676.454	1694.377	5791.861	5917.655	19.98162	87.96455	175.1699	9.313863

Maripí District : 1 percentile	23.3	44298	1887	1621.2	81442	304280	5.0046	122.16	11.912	5.4928
Maripí District : 5 percentile	25	47070	2284	2051	84470	309000	8.34	134.4	16.36	5.837
Maripí District : 10 percentile	26.48	48400	2898	2574	86640	312000	11.96	147.8	42.1	6.388
Maripí District : 25 percentile	29.9	50600	3585	3230	91150	315000	16.15	165	61.65	7.2
Maripí District : 75 percentile	38.45	54700	5970	5780	99500	322000	33.05	207	254.5	9.795
Maripí District : 90 percentile	44.56	56400	7130	6732	102000	325000	46.44	235	456.6	22.12
Maripí District : 95 percentile	55.59	57400	8161	7597	104000	328300	54.73	261	585.3	29.62
Maripí District : 99 percentile	62.572	58758	9601.6	8875.8	106000	339720	95.834	465.76	765.92	48.17
Muzo District : Count Numeric	424	424	424	216	424	216	418	203	421	216
Muzo District : Minimum	21.9	40800	700.6903	975	77800	294000	1.281732	115	2.738814	3.9
Muzo District : Maximum	421	67100	10700	10700	118000	342000	270	1680	815.8701	111
Muzo District : Mean	42.97683	55054.95	3874.578	3318.616	95611.56	323745.4	27.9089	195.8621	81.97814	14.61764
Muzo District : Median	37.25	56308.14	3827.723	3060	93748.32	325000	25.94964	183	51.8664	9.515
Muzo District : Range	399.1	26300	9999.31	9725	40200	48000	268.7183	1565	813.1313	107.1
Muzo District : Interquartile Range	9.283474	5963.03	1946.053	1977.5	6092.961	12750	24.24489	40	68	4.635
Muzo District : Standard Deviation	29.46087	4563.369	1516.365	1601.764	5699.216	8053.598	20.1772	112.0581	95.40323	15.26094
Muzo District : 1 percentile	25.22897	43375	791.1902	980.08	82825	307170	1.684152	117.36	3.719475	4.0968
Muzo District : 5 percentile	27.84713	46600	1421.692	1515.5	88928.29	311000	6.044	137	6.320233	5.323
Muzo District : 10 percentile	29.85	48450	1850	1635	90675.99	312700	8.596	148.4	11.46	6.295
Muzo District : 25 percentile	32.61653	51425	2842.5	2150	92182.04	317000	13.94447	165	25.15	7.94
Muzo District : 75 percentile	41.9	57388.03	4788.553	4127.5	98275	329750	38.18936	205	93.15	12.575
Muzo District : 90 percentile	58.181	60800	5700	5193	105000	333000	46.801	227.6	212.78	32.06

	46						85		57	
Muzo District : 95 percentile	76.08562	61800	6348.393	6091.5	107000	337000	51.225	263.4	281.3518	48.295
Muzo District : 99 percentile	146.8094	64500	7917.5	9814.1	112000	341830	94.955	414.44	470.634	80.103
Pauna District : Count Numeric	208	208	208	208	208	208	190	208	208	208
Pauna District : Minimum	23.5	43000	546	273	73300	304000	1.37	115	7.66	5.5
Pauna District : Maximum	260	57000	9010	8180	111000	339000	263	747	329	77.4
Pauna District : Mean	51.24375	49511.54	2536.668	2093.173	92241.83	317620.2	16.77774	210.2837	51.95317	13.01139
Pauna District : Median	41.75	49750	2140	1670	91500	317000	6.41	190	36.65	9.145
Pauna District : Range	236.5	14000	8464	7907	37700	35000	261.63	632	321.34	71.9
Pauna District : Interquartile Range	33.825	5400	865	847.5	8575	8000	14.975	50.75	33.975	3.0975
Pauna District : Standard Deviation	25.81464	3347.27	1336.299	1275.586	6870.713	6317.293	29.98454	82.15222	38.90775	12.2563
Pauna District : 1 percentile	24.6	43163	817.17	603.62	76200	304090	1.3791	128	10.563	5.628
Pauna District : 5 percentile	28.545	44200	1379	965.9	81260	308450	1.9855	146.9	20.31	6.7815
Pauna District : 10 percentile	30.29	44890	1559	1160	83860	310000	2.442	151.9	23.98	7.253
Pauna District : 25 percentile	33.425	46600	1815	1420	87825	313000	3.075	165	29.025	8.0775
Pauna District : 75 percentile	67.25	52000	2680	2267.5	96400	321000	18.05	215.75	63	11.175
Pauna District : 90 percentile	79.27	54000	4132	3308	102000	327000	38.97	282.6	102.5	24.42
Pauna District : 95 percentile	84.975	54855	5351	4852.5	106000	330000	53.04	397.2	132.95	37.655
Pauna District : 99 percentile	180.26	56900	8217.4	7345.5	107000	335820	209.31	645.32	187.02	76.474
Peñas Blancas District : Count Numeric	140	140	140	140	140	140	134	140	140	140
Peñas Blancas District : Minimum	29.2	44700	637	324	83600	303000	1.4	102	4.6	3.45
Peñas Blancas District : Maximum	114	59600	7570	7320	110000	330000	114	61800	1480	144
Peñas Blancas District : Mean	49.01071	51275.71	3884.614	3409.4	95663.57	315571.4	23.57306	1273.386	99.31457	10.81743
Peñas Blancas District : Median	42.1	51000	4515	4065	95550	316000	20	189.5	65.25	8.75
Peñas Blancas District : Range	84.8	14900	6933	6996	26400	27000	112.6	61698	1475.4	140.55
Peñas Blancas District : Interquartile Range	16.25	3750	3577.5	3265	7725	6000	21.0475	161.25	81.925	2.3925

Peñas Blancas District : Standard Deviation	17.31526	2508.83	1924.406	1841.065	5328.628	4780.269	18.27238	6257.595	220.9955	12.77401
Peñas Blancas District : 1 percentile	29.692	45438	733.76	385.91	84379	303410	1.4105	102.41	4.8337	4.2577
Peñas Blancas District : 5 percentile	33.525	47525	1031	658.7	86930	306000	2.3825	129.05	7.7275	6.4175
Peñas Blancas District : 10 percentile	36.01	48400	1172	747.8	88800	309100	4.145	140.1	9.468	6.865
Peñas Blancas District : 25 percentile	38.1	49225	1755	1462.5	92000	313000	9.9275	157	16.6	7.6075
Peñas Blancas District : 75 percentile	54.35	52975	5332.5	4727.5	99725	319000	30.975	318.25	98.525	10
Peñas Blancas District : 90 percentile	75.57	54780	6075	5438	103000	321000	47.4	949.7	128.3	12.38
Peñas Blancas District : 95 percentile	93.715	55395	6648	5977	105000	322950	56.8	1718	172.8	17.59
Peñas Blancas District : 99 percentile	113.59	58903	7537.2	7274.9	109180	329180	103.36	50812	1447.2	111.528
Somondoco District : Count Numeric	45	45	45	45	45	45	45	45	45	45
Somondoco District : Minimum	50.1	40500	862	570	86000	303000	1.56	145	8.65	6.43
Somondoco District : Maximum	123	54300	54400	2340	147000	373000	177	530	115	48.3
Somondoco District : Mean	64.70222	49448.89	3810.644	1482.444	100095.6	318511.1	16.098	195.6889	53.01089	10.59356
Somondoco District : Median	59.6	49600	1830	1450	101000	316000	5.03	181	56.6	9
Somondoco District : Range	72.9	13800	53538	1770	61000	70000	175.44	385	106.35	41.87
Somondoco District : Interquartile Range	9.3	4950	515	425	7000	11000	5.005	31.5	37.35	2.675
Somondoco District : Standard Deviation	17.50125	3079.228	8942.184	332.3549	8825.247	11112.28	31.25579	62.07028	26.59038	7.106418
Somondoco District : 1 percentile	50.1	40500	862	570	86000	303000	1.56	145	8.65	6.43
Somondoco District : 5 percentile	50.23	43980	1066.9	771	87620	305300	2.366	150.9	8.851	6.997
Somondoco District : 10 percentile	52.2	46000	1456	1176	90540	308000	3.348	156.4	9.502	7.19
Somondoco District : 25 percentile	55.65	47200	1610	1280	96000	312000	4.01	167.5	34.95	7.625
Somondoco District : 75 percentile	64.95	52150	2125	1705	103000	323000	9.015	199	72.3	10.3
Somondoco District : 90 percentile	88.88	53380	2692	1898	104800	328800	57	238.4	85.92	12.9
Somondoco District : 95 percentile	121.2	54210	24585	2115	108700	334700	83.5	320.7	94.29	28.86
Somondoco District : 99 percentile	123	54300	54400	2340	147000	373000	177	530	115	48.3
Ubalá District : Count Numeric	132	132	132	132	132	132	130	130	132	132
Ubalá District : Minimum	44.8	44600	1570	1190	78700	308000	3.47	118	24.9	6.1

Ubalá District : Maximum	290	57100	8790	17300	105000	336000	83.4	34000	2020	77.5
Ubalá District : Mean	81.26515	51431.06	4114.47	3652.5	92075	318462.1	21.45277	461.5615	451.575	10.27879
Ubalá District : Median	70.05	51500	3755	3105	92650	318000	18.55	175	409	8.265
Ubalá District : Range	245.2	12500	7220	16110	26300	28000	79.93	33882	1995.1	71.4
Ubalá District : Interquartile Range	18.175	4575	2490	2297.5	7975	6000	17.775	55.5	344	2.015
Ubalá District : Standard Deviation	42.77238	2778.163	1494.378	1862.749	5981.401	5081.632	14.5642	2965.741	321.2484	8.690939
Ubalá District : 1 percentile	44.932	44996	1708.6	1308.8	78997	308000	3.7273	118.93	27.573	6.1033
Ubalá District : 5 percentile	52.115	46700	2139.5	1762	81330	310000	7.5465	127.1	45.615	6.683
Ubalá District : 10 percentile	56.17	47660	2542	2053	83280	312000	8.478	135.6	64.89	6.905
Ubalá District : 25 percentile	62.4	49200	3012.5	2425	87500	315000	10.175	158	222.5	7.51
Ubalá District : 75 percentile	80.575	53775	5502.5	4722.5	95475	321000	27.95	213.5	566.5	9.525
Ubalá District : 90 percentile	105.7	54970	6330	5814	100000	325700	40.28	287.9	969.9	12.9
Ubalá District : 95 percentile	198.2	55500	6707	6164	102350	329000	49.635	362	1040	21.895
Ubalá District : 99 percentile	282.08	56902	8532.6	14204.6	104670	334020	79.99	23672.97	1732.9	72.781

	47Ti	51V	52Cr	53Cr	55Mn	57Fe	69Ga	71Ga	85Rb	133Cs
Chivor District : Count Numeric	484	484	370	484	343	484	484	484	483	484
Chivor District : Minimum	0.070583	142.5128	174	172	0.032124	66.82364	7.59	7.79	0.16	3.006715
Chivor District : Maximum	166	2319.817	5450	6750.228	219	1820	39	29.3	12.7	38.4
Chivor District : Mean	4.801174	842.06	2000.057	2154.211	5.299426	312.4158	16.44896	16.78092	1.32197	8.946838
Chivor District : Median	2.98	794	1525	1670	1.67	274	16.85629	17.3	1.239367	7.915
Chivor District : Range	165.9294	2177.304	5276	6578.228	218.9679	1753.176	31.41	21.51	12.54	35.39329
Chivor District : Interquartile Range	1.795	528.25	2047.5	2068.598	5.88683	228	6.258972	6.425208	0.727296	4.548708

Chivor District : Standard Deviation	11.26754	421.5438	1273.306	1419.014	14.59438	186.7293	4.409586	4.41511	0.941278	4.177331
Chivor District : 1 percentile	0.131299	194.3419	261.41	286.3751	0.034523	79.87869	8.207385	8.278394	0.245285	3.8485
Chivor District : 5 percentile	0.253834	269.6642	486.55	513.5	0.043367	114.7291	9.1525	9.5625	0.358818	4.515498
Chivor District : 10 percentile	0.443174	326.4061	614.2	661.5	0.053347	133.2544	10.1591	10.4	0.457604	5.225
Chivor District : 25 percentile	2.1625	531.75	1030	1080	0.08317	176	13.3	13.43953	0.88	6.3125
Chivor District : 75 percentile	3.9575	1060	3077.5	3148.598	5.97	404	19.55897	19.86474	1.607296	10.86121
Chivor District : 90 percentile	6.135	1374.276	3889	4269.186	13.6	512	21.37406	22.10383	2.016	14.15
Chivor District : 95 percentile	11.85	1720	4282.5	4797.5	18.06	628	23.03377	23.575	2.346	15.3
Chivor District : 99 percentile	59.549	2196.135	5245.8	6090.515	52.928	1033	26.08567	26.345	3.7112	26.28
Coscuez District : Count Numeric	255	255	182	255	207	255	255	255	255	255
Coscuez District : Minimum	0.273505	258.4813	91.1	84.19373	0.052898	114.4562	11.85122	11.86682	0.164568	4.46
Coscuez District : Maximum	227	11300	5870	6160	83.2	2490	55.8	57.4	5.91	22.9
Coscuez District : Mean	6.807681	2255.96	1425.731	1267.322	1.084461	530.4124	32.06933	32.70153	1.731706	10.48062
Coscuez District : Median	3.7	1790	932	856.7795	0.39	450	31.5	32.1	1.19	10
Coscuez District : Range	226.7265	11041.52	5778.9	6075.806	83.1471	2375.544	43.94878	45.53318	5.745432	18.44
Coscuez District : Interquartile Range	3.47	1587.465	1342	1141.352	0.41	281	14.51618	14.37309	1.634622	4.06
Coscuez District : Standard Deviation	15.99191	1765.122	1334.929	1289.572	5.833466	333.3323	9.547186	9.749057	1.22886	3.350002
Coscuez District : 1 percentile	0.291648	309.64	115.917	106.7845	0.0667	120.0036	12.2633	12.36783	0.2592	4.667084
Coscuez District : 5 percentile	0.5271	578.16	212.9	211.4	0.0997	179.35	17.14	17.68	0.4571	5.4754

	17	18			43	56			01	22
Coscuez District : 10 percentile	0.974631	737.3478	308.3	299.0324	0.147596	213.6223	20.2	20.42583	0.587056	6.410764
Coscuez District : 25 percentile	2.53	1180	468	418.6483	0.27	328	25.1	25.61087	0.83	8.34
Coscuez District : 75 percentile	6	2767.465	1810	1560	0.68	609	39.61618	39.98396	2.464622	12.4
Coscuez District : 90 percentile	10.60596	3862	3321	2850	1.136	1054	45.48	46.52	3.77	15.44
Coscuez District : 95 percentile	20.15875	6176	5001	4840	3.234	1204	47.46	48.62	4.342	17.12
Coscuez District : 99 percentile	55.76	10476	5745.5	5724.4	9.478	1757.6	52.356	52.78	5.3988	21.128
Gachalá District : Count Numeric	382	383	251	383	272	383	383	383	382	383
Gachalá District : Minimum	0.218132	37.5	16.2	15.4	0.052914	44.8	2.81	2.79	0.13	2.66
Gachalá District : Maximum	158	2240	5220	5690	70.1	3350	37.35122	38.4	7.27	41.6
Gachalá District : Mean	5.238541	1140.173	2304.278	2295.714	2.302541	637.0417	21.17652	21.61859	1.071976	16.03894
Gachalá District : Median	3.02	1172.682	2220	2144.773	0.31	589	21.6	21.98131	0.94	14.6
Gachalá District : Range	157.7819	2202.5	5203.8	5674.6	70.04709	3305.2	34.54122	35.61	7.14	38.94
Gachalá District : Interquartile Range	3.872514	699.8505	2746	2130	1.364702	380	6.4	6.280318	0.901558	7.8
Gachalá District : Standard Deviation	13.09582	507.4213	1475.842	1437.117	6.256347	394.5819	6.279732	6.46186	0.736501	6.55057
Gachalá District : 1 percentile	0.283423	40.604	16.852	16.684	0.064187	129.728	2.9324	3.0692	0.1483	5.7012
Gachalá District : 5 percentile	0.395353	245.0204	48.38	92.6	0.075737	231.2	9.656	9.636989	0.229078	8.834034
Gachalá District : 10 percentile	0.464972	480.6514	372	607.8715	0.086943	282	10.84	11.48	0.306419	9.694441
Gachalá District : 25 percentile	0.961375	707	934	1070	0.182798	359	18.3	18.7	0.58	11.3

Gachalá District : 75 percentile	4.833889	1406.851	3680	3200	1.5475	739	24.7	24.98032	1.481558	19.1
Gachalá District : 90 percentile	9.64	1870	4338	4478.667	6.72	1122.135	29.33617	30.18	1.907	25.58
Gachalá District : 95 percentile	13.77	2016	4634	4918	10.535	1370	31.54	32.62	2.4285	30.5
Gachalá District : 99 percentile	71.907	2131.6	4934.8	5403.6	33.412	2021.2	36.448	37.50797	3.454042	36.376
Maripí District : Count Numeric	212	213	213	213	124	213	213	213	213	213
Maripí District : Minimum	1.52	190	116	116	0.24	116	12.6	12.4	0.83	4.7
Maripí District : Maximum	84.3	8140	6150	6780	68	644	53.6	53.6	5.82	22.6
Maripí District : Mean	6.641132	2587.812	1520.883	1628.23	2.075161	294.1315	31.88404	32.86808	2.784554	9.556009
Maripí District : Median	3.625	1700	997	1070	0.49	283	33.3	34.3	2.59	9.24
Maripí District : Range	82.78	7950	6034	6664	67.76	528	41	41.2	4.99	17.9
Maripí District : Interquartile Range	2.5275	2935	1864	2001	0.5025	130.5	11.95	12.3	1.3	3.51
Maripí District : Standard Deviation	9.313706	2166.276	1311.547	1451.508	7.111794	83.54556	8.609797	8.805841	1.07228	2.675049
Maripí District : 1 percentile	1.6017	191	118.28	120.42	0.2425	128.84	12.628	13.1	0.8628	4.8556
Maripí District : 5 percentile	2.0265	430.7	164.7	163.1	0.26	175.7	17.01	17.37	1.097	5.37
Maripí District : 10 percentile	2.272	464.6	180.8	180.4	0.28	192.4	18.58	19.34	1.482	6.696
Maripí District : 25 percentile	2.8025	1035	456	469	0.34	228	25.2	26.05	2.13	7.59
Maripí District : 75 percentile	5.33	3970	2320	2470	0.8425	358.5	37.15	38.35	3.43	11.1
Maripí District : 90 percentile	19.89	6336	3628	4068	4.56	397.4	42.3	43.7	4.306	13.2
Maripí District : 95 percentile	26.455	7548	4183	4514	7.79	436.8	44.59	45.69	4.836	13.86
Maripí District : 99 percentile	40.962	8080.2	5185	5722	60	494.88	51.09	52.03	5.6086	19.558
Muzo District : Count Numeric	423	424	216	424	345	424	424	424	424	424
Muzo District : Minimum	0.290705	91.56541	56.4	45.96175	0.046514	89	4.533194	4.519671	0.220387	2.57
Muzo District : Maximum	98	7548.525	1970	3718.848	73.1	1390	91.7	61.57172	11.5	32.5
Muzo District : Mean	7.352521	942.76	434.5519	635.5108	0.877681	408.8682	22.16082	22.25776	2.929981	10.44924

Muzo District : Median	3.01	464	257.5	483.5	0.317451	370.8798	19.2	19.42197	2.799145	10.29778
Muzo District : Range	97.7093	7456.96	1913.6	3672.886	73.05349	1301	87.16681	57.05205	11.27961	29.93
Muzo District : Interquartile Range	4.592468	861.7864	381	737.2278	0.229979	299.6993	12.04743	11.57279	2.177652	6.715527
Muzo District : Standard Deviation	12.61861	1047.325	418.2483	586.8302	5.424243	215.2133	11.23566	10.63979	1.682258	4.638539
Muzo District : 1 percentile	0.446933	108.5	59.793	56.075	0.063971	122.5	6.4225	6.57	0.290746	2.895
Muzo District : 5 percentile	0.648216	145	75.48	83.15	0.104405	148.25	8.513343	8.621014	0.712661	3.940322
Muzo District : 10 percentile	0.942468	206.5	90.68	107.4513	0.14786	177.9502	9.925	10.5	1.025	4.27064
Muzo District : 25 percentile	1.667405	329	152	164	0.230022	237.25	14.93443	15.325	1.597302	6.684473
Muzo District : 75 percentile	6.259873	1190.786	533	901.2278	0.46	536.9493	26.98186	26.89779	3.774954	13.4
Muzo District : 90 percentile	19.09511	2412.474	1185	1429.899	0.67	691.5	39.52168	39.25055	5.29	16.15
Muzo District : 95 percentile	33.07177	3041.945	1446	1702.644	1.307	792.75	43.78476	43.26585	5.98	18.31823
Muzo District : 99 percentile	71.268	5530.051	1698.3	2828.181	8.002	1190	55.99987	54.07912	8.241633	23.1
Pauna District : Count Numeric	208	208	208	208	109	208	208	208	208	208
Pauna District : Minimum	1.18	301	141	138	0.2	124	4.81	4.9	0.083	0.4
Pauna District : Maximum	71.3	2810	2160	2300	40.5	2680	25	25.6	4.43	23.6
Pauna District : Mean	7.99	992.4087	660.4423	691.0913	2.560092	479.4327	10.46524	10.81774	0.808572	6.84875
Pauna District : Median	3.51	906	598	611	0.96	407	10.65	10.9	0.63	5.885
Pauna District : Range	70.12	2509	2019	2162	40.3	2556	20.19	20.7	4.347	23.2
Pauna District : Interquartile Range	2.7175	677.25	519.75	566.25	2.435	346.25	3.4625	3.555	0.2975	3.6275
Pauna District : Standard Deviation	12.69156	435.8924	378.8571	411.6008	4.991541	333.0148	2.808406	2.968465	0.615277	3.243648

Pauna District : 1 percentile	1.5918	410.44	144.36	145	0.2	144.25	4.9749	5.1212	0.1709	2.5334
Pauna District : 5 percentile	2.139	471.7	187.35	189.35	0.21	188.45	6.599	6.448	0.349	3.3635
Pauna District : 10 percentile	2.358	553.7	224.9	233.7	0.33	204.7	7.27	7.379	0.38	3.989
Pauna District : 25 percentile	2.68	622.75	351	352.25	0.51	250.25	8.4125	8.745	0.51	4.605
Pauna District : 75 percentile	5.3975	1300	870.75	918.5	2.945	596.5	11.875	12.3	0.8075	8.2325
Pauna District : 90 percentile	21.81	1604	1071	1163	5.52	761.5	13.7	14	1.586	10.8
Pauna District : 95 percentile	35.355	1831	1453	1568.5	8.13	1125.5	15.12	16.1	2.1465	13.62
Pauna District : 99 percentile	69.592	1997.3	1957.3	2096.4	39.19	2188.7	22.368	23.687	3.7121	20.076
Peñas Blancas District : Count Numeric	140	140	140	140	110	140	140	140	139	140
Peñas Blancas District : Minimum	2.4	833	512	528	0.26	53.7	7.9	7.63	0.051	1.51
Peñas Blancas District : Maximum	61.4	4810	5270	5800	217	947	29.2	31.1	7.24	16.3
Peñas Blancas District : Mean	5.699429	2607.871	2346.536	2569.493	5.390636	358.0664	19.47136	20.1245	2.231417	7.260786
Peñas Blancas District : Median	3.985	2710	2175	2360	1.035	387	21.2	21.75	2.4	8.115
Peñas Blancas District : Range	59	3977	4758	5272	216.74	893.3	21.3	23.47	7.189	14.79
Peñas Blancas District : Interquartile Range	2.0575	1582.5	1217.5	1412.5	3.31	282.75	9.35	10.05	2.45	5.885
Peñas Blancas District : Standard Deviation	6.98877	908.6737	1007.723	1149.381	21.46102	197.4787	5.562836	5.779192	1.614061	3.616883
Peñas Blancas District : 1 percentile	2.4205	850.63	573.09	578.84	0.2622	55.914	7.9246	7.8063	0.0518	1.5305
Peñas Blancas District : 5 percentile	2.6355	1201	872.25	889.45	0.3155	87.475	9.7615	10.2	0.13	1.883
Peñas Blancas District : 10 percentile	2.932	1371	1053	1122	0.36	111.1	11.12	11.63	0.24	2.371
Peñas Blancas District : 25 percentile	3.3025	1785	1660	1765	0.5025	179.5	14.55	14.625	0.7	3.6625
Peñas Blancas District : 75 percentile	5.36	3367.5	2877.5	3177.5	3.8125	462.25	23.9	24.675	3.15	9.5475
Peñas Blancas District : 90 percentile	8.329	3569	3758	4070	9.511	579.7	25.79	26.59	4.3	11.3
Peñas Blancas District : 95 percentile	12.235	3736.5	4662.5	5219.5	14.8	727.9	27.29	28.295	4.73	13.635
Peñas Blancas District : 99 percentile	57.136	4810	5245.4	5791.8	198.872	938.8	29.118	30.895	7.068	16.013
Somondoco District : Count Numeric	45	45	45	45	10	45	45	45	45	45
Somondoco District : Minimum	1.72	117	169	171	0.23	156	8.2	8.18	0.4	8.16
Somondoco District : Maximum	43.7	795	830	881	16.6	510	29.3	31.6	6.21	26.5

Somondoco District : Mean	4.936667	437.9111	417.2667	429.8667	3.446	220.6222	15.87489	16.36467	1.341333	11.638
Somondoco District : Median	3.61	438	428	421	0.445	207	16.3	16.8	1.16	11.1
Somondoco District : Range	41.98	678	661	710	16.37	354	21.1	23.42	5.81	18.34
Somondoco District : Interquartile Range	1.725	163.5	251	268	5.0375	45	2.3	2.65	0.255	1.9
Somondoco District : Standard Deviation	6.918724	144.8047	174.8887	188.0397	5.39466	62.59331	3.503198	3.797878	0.836262	2.964582
Somondoco District : 1 percentile	1.72	117	169	171	0.23	156	8.2	8.18	0.4	8.16
Somondoco District : 5 percentile	2.053	122.3	177.9	180.3	0.23	157.8	8.425	8.962	0.55	8.321
Somondoco District : 10 percentile	2.172	228.4	196.8	195.8	0.23	167.6	10.56	10.64	0.946	9.486
Somondoco District : 25 percentile	2.5	373.5	291.5	289.5	0.2675	186	14.95	15.3	1.07	10.1
Somondoco District : 75 percentile	4.225	537	542.5	557.5	5.305	231	17.25	17.95	1.325	12
Somondoco District : 90 percentile	5.902	607.2	654	686	15.832	285.6	18.58	19.04	1.818	14.64
Somondoco District : 95 percentile	20.538	640.3	794.9	853.6	16.6	364.4	20.41	21.7	2.584	17.38
Somondoco District : 99 percentile	43.7	795	830	881	16.6	510	29.3	31.6	6.21	26.5
Ubalá District : Count Numeric	131	132	132	132	106	132	132	132	132	132
Ubalá District : Minimum	1.71	613	144	139	0.3	249	8.82	8.87	0.9	11.5
Ubalá District : Maximum	62	5040	8480	9080	638	7500	47.9	49.1	5.29	30.3
Ubalá District : Mean	4.834198	2316.606	3262.106	3562.5	8.904906	536.1439	20.93689	21.71644	2.12447	19.33561
Ubalá District : Median	3.18	2115	2815	3120	0.8	451.5	18.8	19.5	1.85	19.35
Ubalá District : Range	60.29	4427	8336	8941	637.7	7251	39.08	40.23	4.39	18.8
Ubalá District : Interquartile Range	1.21	2032.5	1540	1732.5	2.3	199.25	10.95	11.275	0.9575	4.275
Ubalá District : Standard Deviation	7.661105	1228.172	2058.099	2232.569	61.914	635.6303	7.3845	7.709196	0.80248	3.75819
Ubalá District : 1 percentile	1.8028	660.52	145.32	141.97	0.3007	249.66	9.1269	9.4409	0.9198	11.797
Ubalá District : 5 percentile	2.156	809.05	802.4	800.5	0.3535	297.95	12.365	12.6	1.292	13.465
Ubalá District : 10 percentile	2.292	1000	1292	1333	0.387	315.5	13.16	13.73	1.42	14.33
Ubalá District : 25 percentile	2.71	1170	1820	1977.5	0.4975	359	15.025	15.7	1.615	16.8
Ubalá District : 75 percentile	3.92	3202.5	3360	3710	2.7975	558.25	25.975	26.975	2.5725	21.075
Ubalá District : 90 percentile	5.89	4285	6811	7416	10.6	670.7	30.44	31.72	3.207	23.8

Ubalá District : 95 percentile	12.08	4632	7843.5	8381	14.095	1017	34.69	36.22	3.731	26.64
Ubalá District : 99 percentile	60.752	5036.7	8430.5	9066.8	595.79	5411.1	46.019	47.516	5.1382	30.102